Experimental entanglement distillation of continuous-variable optical states

Tim J. Bartley
St Hugh's College, University Oxford



Submitted in partial fulfilment of the requirements for the degree of Doctor of Philosophy
Trinity Term 2013

Supervised by
Prof. Ian A. Walmsley

Clarendon Laboratory
University of Oxford
United Kingdom

To my father, *in memoriam*.

Experimental entanglement distillation of continuous-variable optical states

Tim J. Bartley
St Hugh's College, University of Oxford

Submitted for the degree of Doctor of Philosophy
Trinity Term 2013

Abstract

Entangled photons are ideally suited to the transmission of photonic quantum information. Mitigating the effects of decoherence is fundamental to distributing photonic entanglement across large distances. One such proposal is entanglement distillation, in which operations on a large ensemble of weakly entangled states generate a smaller ensemble of more strongly entangled states.

In this thesis, we experimentally and theoretically analyse various tools required for demonstrating continuous-variable (CV) entanglement distillation, following the proposal by Browne et al., [Phys. Rev. A **67**, 062320 (2003)]. Specifically, we propose figures of merit to account for the practical limitations of non-deterministic non-Gaussian operations, and analyse the experimental parameters necessary to optimise them. We develop a source of pulsed two-mode squeezed states, which are the initial states of our entanglement distillation protocol. We use weak-field homodyne detection as a phase-dependent photon counting detector, and demonstrate its utility in conditional state generation. Using these states, we demonstrate sub-binomial light as a tool for benchmarking quantum states. Finally, we applied two-mode weak-field homodyne detection to two entangled states and demonstrate correlations in the photon counting statistics which depend on a joint phase from two independent local oscillators. This setup is sufficient to apply an entanglement witness developed by Puentes et al. [New J. Phys. **12**, 033042 (2010)]. Despite encouraging simulations, we do not witness entanglement with this scheme, which we attribute to a noise source unaccounted for in the simulations.

Although we do not demonstrate entanglement distillation outright, the tools we develop to do so represent a general, hybrid approach to CV quantum optics. Developing tools such as phase-resolved projective measurement on two-mode states allows us to probe both the wave and particle nature of entangled light at the single-photon level. Using and expanding these techniques to probe larger quantum systems may prove useful in studies of fundamental physics and quantum enhanced technologies.

Acknowledgements

First and foremost I must thank my supervisor Ian Walmsley. His encouragement and support was unwavering, be it after long hours in the laboratory or indeed long hours in the saddle. Thanks too for fostering such a fulfilling and collaborative research group within which to work. The day-to-day grind of counting photons should never have been so much fun.

I am extremely grateful to postdocs with whom I have worked over the last four years. Brian: thanks for laying the foundations to my career in Oxford; Lijian and Animesh: thanks for your patience with my forays into theoretical physics, I got there in the end; Xian Min and Marco: thanks for your experimental guidance, limitless ideas and ability to match scientific substance with style; and Josh, for your optimism, encouragement of crazy ideas and constant supply of tea.

Thanks must also go to the other students whom have shared the highs and lows of the distillation setup. Thanks to my predecessor Hendrik, from whom I learnt so much about the vagaries of aligning down-conversion; and best of luck to my successors Gaia and Mihai—the next generation of experiments are right round the corner!

To the rest of the Ultrafast group over the years, you've all made it such a great place to do physics. Dane, Adam, Andrea, Matthias, Illaria, Charles: you always had too many photons for my liking but I did learn a thing or three about big fat lasers. Klaus, KC, Patrick, Michael, Tessa: remembering those photons looks like herding cats. Nick, Ben, Justin, Peter, Merritt: the future may well be integrated after all. And Merlin, Laura, Christoph and Michal: thanks for keeping Brian occupied.

Thanks too to the collaborators who've been extremely helpful over the years: Earl and Jens in Berlin, and Thomas and the group at NIST. And thanks to the support staff in the Clarendon, in particular Sue Gardener, for holding the department together.

Special thanks to Duncan (not a bad fielder for the worst sportsperson in his family) who taught me there *is* such a thing as a free lunch; to Monty: when's the next road trip? Next time it'll have to be an open-top Mustang; to Dave: many apologies for dismissing most of your family the day after the day before the greatest day of your life; and Steve: we really should publish together sometime.

Since there's more to life than physics, I must extend thanks to those who've kept me sane over the last four years. To Lisa, Alison, Navid and the rest at St Hugh's: we made it! Also thanks to my housemates over the years for keeping our houses physics-free zones: Inga, Laura, Mike, Will, Craig, Kat and Betts.

Finally, I must thank my family, who, despite not always understanding what exactly I've been doing for four years, provided fantastic support, encouragement and love throughout. Thanks to Aurélie for always keeping me smiling. Thanks to Mum for always showing an interest and asking questions, whether or not my explanations were convincing, and additional thanks for a thorough proof-read; and thanks to Luke, for always keeping my feet on the ground. And finally, thanks to Dad. Although he will not see the final outcome of the last four years, he had every faith I'd get there in the end.

Contents

1 Introduction **1**
- 1.1 Thesis overview . . . 9
  - 1.1.1 Aims . . . 9
  - 1.1.2 Outline . . . 9
- 1.2 Publications . . . 11
- 1.3 Contribution of the Author . . . 12

2 Background: Quantum Optics **14**
- 2.1 Continuous variables of the electromagnetic field . . . 14
  - 2.1.1 The quantum harmonic oscillator . . . 15
  - 2.1.2 Quantizing the electromagnetic field . . . 16
- 2.2 Modes versus photons . . . 18
  - 2.2.1 States and bases . . . 18
  - 2.2.2 Phase space . . . 23
  - 2.2.3 The Wigner function . . . 24
  - 2.2.4 Gaussian states and operations . . . 27
- 2.3 Entanglement of continuous variables . . . 28
  - 2.3.1 Inseparability . . . 29
  - 2.3.2 Two-mode squeezing . . . 30
  - 2.3.3 Properties of a two-mode squeezed state . . . 31
  - 2.3.4 Quantifying entanglement . . . 34
- 2.4 Distilling entanglement . . . 36
  - 2.4.1 Continuous-variable entanglement distillation . . . 37
  - 2.4.2 The BESP protocol . . . 38

3 A practical approach to entanglement-enhancing non-Gaussian operations **40**
- 3.1 Entanglement-enhancing non-Gaussian operations . . . 41
  - 3.1.1 Photon subtraction . . . 42
  - 3.1.2 Photon addition . . . 43
  - 3.1.3 Photon replacement . . . 45
- 3.2 An operational approach to entanglement distillation . . . 47
  - 3.2.1 Figures of merit . . . 48

3.2.2 Utility . . . 53
3.2.3 Teleportation . . . 58
3.2.4 Concluding remarks . . . 62
3.3 Photon subtraction: a detailed analysis . . . 63
3.3.1 Entanglement gain and rate . . . 64
3.4 The lossy protocol . . . 66
3.4.1 Subtraction . . . 69
3.5 Subtraction using PNRDs . . . 71
3.5.1 Probability of photon subtraction . . . 71
3.5.2 Lossless symmetric subtraction . . . 72
3.5.3 Lossless asymmetric subtraction . . . 75
3.5.4 Losses and imperfect detection . . . 80
3.5.5 Losses in asymmetric subtraction . . . 84
3.6 Subtraction with threshold detectors . . . 85
3.6.1 Probability of photon subtraction using APDs . . . 86
3.6.2 Lossless subtraction . . . 87
3.6.3 Lossy subtraction . . . 88
3.7 Conclusion . . . 89

4 Two-mode squeezed state source engineering 91
4.1 Source requirements . . . 92
4.1.1 Modal definition . . . 92
4.1.2 Re-Gaussification . . . 94
4.1.3 Initial squeezing . . . 96
4.2 Source hardware . . . 97
4.2.1 Laser system . . . 98
4.2.2 Second harmonic generation . . . 100
4.2.3 Parametric down-conversion . . . 102
4.3 Source alignment . . . 103
4.3.1 Initial bright beam alignment . . . 103
4.3.2 Blue alignment . . . 105
4.3.3 Coincidences . . . 106
4.3.4 Troubleshooting tips and tricks . . . 108

5 Measuring local quantum states 111
5.1 Measurement . . . 111
5.1.1 Projective measurement . . . 112
5.1.2 Positive operator valued measures . . . 113
5.2 Detection . . . 114
5.2.1 On-off detectors . . . 115
5.2.2 Photon-number resolving detectors . . . 115
5.2.3 Quadrature detection . . . 118
5.3 Weak-field homodyne detection . . . 120
5.3.1 Joint statistics . . . 121

5.3.2 Practical weak-field homodyne detection . . . 122
5.4 Phase stability and control . . . 127
5.4.1 Passive stability: scope of the problem . . . 127
5.4.2 Active stabilisation . . . 130
5.4.3 Active stability and arbitrary phase setting . . . 131
5.5 Conditional state preparation with weak-field homodyne detection . 136
5.5.1 Non-Gaussian state generation . . . 136
5.5.2 Photon-catalysed optical coherent (PCOC) states . . . 137
5.5.3 Non-classical features of PCOC states . . . 139
5.5.4 Higher-order catalysis . . . 144
5.5.5 Experimental generation of PCOC states . . . 145
5.5.6 Concluding remarks . . . 149
5.6 Sub-binomial light . . . 150
5.6.1 Characterising optical states . . . 151
5.6.2 The SVA parameter . . . 152
5.6.3 Demonstrating sub-binomial light . . . 153

6 Measuring non-local quantum states 158
6.1 Local and non-local phase dependence . . . 159
6.1.1 Demonstrating phase coherence . . . 160
6.1.2 Single-mode measurement of a two-mode state . . . 161
6.1.3 Joint measurements . . . 162
6.1.4 Two-mode weak-field homodyne detection . . . 163
6.2 Non-local phase dependence of a split single photon (SSP) . . . 164
6.2.1 Experimental two-mode weak-field homodyne detection . . . 167
6.3 Non-local coherence of a two-mode squeezed state . . . 173
6.3.1 Phase dependence . . . 173
6.3.2 Experimental demonstration . . . 175
6.3.3 Concluding remarks . . . 181
6.4 Witnessing entanglement . . . 182
6.4.1 A CV entanglement witness . . . 183
6.4.2 Witnessing entanglement experimentally . . . 184
6.4.3 Comparison with simulation . . . 190
6.4.4 Concluding remarks . . . 194

7 Conclusions and outlook 197
7.1 Summary of results . . . 198
7.1.1 A practical analysis of probabilistic non-Gaussian operations 199
7.1.2 Developing a pulsed source of two-mode squeezed states . . . 199
7.1.3 Single-mode measurement with weak-field homodyne detection 200
7.1.4 Two-mode weak-field homodyne detection . . . 202
7.2 Outlook . . . 203
7.2.1 Integration on-chip . . . 204

A Position, momentum and ladder operators **206**
A.1 Ladder operators . . . 206
A.2 Relating $\hat{a}, \hat{a}^\dagger$ with $\hat{x}, \hat{p}$ . . . 207
A.3 Relating position and momentum to quadrature operators . . . 209

B Calculating quadrature expectation values and variances **210**
B.1 Single-mode quadratures . . . 210
B.2 Two-mode quadratures . . . 212
B.2.1 Excess variance . . . 213
B.2.2 Properties of common states . . . 213

C Calculating the log-negativity of a pure two mode squeezed state **215**

D Properties and calculations of photon-replaced states **217**
D.1 Single-mode states . . . 217
D.2 Two-mode states . . . 218
D.2.1 Probability of photon-replacement . . . 218
D.2.2 Entanglement of photon replacement . . . 218
D.2.3 Quadrature variance . . . 219

E Hardware specifications **220**
E.1 Avalanche photodiodes . . . 220
E.2 Coincidence counting electronics . . . 220
E.2.1 NIM . . . 220
E.2.2 FPGA . . . 221

F Active phase stabilisation based on two modes **222**
F.1 Introduction . . . 222
F.2 Continuous phase measurement using two modes . . . 224
F.3 Experimental setup . . . 224
F.3.1 Calibration . . . 225
F.3.2 Feedback . . . 225
F.4 Results . . . 226
F.5 Conclusion . . . 227

G Weak-field homodyne state evolution **228**
G.1 Split single photon . . . 228
G.1.1 Probabilities . . . 230
G.2 Parametric down-conversion . . . 232
G.2.1 Probabilities . . . 234

List of Figures

1.1 Measurement outcomes of tossing a coin 2

2.1 PDC schematic 22
2.2 Wigner functions 24

3.1 Conditional operations on a two-mode squeezed state 42
3.2 Photon subtraction model 42
3.3 Photon addition model 44
3.4 Single-mode and two-mode photon replacement 46
3.5 Entanglement following non-Gaussian operations 49
3.6 Probability of non-Gaussian operations 50
3.7 Combined entanglement and probability 51
3.8 Entanglement rate 52
3.9 Difference in entanglement following non-Gaussian operations 53
3.10 Entanglement enhancement rate 54
3.11 Excess variance 55
3.12 TMSS fidelity 57
3.13 Bell state fidelity 58
3.14 Teleportation fidelity 60
3.15 Teleportation fidelity depending on λ 61
3.16 Teleportation fidelity as a function of entanglement 62
3.17 Modelling lossy photon subtraction 66
3.18 Perfect, symmetric single-photon subtraction with PNRDs 74
3.19 Lossless symmetric subtraction with PNRDs 76
3.20 Lossless symmetric and asymmetric subtraction with PNRDs 79
3.21 Lossy symmetric subtraction with PNRDs. 80
3.22 Lossy symmetric subtraction with PNRDs 84
3.23 Lossy asymmetric subtraction with PNRDs 85
3.24 Lossy asymmetric subtraction using PNRDs 85
3.25 Comparing lossless subtraction strategies between APDs and PNRDs. 86
3.26 Lossy subtraction with APDs 88
3.27 Comparing symmetric and asymmetric subtraction with APDs under loss. 89

4.1 Joint spectral intensity examples . . . 96
4.2 Schematic of the elements of the experiment . . . 97
4.3 Laser system . . . 98
4.4 Second harmonic generation . . . 100
4.5 Parametric down-conversion . . . 103
4.6 General detection setup . . . 105

5.1 Time-multiplexed detector . . . 117
5.2 Homodyne detection . . . 119
5.3 Weak-field homodyne detection . . . 121
5.4 HOM dip setup . . . 124
5.5 HOM dip . . . 125
5.6 Phase measurement setup . . . 128
5.7 Spectral interference . . . 129
5.8 Unstabilised phase noise . . . 129
5.9 HeNe stabilisation setup . . . 133
5.10 Stabilised fringe pattern . . . 134
5.11 Berry-phase setup . . . 135
5.12 PCOC state schematic . . . 138
5.13 Probability of photon catalysis . . . 140
5.14 PCOC properties: quadrature squeezing . . . 141
5.15 PCOC and Schrödinger kitten state Wigner functions . . . 143
5.16 Higher-order PCOC state Wigner functions . . . 145
5.17 PCOC experimental setup . . . 146
5.18 PCOC photon statistics . . . 147
5.19 PCOC second-order autocorrelation function . . . 149
5.20 Comparing the Mandel and SVA parameters . . . 154
5.21 Joint click statistics arising directly from parametric down-conversion 156
5.22 Sub-binomial light from parametric down-conversion . . . 157

6.1 Split single photon . . . 160
6.2 Two-mode weak-field homodyne detection . . . 164
6.3 Non-local interference between a split single photon and independent coherent states . . . 165
6.4 Interference visibility as a function of local oscillator intensities of two-mode weak-field homodyne detection of a split single photon state 166
6.5 Experimental setup for two-mode weak-field homodyne detection of a split single photon state . . . 167
6.6 Local measurements on a split single photon state . . . 169
6.7 Phase-dependent joint statistics of weak-field homodyne detection on a split single photon state . . . 171
6.8 Marginal distributions of two-mode weak-field homodyne detection of a split single photon state . . . 172

6.9 Two-mode interference between a two-mode squeezed state and independent coherent states 174
6.10 Interference visibilities from two-mode weak-field homodyne detection on a two-mode squeezed state 174
6.11 Two-mode weak-field homodyne detection of a two-mode squeezed state 175
6.12 Marginal distributions of a two-mode weak-field homodyne detection of a TMSS 177
6.13 Raw joint statistics of weak-field homodyne detection on a two-mode squeezed state 178
6.14 Joint statistics of weak-field homodyne detection on a two-mode squeezed state corrected for polarisation steering 179
6.15 Graphical representation of witness 186
6.16 Setup for characterising TMSS and LO 187
6.17 Joint photon number distributions for TMSS and LO 188
6.18 Difference between simulated and measured data as a function of λ . 193
6.19 Difference between simulated and measured data as a function of fraction of vacuum mixed with the state 194

F.1 Setup for arbitrary-phase stabilisation scheme based on orthogonal polarisation modes 223
F.2 Calibration data and stability results for a stabilisation scheme based on orthogonal polarisation modes 226

Chapter 1

Introduction

The phenomenon of entanglement lies at the heart of quantum mechanics, encapsulating much that is counter-intuitive and distinctly non-classical about our description of nature. Entanglement manifests itself as particular correlations between spatially separated systems; correlations that Einstein famously attributed to "spooky action at a distance" [1].

To illustrate entanglement, consider a fair coin. When the coin is tossed, it will land showing a specific face (heads or tails) and with a particular orientation (with its face right-side up or upside down), as shown in figure 1.1.

In the language of quantum mechanics, the face and the orientation of the coin are known as *observables*; they can be determined from the outcome of a measurement. To find the value of a particular observable, one must ask an appropriate question. More formally, the outcome of a particular measurement depends on the *basis* in which that measurement is made. One may ask the question "did the coin land

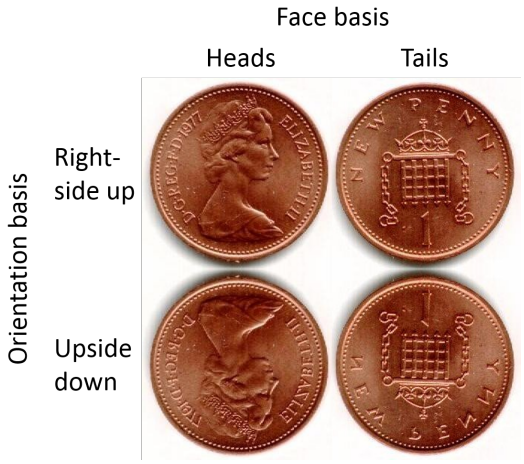


Figure 1.1: When tossing a coin, it will land either heads or tails, and with the symbols facing either right-side up or upside down. We term these the different "measurement bases." Classically, the outcomes of measurements in each basis are independent of the order in which the measurements were made. Quantum mechanically, measurement outcomes on conjugate observables will change.

heads?" *i.e.* what is its value in the "face" basis? Similarly one can ask "did the coin land right-side up?" *i.e.* what is its value in the "orientation" basis?

In classical physics, one can easily determine both the face and orientation of the coin simultaneously. One could first determine that a coin is heads, and subsequently that it is orientated the right way up. Reversing the order of the questions asked of the coin does not change the answers. In contrast, a fundamental feature of quantum mechanics is that this need not be the case. For some pairs of observables, measurements do not *commute*. That is to say, the outcomes of measurements on independent observables will change depending on the order in which they were carried out. A perfectly valid set of measurement outcomes on a quantum coin could be first measuring heads, then measuring right-side up orientation, and then tails. This is an example of measurements in *non-commuting* bases on *conjugate*

observables.

The situation can get even more counterintuitive when one considers two quantum coins. If the two coins are independent, tossing each coin multiple times will generate two different random strings of heads and tails, or a random string of ups and downs, depending on the basis in which one chooses to make the measurements. However, if the coins are *entangled*, the situation changes. While the string of heads/tails and ups/downs will be random when looking at outcomes for a single coin, the string of results for both coins will be identical: the results are completely correlated. This correlation exists *independently whether you choose to measure face or orientation.* Moreover, these correlations between entangled objects persist regardless of their spatial separation: one coin could be on the moon while the other is on Mars. Provided both coins are measured in the same basis, the outcomes will be completely correlated.

The conclusion is that these coins cannot be described separately, rather their state exists somehow delocalised in space. The notion of *nonlocal inseparability* is used to qualify formally the degree of entanglement, and there exists strong experimental evidence for this bizarre phenomenon [2–11].

The quantum coins described above are examples of two-dimensional systems; measurement outcomes in these bases are dichotomic. The idea of entangled systems can be readily extended to higher dimensions. Rolling a quantum die would have six possible outcomes in the number basis, so is six-dimensional. Quantum coins and dice are examples finite-dimensional, discrete-variable quantum systems. Entangle-

ment can also exist among properties that are described by continuous variables, which allow infinitely many measurement values.

We illustrate this with an example proposed by Einstein, Podolsky and Rosen in 1935, which is one of the earliest descriptions of entanglement [12]. They considered the position and momentum of a pair of particles, which are both continuous variables. If the particles are allowed to interact elastically, then their positions and momenta become correlated. According to classical mechanics, given precise knowledge of the initial conditions, interaction and environment, one can calculate the final positions and momenta of each particle. This may be difficult in practice, but in quantum mechanics, this is impossible even in principle. For a pair of conjugate (non-commuting) variables, of which position and momentum are an example, Heisenberg's uncertainty principle [13] states that one cannot gain arbitrary knowledge of one without losing precision in a measurement of the other.

Thus a paradox arises: I can measure precisely the position of one particle, and infer precisely the position of the second particle based on their correlation. Similarly, I can precisely infer the momentum of one particle based on measurements of the other. In this way, the measurement of one particle appears to define *instantaneously* the properties of another, regardless of their mutual separation.

Following these arguments, Einstein, Podolsky and Rosen concluded that "the quantum-mechanical description of physical reality given by the wave functions is not complete." In short, they believed that quantum mechanics required further "hidden" variables to fully account for the apparent violation of information travel-

ling instantaneously, *i.e.* faster than the speed of light. However, the authors note that

> "One could object to this conclusion ... if one insisted that two or more physical quantities can be regarded as simultaneous elements of reality *only when they can be simultaneously measured or predicted.* ... This means the reality of [canonical variables] P and Q depend upon the process of measurement carried out on the first system, which does not disturb the second system in any way. No reasonable definition of reality could be expected to permit this."

The implicit assumption here is one of local realism of each system. This assumption is completely consistent with Einstein's own theory of relativity; the idea that measurements on one subsystem could instantaneously affect the state of another would have been impossible to accept.

The resolution to this apparent superluminal interaction was alluded to in the explanation of entanglement above. The definition of entanglement as a nonlocal superposition state means one cannot choose which particular state to project the other particle into, therefore one cannot "send" anything other than a random set of measurement outcomes. Since no information can be sent in a random data set, there is no violation of faster-than-light travel. This is known as the *no signalling theorem*[14].

In certain scenarios, such as cryptography, sharing a set of random but completely correlated measurement outcomes is extremely useful. Such random numbers

form the basis of secret keys with which data can be completely securely encoded. This process is extremely potent and forms the basis of the first demonstrable application of entanglement[1].

From what was initially thought of as a disconcerting consequence of quantum mechanics, entanglement now has become an important resource in the burgeoning field of quantum information processing. This transition, from oddity to commodity, was borne out of our ability to measure and quantify the effects of entanglement. The field of quantum information science[17] began to be formulated towards the end of the 20th century to exploit quantum effects to provide enhancement on classical computation[18,19], facilitating provably secure communication[15,20] and enabling resource-efficient metrology[21,22]. Since then, a significant research effort has been made in advancing the capabilities of these schemes and making them more practical under real-world conditions.

Quantum information and communication protocols are based on the fact that a quantum system may exist in a coherent superposition of states, and that these superpositions can exist across different measurement bases and persist nonlocally, characteristic of entanglement. The limiting factor when using entanglement as a resource is its inherent fragility. Any interaction of entangled states with the environment causes decoherence and the entanglement is degraded. At best, this manifests itself as a decrease in the success rates of quantum algorithms; at worst,

[1]Strictly speaking, entanglement is a sufficient but not necessary resource for quantum key distribution. The original protocol, set out by Bennett and Brassard in 1984[15], is equivalent to the entanglement-based protocol put forward by Ekert in 1991[16]. A necessary condition is that the quantum channel does not "break" entanglement, *i.e.* that coherent superpositions (nonlocal or otherwise) are maintained.

it may prevent the algorithms all together. The motivation in this thesis, therefore, is to reduce the effect of such decoherence processes, or, where this is not possible, compensate for them. One scheme to achieve this is entanglement distillation, a protocol designed to increase the amount of entanglement available to implement a quantum communication scheme. It consists of transforming an ensemble of weakly entangled states into a smaller ensemble of more highly entangled states [23].

Optics is well-established as the most efficient means of long-distance communication. Photons interact very weakly with their surroundings and each other, since they are massless and chargeless, therefore losses can be low. Additionally, the energy of photons—a few eV—is far greater than room temperature, therefore thermal noise is negligible. Thus it makes sense to use *quantum* optics to implement *quantum* communication and investigate a quantum optical entanglement distillation protocol.

Such distillation protocols exist in the discrete-variable regime [23] and have been demonstrated experimentally [24]. For optical continuous variables—the quadratures of the electromagnetic field analogue of the position and momentum—equivalent protocols also exist [25–27], with partial demonstration [28–32].

In general, single-photon realisations tend to be more established than their continuous-variable (CV) counterparts, due in part to the theoretical simplifications invoked when dealing with discrete systems. However, producing such discrete-variable (DV) states is, in general, probabilistic. By contrast, some continuous-variable states can be generated deterministically. However, protocols based on

CV states contain inherent errors arising from their non-orthogonality; the states' probability distributions spread across a continuous space meaning every continuous-variable state shares some non-zero overlap with every other. The difference between the discrete and continuous regimes is neatly summarised by Braunstein and van Loock[33]:

> "...in the most commonly used optical approaches, the continuous variable implementations *always* work *pretty well*, but never perfectly. Their discrete-variable counterparts only work *sometimes*, but they succeed, in principle, *perfectly*."

The apparent deterministic nature of CV protocols, albeit with errors, is highly attractive. However, it is only when the continuous variables involved exist in Gaussian states, and undergo Gaussian operations, that deterministic protocols exist in practice. What it means for a state or operation to be Gaussian will become apparent in subsequent chapters.

The "elephant in the room" in the CV domain is that certain CV protocols, of which entanglement distillation is one example, require non-Gaussian states. Such states cannot easily be deterministically produced from Gaussian input states. However, such protocols do tend to maintain their in-built loss tolerance. One can think of this as follows: it is impossible to lose a mode (measurements on which determine the protocol), whereas it is easy to lose photons. In the DV regime, this means photonic information is lost to the environment, reducing the data rate and potentially impacting *e.g.* the security of a cryptography protocol. In the CV case, losing

photons from the mode under investigation just reduces data rate; in principle, the security implications of the lost photons can be mitigated against [34]. It is added noise, rather than loss, that impacts the efficacy of a CV protocol.

1.1 Thesis overview

1.1.1 Aims

The principle aim of this thesis was to develop the experimental and theoretical tools necessary to demonstrate the CV entanglement distillation protocol developed by Browne, Eisert, Scheel and Plenio (BESP) [25]. Our experimental starting point comprised the source of entanglement developed by Mosley [35] and CV detector characterisation work by Coldenstrodt-Ronge [36]. As it turned out, combining these technologies led to a lot of very interesting and novel physics. Against the background of CV distillation, we aimed to show the wider implications of the role that discrete variables—photons—play in CV quantum optics. To that end, we have investigated non-Gaussian state generation [37], quantum-classical state discrimination [38] and fundamental investigations of non-local wave-particle duality.

1.1.2 Outline

This thesis is organised into seven chapters. In chapter 2 we introduce the background theory on which the rest of the thesis is based. We take a pedagogical approach to emphasise how continuous variables exist in a fundamentally quantised theory. We conclude chapter 2 with a brief summary of the CV distillation protocol

under investigation.

In chapter 3 we develop novel metrics for assessing the feasibility of non-Gaussian operations by incorporating success probability into the analysis. We analyse several such operations in detail, with respect to the distillation protocol as well as a number of other figures of merit. We pay special attention to photon subtraction, the most experimentally feasible non-Gaussian operation, particularly its behaviour under loss. We analyse variations of the subtraction protocol and optimise over a variety of experimental parameters to determine the most efficient demonstration of the protocol.

In chapter 4, we extend the source engineering work by Mosley [35] to the high-pump-power regime. This source of quantum light produces two-mode squeezed vacuum states, based on type-II collinear parametric down conversion in potassium dihydrogen phosphate (KDP). The alignment procedures are discussed in detail, since pumping in the high power regime leads to a number of changes from the original source.

Chapter 5 presents weak-field homodyne detection as both a phase-sensitive measurement device and a novel state-engineering tool. These states are useful for probing the quantum-classical boundary, and we demonstrate a novel strategy for classifying multiphoton states based on arrays of "on-off" detectors.

In chapter 6 we show how applying weak-field homodyne detection across two modes of an entangled state can show nonlocal coherence across each mode. We also detail progress towards a novel non-Gaussian detection scheme: an entanglement

witness.

Finally, in chapter 7, we conclude with a summary of the main results in this thesis. We place these results in the context of the prospects for continuous-variable entanglement distillation, its scalability requirements and whether weak-field homodyne is best-placed for verifying this scheme.

1.2 Publications

The work presented in this thesis has formed the basis for the following peer-reviewed journal publications:

1. G. Jotzu, **T. J. B.**, H. B. Coldenstrodt-Ronge, B. J. Smith and I. A. Walmsley, "Continuous phase stabilization and active interferometer control using two modes," Journal of Modern Optics, 59 (2012) arXiv:1101.1906
2. **T. J. B.**, G. Donati, J. B. Spring, X.-M. Jin, M. Barbieri, A. Datta, B. J. Smith and I. A. Walmsley "Quantum catalysis of multi-photon non-classical states" Physical Review A 86, 043820 (2012), arXiv:1205.0497
3. **T. J. B.**, P. J. D. Crowley, A. Datta, J. Nunn, L. Zhang and I. A. Walmsley "Strategies for enhancing quantum entanglement by local photon subtraction" Physical Review A 87, 022313 (2013), arXiv:1211.0231
4. M. Vidrighin, **T. J. B.**, G. Donati, X.-M. Jin, M. Barbieri, W. S. Kolthammer, A. Datta and I. A. Walmsley "Requirements for two-source entanglement concentration" Quantum Measurements and Quantum Metrology 1 5-11 (2013), arXiv:1302.3186
5. **T. J. B.**, G. Donati, X.-M. Jin, A. Datta, M. Barbieri and I. A. Walmsley "Direct observation of sub-binomial light" Phys. Rev. Lett. 110, 173602 (editor's suggestion) (2013) arXiv:1302.0229

As a guide to the reader, chapter 3 primarily consists of results published in (3). Chapter 5 contains results in (2,5) and contains work subsuming publication (1), which is reproduced in appendix F. Chapter 7 pertains to publication (4).

In addition, the following have been presented at peer-reviewed conferences:

1. **T. J. B.**, H. Coldenstrodt-Ronge, G. Donati, L. Zhang, A. Datta, X.-M. Jin, B. J. Smith and I. A. Walmsley "Toolbox for robust, scalable distillation of continuous variable entanglement," talk, QIPC'11, Zurich, Switzerland (2011)

2. G. Donati, **T. J. B.**, M. Barbieri, X.-M. Jin, B. J. Smith and I. A. Walmsley "Towards The Realisation of an Entanglement Distillation Protocol" poster, Oxford Photonics Workshop, Oxford, UK (April 2012)

3. **T. J. B.**, G. Donati, X.-M. Jin, M. Barbieri, A. Datta, B. J. Smith and I. A. Walmsley "Direct control of non-classical multi-photon states by quantum catalysis," poster, Oxford Photonics Workshop, Oxford, UK (April 2012)

4. **T. J. B.**, G. Donati, X.-M. Jin, J. B. Spring, M. Barbieri, B. J. Smith, A. Datta, L. Zhang and I. A. Walmsley "Turning classical states quantum with linear optics and photon counting," poster, CLEO:2012, San Jose, CA, USA (2012)

5. **T. J. B.**, G. Donati, M. Barbieri, A. Datta, X.-M. Jin, E. T. Campbell, B. J. Smith, J. Eisert, I. A. Walmsley "Probing entanglement in continuous variable quantum optics," talk, Oxford Photonics Workshop, Oxford, UK (September 2012)

6. **T. J. B.**, G. Donati, X.-M. Jin, A. Datta, M. Barbieri and I. A. Walmsley "Direct observation of sub-binomial light," poster, CLEO:Europe, Munich, Germany (2013)

7. **T. J. B.**, G. Donati, X.-M. Jin, A. Datta, M. Barbieri and I. A. Walmsley "Measuring nonlocal coherence with weak-field homodyne detection," talk, CLEO:Europe, Munich, Germany (2013)

Work in (1,2) are presented in chapter 4, (3,4,6) in chapter 5 and (5,7) in chapter 6.

1.3 Contribution of the Author

As the author lists above show, the work presented herein could not have been completed in isolation and I am very grateful to my colleagues for their support. The foundations of the experiment were laid by two of my predecessors, Peter Mosley [39] and Hendrik Coldenstrodt-Ronge [36]. However, significant and necessary changes to

their original setups were completed, which are entirely my own, details of which are given in chapter 4. I have overhauled the signal processing hardware and software (from the earlier systems used by Mosley and Coldentrodt-Ronge), employing field-programmable gate array (FPGA) electronics developed by another D.Phil student, Justin Spring. This included interfacing with the time-multiplexed detectors (TMDs), with assistance from summer student Adam Katcher.

Following my redesign, all day-to-day alignment and data-taking was carried out by myself, with assistance from D.Phil student Gaia Donati.

Much of the theoretical work was also collaborative. In particular, the analysis of the subtraction strategies in chapter 3 was carried out with significant contributions by all authors listed in the paper above. My work consisted of proposing the problem, including devising the figures of merit, and completing initial calculations, with guidance from Animesh Datta and Lijian Zhang. Further numerics were carried out by Philip Crowley. The final analysis was completed by myself with assistance from Joshua Nunn.

The underlying theory for the witness, detailed in chapter 6, predates this work by several years. However, adapting it and applying it to our data was carried out in the early stages by postdocs Lijian Zhang and Animesh Datta in Oxford, and latterly by Earl T. Campbell with Jens Eisert at the Freie Universtät, Berlin.

Chapter 2

Background: Quantum Optics

In this chapter we will outline the theoretical concepts used in subsequent chapters, in which we investigate the various stages of the entanglement distillation protocol and associated experiments. We begin by defining the optical continuous variables (CV) upon which the protocol is based. We highlight the similarities and differences between the CV and discrete variable (DV) pictures. We describe how CV entanglement between two modes can manifest itself in the joint variance of quadratures of the two-mode system. Finally, we define distillation as a scheme for increasing entanglement between communicating parties, and outline the components required to achieve this using continuous variables.

2.1 Continuous variables of the electromagnetic field

The quantum mechanical theory of the continuous variables of an electromagnetic field is contained in many textbooks; we mainly follow Loudon[40]. Our point of

departure is the quantum harmonic oscillator.

2.1.1 The quantum harmonic oscillator

The one-dimensional harmonic oscillator is one of the quintessential models in physics. In the quantum mechanical picture, variables position x and momentum p are replaced by operators $\hat{x}$ and $\hat{p} = -i\hbar\partial/\partial x$ respectively. The energy in the system is governed by the Hamiltonian

$$\hat{H} = \frac{\hat{p}^2}{2m} + \frac{1}{2}m\omega^2\hat{x}^2 \ , \tag{2.1}$$

for a mass m with angular frequency ω. The time-independent Schrödinger equation,

$$\hat{H}|\psi_n\rangle = E_n|\psi_n\rangle \ , \tag{2.2}$$

yields solutions with quantised eigenenergies

$$E_n = \hbar\omega\left(n + \frac{1}{2}\right) \ , \tag{2.3}$$

where $n \in \mathbb{N}$ and $\hbar = 6.63 \times 10^{-34}/2\pi$ Js is the reduced Planck's constant.

2.1.2 Quantizing the electromagnetic field

As with the harmonic oscillator model, we begin by considering the Hamiltonian that governs the energy contained within an electromagnetic field. This is given by

$$\hat{H} = \int_{\infty} \mathrm{d}r^3 \epsilon_0 \sum_j \hat{E}_j \left(\mathbf{r}, \mathbf{t}\right)^2 \ , \tag{2.4}$$

where $\epsilon_0 = 8.85 \times 10^{-12}\,\mathrm{Fm}^{-1}$ is the permittivity of free space and $\hat{E}_j\left(\mathbf{r}, \mathbf{t}\right)$ is the electric field operator of a mode j. For a plane wave travelling in the $\mathbf{r}$ direction with wavevector $\mathbf{k}_j$, this is defined

$$\hat{E}\left(\mathbf{r}, t\right) = E_{0j}\left[\hat{X}_j \cos\left(\mathbf{k}_j \cdot \mathbf{r} - \omega t\right) + \hat{P}_j \sin\left(\mathbf{k}_j \cdot \mathbf{r} - \omega t\right)\right] \ , \tag{2.5}$$

where $E_{0j} = \sqrt{\frac{2\hbar\omega_j}{\epsilon_0 V}}$ is the amplitude of the field, dependent on the energy $\hbar\omega_j$ contained within the volume V. The quadrature operators $\hat{X}_j$ and $\hat{P}_j$ represent two continuous field-mode amplitude operators oscillating with a phase difference of $\pi/2$—i.e. in quadrature. The Hamiltonian in Eq. (2.4), time-averaged over one cycle, may be written

$$\hat{H} = \sum_j \hbar\omega_j \left(\hat{X}_j^2 + \hat{P}_j^2\right) \ . \tag{2.6}$$

This is identical in form to Eq. (2.1), where the quadrature operators correspond to a dimensionless form of position and momentum. Indeed, following the analysis of

the harmonic oscillator, the Hamiltonian may also be written

$$\hat{H} = \sum_j \hbar\omega_j \left(\hat{n}_j + \frac{1}{2}\right) \ , \tag{2.7}$$

where $\hat{n}_j$ is the number operator of the mode j, which describes its photonic occupation. As detailed in appendix A, one can describe the raising and lowering of the occupation of the mode j by the ladder operators $\hat{a}_j^\dagger$, $\hat{a}_j$ respectively. These are related to the quadrature operators by

$$\hat{X}_j = \frac{1}{2}\left(\hat{a}_j^\dagger + \hat{a}_j\right) \ , \tag{2.8a}$$

$$\hat{P}_j = \frac{\mathrm{i}}{2}\left(\hat{a}_j^\dagger - \hat{a}_j\right) \ , \tag{2.8b}$$

with the commutator

$$\left[\hat{X}, \hat{P}\right] = \frac{\mathrm{i}}{2} \ . \tag{2.9}$$

The explicit relationship between the number operator and quadratures is thus

$$\hat{n}_j = \hat{a}_j^\dagger \hat{a}_j = \hat{X}_j^2 + \hat{P}_j^2 - \frac{1}{2} \ . \tag{2.10}$$

This is the crux of optical continuous variables arising from discrete energy quanta. The electromagnetic field is quantized by associating the discrete eigenenergies n of a quantum harmonic oscillator with an infinite set of radiation modes j, characterised by continuous quadratures X, P.

2.2 Modes versus photons

The concept of photons occupying modes leads to two distinct but complementary frameworks in quantum optics. The discrete variable (DV) picture follows the trajectory of individual photons as they propagate in different modes. By contrast, the continuous variable picture considers the dynamics of the occupation of the modes themselves. While the physical reality of the two descriptions must be equivalent, the mathematics and intuition governing them are rather different. To highlight the distinction, we consider the standard abstraction for describing quantum states.

2.2.1 States and bases

All information about a particular quantum state is contained within its density operator $\hat{\rho}$

$$\hat{\rho} = \sum_j p_j |\psi_j\rangle\langle\psi_j| \ , \tag{2.11}$$

which describes the incoherent mixture of pure states $|\psi_j\rangle$ with classical probability weightings p_j satisfying $\sum_j p_j = 1$. It is typical to express $\hat{\rho}$ as a matrix, and we use the terms "density operator" and "density matrix" interchangeably throughout this thesis. While all states satisfy $\mathrm{Tr}[\hat{\rho}] = 1$, a state is defined to be pure iff $\mathrm{Tr}[\hat{\rho}^2] = 1$. A pure quantum state vector $|\psi\rangle$ may be decomposed into the set of orthonormal basis vectors $\{|\phi_i\rangle\}$, such that

$$|\psi\rangle = \sum_i c_i |\phi_i\rangle \ , \tag{2.12}$$

where the coefficients c_i represent complex probability amplitudes of the basis states $|\phi_i\rangle$, under the constraint $\sum_i^\infty |c_i|^2 = 1$. The state $|\psi\rangle$ along with its abstract basis set $\{|\phi_i\rangle\}$, lives in a vector space known as Hilbert space. In the DV picture, the basis is discrete, and often coincides with a set of modes of an optical field, for example, the two-dimensional polarisation space is spanned by the $|H\rangle$ and $|V\rangle$ basis vectors. In the CV regime, the basis vectors are continuous. Furthermore, due to the superposition principle, a continuous basis can be constructed from the superposition of an infinite set of discrete basis vectors. Indeed, the natural basis for the photonic occupation of a particular mode is the superposition of (discrete) photon numbers $\{|n\rangle\}$. Following Eq. (2.12) one may express CV states as the weighted sum of coefficients in the number basis by

$$|\psi\rangle = \sum_{n=0}^{\infty} c_n |n\rangle \ , \tag{2.13}$$

where the numbers basis states $|n\rangle$ are sometimes referred to as *Fock layers*. The number operator $\hat{n}$ extracts the mean photon number of this superposition, *i.e.*

$$\langle\psi|\hat{n}|\psi\rangle = \sum_{n=0}^{\infty} n|c_n|^2 = \bar{n} \ , \tag{2.14}$$

where we have implicitly used the eigenvalue equation of the number operator

$$\hat{n}|n\rangle = n|n\rangle \ , \tag{2.15}$$

which extracts the discrete occupation n of a particular eigenstate $|n\rangle$.

The quadrature basis

Just as the number operator eigenvalue equation, Eq. (2.15), defines the number basis, the quadrature operators also have a corresponding pair of eigenvalue equations

$$\hat{X}|X\rangle = X|X\rangle \ , \tag{2.16a}$$

$$\hat{P}|P\rangle = P|P\rangle \ , \tag{2.16b}$$

whereby each quadrature basis satisfies the standard orthogonality and completeness conditions. Furthermore, the quadrature eigenstates are related by Fourier transforms:

$$|X\rangle = \frac{1}{\sqrt{2\pi}} \int_{-\infty}^{\infty} \mathrm{d}P \ e^{-\mathrm{i}XP}|P\rangle \ , \tag{2.17a}$$

$$|P\rangle = \frac{1}{\sqrt{2\pi}} \int_{-\infty}^{\infty} \mathrm{d}X \ e^{+\mathrm{i}XP}|X\rangle \ . \tag{2.17b}$$

That $\hat{X}$ and $\hat{P}$ are Fourier transforms of one another implies that a quantum electric field cannot be uniquely defined as a point in quadrature space. The uncertainty arises from their non-commutativity, encapsulated in the Heisenberg uncertainty relation.

Heisenberg uncertainty relation

For any pair of non-commuting Hermitian operators $\hat{A}$, $\hat{B}$, there exists an uncertainty relation (see *e.g.* Bransden and Joachain[41])

$$(\Delta\hat{A})^2(\Delta\hat{B})^2 \geq \frac{1}{4}|[\hat{A},\hat{B}]|^2 \ , \tag{2.18}$$

where the standard deviation of measurement on a general operator $\hat{O}$ is given by

$$\Delta\hat{O} = (\langle\hat{O}^2\rangle - \langle\hat{O}\rangle^2)^{1/2} \tag{2.19}$$

where $\langle\hat{O}\rangle$ dotes the expectation value of the operator $\hat{O}$. From the commutation relation between $\hat{X}$ and $\hat{P}$ in Eq. 2.9, their variances are therefore related by

$$\Delta\hat{X}\Delta\hat{P} \geq \frac{1}{4} \ . \tag{2.20}$$

The significance of this form of the Heisenberg uncertainty relation will become clear when discussing squeezing in subsequent sections.

Squeezing

Heisenberg's uncertainty principle dictates that the product of the variance of conjugate variables must always exceed some minimum value. While the variance of one quadrature may be below this limit, the variance of the conjugate variable must increase to compensate.

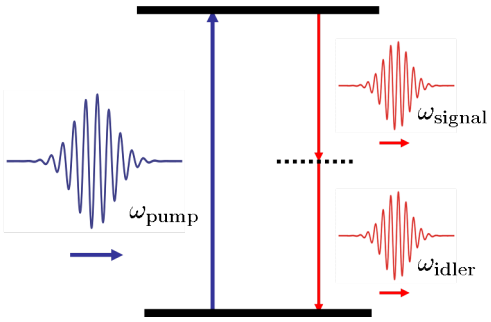


Figure 2.1: Graphical representation of spontaneous parametric down-conversion, the non-linear interaction that produces quadrature squeezing. An input photon with frequency ω_{pump} may spontaneously decay into two daughter photons, with frequencies ω_{signal} and ω_{idler} respectively.

Quadrature squeezing arises from parametric down-conversion (PDC), a second-order non-linear interaction. This interaction is shown graphically in figure 2.1. It is governed by the quadratic (and therefore Gaussian) Hamiltonian

$$\hat{H} = \kappa \hat{a}_i^\dagger \hat{a}_j^\dagger + \kappa^* \hat{a}_i \hat{a}_j \ , \tag{2.21}$$

which describes the creation and annihilation of pairs of photons in modes i and j, modulated by a complex interaction constant κ. For the case $i = j$, the squeezing is in a single mode. For $i \neq j$, the Hamiltonian cannot be separated into separate operators for each mode. Therefore, under the action of this Hamiltonian, a separable initial state of the two modes evolves to an entangled two-mode state, as discussed in section 2.3.2.

For both single- and two-mode squeezing, this Hamiltonian describes a three-wave mixing process in a non-linear material. Note that the pump is treated classically and is contained in the interaction constant κ.

2.2.2 Phase space

In classical physics, objects defined by conjugate variables—*e.g.* their position and momentum—reside in phase space. Analogously, phase space is the space in which the quantum states defined by $\hat{X}$ and $\hat{P}$ reside, whereby the quadratures $X,\ P$ form the orthogonal axes of phase space. An arbitrary quadrature operator can be defined as the linear combination of X and P

$$\hat{Q}(\phi) = X\cos(\phi) + P\sin(\phi)\ . \tag{2.22}$$

As such, an arbitrary basis of phase space is $\{Q, Q'\}$, where $Q' = Q(\phi + \pi/2)$, which is simply a rotation of the axes $\{X, P\}$ by ϕ.

Since the field cannot be defined as a single point in phase space, it is most conveniently represented by a distribution function. Classically, a bivariate probability distribution function should satisfy the conditions of positivity, correct normalisation and return the expected marginal distributions and expectation values for observables. Quantum mechanically, a number of *quasi*-probability distribution functions exist that fulfil some of these criteria, however none meet them all (see *e.g.* Gerry and Knight[42]). Here we concentrate on the Wigner function[43], the properties of which make it ideally suited to the studies that follow in this thesis.

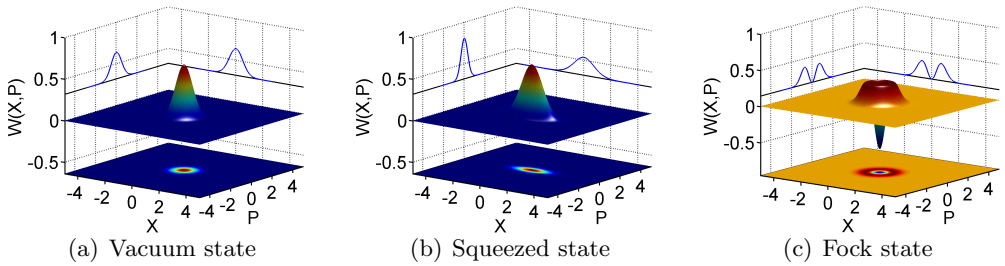
2.2.3 The Wigner function

The Wigner function is a statistical representation of quantum operators in phase space. It fulfils the requirements of correct normalisation, real expectation values and the expected marginal distributions of a classical probability distribution. However, it is not positive-definite. For some operators, the Wigner function may be negative over some region. For an operator $\hat{O}$, it is defined as

$$W_{\hat{O}}(X,P) = \frac{1}{\pi\hbar}\int_{-\infty}^{\infty} \left\langle X-Y \left| \hat{O} \right| X+Y \right\rangle e^{\frac{2iPY}{\hbar}} dY \ , \tag{2.23}$$

where $|X \pm Y\rangle$ are eigenstates of $\hat{X}$ with eigenvalues $X \pm Y$ respectively. Further details on the mathematical origin of the Wigner function can be found in *e.g.* Leonhardt [44] and Gerry and Knight [42].

Since a density operator $\hat{\rho}$ fully describes a quantum state, the Wigner function of the density operator is literally a statistical picture of the state. Examples of the Wigner function of various states are shown in figure 2.2.



(a) Vacuum state (b) Squeezed state (c) Fock state

Figure 2.2: Wigner function representations of (a) the vacuum state, (b) a state squeezed in the P quadrature and (c) a single photon state. The solid lines show the marginal distributions of each distribution.

One property that is used regularly in this thesis is the overlap formula

$$\mathrm{Tr}[\hat{A}\hat{B}] = 2\pi \iint_{-\infty}^{+\infty} W_A(X,P)\, W_B(X,P)\, \mathrm{d}X\mathrm{d}P \ , \tag{2.24}$$

which quantifies the Hilbert-Schmidt inner product [17] of two arbitrary operators $\hat{A},\ \hat{B}$ in terms of their Wigner representations $W_A(X,P)$, $W_B(X,P)$ respectively. The power of this formula can be seen by replacing the arbitrary operators $\hat{A},\ \hat{B}$ with various combinations of density operators and measurement operators. This is particularly useful for illustrating continuous variable states since, in general, their density operators are infinite-dimensional. For example, the coherent state $|\alpha\rangle = \exp\left(-|\alpha|^2/2\right) \sum_{n=0}^{\infty} \frac{\alpha^n}{\sqrt{n!}} |n\rangle$ has components for all n up to infinity, albeit arbitrarily small.

Expectation values

The expectation value of an operator $\hat{A}$ is found by multiplying it by the state $\hat{\rho}$, and then taking the trace, i.e.

$$\langle \hat{A} \rangle \equiv \mathrm{Tr}[\hat{A}\hat{\rho}] \ . \tag{2.25}$$

From Eq. (2.24), it is clear that $\hat{B}$ has been replaced by the density operator $\hat{\rho}$, such that the expectation value may be expressed in terms of the Wigner function as

$$\mathrm{Tr}[\hat{A}\hat{\rho}] = 2\pi \iint_{-\infty}^{+\infty} W_A(X,P)\, W_{\hat{\rho}}(X,P)\, \mathrm{d}X\mathrm{d}P \ . \tag{2.26}$$

This relation is of central importance in quantum operator reconstruction. If one knows the expectation value and Wigner function of $\hat{A}$, then one can extract $W_{\hat{\rho}}(X,P)$ and therefore $\hat{\rho}$ from measurement data. This process is known as quantum state tomography[45,46] and is described extensively in Leonhardt[44]. Conversely, one can probe $\hat{A}$ by acting on known states $\hat{\rho}$ and reconstructing its effect. Depending on the nature of $\hat{A}$, this is either *process tomography*[47,48] or *detector tomography*[49].

State overlap

The inner product of two pure states can be expressed in terms of the overlap of their respective Wigner functions, *i.e.*

$$|\langle\psi_1|\psi_2\rangle|^2 = 2\pi \iint_{-\infty}^{+\infty} W_{\psi_1}(X,P)\, W_{\psi_2}(X,P)\, \mathrm{d}X\mathrm{d}P \ . \tag{2.27}$$

This quantity is zero for orthogonal states and unity for identical states (provided they are pure).

Purity

As stated in section 2.2.1 the purity of a quantum state is $\mathrm{Tr}[\hat{\rho}^2]$. In the quantum Wigner picture, this therefore becomes

$$\mathrm{Tr}[\hat{\rho}^2] = 2\pi \iint_{-\infty}^{+\infty} W_{\hat{\rho}}(X,P)^2\, \mathrm{d}X\mathrm{d}P \ . \tag{2.28}$$

This representation allows the purity of a continuous variable, infinite dimensional state to be readily calculated.

2.2.4 Gaussian states and operations

The Wigner function also helps us to define a subclass of states called Gaussian states. These are states whose Wigner function can be written as Gaussian functions of X and P. Figure 2.2 illustrates two examples of Gaussian states—2.2(a) coherent and 2.2(b) squeezed states. All other pure quantum states, such as the single photon shown in figure 2.2(c), have some negative region in their Wigner distribution and are therefore non-Gaussian [50].

Complementary to Gaussian states are Gaussian operations. These are a class of operations that map Gaussian states onto other Gaussian states. Gaussian operations form the majority of simple linear transformations such as those carried out by beam splitters, phase shifters, squeezers and homodyne detection [51–53]. Such operations are generated by Hamiltonians which are at most quadratic in X and P (or indeed in $\hat{a}$ and $\hat{a}^\dagger$).

Although somewhat restrictive in their definition, Gaussian states are in fact the easiest to generate in the laboratory. This is because laser light emitted in a pure Gaussian state, and the passive optical operations are also Gaussian. Indeed, it is generating non-Gaussian states that is most challenging, techniques for which are developed in this thesis.

Quadrature expectation values in the number basis

Gaussian states and operations, by definition, are uniquely defined by the first and second moments of their distribution $\langle \hat{O} \rangle$, $\langle \hat{O}^2 \rangle$, their mean and variance respectively. This fact is utilised in the covariance matrix representation of such states [54]. While the covariance matrix formalism is a compact and convenient way of describing Gaussian states and operations, more parameters are required to do so for non-Gaussian states. Indeed, since Gaussian states and operations can be simulated with classical computation [55], using covariance matrices in describing the evolution of exotic CV quantum states is limited.

An alternative is to write the state in the photon-number basis $\{|n\rangle\}$, and calculate the quadrature expectation values by expressing the quadratures in terms of creation and annihilation operators. In appendix B, we give general expressions for the first and second moments of the quadrature expectation values for states written in the form of Eq. (2.13). Writing the state in the number basis necessarily includes all information and is readily illustrated by its Wigner distribution by calculating Eq. (2.23). This is typically evaluated numerically, for which the state must be truncated.

2.3 Entanglement of continuous variables

The Wigner function is excellent at depicting single-mode states of the electromagnetic field. For states that exist across multiple modes, the Wigner function depends on the quadratures of each mode, therefore becomes impossible to depict

in 3-D space. Entanglement concerns correlations that exist between such modes—correlations that cannot be understood by classical mechanics alone, or indeed by invoking "local hidden variables." At its core, entanglement manifests itself as a quantum superposition that exists delocalised in space. The concept of states existing delocalised across modes is encapsulated in the definition of entanglement in terms of separability.

2.3.1 Inseparability

If a state cannot be written as two independent systems, it is regarded as inseparable and therefore entangled [56]. Mathematically speaking, the subsystems A and B are inseparable if

$$|\Psi_{AB}\rangle \neq |\psi_A\rangle \otimes |\psi_B\rangle \ , \tag{2.29}$$

where $|\Psi_{AB}\rangle$ is the overall system and $|\psi_A\rangle$ and $|\psi_B\rangle$ are the individual wavefunctions of each subsystem. This means that $|\Psi_{AB}\rangle$ cannot be factorised into a product state in which the subsystems can be treated independently. This formalism can be applied to a density matrix $\hat{\rho}^{AB}$, the subsystems A, B of which are entangled if

$$\hat{\rho}^{AB} \neq \sum_n P_n \hat{\rho}_n^A \otimes \hat{\rho}_n^B \ . \tag{2.30}$$

It is worth noting that whilst this formalism considers just two subsystems A, B (*i.e.* bi-partite entanglement), this may be extended to factorability into many subsystems (multipartite entanglement) [57].

Inseparability extends to any basis, including quadratures. For two-mode quadrature-entangled states, inseparability implies one cannot express the individual quadratures of each mode independently; there exist correlations between them. Furthermore, these "non-local" quadratures must satisfy the Heisenberg uncertainty relation outlined in section 2.2.1. Non-classical correlations between conjugate non-local quadratures thus arise from two-mode squeezing, the foundation of CV entanglement.

2.3.2 Two-mode squeezing

From the Hamiltonian (2.21) we define the two-mode squeezing operator

$$\hat{S}(\zeta) = \exp\left(-\frac{\mathrm{i}t\hat{H}}{\hbar}\right) = \exp\left(-\zeta\hat{a}_1^\dagger\hat{a}_2^\dagger + \zeta^*\hat{a}_1\hat{a}_2\right) , \tag{2.31}$$

where $\zeta = \mathrm{i}\kappa t/\hbar = se^{\mathrm{i}\varphi}$ is a complex constant parameterised by the magnitude s and phase ϕ. Following Barnett and Radmore[58], this operator acts on the vacuum state which generates the state

$$|\zeta\rangle = \hat{S}(\zeta)|0,0\rangle = \mathrm{sech}s\sum_{n=0}^{\infty}(-\exp(\mathrm{i}\varphi)\tanh s)^n|n,n\rangle , \tag{2.32}$$

where the ket $|n,n\rangle = |n\rangle_A \otimes |n\rangle_B$ indicates that the photon numbers are correlated across two modes A and B. It is customary to make the substitution $\lambda = -e^{\mathrm{i}\varphi}\tanh s$,

whereby $0 \leq \lambda < 1$, such that the two-mode squeezed state (TMSS) may be written

$$|\psi_{\text{TMSS}}\rangle = \sqrt{1-\lambda^2} \sum_{n=0}^{\infty} \lambda^n |n, n, \rangle \ . \tag{2.33}$$

From the definition of the density operator, Eq. 2.11, $\hat{\rho}_{\text{TMSS}}$ is given by

$$\hat{\rho}_{\text{TMSS}} = \left(1-\lambda^2\right) \sum_{n} \lambda^{2n} |n, n\rangle\langle n, n| \ . \tag{2.34}$$

2.3.3 Properties of a two-mode squeezed state

Given this expression for the density operator for the TMSS, we can calculate a number of properties.

Mean photon number

When looking at the properties of a single mode of a two-mode squeezed state, the other mode must be "traced-out." This is calculated as by

$$\hat{\rho}_A = \text{Tr}[\hat{\rho}_{AB}]|_B \ , \tag{2.35}$$

which for $\hat{\rho}_{\text{TMSS}}$ yields

$$\hat{\rho}_{\text{TMSS}_A} = \left(1-\lambda^2\right) \sum_{n=0}^{\infty} \lambda^{2n} |n\rangle\langle n| \ . \tag{2.36}$$

The mean photon number for each mode is thus calculated from Eq. (2.25) as

$$\langle \hat{n}_1 \rangle = \langle \hat{n}_2 \rangle = \mathrm{Tr}[\hat{n}\hat{\rho}_{\mathrm{TMSS}_A}] = \frac{\lambda^2}{1-\lambda^2} \ . \tag{2.37}$$

Variance of single-mode quadratures

The quadrature variance of this state is calculated using Eq. (2.19), where Eq. (2.25) is used to calculate the relevant expectation values. In fact, since $\langle \hat{X} \rangle = \langle \hat{P} \rangle = 0$ for both the single- and two-mode squeezed states, the variances are simply $\langle \hat{X}^2 \rangle$, $\langle \hat{P}^2 \rangle$ respectively, given by

$$\Delta\hat{X} = \Delta\hat{P} = \frac{1}{4} + \frac{\langle \hat{n} \rangle}{2} \ . \tag{2.38}$$

Since $\langle \hat{n} \rangle$ is always positive as calculated above, no squeezing can be seen in the quadratures of each mode of a TMSS when measured in isolation.

Variance of two-mode quadratures

To show that the TMSS is indeed squeezed we must calculate the joint quadrature variances. To describe two-mode squeezing, we define two-mode superposition quadratures

$$\hat{\mathcal{X}} = \frac{1}{2^{\frac{3}{2}}} \left(\hat{a}_1^\dagger + \hat{a}_2^\dagger + \hat{a}_1 + \hat{a}_2 \right) = \frac{1}{\sqrt{2}} \left(X_1 + X_2 \right) \tag{2.39a}$$

$$\hat{\mathcal{P}} = \frac{i}{2^{\frac{3}{2}}} \left(\hat{a}_1^\dagger + \hat{a}_2^\dagger - \hat{a}_1 - \hat{a}_2 \right) = \frac{1}{\sqrt{2}} \left(P_1 + P_2 \right) \ . \tag{2.39b}$$

From these relations, the variances $\left(\Delta\hat{\mathcal{X}}\right)^2$, $\left(\Delta\hat{\mathcal{P}}\right)^2$ for the two-mode squeezed vacuum state in Eq. (2.32) may be calculated as detailed in appendix B.2. Since $\langle\hat{\mathcal{X}}\rangle = \langle\hat{\mathcal{P}}\rangle = 0$, the joint two-mode quadrature variances are given by

$$\begin{aligned}\left(\Delta\hat{\mathcal{X}}\right)^2 = \langle\hat{\mathcal{X}}^2\rangle &= \frac{1}{4}\left(\sinh^2 s + \cosh^2 s - 2\sinh s\cosh s\cos\varphi\right) \\ &= \frac{1}{4\left(1-\lambda^2\right)}\left(\lambda^2 - 2\lambda\cos\varphi + 1\right) \qquad (2.40a)\\ \left(\Delta\hat{\mathcal{P}}\right)^2 = \langle\hat{\mathcal{P}}^2\rangle &= \frac{1}{4}\left(\sinh^2 s + \cosh^2 s + 2\sinh s\cosh s\cos\varphi\right) \\ &= \frac{1}{4\left(1-\lambda^2\right)}\left(\lambda^2 + 2\lambda\cos\varphi + 1\right) \qquad (2.40b)\end{aligned}$$

Thus, the constant s determines the "strength" of squeezing in the direction φ in phase space. Setting the phase $\varphi = 0$ yields

$$\left(\Delta\hat{\mathcal{X}}\right)^2 = \frac{1}{4}e^{-2s} = \frac{1-\lambda}{4\left(1+\lambda\right)}\,, \qquad (2.41a)$$

$$\left(\Delta\hat{\mathcal{P}}\right)^2 = \frac{1}{4}e^{2s} = \frac{1+\lambda}{4\left(1-\lambda\right)}\,. \qquad (2.41b)$$

This quantifies the magnitude of the correlated fluctuations between two modes. For the $\hat{\mathcal{X}}$ quadrature, these are below the vacuum fluctuations by an amount $e^{-2s} = (1-\lambda)/(1+\lambda)$, whereas they are greater in the $\hat{\mathcal{P}}$ quadrature by the same factor.

Units

One can formally quantify this "squeezed" variance on a logarithmic scale. The amount of squeezing S_{dB} is given by fractional reduction in the variance of one

quadrature from that of the vacuum state. For the two-mode squeezed states above, this is given by

$$S_{\mathrm{dB}} = -10\log\left[\frac{\left(\Delta\hat{\mathcal{X}}\right)^2}{\left(\Delta\hat{\mathcal{X}}_{\mathrm{vacuum}}\right)^2}\right] = -10\log\left(e^{-2s}\right) = -10\log\left(\frac{1-\lambda}{1+\lambda}\right) \ . \qquad (2.42)$$

Equivalently, $\lambda = \tanh\left[S_{\mathrm{dB}} \times \ln(10)/20\right]$, which converts dBs squeezing into a squeezing parameter λ. For example, a reduction of half the vacuum variance corresponds to 3dB squeezing and $\lambda = 1/3$.

2.3.4 Quantifying entanglement

The amount of two-mode squeezing is related to the magnitude of non-local correlations between the modes, *i.e.* the amount of entanglement of the two-mode state. For a Gaussian state, of which the TMSS is an example, entanglement increases monotonically with squeezing λ. A non-Gaussian state, on the other hand, may exhibit no non-local quadrature squeezing, but it may still be entangled. We therefore require a more general metric with which to quantify entanglement in both Gaussian and non-Gaussian states.

A number of measures of entanglement exist, see *e.g.* Plenio and Virmani [51] for a review. Here we use the *logarithmic negativity* [59], the measure most frequently used in distillation protocols due to its applicability to mixed states.

Log-negativity

The starting point for the log-negativity arises from the Peres-Horodecki criterion [56,60]. This states that if a system is separable then the eigenvalues of its partial transpose are necessarily positive. Therefore, negative eigenvalues of the partial transpose are sufficient to show entanglement[1]. Summing the magnitudes of these negative eigenvalues is one way to quantify entanglement, known as the *negativity*. Taking the logarithm of this quantity provides an operational measure of entanglement as an upper-bound of the distillable entanglement of the state [61].

Mathematically, the logarithmic negativity $E_N(\hat{\rho})$ is expressed

$$E_N(\hat{\rho}) = \log_2 \left|\left|\hat{\rho}^\Gamma\right|\right|_1 \ , \tag{2.43}$$

where $\hat{\rho}^\Gamma$ is the partial transpose [56] and $||x||_1 = \mathrm{Tr}\left[\sqrt{x^\dagger x}\right]$ denotes the trace-norm of x [59]. Put simply, the larger the log-negativity, the more entangled the state. For pure states written in the Schmidt form, Eq. 2.13, the logarithmic negativity can be calculated

$$E_N(\hat{\rho}) = \log_2 \left[\left(\sum_{n=0}^{\infty} |c_n|\right)^2\right] \ . \tag{2.44}$$

We will use this equation frequently in subsequent chapters when calculating entanglement. For a pure two-mode squeezed state, the log-negativity is readily calculated (see Appendix C) as

$$E_N(\hat{\rho}_{\mathrm{TMSS}}) = \log_2\left(\frac{1+\lambda}{1-\lambda}\right) \ . \tag{2.45}$$

[1] In the DV case, negative eigenvalues of the partial trace are both necessary and sufficient.

Units

The units of log-negativity $E_N(\hat{\rho})$ are "ebits". Maximally entangled DV states, the set of four Bell states, have 1 ebit of entanglement [17]. A TMSS with 1 ebit entanglement corresponds to $\lambda = 1/3$, *i.e.* 3 dB squeezing.

Maximum entanglement in the CV regime, that is, in position and momentum, occurs when $\lambda \to 1$ and implies infinite squeezing. Indeed, in Einstein, Podolski and Rosen's seminal paper [12], the (EPR) state they describe is maximally entangled in position and momentum. This is, however, unphysical, since infinite squeezing requires infinite energy. Rather, the two-mode squeezed state is the maximally entangled continuous-variable state for fixed energy. Continuous variable entanglement is discussed in more detail in the reviews by Eisert and Plenio [62] and Braunstein and van Loock [33] and references therein.

2.4 Distilling entanglement

Having introduced a way to quantify entanglement, we are equipped to investigate processes that change the amount of entanglement during a given protocol. Whilst it is easy for entanglement to decrease, through loss or some decoherence channel, increasing entanglement is a far more involved process.

A protocol that can increase entanglement is *entanglement distillation*, proposed by Bennett *et al.* [23,63]. The aim is to extract a set of strongly-entangled pairs of states from a set of pairs of weakly entangled states. Moreover, this extraction is achieved by local operations and classical communication (LOCC) alone. Although

entanglement cannot increase *on average* under LOCC, the subset of successful distillation events has more entanglement than the initial states. While entanglement distillation in the DV regime has been shown [24], scalable CV entanglement distillation has yet to be demonstrated, although elements of various protocols have been shown [28–32].

2.4.1 Continuous-variable entanglement distillation

Unlike in the DV regime, CV entanglement can be generated deterministically by two-mode squeezing as outlined in section 2.3.2. This makes it highly attractive as a resource in quantum protocols, particularly communication. The ability to recover entanglement after some lossy channel is crucial in extending transmission distances. Therefore, entanglement distillation is a highly desirable goal in CV quantum information processing.

No-go theorem

Given the relative ease with which Gaussian CV entanglement can be generated, it had been hoped that CV entanglement distillation could be achieved with the set of Gaussian operations (as defined in section 2.2.4). However, there exists a no-go theorem stating that it is impossible to distill entanglement from Gaussian states using Gaussian operations alone [52,64,65]. As a result, all CV distillation protocols require at least some non-Gaussian element.

De-Gaussification

The de-Gaussification step transforms Gaussian states into non-Gaussian states. Some schemes overcome this limitation by introducing non-Gaussian amplitude [28] or phase [66] noise. While these schemes increase entanglement following loss, they cannot generate more entanglement than the states exhibited prior to that loss.

One alternative is non-Gaussian measurement-induced non-linearity, such as partial measurement (photon-subtraction) [31] or heralded interference with some non-Gaussian ancilla mode. These strategies, and others, are explored in chapter 3. Some of these strategies have the advantage on increasing entanglement *beyond the amount present in the initial state*, conditional on success of the measurement. The ability to generate more entanglement than that with which one starts is highly desirable.

2.4.2 The BESP protocol

Gaussian states are central to many CV communication protocols, therefore it is desirable for a distillation protocol to return a state that is close to being Gaussian. That is to say, despite the requirement of a non-Gaussian element during the distillation protocol, the resulting states have arbitrarily small higher-order moments (> 2) of their probability distribution. To this end, Browne, Eisert, Scheel and Plenio (BESP) developed an iterative protocol [25,26] to generate a state arbitrarily

close to Gaussian state, given a set of de-Gaussified states of the form

$$|\psi\rangle = \sum_{n=0}^{\infty} c_n |n, n\rangle \ . \tag{2.46}$$

The protocol comprises interfering many copies of such states pairwise on a beam splitter and, by projecting one output mode onto the vacuum state, the remaining mode converges to a Gaussian state with higher entanglement. This procedure is not scalable; success probability scales doubly exponentially with iteration number, though this may be mitigated somewhat by the use of *quantum memories* [67].

In terms of experimental feasibility, the scheme relies on many techniques at the cutting edge of quantum optics: vacuum detection from ultra-high efficiency detectors [68], high-efficiency multi-source interference [35] and novel entanglement detection protocols [69]. In this thesis, we develop and use some of these methods in the context of novel CV state engineering. In chapter 3 we investigate in particular the feasibility of the non-Gaussian elements of the BESP protocol with the experimental state of the art.

Chapter 3

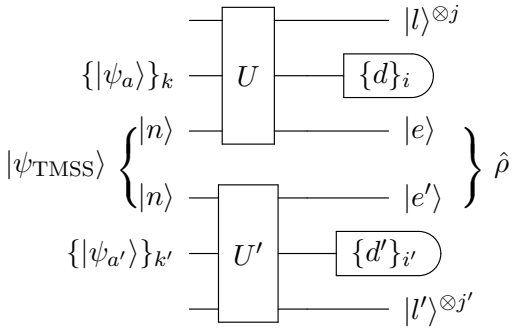
A practical approach to entanglement-enhancing non-Gaussian operations

In this chapter, we analyse several non-Gaussian operations that increase entanglement. We consider an operational approach in terms of the resources required, defining novel figures of merit to account for the probabilistic nature of the operations. We probe some useful figures of merit of these protocols, including overlap to benchmark Gaussian and non-Gaussian entangled states and teleportation fidelity. We identify photon subtraction as the most experimentally feasible non-Gaussian operation and analyse in detail the optimal parameters for increasing entanglement using this scheme.

3.1 Entanglement-enhancing non-Gaussian operations

In this section we compare and contrast a number of different non-Gaussian operations that increase entanglement, namely photon subtraction, photon addition, and a coherent superposition of the two: photon replacement. These are well-established entanglement-enhancing non-Gaussian operations, although the analysis of practical considerations that follows has not been performed previously.

The starting point for all these operations is the two-mode squeezed state in Eq. (2.33), which exhibits a log-negativity of $\log_2\left(\frac{1+\lambda}{1-\lambda}\right)$. This is the benchmark against which any increase in entanglement will be measured. The most general form of operations we consider on this state may be modelled by the circuit



. (3.1)

This describes each mode of a two-mode squeezed state $|\psi_{\text{TMSS}}\rangle$ interacting with k, k' ancilla single-mode states $|\psi_a\rangle, |\psi_{a'}\rangle$, i, i' projective measurements and allowing for j, j' loss modes. Note that conservation of mode number is ensured by setting $k = j + i$ (and similarly $k' = j' + i'$), given we seek a two-mode state $\hat{\rho}$ at the output. The particular ancillae, their interaction with each mode U, U' and projective measurements all determine the conditional operations we wish to implement. We

consider operations that can be modelled by the setup shown in figure 3.1.

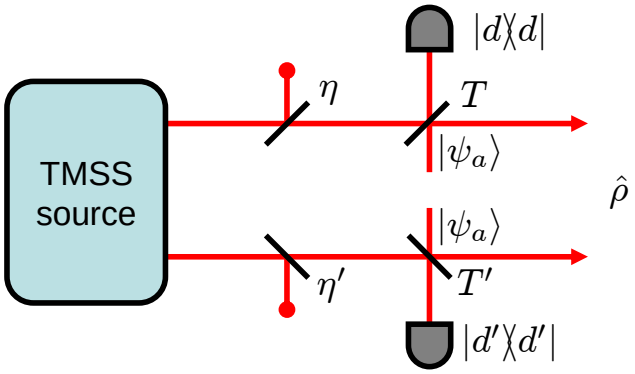


Figure 3.1: Setup for performing conditional operations on a two-mode squeezed state. Each mode of the TMSS can undergo various processes, including losses η, η', interference at a beam splitter of transmissivity T, T' with an ancilla mode $|\psi_a\rangle$, $|\psi_{a'}\rangle$ and projective photon-number measurement $|d\rangle\langle d|$, $|d'\rangle\langle d'|$. The final state $\hat{\rho}$ depends on all of these interactions.

3.1.1 Photon subtraction

Photon subtraction [70,71] is perhaps the most straightforward non-Gaussian conditional operation to carry out [72,73]. We consider the lossless symmetric case, whereby

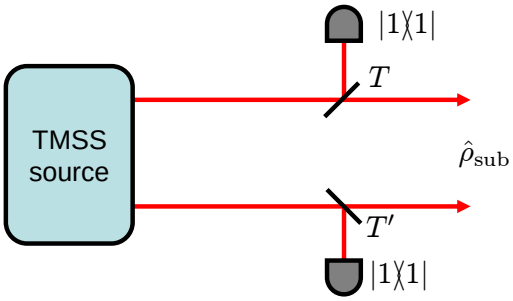


Figure 3.2: Setup for performing symmetric single-photon subtraction on a two-mode squeezed state. The success probability P_{sub} for this operation and the final entanglement $E_N(\hat{\rho}_{\text{sub}})$ depend on the beam splitter transmissivity $T = T'$.

all ancilla modes are in the vacuum state such that $\{|\psi_a\rangle\} = \{|\psi_{a'}\rangle\} = |0\rangle$, the uni-

taries U, U' are implemented by beam splitters and the measurement is a projection onto the single photon Fock state $|d\rangle\langle d| = |d'\rangle\langle d'| = |1\rangle\langle 1|$. This is shown in figure 3.2. The resulting state is

$$|\psi_{\text{sub}}\rangle = \mathcal{N}_{\text{sub}} \sum_{n=0}^{\infty} \sqrt{1-\lambda^2}\lambda^{n+1} (n+1) T^{2n} \left(1-T^2\right) |n,n\rangle \ , \tag{3.2}$$

where T is the reflectivity of the subtracting beam splitter (as identified in figure 3.1) and $\mathcal{N}_{\text{sub}}$ is a normalisation constant. Writing $\mathcal{N}_{\text{sub}}$ in this form relates this constant to the probability of subtracting a photon $P_{\text{sub}} = \mathcal{N}_{\text{sub}}^{-2}$, *i.e.*

$$P_{\text{sub}} = \frac{\lambda^2 \left(1-T^2\right)^2 \left(1-\lambda^2\right) \left(1+\lambda^2 T^4\right)}{\left(1-\lambda^2 T^4\right)^3} \tag{3.3}$$

This state has log-negativity, calculated following Eq. 2.44,

$$E_N\left(\rho_{\text{sub}}\right) = \log_2 \left[\frac{\left(1+T^2\lambda\right)^3}{\left(1+T^4\lambda^2\right)\left(1-T^2\lambda\right)} \right] \ . \tag{3.4}$$

For a particular range of T and λ, the log-negativity is greater than that of the initial TMSS, as we will show in section 3.2.1; increasing entanglement by photon subtraction has been experimentally demonstrated [31,32].

3.1.2 Photon addition

Photon addition consists of single photons in the ancilla modes $|\psi_a\rangle = |\psi_{a'}\rangle = |1\rangle$, beam splitter unitary interaction and vacuum projection $|d\rangle\langle d| = |d'\rangle\langle d'| = |0\rangle\langle 0|$ in

the detected mode, as shown in figure 3.3 This creates the state

$$|\psi_{\text{add}}\rangle = \mathcal{N}_{\text{add}} \sum_{n=0}^{\infty} \sqrt{1-\lambda^2}\lambda^{n-1} n T^{2(n-1)} \left(1-T^2\right) |n,n\rangle \ , \tag{3.5}$$

where again T is the transmissivity of the addition beam splitter in figure 3.1 and $\mathcal{N}_{\text{add}}^{-2} = P_{\text{add}}$ is the probability of photon addition, given explicitly by

$$P_{\text{add}} = \frac{\left(1-T^2\right)^2 \left(1-\lambda^2\right)\left(1+\lambda^2 T^4\right)}{\left(1-\lambda^2 T^4\right)^3} \ . \tag{3.6}$$

For fixed transmissivity T, this is always higher than P_{sub}, differing as it does by a factor of λ^{-2}.

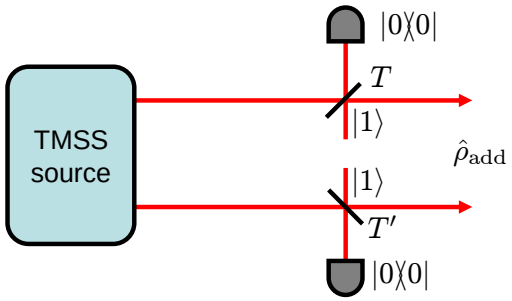


Figure 3.3: Setup for performing symmetric single-photon addition on a two-mode squeezed state. The success probability for this operation P_{add} and the final entanglement $E_N\left(\hat{\rho}_{\text{add}}\right)$ depend on the beam splitter transmissivity $T = T'$.

The log-negativity of this state $E_N\left(\hat{\rho}_{\text{add}}\right)$ is identical to the subtracted case:

$$E_N\left(\hat{\rho}_{\text{add}}\right) = \log_2\left[\frac{\left(1+T^2\lambda\right)^3}{\left(1+T^4\lambda^2\right)\left(1-T^2\lambda\right)}\right] \ . \tag{3.7}$$

Again, for a range of T, λ, entanglement may be increased from the initial value,

also detailed in section 3.2.1.

Regarding the experimental feasibility of photon addition, it is immediately apparent that it is more involved than subtraction. In the model described above, one requires a reservoir of single photons to add to the correct mode, and vacuum detection to herald success. Vacuum projection onto the correct mode is experimentally challenging, and is yet to be shown experimentally. This is largely because extremely high-efficiency detectors are required, although such detectors [68] are beginning to be used [11,74]. To overcome both of these problems, experimental schemes typically use seeded parametric down-conversion to herald photons added to the mode of interest [75–78]. This approach does not lend itself to our model above, and has not been applied as a non-Gaussian operation on a TMSS to date.

3.1.3 Photon replacement

Photon replacement [79,80] is a coherent superposition of the above operations. A photon-replaced state is probabilistically generated following the measurement of a single photon following interference with a single-photon ancilla state, as shown in figure 3.4.[1] Since this operation conserves photon number, we investigate cases of replacement on one or both modes. In fact, two-mode photon replacement is entirely equivalent to two iterations of single photon replacement on the same mode

[1] Further details on this scheme as applied to a single-mode coherent state are given in section 5.5.2.

(although not equivalent to replacing two photons). The states are given by

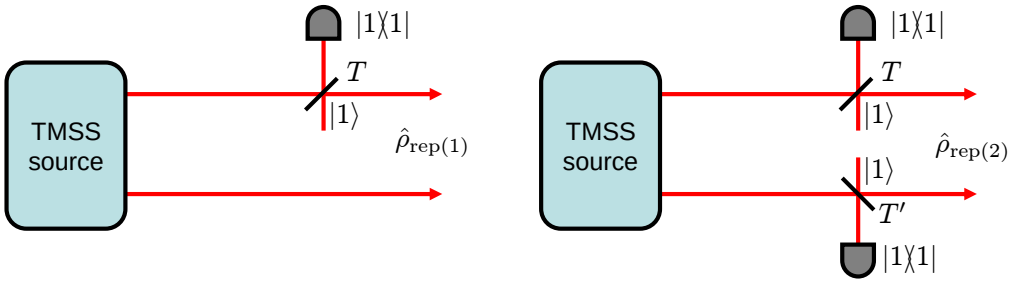
$$|\psi_{\text{rep}(1)}\rangle = \mathcal{N}_{\text{rep}(1)} \sum_{n=0}^{\infty} \sqrt{1-\lambda^2}\lambda^n T^{n-1} \left[T^2 - n\left(1-T^2\right)\right] |n,n\rangle \ , \tag{3.8a}$$

$$|\psi_{\text{rep}(2)}\rangle = \mathcal{N}_{\text{rep}(2)} \sum_{n-0}^{\infty} \sqrt{1-\lambda^2}\lambda^n T^{2(n-1)} \left[T^2 - n\left(1-T^2\right)\right]^2 |n,n\rangle \ . \tag{3.8b}$$

The probability of success for single-mode replacement is

$$P_{\text{rep}(1)} = \frac{\left(1-\lambda^2\right)\left\{\lambda^2 + T^2\left[1+\left(T^2-4\right)\lambda^2+\lambda^4\right]\right\}}{\left(1-T^2\lambda^2\right)^3} \ . \tag{3.9}$$

The expression for the two-mode replaced case is rather lengthy and is banished to appendix D (Eq. (D.8b)) for brevity.



(a) Single photon replacement (b) Double photon replacement

Figure 3.4: Setup for (a) single- and (b) two-mode photon replacement. The success probabilities $P_{\text{rep}(1)}$, $P_{\text{rep}(2)}$ for these operations and the final entanglement $E_N\left(\hat{\rho}_{\text{rep}(1)}\right)$, $E_N\left(\hat{\rho}_{\text{rep}(2)}\right)$ depend on the beam splitter transmissivity T, T'.

As before, the log-negativity is calculated by Eq. 2.44. For the single-mode replaced state $|\psi_{\text{rep}(1)}\rangle$, given $0 \leq T \leq 1$, the only positive c_n is c_0. All other $c_{n>0}$ are negative for the range $0 \leq T\sqrt{n/n+1}$. The entanglement is thus calculated for

$0 < T < 1/\sqrt{2}$ to be

$$E_N\left(\hat{\rho}_{\mathrm{rep}(1)}\right) = \log_2\left[\left(c_0 - \sum_{n=1}^{\infty} c_n\right)^2\right]$$
$$= \log_2\left[\frac{(1+T\lambda)^3\left\{\lambda + T\left[1 + 2T\lambda\left(T\lambda - 2\right)\right]\right\}^2}{(1-T\lambda)\left\{\lambda^2 + T^2\left[1 + \left(T^2-4\right)\lambda^2 + \lambda^4\right]\right\}}\right] . \tag{3.10}$$

Again, the expression for the entanglement following two-mode replacement is left to appendix D, Eq. (D.10a). Here, however, c_n are always positive so the expression is valid for all T.

3.2 An operational approach to entanglement distillation

Equipped with the expressions for the entanglement and success probabilities of various entanglement-enhancing de-Gaussification protocols, we are now in a position to compare and contrast them in an operational sense. A number of factors influence the efficacy of practical entanglement enhancement protocols. One might be interested in, for example:

- the total entanglement generated;
- the probability of success of a protocol;
- the rate at which entanglement is increased;
- the "quality" of the states generated, *i.e.* their suitability for a particular task,

e.g. teleportation fidelity [81];

- the resource costs of running each protocol;
- the tolerance of loss.

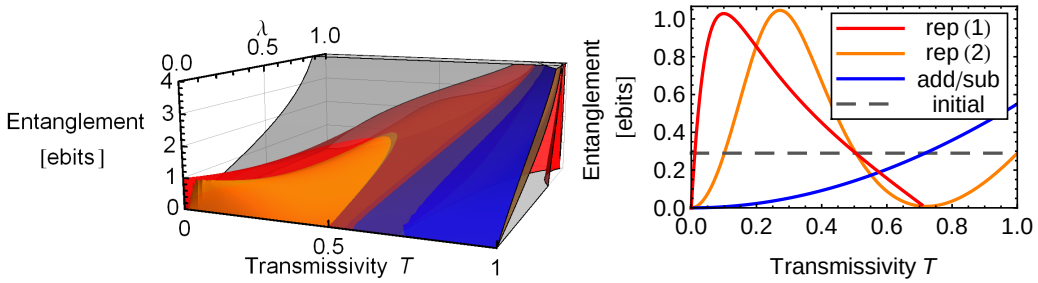
If entanglement-based quantum communication is to become widespread, some if not more of such factors should be considered collectively and, where possible, quantified.

3.2.1 Figures of merit

Based on the considerations of a realistic entanglement-enhancement protocol above, any number of figures of merit can be constructed. We suggest several and show how each entanglement-enhancing de-Gaussification strategy performs. These are all analytic calculations carried out in Mathematica.

Total entanglement

Perhaps the most straightforward question to ask is how much entanglement exists after a successful de-Gaussification event. This is shown in figure 3.5. It is apparent from figure 3.5(b) that photon replacement, both from one and two modes, produces more entanglement than subtraction/addition at low initial squeezing λ, the experimentally accessible region. For subtraction and addition, entanglement approaches its maximum value as $T \to 1$ for all λ (albeit with vanishing probability). The replacement schemes have maxima that depend on λ: at $\lambda = 0.1$ these occur at $T = 0.1$ and $T = 0.27$ for single- and double-photon replacement, respectively.

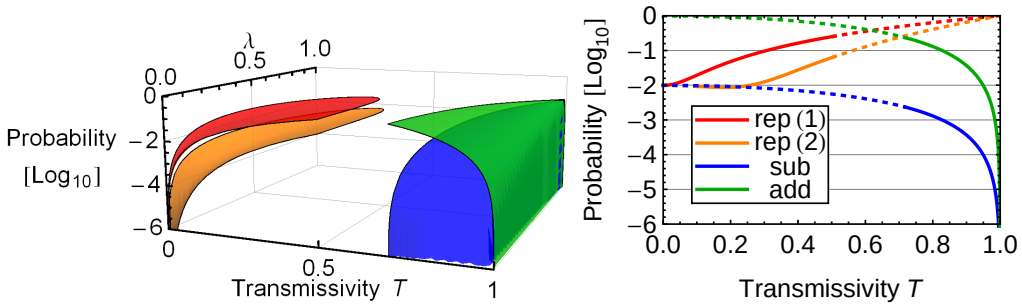


(a) (b) $\lambda = 0.1$

Figure 3.5: Log-negativity as a function of interaction parameters T (beam splitter transmissivity) and λ (initial squeezing) for the non-Gaussian operations described, namely, single-mode photon replacement (red), double-mode photon replacement (orange) and photon subtraction/addition (blue). The initial entanglement is shown in semi-transparent grey. (a) Final entanglement following successful non-Gaussian operations; (b) a cross-section through (a) at $\lambda = 0.1$.

Success probability

As with all nondeterministic operations, success probability is an important quantity. In figure 3.6 we show the probability for each scheme as a function of the initial squeezing λ and beam splitter transmissivity T. It is clear that protocols that involve introducing an extra photon are more probable; all but photon subtraction have probabilities greater than 10^{-2} for some set of parameters. However, this requires a source of single-photon ancilla states that are readily accessible. Strictly speaking, one should build in the probability of generating the required single-photons in the analysis. Typically, single photons are generated by pumping another down-conversion crystal, which for $\lambda = 0.1$ would give precisely an additional factor of 10^{-2}, thereby cancelling any advantage.



(a) (b) $\lambda = 0.1$

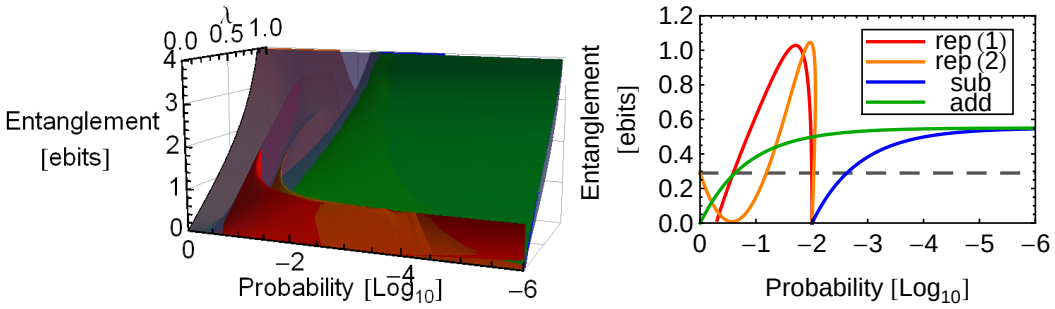
Figure 3.6: Success probability of non-Gaussian operations: single-mode photon replacement (red), double-mode photon replacement (orange), photon subtraction (blue) and photon addition (green). (a) Probability as a function of initial squeezing λ and beam splitter transmissivity T; (b) probability given initial squeezing $\lambda = 0.1$. Solid lines are the region for which entanglement is increased from the initial value; dotted lines show the probability of success for the case where entanglement has decreased.

Combining entanglement and probability

To consider the effects of both final entanglement and success probability, we can use the beam splitter transmissivity T to parametrically plot these quantities as a function of initial squeezing λ. This is shown in figure 3.7. These plots show that single-mode replacement is the best of the four strategies at low λ, since it produces (almost!) the most entanglement with the highest probability. Note that photon subtraction never outperforms photon addition.

Entanglement rate

Perhaps most interesting from figures 3.5 and 3.6 is that the replacement schemes produce the highest entanglement at reasonable probabilities. In subtraction and addition, the highest increase in entanglement occurs when $T = 1$, for which the



(a) (b) $\lambda = 0.1$

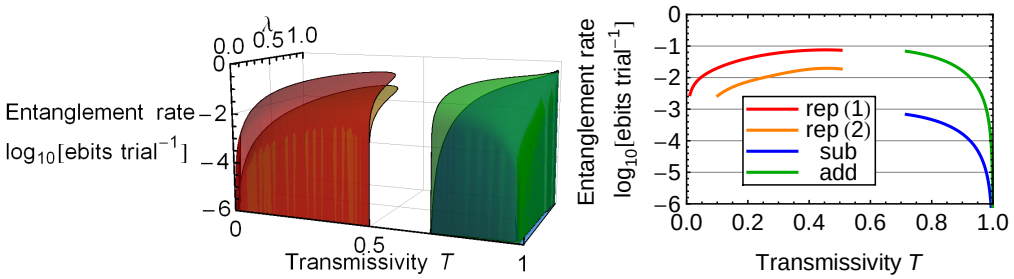
Figure 3.7: Parametric plot of final entanglement and success probability of non-Gaussian operations: single-mode photon replacement (red), double-mode photon replacement (orange), photon subtraction (blue) and photon addition (green). (a) Comparison as a function of initial squeezing λ and beam splitter transmissivity T; (b) comparison given initial squeezing $\lambda = 0.1$.

probability is precisely zero. However, the optimal transmissivities for single and double replacement are, for $\lambda = 0.1$, $T = 0.1$ and $T = 0.27$ respectively, corresponding to success probabilities 0.02 and 0.01, respectively.

To account for this property, we can define a new figure of merit, the entanglement rate $E_r(\hat{\rho})$, by simply multiplying entanglement and probability together, that is

$$E_r(\hat{\rho}) = E_N(\hat{\rho})\, P(\hat{\rho}) \ , \tag{3.11}$$

where $\hat{\rho}$ is the final state. This gives the average entanglement per trial of the protocol, and is shown for the four protocols in figure 3.8. Here again, it is clear that protocols that introduce a single photon give a higher entanglement rate.



(a) (b) $\lambda = 0.1$

Figure 3.8: Entanglement per trial of a non-Gaussian protocol: single-mode photon replacement (red), double-mode photon replacement (orange), photon subtraction (blue) and photon addition (green). (a) Rate as a function of initial squeezing λ and beam splitter transmissivity T; (b) rate given initial squeezing $\lambda = 0.1$.

Entanglement difference

In addition to the absolute level of entanglement obtained following a successful protocol, and the rate at which this is achieved, one may also be interested in the absolute *increase* in entanglement. We define this as the entanglement difference, $\Delta E_N(\hat{\rho})$, which is calculated

$$\Delta E_N(\hat{\rho}) = E_N(\hat{\rho}) - E_N(\hat{\rho}_{\text{init}}) \ , \tag{3.12}$$

and shown in figure 3.9. Again, this plot confirms that at experimentally accessible values of initial squeezing λ, both single- and double-mode photon replacement yields the highest increase in entanglement.

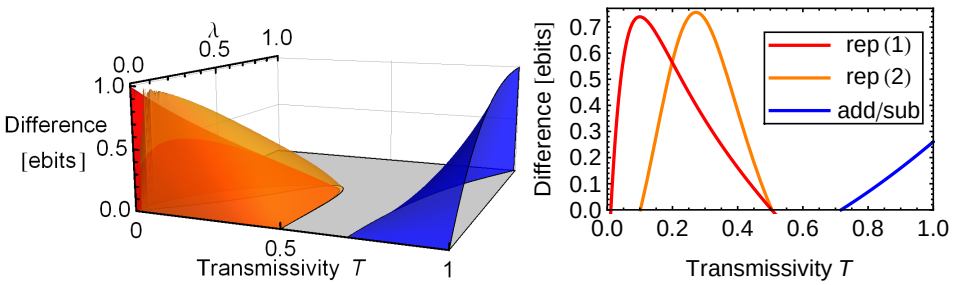


Figure 3.9: Entanglement difference following the non-Gaussian protocol: single-mode photon replacement (red), double-mode photon replacement (orange) and photon subtraction/addition (blue). (a) Difference as a function of interaction parameters beam splitter transmissivity T and initial squeezing λ; (b) difference as a function of T at $\lambda = 0.1$. (Note that this 2D line-out corresponds directly to 3.5(b).)

Enhancement rate

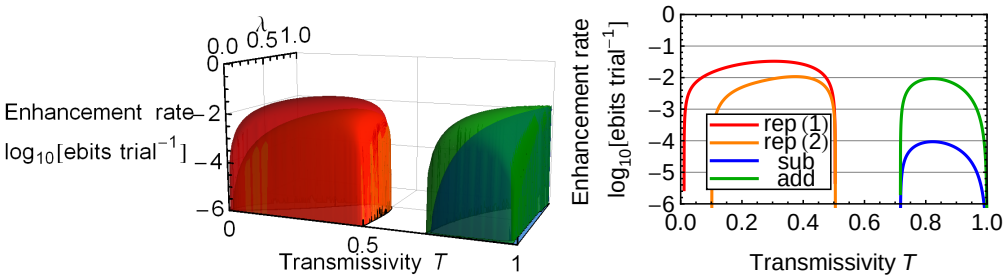
As before, we can calculate the average increase per trial, which we define as the enhancement rate ΔE_r, where

$$\Delta E_r\left(\hat{\rho}\right) = P\left(\hat{\rho}\right)\left(E_N\left(\hat{\rho}\right) - E_N\left(\hat{\rho}_{\text{init}}\right)\right) \ . \tag{3.13}$$

As it is a difference in log-negativities multiplied by a probability (necessarily dimensionless), this has units of ebits. This is shown in figure 3.10. Again, this confirms that single-mode photon replacement performs better than the other protocols.

3.2.2 Utility

In terms of log-negativity, (and with apologies to George Orwell), all entangled states are equal, but some are more equal than others. That is to say, our states have more entanglement than the two-mode squeezed state with which we started



(a) (b) $\lambda = 0.1$

Figure 3.10: Enhancement rate (increase in entanglement increase per trial) of a non-Gaussian protocol: single-mode photon replacement (red), double-mode photon replacement (orange), photon subtraction (blue) and photon addition (green). (a) Rate as a function of initial squeezing λ and beam splitter transmissivity T; (b) rate given initial squeezing $\lambda = 0.1$.

(at least for some range of parameters), but are they any more useful? Utility in this sense is a rather loaded term, depending entirely on the protocol to be employed. To that end, we investigate a number of figures of merit relating to tasks that require entanglement and calculate them for our four states.

Gaussianity

One of the principal motivations behind continuous-variable entanglement distillation is to generate Gaussian states with higher entanglement than the initial two-mode squeezed states. Conceptually, they are easier states with which to work (as discussed in section 2.2.4); operationally, this is because the teleportation fidelity increases with entanglement (see section 3.2.3).

Pure Gaussian states are minimum uncertainty states, therefore calculating excess variance is a suitable proxy for Gaussianity; the lower the excess variance, the closer the state is to being Gaussian. Other metrics for "closeness" exist, for example

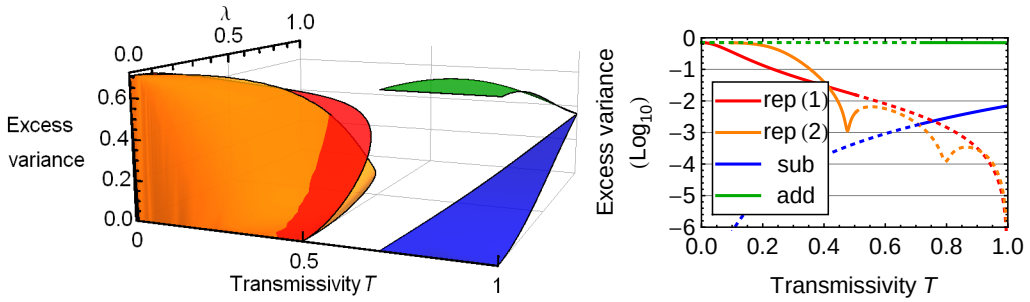
maximising the fidelity to a general Gaussian state. For pure states, excess variance can be related directly to negativity of the Wigner function [50]. An extensive study of the role played by non-Gaussianity in entanglement enhancement strategies was performed by Navarrete-Benlloch *et al.* [82].

We define the excess variance as

$$\Delta\mathrm{Var} = \sqrt{\langle(\Delta\hat{\mathcal{X}})^2\rangle\langle(\Delta\hat{\mathcal{P}})^2\rangle - 16}\,, \tag{3.14}$$

where $(\Delta\hat{\mathcal{X}})^2, (\Delta\hat{\mathcal{P}})^2$ are the quadrature variances of the two-mode state. Note that while this definition assumes two-mode quadratures $\hat{\mathcal{X}}$, $\hat{\mathcal{P}}$, application to single-mode quadratures readily follows by replacing $\hat{\mathcal{X}}, \hat{\mathcal{P}}$ with $\hat{X}$, $\hat{P}$.

Expressions for the variances of the various non-Gaussian operations are given in appendix B.2.1, and plotted in figure 3.11. This shows that subtraction returns



(a) (b) $\lambda = 0.1$

Figure 3.11: Excess variance following the non-Gaussian operation. This measures the level of non-Gaussianity for pure states. (a) Excess variance as a function of initial squeezing λ and beam splitter transmissivity T; (b) excess variance given initial squeezing $\lambda = 0.1$.

the state closest to a Gaussian state, whereas addition is very non-Gaussian, adding significant excess variance. The excess variance produced by the photon replacement

schemes depends strongly on the parameters.

Gaussian state fidelity: TMSS

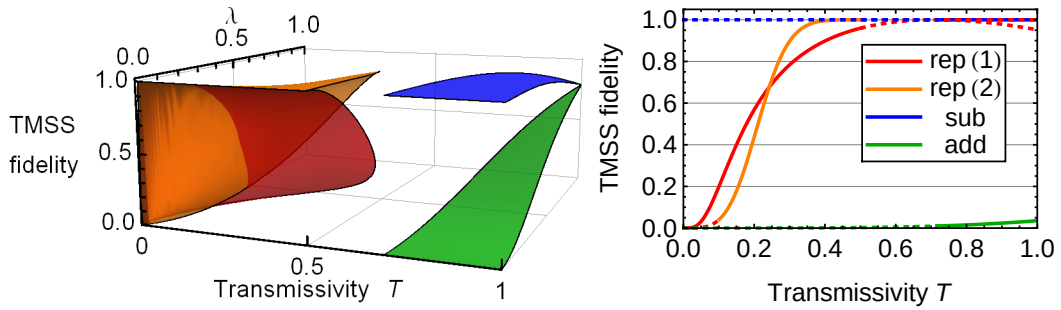
Related to the Gaussianity of the state is its fidelity to a two-mode squeezed state of equivalent entanglement. That is, given a state with entanglement E_N, what is its fidelity to a TMSS exhibiting the same log-negativity E_N. We therefore define an *effective squeezing parameter* λ_{eff}, which is the squeezing parameter of the closest TMSS with the same entanglement as the non-Gaussian state. This is calculated by

$$\lambda_{\text{eff}} = \frac{E_N - 1}{E_N + 1} \,, \tag{3.15}$$

such that the fidelity between the non-Gaussian state $|\psi_{\text{NG}}\rangle$ and the effective TMSS $|\psi_{\text{TMSS}}\rangle$ is readily calculated

$$|\langle\psi_{\text{TMSS}}|\psi_{\text{NG}}\rangle|^2 = \left(\sqrt{1-\lambda_{\text{eff}}}\sum_{n=0}^{\infty}\lambda_{\text{eff}}c_n\right)^2 \,, \tag{3.16}$$

where c_n are the normalised Schmidt coefficients (as defined in Eq. (2.13)) of the non-Gaussian state $|\psi_{\text{NG}}\rangle$. This is shown in figure 3.12. The subtracted state is very close to a TMSS, while the added state exhibits almost no overlap. Both photon-replaced states vary smoothly between low and high overlap whilst still in the parameter region corresponding to increasing entanglement from the initial two-mode squeezed state.



(a) (b) $\lambda = 0.1$

Figure 3.12: Fidelity to a two-mode squeezed state of equivalent entanglement. (a) Fidelity as a function of initial squeezing λ and beam splitter transmissivity T; (b) fidelity given initial squeezing $\lambda = 0.1$.

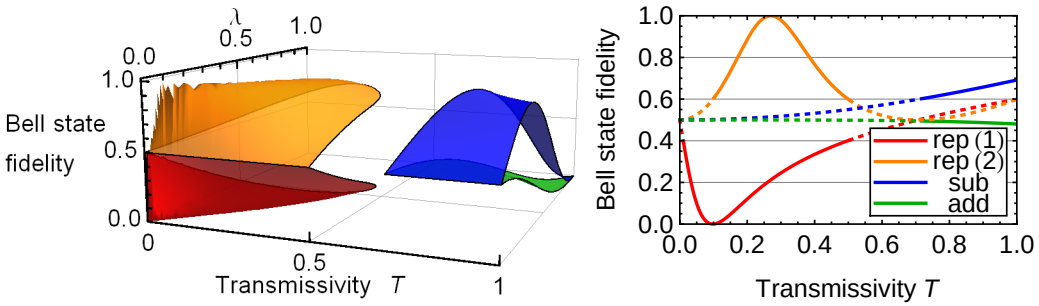
Non-Gaussian state overlap: Bell state

One can calculate the overlap between any number of states. An important set of non-Gaussian entangled states is the set of Bell states. Number correlated states of the kind in which we are interested can approximate the Bell state

$$|\psi^{+}_{\text{Bell}}\rangle = 1/\sqrt{2}\,(|0,0\rangle + |1,1\rangle)\ . \tag{3.17}$$

The accuracy of the approximation is given by their overlap $|\langle\psi_{\text{Bell}}|\psi_{\text{NG}}\rangle|^2$. In this case, neither the subtracted nor added states exhibit much overlap with the Bell state. By contrast, the double mode replaced state has 99.95% overlap at $T = 0.27, \lambda = 0.1$, while the single-photon replaced state shares exactly no overlap for $T = 0.098$ when $\lambda = 0.1$. In fact, for these parameters, the single-mode replaced state approximates an orthogonal Bell state

$$|\psi^{-}_{\text{Bell}}\rangle = 1/\sqrt{2}\,(|0,0\rangle - |1,1\rangle) \tag{3.18}$$



(a) (b) $\lambda = 0.1$

Figure 3.13: Fidelity to the Bell state $1/\sqrt{2}\,(|0,0\rangle + |1,1\rangle)$. (a) Fidelity as a function of initial squeezing λ and beam splitter transmissivity T; (b) fidelity given initial squeezing $\lambda = 0.1$.

with 99.98% fidelity. Interestingly, these are exactly the parameters at which entanglement is maximised, shown in figure 3.5(b).

3.2.3 Teleportation

A typical motivation behind distributing entanglement is to facilitate a quantum teleportation protocol[81,83–87]. Teleportation is a quantum communication task which comprises mapping quantum states from one mode to another, without the modes themselves interacting. The fidelity with which this is achieved is a metric for success of the protocol. Indeed, early theoretical work used the teleportation fidelity as the principal figure of merit for entanglement-enhancement strategies[70,71,88].

Teleportation fidelities following the non-Gaussian operations described have been compared (independently) by Lee *et al.*[80]. Here, we expand on their results by probing the range of parameters that enhance teleportation for each operation.

Teleportation fidelity

The average teleportation fidelity $\overline{F}$ can be calculated by[89]

$$\overline{F} = \int \mathrm{d}^2\beta |\langle\psi|\hat{T}(\beta)|\psi\rangle|^2 \tag{3.19}$$

where $\hat{T}(\beta)$ is known as the transfer function, $|\psi\rangle$ is the state to be teleported and the integral is over all phase space. For states of the form $\sum_{n=0}^{\infty} c_n|n,n\rangle$, Cochrane *et al.*[71] showed that the transfer operator may be written

$$\hat{T}(\beta) = \frac{1}{\sqrt{\pi}} \sum_{n=0}^{\infty} c_n \hat{D}(g\beta)\,|n\rangle\langle n|\hat{D}(-g\beta) \ , \tag{3.20}$$

where $\hat{D}(g\beta)$ is a displacement β in phase space given a gain g of the teleporter. For the purposes of this thesis, we set $g = 1$ since we do not consider gain.

When teleporting a coherent state, $|\psi\rangle = |\alpha\rangle$, the average fidelity is independent of α. In this case, the expression for average teleportation fidelity $\bar{F}$ is

$$\overline{F} = \frac{1}{\pi} \int_{-\infty}^{\infty} \mathrm{d}x\mathrm{d}p \left[\sum_{n=0}^{\infty} c_n \frac{\left(x^2+p^2\right)^n}{n!} e^{-x^2-p^2} \right]^2 . \tag{3.21}$$

For a two-mode squeezed state, the teleportation fidelity is given by

$$\overline{F}_{\mathrm{TMSS}} = \frac{1+\lambda}{2} \ . \tag{3.22}$$

Following each of the non-Gaussian operations, the teleportation fidelities of the

resulting states are given by

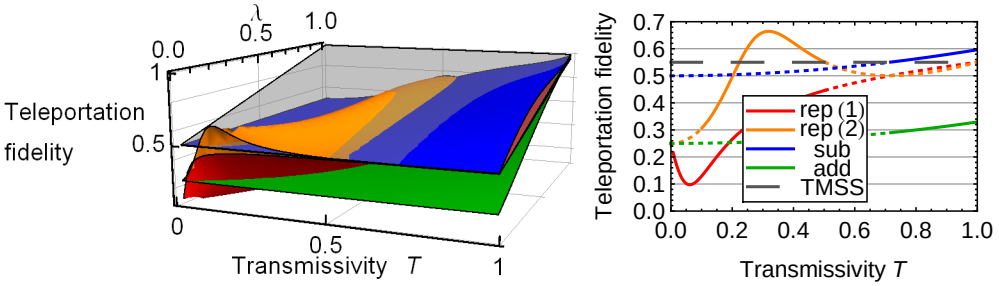
$$\overline{F}_{\text{sub}} = \frac{\left(1+T^2\lambda\right)^3\left[2+T^2\lambda\left(-2+T^2\lambda\right)\right]}{4\left(1+T^4\lambda^2\right)}\,, \tag{3.23a}$$

$$\overline{F}_{\text{add}} = \frac{\left(1+T^2\lambda\right)^3}{4\left(1+T^4\lambda^2\right)}\,, \tag{3.23b}$$

$$\overline{F}_{\text{rep(1)}} = \frac{\left(1+T^2\lambda\right)^3\left\{2T^2-2T\left(1+T^2\right)\lambda+\left[2T^4+2T^2\left(1-T^2\right)+\left(1-T^2\right)^2\right]\lambda^2\right\}}{4\left\{\lambda^2+T^2\left[1+\left(T^2-4\right)\lambda^2+\lambda^4\right]\right\}}\,. \tag{3.23c}$$

Note that $\overline{F}_{\text{rep(2)}}$ is too lengthy to display adequately (even in the appendix!). Suffice it to say the calculation is analytically tractable.

We plot these fidelities in figure 3.14. From these plots it is apparent that



(a) (b) $\lambda = 0.1$

Figure 3.14: Teleportation fidelity following different non-Gaussian operations. (a) Fidelity as a function of initial squeezing λ and beam splitter transmissivity T; (b) fidelity given initial squeezing $\lambda = 0.1$. The dotted lines show the region for which entanglement is not increased following the non-Gaussian operation.

not all entanglement-enhancing non-Gaussian operations increase the teleportation fidelity. Indeed, there is no region for which photon addition or single-mode photon replacement are better than the original two-mode squeezed state. This is in spite of their performance in increasing the most entanglement with the highest probability

(figure 3.8). If the purpose of the protocol is to increase teleportation fidelity, then subtraction or double-mode photon replacement is the only option.

Quantum bounds

Ralph and Lam[85] showed that for teleportation to be unambiguously quantum, the average fidelity must exceed $\bar{F} = 2/3$ (see also Grosshans and Grangier[90]). In figure 3.15, we show where a TMSS, subtracted state and double-mode photon-replaced state exceed this bound as a function of initial squeezing λ. Note that for the subtracted state we have assumed $T = 1$ (*i.e.* an operation producing the highest entanglement but with vanishing success probability), and for the photon-replaced state, T is optimised to maximise the fidelity for each λ. The different states reach

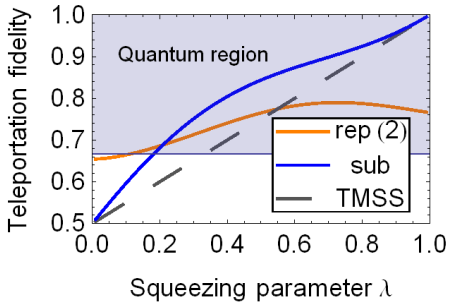


Figure 3.15: Teleportation fidelity as a function of λ following different non-Gaussian operations. Fidelities greater than 2/3 (blue region) require state reproduction that is unambiguously quantum[85], while fidelities above 1/2 require entanglement during the teleportation protocol[86].

the Ralph-Lam bound for different λ: double-mode photon replacement at $\lambda = 0.12$ (and $T = 0.33$), photon subtraction at $\lambda = 0.18$ and the original TMSS at $\lambda = 1/3$. Therefore, replacement appears to be a good strategy for teleportation at low λ (it is also far more probable in this parameter range, as per figure 3.6).

Entanglement utility

The final property we will consider is the efficiency with which entanglement in a state is used in a teleportation protocol. That is to say, given a fixed level of entanglement, which state produces the highest teleportation fidelity? This is shown in figure 3.16 . Both subtraction and double replacement produce states that use

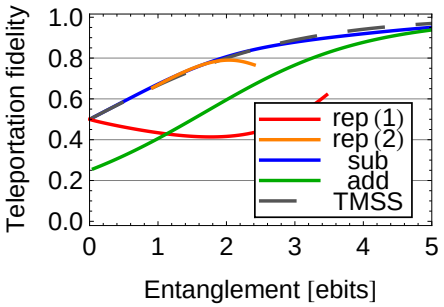


Figure 3.16: Teleportation fidelity as a function of entanglement.

entanglement similarly efficiently as a TMSS.

3.2.4 Concluding remarks

Given this analysis of the many properties of the states generated following non-Gaussian operations, we are in a position to choose which to try and implement in the laboratory.

Resources

In general, the principal resources required for a given protocol are time and energy. One could ask how long a protocol takes to work, and much energy must be provided to generate single photons, for example, or an initial TMSS. In the laboratory,

additional constraints are put on a protocol. It is far easier to measure single photons than it is to generate them, therefore photon subtraction is the most straightforward protocol to implement.

Loss

Until now, this analysis has assumed perfect states with no degradation or mixedness due to loss. Analytic results were possible since, in the absence of loss, the states remained pure. However, the approach is general, since log-negativity is still a valid metric for quantifying the entanglement of mixed states. To that end, a more detailed analysis to account for impure states due to loss is introduced in the remainder of this chapter.

3.3 Photon subtraction: a detailed analysis

Before attempting to show changes in entanglement, it is useful to characterise thoroughly the behaviour of the subtraction protocol under loss, and also which subtraction strategies would be most effective given our experimental constraints. This determines the range of parameters required to carry out the experiment. The primary source for this chapter is Bartley et al., "Strategies for enhancing quantum entanglement by local photon subtraction" [91].

The rest of this chapter is organised as follows: in sec. 3.3.1, we define an additional figure of merit, the entanglement gain, a ratiometric measure of entanglement enhancement. In sec. 3.4, we derive the state evolution of photon subtraction from

a two-mode squeezed state (TMSS) and we provide an analytical form for the probabilities corresponding to different detection strategies. We use the evolved state to analyse the gain in entanglement by different subtraction strategies: using photon-number resolving detectors (PNRDs) in sec. 3.5, and threshold detectors (such as avalanche photodiodes — APDs) in sec. 3.6. For both types of detectors (PNRDs in sec. 3.5.4 and APDs in Sec. 3.6.3), we numerically analyse symmetric and asymmetric subtraction in the presence of loss occurring before, during, and after subtraction, and show how these different parameters affect the success of the protocol.

3.3.1 Entanglement gain and rate

From the initial state $\hat{\rho}_{\text{TMSS}} = |\psi_{\text{TMSS}}\rangle\langle\psi_{\text{TMSS}}|$, given in Eq. (2.33), a subtraction step $\mathfrak{s}$ produces a state $\hat{\rho}_{\mathfrak{s}}$ with entanglement $E_N(\hat{\rho}_{\mathfrak{s}})$. We define the *gain* in entanglement $G(\hat{\rho}_{\mathfrak{s}})$ as the ratio of the entanglement difference ΔE_N, defined in Eq. (3.12), to the initial entanglement, *i.e.*

$$G(\hat{\rho}_{\mathfrak{s}}) = \frac{E_N(\hat{\rho}_{\mathfrak{s}})}{E_N(\hat{\rho}_{\text{TMSS}})} - 1 \ , \tag{3.24}$$

such that $G(\hat{\rho}_{\mathfrak{s}}) > 0$ if the subtraction step increases entanglement. Gain is useful because it reflects the importance of small increases in entanglement for weakly entangled initial states.

The probability of an entanglement enhancing step must be less than unity, since

entanglement cannot be increased on average under LOCC[92]. It is calculated by

$$P\left(\hat{\rho}_{\mathfrak{s}}\right) = \mathrm{Tr}[\mathfrak{s}\left(\hat{\rho}\right)] \ , \tag{3.25}$$

where $\mathfrak{s}\left(\hat{\rho}\right)$ is the unnormalised density matrix following a subtraction operation. The final density matrix $\hat{\rho}_{\mathfrak{s}}$ is found by normalising $\mathfrak{s}\left(\hat{\rho}\right)$ thus

$$\hat{\rho}_{\mathfrak{s}} = \frac{\mathfrak{s}\left(\hat{\rho}\right)}{\mathrm{Tr}[\mathfrak{s}\left(\hat{\rho}\right)]} \ . \tag{3.26}$$

The aim of an entanglement enhancement protocol is to increase entanglement from some initial value. It is therefore desirable not only for subtraction to produce a high gain, but also to do so at a high rate, *i.e.* that the probability of a subtraction event is as high as possible. In general these conditions cannot be met independently, therefore there exists an optimum to be found based on the parameters of a given implementation. We therefore define the *entanglement gain rate* (frequently shortened to "rate" in the remainder of the chapter) $\Gamma\left(\hat{\rho}_{\mathfrak{s}}\right)$ as the gain afforded by a distillation step $G\left(\hat{\rho}_{\mathfrak{s}}\right)$ multiplied by its likelihood

$$\Gamma\left(\hat{\rho}_{\mathfrak{s}}\right) = P\left(\hat{\rho}_{\mathfrak{s}}\right) G\left(\hat{\rho}_{\mathfrak{s}}\right) \ . \tag{3.27}$$

By post-selecting on successful subtraction events, the entanglement of this subensemble can be increased. The increase will depend on the parameters of the subtraction step employed, and can be maximised to determine the values of those

parameters which yield the highest rate.

3.4 The lossy protocol

To effect subtraction and account for loss, we consider an array of 8 beam splitters, each with transmissivity T_i and reflectivity $R_i = \sqrt{1 - T_i^2}$, acting on the TMSS as shown in figure 3.17. This extends the scheme shown in figure 3.1 to include different origins of losses.

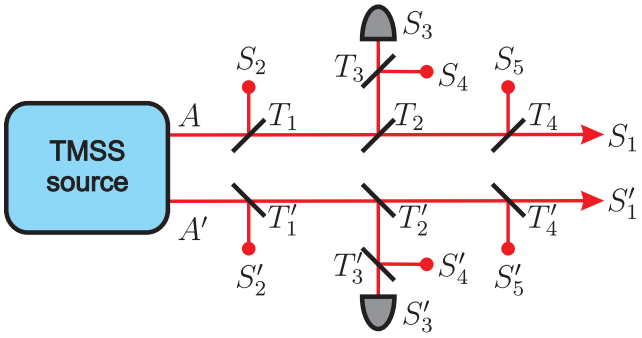


Figure 3.17: A two-mode squeezed state (TMSS) in a photon-subtraction setup. A TMSS initially occupies modes A, A'. Following the array of beam splitters (with transmissivity T_i, T_i'), we seek the entanglement in modes S_1, S_1' following detection in modes S_3, S_3'. Losses are modelled by allowing scattering into modes before (S_2, S_2'), during (S_4, S_4') and after (S_5, S_5') detection.

The state initially occupies modes A, A'. The beam splitters T_2, T_2' effect subtraction, while the other beam splitters T_1, T_3, T_4 model losses before subtraction, during detection and after subtraction, respectively (and similarly for the primed counterparts). As such, the state vector describing the combined state of the input modes may be written $|\Psi_{\text{in}}\rangle = |\psi_{\text{TMSS}}\rangle \otimes |0\rangle^{\otimes 8}$. The evolution of the input modes is governed by the unitary transformation $U \oplus U'$. The unitaries U and U'

actually denote the orthogonal matrices corresponding to transformations in the Heisenberg picture, and operates on the modes as labelled in figure 3.17 and circuit diagram (3.30). The elements of U, U' depend on the arrangement of beam splitters and how they couple their respective modes. For the array of beam splitters shown in figure 3.17, U may be written as

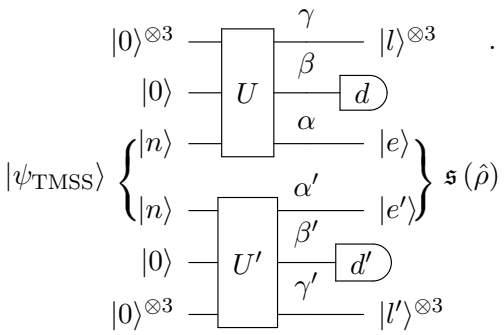
$$U = \begin{pmatrix} T_1T_2T_4 & -R_1T_2T_4 & -R_2T_4 & 0 & -R_4 \\ R_1 & T_1 & 0 & 0 & 0 \\ T_1R_2T_3 & -R_1R_2T_3 & T_2T_3 & -R_3 & 0 \\ T_1R_2R_3 & -R_1R_2R_3 & T_2R_3 & T_3 & 0 \\ T_1T_2R_4 & -R_1T_2R_4 & -R_2R_4 & 0 & T_4 \end{pmatrix} , \tag{3.28}$$

and similarly for U', with all symbols replaced by their primed counterparts. Since the only non-vacuum input modes are A, A', the output modes depend only on the first column of each unitary U, U'. Indeed, we may write the output state vector in the Fock basis as

$$|\Psi_{\text{out}}\rangle = \sqrt{1-\lambda^2} \sum_{n=0}^{\infty} \frac{\lambda^n}{n!} \left(\sum_{m=1}^{5} \sigma_{1,m} s_m^\dagger \right)^n \left(\sum_{m'=1}^{5} \sigma'_{1,m'} s_{m'}^{\prime\dagger} \right)^n |0\rangle \ , \tag{3.29}$$

where $\sigma_{1,m}$ is the $(1,m)$-th element of the unitary U and $s_m^\dagger$ is the creation operator for the mode m. We are interested in the entanglement between the modes S_1, S_1', occupied by e, e' photons respectively, dependent on detecting d, d' photons in modes S_3, S_3', respectively. The modes $S_2, S_4, S_5, S_2', S_4', S_5'$ contain l, l' photons lost to the environment. These loss modes can be combined, simplifying our problem into the

following circuit diagram



(3.30)

The photons in two input modes of the TMSS are divided into three output modes each: entangled, detected and lost, and we assign parameters α, α', β, β' and γ, γ' to be the fraction of photons in each mode, respectively. These may be written in terms of the components of the unitary U thus,

$$\alpha^2 \equiv \sigma_{1,1}^2 = T_1^2 T_2^2 T_4^2 \ , \tag{3.31a}$$

$$\beta^2 \equiv \sigma_{1,3}^2 = T_1^2 R_2^2 T_3^2 \ , \tag{3.31b}$$

$$\gamma^2 \equiv \sum_{m=2,4,5} \sigma_{1,m}^2 = R_1^2 + T_1^2 \left(R_2^2 R_3^2 + T_2^2 R_4^2 \right) \ , \tag{3.31c}$$

where the coefficients satisfy $\alpha^2 + \beta^2 + \gamma^2 = 1$, as defined by the unitarity condition (and similarly for their primed counterparts). Substituting Eqs. (3.31) into Eq. (3.29), yields

$$|\Psi_{\text{out}}\rangle = \sqrt{1-\lambda^2} \sum_{n=0}^{\infty} \lambda^n \sum_{\mathcal{S}} c_{e,d,l} c'_{e',d',l'} |e, e'\rangle |d, d'\rangle |l, l'\rangle \ , \tag{3.32}$$

where the summation is over $\mathcal{S} = \{e, e', d, d', l, l'$ such that $e+d+l = e'+d'+l' = n\}$, and where we have defined

$$c_{e,d,l} = \sqrt{\binom{n}{e,d,l}}\alpha^e\beta^d\gamma^l \ , \tag{3.33}$$

with the multinomial coefficient[93] $\binom{n}{e,d,l}$ (and similarly for the primed quantities). On tracing out the loss and detected modes, we obtain the (mixed) entangled state $\hat{\rho}$ across modes S_1, S_1' as

$$\hat{\rho} = (1-\lambda^2)\sum_{n,\tilde{n}=0}^{\infty}\sum_{d,d'}^{d_{\max},d'_{\max}}\sum_{l,l'}^{l_{\max}} c_{n,\tilde{n},d,d',l,l'}|e\rangle_{S_1}\langle\tilde{e}| \otimes |e'\rangle_{S_1'}\langle\tilde{e}'| \ , \tag{3.34}$$

where $d_{\max} = \min(n,\tilde{n}) - l$, $l_{\max} = \min(n,\tilde{n})$, and $c_{n,\tilde{n},d,d',l,l'}$ are subject to the constraints $e+d+l = e'+d'+l' = n$, $\tilde{e}+d+l = \tilde{e}'+d'+l' = \tilde{n}$, such that

$$c_{n,\tilde{n},d,d',l,l'} = \frac{\lambda^{n+\tilde{n}}n!\tilde{n}!\alpha^{e+\tilde{e}}\alpha'^{e'+\tilde{e}'}\beta^{2d}\beta'^{2d'}\gamma^{2l}\gamma'^{2l'}}{d!d'!l!l'!\sqrt{e!e'!\tilde{e}!\tilde{e}'!}} \ . \tag{3.35}$$

As the mode structure is now clear, we will suppress the mode labels S_1, S_1' in further discussions for compactness.

3.4.1 Subtraction

Subtraction is effected by changing the limits of the summation over d, d' in Eq. (3.34), leading to an unnormalised subtracted state $\mathfrak{s}(\hat{\rho})$. The exact form of this state depends on the subtraction strategy employed and is derived in detail in the relevant sections below. To calculate the entanglement we seek the sum of the negative eigenvalues of the partial transpose of the normalised state. Using Eqs. (3.26) and (2.43),

we therefore seek

$$E_N\left(\hat{\rho}_{\mathfrak{s}}\right) = \log_2\left\{\frac{\left|\left|\mathfrak{s}\left(\hat{\rho}\right)^{\Gamma_{S_1}}\right|\right|_1}{\mathrm{Tr}[\mathfrak{s}\left(\hat{\rho}\right)]}\right\} , \tag{3.36}$$

where $\mathfrak{s}\left(\hat{\rho}\right)^{\Gamma_{S_1}}$ is the partially transposed unnormalised state with respect to mode S_1, and $||x||_1$ is the trace-norm, defined in section 2.3.4. Following the analysis of Kitagawa *et al.*[94] and Zhang and van Loock[95], we can write $\mathfrak{s}\left(\hat{\rho}\right)^{\Gamma_{S_1}}$ in block diagonal form, and we change variables such that

$$n \equiv i + l + d,\ \tilde{n} \equiv j + l + d,\ l' \equiv i + j - K + l + d - d' , \tag{3.37}$$

where the indices i, j denote the rows and columns of the K^{th} block matrix of dimension $K + 1$. Thus $\mathfrak{s}\left(\hat{\rho}\right)^{\Gamma_{S_1}}$ is written explicitly as

$$\mathfrak{s}\left(\hat{\rho}\right)^{\Gamma_{S_1}} = \left(1 - \lambda^2\right) \bigoplus_{K=0}^{\infty} \sum_{i,j=0}^{K} C_{i,j}^{(K)} |j\rangle\langle i| \otimes |K - i\rangle\langle K - j| , \tag{3.38}$$

with coefficients

$$\begin{aligned} C_{i,j}^{(K)} = & \sum_{d,d'=t,t'}^{t_{\max},t'_{\max}} \sum_{l=l_0}^{\infty} \lambda^{i+j+2(l+d)} \alpha^{i+j} \alpha'^{2K-i-j} \beta^{2d} \beta'^{2d'} \gamma^{2l} \gamma'^{2(i+j-K+l+d-d')} \\ & \times \frac{(i+l+d)!\,(j+l+d)!}{l!\,(l+i+j+d-K-d')!d!d'!\sqrt{i!j!\,(K-j)!\,(K-i)!}} , \end{aligned} \tag{3.39}$$

where $l_0 = \max\{0, K + d' - d - i - j\}$ and $t, t', t_{\max}, t'_{\max}$ depend on the type of detector employed. By inspection the matrices $\mathbf{C}^{(K)} = \left[C_{i,j}^{(K)}\right]_{i=0,\ldots,K;j=0,\ldots,K}$ are symmetric, and they are also persymmetric[2] (and therefore centrosymmetric) when

[2]The elements of an $n \times n$ persymmetric matrix are related by $\alpha_{i,j} = \alpha_{n+1-j,n+1-i}$.

the primed parameters are equal to their unprimed counterparts and the range of the summations over d and d' are equal[95]. Eq. (3.39) is central to the derivation of all subsequent analytic results.

The coefficients $C_{i,j}^{(K)}$ lead to a normalised state if d, d' are summed over entirely, *i.e.* the limits on the summation over d, d' are $t = t' = 0,\ t_{\max} = t'_{\max} = \infty$ respectively. The (unnormalised) state $\mathfrak{s}(\hat{\rho})$ following a subtraction event is found by placing limits on the d, d' summation, yielding coefficients $\tilde{C}_{i,j}^{(K)} = C_{i,j}^{(K)}(t, t', t_{\max}, t'_{\max})$, dependent on the strategy employed. For threshold detectors that click on receipt of a minimum number of photons, the sum runs from the threshold value t to $t_{\max} = \infty$ (for instance, single-photon avalanche detectors have $t = 1$). For photon-number-resolving-detectors (PNRDs) operating within their resolution regime, the summation disappears since $t_{\max} = t$.

3.5 Subtraction using PNRDs

We will first briefly consider the case when subtracted photons are measured using perfect PNRDs. This amounts to removing the sums over d, d' in Eq. (3.39).

3.5.1 Probability of photon subtraction

The probability $P(t, t') = P(\hat{\rho}_{\mathfrak{s}})$ of detecting $t = t_{\max},\ t' = t'_{\max}$ photons, respectively, is given by the trace of the unnormalised state $\mathfrak{s}(\hat{\rho})$ after a subtraction event. Detecting t, t' subtracted photons by PNRDs projects onto modes S_1, S'_1 the

unnormalised state

$$\mathfrak{s}\left(\hat{\rho}\right)=\left(1-\lambda^{2}\right)\bigoplus_{K=0}^{\infty}\sum_{i,j=0}^{K}\tilde{C}_{i,j}^{(K)}|i\rangle_{E}\langle j|\otimes|K-i\rangle_{E'}\langle K-j|\ , \tag{3.40}$$

where the coefficients $\tilde{C}_{i,j}^{(K)}=C_{i,j}^{(K)}\left(t,t',t,t'\right)$ are identical to those in Eq. (3.39) for $t_{\max}=t, t'_{\max}=t'$ and therefore the summation over d is dropped. This has probability

$$\begin{aligned}P\left(t,t'\right)=\mathrm{Tr}[\mathfrak{s}\left(\hat{\rho}\right)]=&\frac{\left(1-\lambda^{2}\right)\lambda^{2t'}\beta'^{2t'}\beta^{2t}\left(\alpha^{2}+\gamma^{2}\right)^{t'-t}}{\left[1-\left(\alpha^{2}+\gamma^{2}\right)\left(\alpha'^{2}+\gamma'^{2}\right)\lambda^{2}\right]^{t'+1}}\\&\times P_{t}^{(t'-t,0)}\left[\frac{1+\left(\alpha^{2}+\gamma^{2}\right)\left(\alpha'^{2}+\gamma'^{2}\right)\lambda^{2}}{1-\left(\alpha^{2}+\gamma^{2}\right)\left(\alpha'^{2}+\gamma'^{2}\right)\lambda^{2}}\right]\ ,\end{aligned} \tag{3.41}$$

where $P_{n}^{(a,b)}[z]$ denotes the n^{th}-order Jacobi polynomial. We have assumed, without loss of generality, that $t\leq t'$; owing to the symmetry of the problem a corresponding equation for $t\geq t'$ can be found by swapping all of the primed values with their unprimed counterparts. This expression is valid if t,t' are known, *i.e.* in the case where detection resolves photon number. This may be extended to threshold detectors by summing over t,t' from the threshold $\tilde{t},\tilde{t}'$ (typically unity) to $t_{\max},t'_{\max}$. We deal with this scenario in greater detail in sec. 3.6.

3.5.2 Lossless symmetric subtraction

Perfect, symmetric photon subtraction detects an equal number of photons in both modes with 100% efficiency. This is equivalent to setting $\gamma=\gamma'=0$, meaning $l=l'=0$ and $\alpha=T_2$ (whereby T_2 is the transmissivity of the subtraction beam

splitter). Symmetry implies $t = t'$, $\alpha = \alpha'$ and $\beta = \beta'$, implying $K = i + j$, which simplifies Eq. (3.39) to

$$C_{i,j}^{(K)} = \frac{\lambda^{K+2t}\alpha^{2K}\beta^{4t}\,(i+t)!\,(j+t)!}{t!^2\sqrt{i!j!\,(K-i)!\,(K-j)!}}\delta_{K,i+j}\ , \tag{3.42}$$

where the Kronecker delta function $\delta_{K,i+j}$ means that all off-anti-diagonal elements are zero. In this case, each of the $(K+1)\times(K+1)$ blocks $\mathbf{C}^{(K)}$ are both symmetric, $C_{i,j}^{(K)} = C_{j,i}^{(K)}$, and persymmetric $C_{i,j}^{(K)} = C_{K-i,K-j}^{(K)}$, which can be exploited[95,96] to compute the log-negativity using

$$E_N\left(\hat{\rho}\right) = \log_2\left\{\frac{(1-\lambda^2)\sum_{K=0}^{\infty}\mathrm{Tr}[\mathbf{J}^{(K)}\mathbf{C}^{(K)}]}{P\left(t,t\right)}\right\}\ , \tag{3.43}$$

where $\mathbf{J}^{(K)} = [\delta_{i+j,K}]$ is the anti-identity matrix and we include explicitly the normalisation factor in the denominator. The numerator traces over the antidiagonal elements $C_{i,K-i}^{(K)}$ while the denominator traces over the diagonal elements $C_{i,i}^{(K)}$. This yields

$$\begin{aligned}\sum_{K=0}^{\infty}\mathrm{Tr}[\mathbf{J}^{(K)}\mathbf{C}^{(K)}] &= \left(\lambda\beta^2\right)^{2d}\sum_{K=0}^{\infty}\sum_{i=0}^{K}\left(\lambda\alpha^2\right)^K\frac{(i+t)!\,(K-i+t)!}{t!^2 i!\,(K-i)!}\\ &= \left(\frac{\lambda\beta^2}{1-\lambda\alpha^2}\right)^{2t}\frac{1}{\left(1-\lambda\alpha^2\right)^2}\ ,\end{aligned} \tag{3.44}$$

and from Eq. (3.41), the probability simplifies to

$$P\left(t,t\right) = \frac{\left(1-\lambda^2\right)\lambda^{2t}\beta^{4t}}{\left(1-\lambda^2\alpha^4\right)^{t+1}}P_t\left[\frac{1+\left(\lambda\alpha^2\right)^2}{1-\left(\lambda\alpha^2\right)^2}\right]\ , \tag{3.45}$$

where $P_n[z]$ is the n^{th} Legendre polynomial, a special case of the Jacobi polynomial $P_n^{(a,b)}[z]$ found in Eq. (3.41) given by $P_n^{(0,0)}[z] = P_n[z]$. This is an analytic, closed-form expression of earlier results [94,95], and yields an entanglement of

$$E_N\left(\hat{\rho}_{\mathfrak{s}}\right) = \log_2\left\{\left(\frac{1+\lambda\alpha^2}{1-\lambda\alpha^2}\right)^{t+1} \Big/ P_t\left[\frac{1+\left(\lambda\alpha^2\right)^2}{1-\left(\lambda\alpha^2\right)^2}\right]\right\} . \tag{3.46}$$

Figure 3.18 depicts the result for varying squeezing parameter λ and subtraction coefficient α^2. The behaviour of the entanglement gain rate in figure 3.18(c) shows that there exists an optimum value that provides the best entanglement yield per trial. High gain is less likely, such that the rate is peaked at particular values of $\lambda_{\text{opt}} = 0.66$ and $\alpha^2_{\text{opt}} = 0.83$. On average, these parameters produce the highest gain in entanglement per trial.

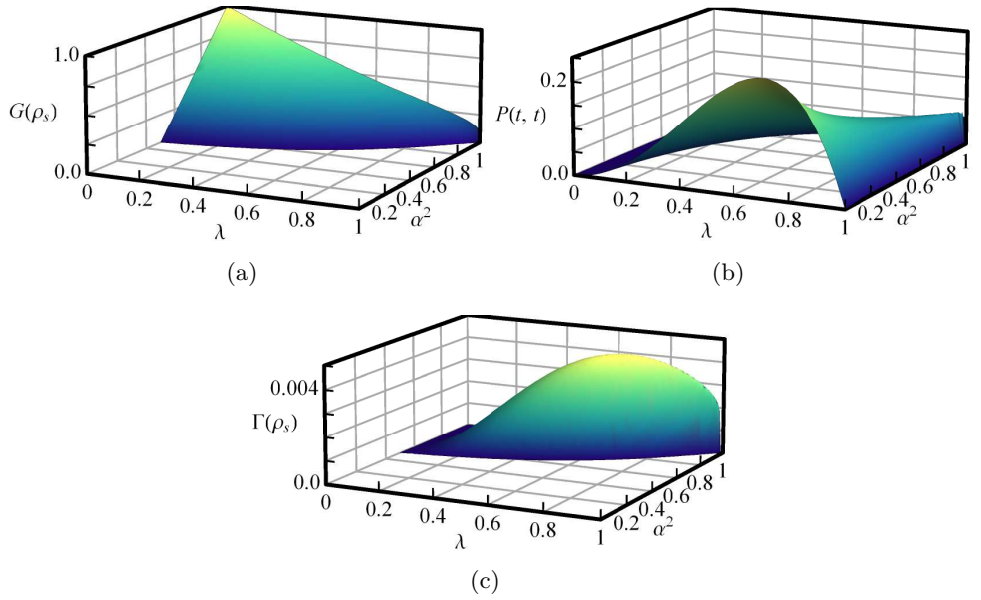


Figure 3.18: Lossless symmetric subtraction of a single photon using perfect photon-number resolving detectors. (a) Entanglement gain, (b) distillation probability and (c) rate are shown for $\lambda \in [0, 1)$ and $\alpha^2 \in [0, 1)$.

In general, the parameter α^2 is freely tunable when performing the protocol, whereas λ is restricted by the maximum squeezing available. Therefore it is useful to obtain an expression for the optimal subtraction parameter α^2_{opt} in terms of the initial squeezing λ that maximises the entanglement gain rate $\Gamma(\hat{\rho}_s)$. These values are obtained from figure 3.18(c), and are plotted as a function of λ in figure 3.19(a). For $t = 1$, the fit to these data is a second-order polynomial of the form

$$\alpha^2_{\text{opt}} = 0.238\,(\lambda - 1)^2 + 0.576\,(\lambda - 1) + 1\ . \tag{3.47}$$

Thus, given that in the lossless case $\alpha = T_2$, we have the recipe to dial up the most effective subtraction rate to maximise the gain in entanglement per trial.

It has been shown previously that all things being equal, subtracting more photons increases the gain after subtraction[95]. However, by optimizing α^2 with respect to the rate, this gain is only marginally higher with increasing d, as shown in figure 3.19(c). Indeed, at $\lambda > 0.6$, there is no advantage to subtracting more photons. As expected, even with the optimal α^2, the probability of entanglement gain decreases significantly with increasing t, shown in figure 3.19(b). These effects combine to yield a lower entanglement gain rate as the number of subtracted photons is increased, as shown in figure 3.19(d).

3.5.3 Lossless asymmetric subtraction

We now consider the case of perfect *asymmetric* subtraction, *i.e.* detecting different numbers of photons $t \neq t'$ in each subtracted mode. When counting resources in

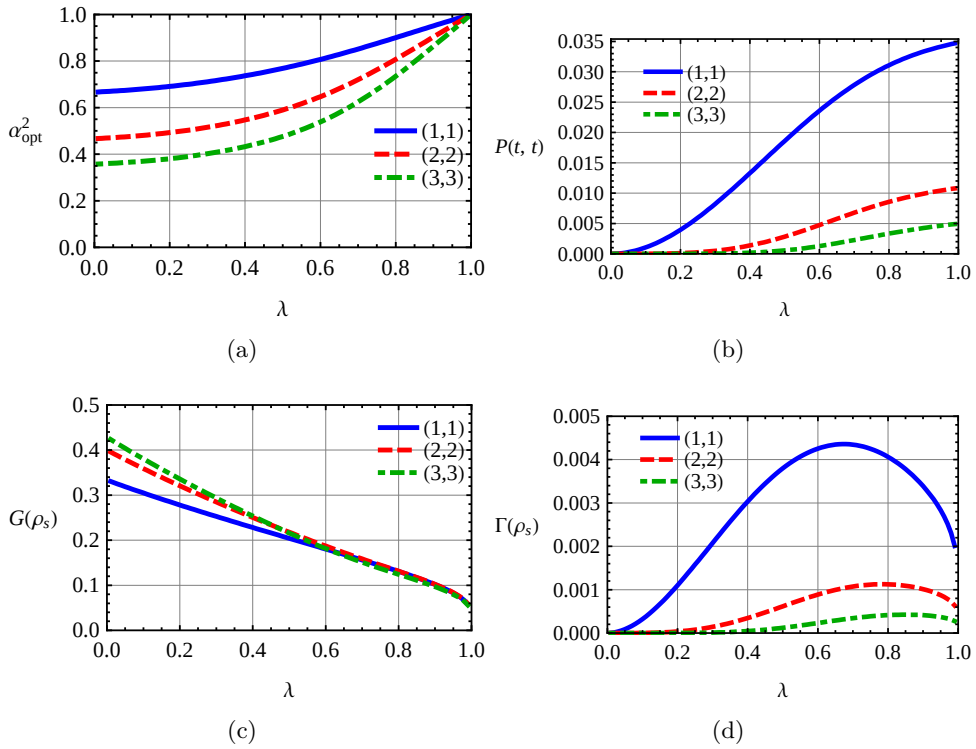


Figure 3.19: Lossless symmetric subtraction with PNRDs. (a): α^2 optimised over entanglement gain rate for a given λ for different numbers of subtracted photons t. (b), (c) and (d): the maximum probability, gain and rate, respectively, achieved with the optimal α^2 as a function of λ, for different values of t.

terms of total photons subtracted, asymmetric subtraction allows us to double our space to include odd photon numbers. This additional degree of freedom lifts the degeneracy in the coefficients, *i.e.* the primed quantities may take different values from their unprimed counterparts. This doubles the number of parameters over which the protocol can be optimised.

Starting again from Eq. (3.39), we detect t, t' photons in each mode with unit efficiency. Since we are neglecting the effects of loss in the system, $\gamma = \gamma' = 0$ and as such the only non-zero contribution to the summation over l is the $l = 0$ term. Photon number resolution is maintained by setting $t_{\max} = t, t'_{\max} = t'$ in Eq. (3.39) as before, however they need not be equal as in the case above. In this scheme the relation $\gamma = \gamma' = 0$ ensures that all elements of $\mathbf{C}^{(K)}$, except those that satisfy $i + j = K + t' - t$, are zero. We may thus express the elements of $\mathbf{C}^{(K)}$ as

$$C_{i,j}^{(K)} = \frac{\left(1-\lambda^2\right)\lambda^{i+j+2t}\alpha^{i+j}\alpha'^{2K-i-j}\beta^{2t}\beta'^{2t'}(i+t)!(j+t)!}{t!t'!\sqrt{i!j!(K-i)!(K-j)!}}\delta_{i+j,K+t'-t} \ .$$

The matrices $\mathbf{C}^{(K)}$ only have elements along one of their skew diagonals, shifted from the main skew diagonal by $t' - t$. This allows us to define an antidiagonal submatrix $\mathbf{B}^{(\bar{K})}$, where $\mathbf{B}^{(\bar{K})}$ is a $\left(\bar{K}+1\right) \times \left(\bar{K}+1\right)$ matrix and where $\bar{K} = K - t' + t$, which contains the elements on its main skew diagonal. Without loss of generality, we are able to choose $t \leq t'$, whereby the elements of $\mathbf{B}^{(\bar{K})}$ are $B_{i,j}^{(\bar{K})} = C_{i+t'-t,j+t'-t}^{(K)}$. This is both symmetric and persymmetric, so the above approach can again be used in computing the negativity. When evaluating $\mathrm{Tr}[\mathbf{B}^{(\bar{K})}\mathbf{J}^{(\bar{K})}]$ the elements of interest

are $B^{(\bar{K})}_{i,\bar{K}-i} = C^{(K)}_{i+t'-t,K-i}$, where

$$B^{(\bar{K})}_{i,\bar{K}-i} = \frac{(1-\lambda^2)\lambda^{\bar{K}+2t'}\alpha^{\bar{K}+2(t'-t)}\alpha'^{\bar{K}}\beta^{2t}\beta'^{2t'}(i+t')!(\bar{K}-i+t')!}{t!t'!\sqrt{(i+t'-t)!(\bar{K}-i+t'-t)!(\bar{K}-i)!i!}} \,. \tag{3.48}$$

Eqs. (3.48,3.41) together lead to the relations

$$P\left(t,t'\right) = \frac{\left(1-\lambda^2\right)\lambda^{2t'}\beta'^{2t'}\beta^{2t}\alpha^{2(t'-t)}}{\left(1-\alpha^2\alpha'^2\lambda^2\right)^{t'+1}} P_t^{(t'-t,0)}\left[\frac{1+\left(\alpha\alpha'\lambda\right)^2}{1-\left(\alpha\alpha'\lambda\right)^2}\right] \,, \tag{3.49}$$

and

$$\begin{aligned}\sum_{\bar{K}=0}^{\infty} \mathrm{Tr}[\mathbf{B}^{(\bar{\mathbf{K}})}\mathbf{J}^{(\bar{\mathbf{K}})}] =& (1-\lambda^2)(\lambda\beta')^{2t'}\beta^{2t}\alpha^{2(t'-t)} \\ &\times \left(\sum_{i=0}^{\infty}(\lambda\alpha\alpha')^i \frac{(i+t')!}{\sqrt{i!\,(i+t'-t)!t!t'!}}\right)^2 \,.\end{aligned} \tag{3.50}$$

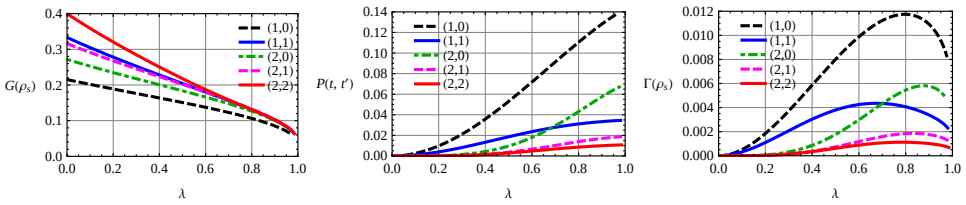
Unfortunately, no analytical expression could be found for the sum in brackets. However, by considering the ratios between successive terms in the series, it is clear that it converges over the relevant range $0 \leq \lambda\alpha\alpha' < 1$. This gives an exact, but not closed, form for the log-negativity of the state

$$E_N(\hat{\rho}_{\mathfrak{s}}) = \log_2\left\{\frac{\left(1-\chi^2\right)^{t'+1}}{P_t^{(t'-t,0)}\left[\frac{1+\chi^2}{1-\chi^2}\right]}\right\} + 2\log_2\left\{\sum_{i=0}^{\infty}\chi^i\frac{(i+t')!}{\sqrt{i!\,(i+t'-t)!t!t'!}}\right\} \,, \tag{3.51}$$

where $\chi = \alpha\alpha'\lambda$.

Comparing symmetric and asymmetric subtraction

As with the symmetric case earlier, we can directly compare the entanglement gain, probability and rate for asymmetric subtraction. For illustration purposes, we compare different ways of subtracting up to two photons from each mode. The results are shown in figure 3.20.



(a) (b) (c)

Figure 3.20: Lossless symmetric and asymmetric subtraction with PNRDs. Using α, α' optimised over entanglement gain rate for different combinations of subtracted photons ($t, t' \leq 2$), we calculate (a) the achievable gain, (b) the success probability and (c) entanglement gain rate as a function of λ.

It is clear from Fig. 3.20(a) that the symmetric cases, $(t, t') = (1, 1)$ and $(2, 2)$, produce more gain than their asymmetric counterparts for a fixed number of subtracted photons. From figure. 3.20(b), there exists a regime of $\lambda \gtrsim 0.7$ for which the probability of subtracting (2,0) photons is greater than the (1,1) case, therefore the gain rate, shown in figure 3.20(c) is correspondingly higher in this regime. This is because the (2,0) subtraction event is more likely than the (1,1) for high values of λ. However, it is clear that in general the asymmetric (1,0) case produces the most entanglement gain per trial, once again due to the high likelihood of subtracting 1 photon as opposed to 2 photons in any combination.

3.5.4 Losses and imperfect detection

In any realistic scenario, where the process of entanglement distillation and entanglement enhancement will be most essential, the detectors are imperfect and evolving quantum states suffer losses. Losses are accounted for by setting $\gamma, \gamma' > 0$, and the summation over l (which denotes the number of photons lost) includes contributions from $l \geq 1$ which are non-zero. Losses are modelled by beam splitters before, during and after subtraction, as shown in figure 3.17. The effect of loss, for the symmetric cases where one (blue), two (red) and three (green) photons are detected from each mode, is shown in figure 3.21. As the combined loss γ^2 increases, op-

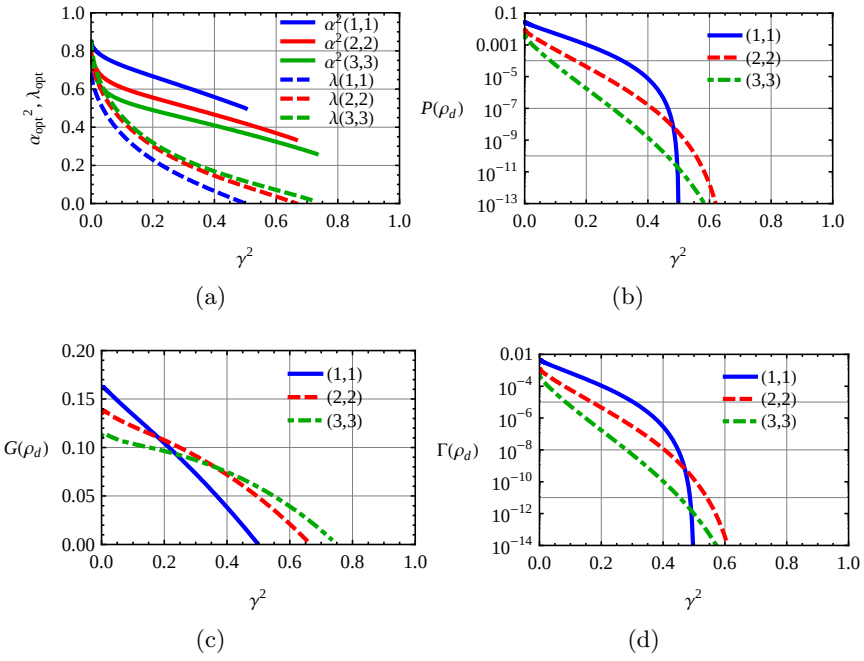


Figure 3.21: Lossy symmetric subtraction with PNRDs. (a) Squeezing λ and subtraction α^2 parameters, optimised to produce the highest entanglement gain rate at a given loss; and the resulting (c) gain, (b) probability and (d) rate resulting from these parameters.

timal initial squeezing λ for which entanglement can be enhanced by local photon subtraction decreases. Furthermore, detecting higher numbers of photons is more loss-tolerant; since a smaller α^2 is required to subtract more photons, the restriction on $\gamma^2 \leq 0.5$ is reduced. Indeed, we can define $\gamma^2_{\max}$ as the maximum loss for which entanglement still increases on subtraction. The dependence of the maximum losses $\gamma_{\max} = 1/t + 1$ comes from the gain as a function of loss, setting to zero and solving for t the difference of Eqs. (3.53) and (2.45).

The constituents of γ, γ' are determined by Eq. (3.31c), where we define efficiencies before, during and after detection as T_1^2, T_3^2, and T_4^2 respectively. From the expressions of γ, γ', it is clear that each of these efficiencies contribute differently to losses. The effect of detector efficiency, parameterised by T_3, is almost negligible. This can be interpreted by considering the subtraction detector as something of a post-selector: it may not often click, but when it does one can be fairly certain that entanglement has been increased. Losses after subtraction may be mitigated in a similar way, by using a loss-tolerant entanglement detection strategy, such as post-selection or a loss-tolerant entanglement witness [69,97]. Loss before subtraction, which may be modelled as a mixing of the state due to non unit channel transmission, is unavoidable and its contribution is significant.

Entanglement gain and rate under loss

To study the enhancement of entanglement in the presence of losses and imperfection, we again start from Eq. (3.39), which in the symmetric detection PNRD case

for $t = t'$, is given by

$$C_{i,j}^{(K)} = \sum_{l=l_0}^{\infty} \frac{\lambda^{i+j+2(t+l)} \alpha^{2K} \beta^{4t} \gamma^{2(i+j-K+2l)} (i+l+t)! (j+l+t)!}{l! (l+i+j-K)! t!^2 \sqrt{i! j! (K-j)! (K-i)!}} ,$$

where $l_0 = \max(0, K-i-j)$. Since this matrix is symmetric and persymmetric, we can calculate the entanglement following[95]. Defining $x = 1 - \alpha^2 \lambda$ and $y = \left(\alpha^2 + \gamma^2\right) \lambda$ allows us to write

$$\mathrm{Tr}[\mathbf{J}^{(\mathrm{K})} \mathbf{C}^{(\mathrm{K})}] = \frac{\left(1-\lambda^2\right) \beta^{4t} \lambda^{2t}}{\left(x^2 - \gamma^4 \lambda^2\right)^{t+1}} P_t \left[\frac{x^2 + \gamma^4 \lambda^2}{x^2 - \gamma^4 \lambda^2}\right] ,$$

and the success probability is given by

$$P(t,t) = \frac{\left(1-\lambda^2\right) \beta^{4t} \lambda^{2t}}{\left[1 - y^2 \lambda^2\right]^{t+1}} P_t \left[\frac{1+y^2}{1-y^2}\right] . \tag{3.52}$$

This yields a log-negativity of

$$E_N(\hat{\rho}) = \log_2 \left[\left(\frac{1-y^2}{x^2 - \gamma^4 \lambda^2}\right)^{t+1} \frac{P_t\left[\frac{x^2+\gamma^4\lambda^2}{x^2-\gamma^4\lambda^2}\right]}{P_t\left[\frac{1+y^2}{1-y^2}\right]} \right] . \tag{3.53}$$

These results reduce to the lossless symmetric detection case given by Eqs. (3.44,3.45) when $\gamma = \gamma' = 0$.

Optimising parameters under loss

Subtraction is a general strategy for increasing entanglement. However, it is interesting to investigate which two-mode squeezed states, parameterised by λ, are

most improved by this scheme. Furthermore, using Eqs. (3.52) and (3.53), we can incorporate loss as an additional input parameter. For a given implementation, the experimentalist has free choice of the reflectivity of the subtraction beam splitter (proportional to α). Therefore a logical question to ask would be: given losses of a certain level, what is the optimum range of λ for which subtraction yields the highest entanglement gain rate, and to what value should the subtraction beam splitter reflectivity be set in order to achieve this?

Figure 3.21(a) shows the pairs of λ and α^2 values required to produce the highest entanglement gain rate in the presence of losses. Finding an empirical fit to these data one obtains the following formulae for setting the optimal λ and α^2:

$$\alpha_{\text{opt}}\left(\gamma^2\right) = e^{-38.1\left(\gamma^2+0.1\right)} - 0.6\gamma^2 + 0.8 \ , \tag{3.54}$$

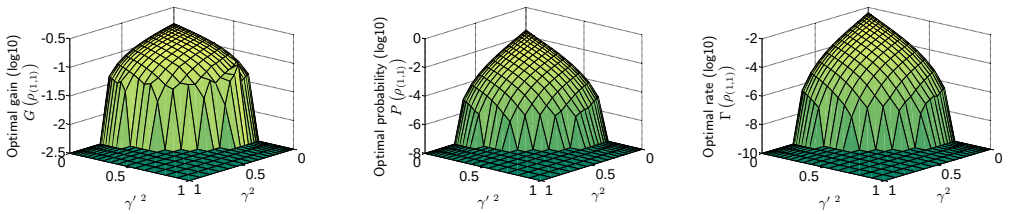
$$\lambda_{\text{opt}}\left(\gamma^2\right) = e^{-107.1\left(\gamma^2+0.1\right)^2} + e^{-2.8\left(\gamma^2+0.1\right)} - 0.2 \ . \tag{3.55}$$

The gain and rate resulting from these parameters are plotted as functions of the loss parameter γ in figures 3.21(c) and 3.21(d) respectively. One can immediately see that there is an upper threshold on loss, above which entanglement cannot be increased.

Symmetric subtraction, asymmetric loss

By setting $t' = t$ in Eq. (3.41), one may calculate the probability of symmetric subtraction allowing for different parameters α, β, γ on each mode. However, lifting the degeneracy of the parameters across the different modes means the submatrices

$\mathbf{C}^{(K)}$ are no longer centrosymmetric, and therefore the entanglement is not analytically tractable. Instead we calculate numerically the entanglement from Eq. (3.39). Figure 3.22 shows the gain, probability and rate for non-degenerate losses when subtracting a single photon from each mode. The results in figure 3.21 are simply line-outs for $\gamma = \gamma'$.



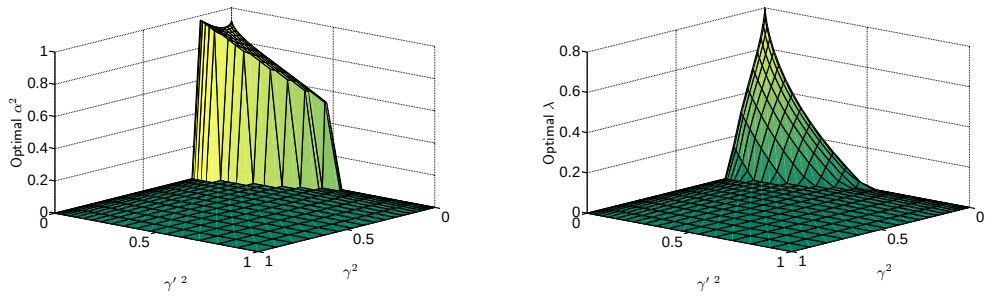
(a) (b) (c)

Figure 3.22: Lossy symmetric subtraction with PNRDs. The (a) gain, (b) probability and (c) rate of entanglement increase as a function of loss γ^2, γ'^2, given one photon subtracted from each mode.

3.5.5 Losses in asymmetric subtraction

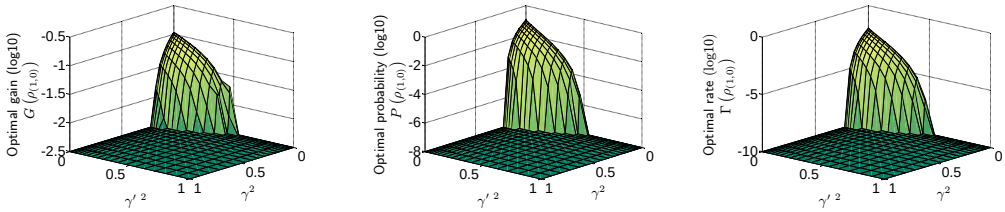
When subtracting photons asymmetrically, the effect of loss on each mode may not be equivalent. As the simplest example of asymmetric subtraction, we consider the $(t, t') = (1, 0)$ case, whereby one photon is subtracted from one mode, and the other mode is left unchanged. As shown in figure 3.20(c), this case produces the highest entanglement gain rate for all λ. We calculate numerically the optimal parameters α^2_{opt}, λ_{opt} that give the largest rate of gain, as shown in figure 3.23. Note that, since we do not subtract from the second mode, the optimal α'^2 is, trivially, $1 - \gamma'^2$ for all γ^2.

The resulting gain, probability and rate are shown in figure 3.24(a), (b) and (c)



(a) (b)

Figure 3.23: Lossy asymmetric subtraction with PNRDs. (a) Optimised subtraction parameter α^2_{opt} and (b) squeezing parameter λ_{opt} under loss given asymmetric (1,0) subtraction.



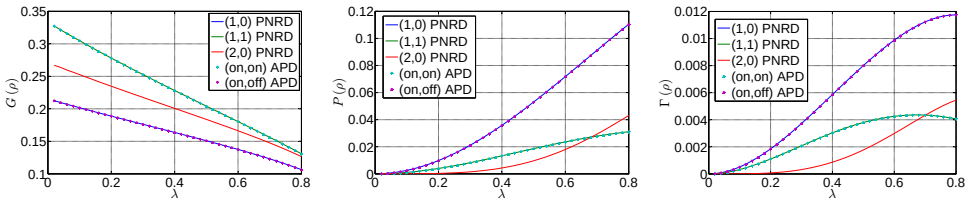
(a) (b) (c)

Figure 3.24: Lossy asymmetric subtraction using PNRDs. (a) Gain, (b) probability and (c) rate of entanglement gain as a function of the losses γ^2, γ'^2 on modes one and two respectively. The probability of successful subtraction decreases very quickly with loss, and the positive gain region is bounded asymmetrically, being roughly twice as sensitive to losses on the unsubtracted mode.

respectively. As is to be expected, the effect of loss is not symmetric in this case. The gain region is bounded more sharply by losses in the unsubtracted mode, whereas the losses in the subtracted mode follow the scaling of the symmetric case, figure 3.21(a).

3.6 Subtraction with threshold detectors

We now proceed to study the enhancement of entanglement that can be effected by subtracting photons locally using threshold detectors. We consider avalanche pho-



(a) (b) (c)

Figure 3.25: Comparing lossless subtraction strategies between APDs and PNRDs. (a) Subtraction gain, (b) probability and (c) rate for lossless PNRDs and APDs in various subtraction strategies. The results for APDs and PNRDs for simialr strategies, up to $\lambda = 0.8$, are identical.

todiodes (APDs), detectors that click when at least one photon is incident. Starting from Eq. (3.39), the effect of such detectors is described by the summations over d from $t = t_{\max} = 0$ for "off" or from $t = 1$ to $t_{\max} = \infty$ for "on", and similarly for t'. This analysis can be extended to higher photon number threshold detectors by changing the ranges corresponding to the "on" and "off" detection. A physical example of such a detector would be a multiplexed array of n APDs with a detection event triggered off n-fold coincidences.

3.6.1 Probability of photon subtraction using APDs

The four measurement outcomes to consider when using APDs are as follows: both detectors clicking (on,on), neither clicking (off,off) or just one clicking (on,off) or (off,on). The probabilities corresponding to these events must sum to unity.

The (off,off) case is identical to the case where both PNRDs register no photons.

Defining $y = \left(\alpha^2 + \gamma^2\right)\lambda,\ y' = \left(\alpha'^2 + \gamma'^2\right)\lambda$, the probability in this case is

$$P(\text{off,off}) = \frac{1-\lambda^2}{1-yy'} \ . \tag{3.56}$$

The (off,on) case is also analytically tractable when incorporating losses. From Eq. (3.41), $P\left(\text{off,on}\right)$ is given by

$$P\left(\text{off,on}\right) = \sum_{t'=1}^{\infty} P\left(0,t'\right) = \frac{\left(1-\lambda^2\right)y\left(\lambda - y'\right)}{\left(1-y\lambda\right)\left(1-yy'\right)} \ . \tag{3.57}$$

Note that $P\left(\text{on,off}\right)$ is identical to the result above under exchange of primed and unprimed parameters. The probability of both detectors registering photons $P\left(\text{on,on}\right)$ can be tackled by using the relation $\sum_{p,q=(\text{on,off})} P\left(p,q\right) = 1$, yielding

$$P\left(\text{on,on}\right) = \frac{\left(y-\lambda\right)\left(y'-\lambda\right)\left(1-yy'\lambda^2\right)}{\left(1-y\lambda\right)\left(1-y'\lambda\right)\left(1-yy'\right)} \ . \tag{3.58}$$

3.6.2 Lossless subtraction

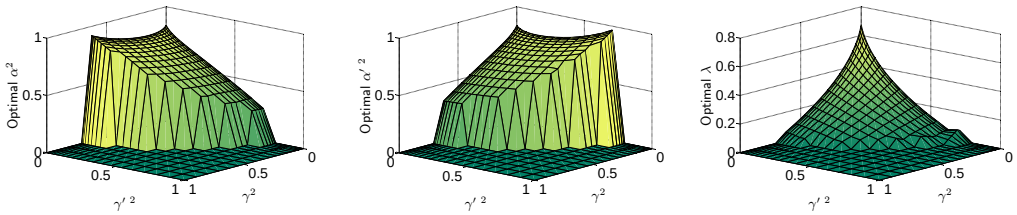
The idealised case of lossless symmetric subtraction using APDs with unit efficiency is analytically tractable[95]. However, lifting the degeneracy of the parameters means the submatrices $\mathbf{C}^{(K)}$ are no longer centrosymmetric, rendering intractable the analytical method used previously. All subsequent results are therefore numerical.

Zhang and van Loock[95] showed that for squeezing parameters $\lambda < 0.95$, the results are essentially equivalent to those with PNRDs. The same is true for perfect asymmetric subtraction: the case where (1,0) photons are simultaneously detected

on each mode respectively, is, within the limits of our numerical analysis, identical to the case where (on,off) is detected with APDs, as shown in figure 3.25 up to $\lambda = 0.8$.

3.6.3 Lossy subtraction

As with the PNRD case calculated above, we can use entanglement gain rate as the figure of merit to be optimised, from which the optimal parameters can be extracted. The optimal parameters α^2_{opt} and λ_{opt} are shown in figure 3.26, with the resulting gain, probability and rate identical to that shown for PNRDs in figure 3.24, as a function of the asymmetric loss parameters γ^2, γ'^2. Note that the optimal parameters are also the same for both the PNRD and APD cases.



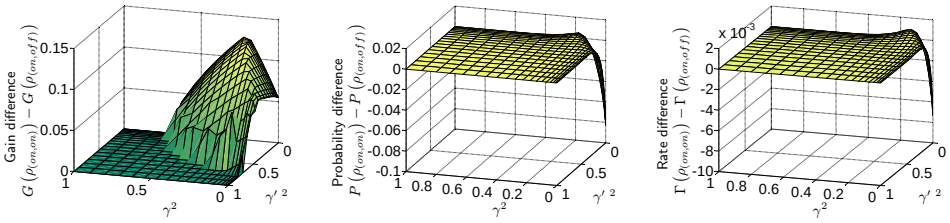
(a) (b) (c)

Figure 3.26: Lossy subtraction with APDs. (a), (b) Subtraction parameters α^2, α'^2, respectively, and (c) squeezing parameter λ, optimised to produce the highest entanglement gain rate under loss given symmetric subtraction with APDs.

Imperfect Asymmetric Detection

As with perfect subtraction, the behaviour of APDs and PNRDs under loss is the same at experimentally accessible values of λ. In the lossless case, we have shown that asymmetric subtraction always produces a higher rate of entanglement gain,

sec 3.5.3, figure 3.24. We now ask whether one strategy is always better than the other for all losses. This turns out not to be the case, as shown in figure 3.27.



(a) (b) (c)

Figure 3.27: Comparing symmetric and asymmetric subtraction with APDs under loss. The difference between (on,on) and (on,off) subtraction events in (a) gain, (b) probability and (c) rate as a function of the losses γ^2, γ'^2 on modes one and two respectively.

While the gain produced when subtracting from both modes is always greater than when subtracting from a single mode (figure 3.27(a)), for a particular range of losses on each mode γ, γ', the probability favours subtracting from just a single mode. This result is repeated in the plot showing the comparative rate of gain (figure. 3.27(c)).

3.7 Conclusion

We have investigated photon subtraction from a two-mode squeezed state as a means to probabilistically increase entanglement under LOCC. By defining the entanglement gain rate as our figure of merit, we are able to optimise over the subtraction beam splitter transmissivity T_2 to maximise this quantity, in the presence of unequal losses on each mode. Our results may be summarised as follows:

1. If the losses are above a threshold, which depends on the number of photons to be subtracted, local subtraction cannot enhance entanglement.

2. When it can, (1,0) subtraction seems to be the best strategy, whether APDs or PNRDs are used to detect the subtracted photon.

3. However, depending on how losses are distributed across the modes, symmetric subtraction may be advantageous.

4. Subtracting more photons produces marginal enhancement in entanglement and is far less probable.

5. APDs are essentially equivalent to PNRDs for most of the λ regime, including when accounting for asymmetric losses.

Given any realistic scenario with lossy transmission channels and imperfect detectors, our conclusions outline the most suitable strategy that must be adopted to achieve entanglement enhancement in CV systems most effectively. This approach also specifies the initial squeezing parameter λ_{opt} for which this particular protocol works best. The figure of merit we use in this thesis is the entanglement gain rate, relevant to quantum communication applications. For other applications, it may be the final entanglement, or indeed the gain alone, that is more important. The methods presented in this thesis can be easily modified for those purposes.

Photon subtraction is one of the simplest operations introducing non-Gaussianity, thereby opening the gate to a large class of CV quantum information processing protocols such as entanglement distillation that are not possible in the Gaussian regime.

Chapter 4

Two-mode squeezed state source engineering

Given the theoretical results of the previous chapter, we aim to develop the experimental tools required to investigate entanglement distillation, and non-Gaussian operations in general. A fundamental requirement of any continuous variable distillation protocol is a source of two-mode squeezed states (TMSSs) from which to distill entanglement. In this chapter, we discuss the specifications for such a source incorporating the results from the previous chapter. We show how the source developed in our group[35] can be engineered to satisfy the requirements for the BESP distillation scheme[25] and provide the full alignment procedure.

4.1 Source requirements

Broadly speaking, the specifications of the source are dictated by the protocol we are aiming to implement. Some considerations, such as a well-defined mode structure, apply to all CV implementations of quantum protocols. Others are specific to the protocol; for example, showing increased entanglement by photon subtraction is strongly dependent on the initial squeezing.

In this section, we briefly outline the constraints on our source. In subsequent sections, we describe how we addressed these issues.

4.1.1 Modal definition

Central to continuous-variable quantum optics is the definition of the mode structure in which the states reside. Correctly running any CV protocol boils down to measuring the relevant modes whilst suppressing additional modes. In short, it is vital to efficiently measure the right modes to reduce loss and sufficiently filter the wrong modes to reduce noise. It is therefore imperative to use detectors that measure only the mode of interest. This is achieved by ensuring that the source emits into a single mode (or two modes in the case of an entangled state), and that this mode is overlapped as closely as possible with the mode that is measured by the detector.

Optical modes are defined by the electromagnetic degrees of freedom, *i.e.* polarisation, position and direction (momentum), time and frequency. Polarisation is very well-defined for optical beams arising from a coherent pump inducing both lin-

ear and non-linear interactions. The transverse spatial mode may also be precisely controlled and filtered using single-mode fibre.

Temporal versus spectral definition

Controlling time and frequency modes is more difficult. For example, protocols run in the continuous-wave (CW) regime are extremely well defined in frequency, but there is no natural clock to determine when iterations of the protocol have taken place. As such, concepts like success probability become very difficult to define. Indeed, nearly all proof-of-principle demonstrations of continuous-variable entanglement enhancement have been in this regime [29,31,66,98]. A notable exception is the work by Dong *et al.* [28] in which the initial states were generated by a pulsed pump laser. However, the detection scheme in this case electronically down-sampled the repetition rate. The only experimental demonstration of CV entanglement distillation fully in the time-domain in which every pulse is counted has recently been achieved by Kurochkin *et al.* [32].

The primary motivation behind working in the CW regime is ease of detection. As discussed, central to the success of CV schemes is maximising the overlap of the modes of interest with the detected modes. This is relatively straightforward using standard homodyne detection, as described in section 5.2.3. The use of a local oscillator not only provides a coherent phase reference against which the signal is measured, but also acts as a mode filter: the measured mode is entirely defined by the mode profile of the local oscillator. The noise bandwidth of the electronics used

in standard homodyne detection means that it is far easier to run these detectors slowly, requiring a local oscillator with a long temporal mode.

However, as homodyne detectors increase their low-noise bandwidths they can be used with high-frequency (MHz) trains of ultrashort pulses [99]. Indeed, pulsed implementations of CV experiments are becoming increasingly prevalent [32,73,100–103].

Temporal definition is a crucial criterion for scalability. This ensures that probabilistic operations are carried out on the correct mode as well as enabling conditional switching based on such operations. Combined with quantum memories, these provide the necessary ingredients for scalability. This therefore necessitates a pulsed source of TMSSs.

4.1.2 Re-Gaussification

In addition to modal definition, all schemes which rely on interference between multiple sources necessarily require a high degree of indistinguishability. That is to say, not only must the modes of the sources be well-defined (*i.e.* not emit into multiple ancillary modes), they should also be identical. Generating a reservoir of indistinguishable non-classical sources is a significant challenge in quantum engineering [104].

Indistinguishability

The indistinguishablility of two modes is typically measured by the interference visibility between them. Classically, this is typically performed by varying the phase between the modes in an interferometer. Quantum mechanically, states with no

well-defined phase undergo Hong-Ou-Mandel interference [105], based on the bosonic commutation relations, Eq. (A.6) derived in appendix A.

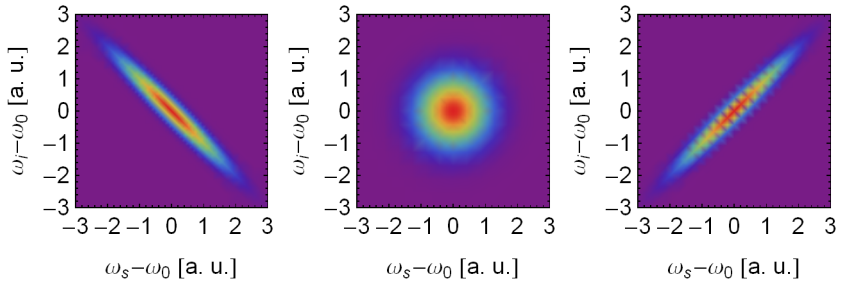
Factorability

Related to indistinguishability is the idea of a *factorable* source. Photon-number correlated sources are frequently used in heralded schemes, whereby detection of one photon in one mode heralds the presence of a photon in the other mode. It is crucial that the heralding detector imparts no additional distinguishing information onto the heralded photon, other than its existence. For a spectrally factorable source [39], no herald detector can be constructed, even in principle, which resolves any frequency information about the photon which is heralded. One approach to remove these spectral correlations is filtering, although this is typically at a significant cost of count rates. A more elegant approach is to engineer the source itself, through control of the pump and non-linear interaction properties (phase-matching) [35]. This is the approach adopted in our experiments.

Spectral purity

Related to the factorability of two-mode sources is the concept of spectral purity. If the two modes generated in the non-linear interaction are spectrally uncorrelated, the source is spectrally factorable. Spectral correlation (or absence of it) can be seen in the joint spectral intensity (JSI) of the source. Examples of the JSI are shown in figure 4.1. For the source described by Mosley [39], the JSI shows that a factorable

source with high indistinguishablity can be generated.



(a) Negative correlation (b) No correlation (c) Positive correlation

Figure 4.1: Examples of joint spectral intensity distributions in parametric down-conversion. These relate the frequency of the signal photon ω_s to that of the idler ω_i and $\omega_0 = \omega_p/2$ since we consider the spectrally degenerate parametric down-conversion (see figure 2.1). (a) Negatively correlated spectra; (b) uncorrelated spectra; and (c) positive correlation between spectra. Note that (b) corresponds to the spectrally factorable case since measurement of the signal leads to no information about the spectrum of the idler photon.

For sources pumped at lower repetition rates and higher peak powers, the JSI is hard to measure due to low data rates. Whilst we assume that the JSI of our source does not change with increasing pump pulse energy, this assumption has not been tested. However, fast, high efficiency detectors [106] could pave the way for such measurement to be made in reasonable timescales.

4.1.3 Initial squeezing

The maximum initial squeezing of the TMSS is determined by the pump power. However, one cannot simply increase this arbitrarily, not only because there is a limit to the power output from the pump laser, but also other non-linear interactions may be stimulated in the source. At higher pump powers, such spurious effects play an increasingly significant role in modal degradation; there exists an optimum to be

found between pump intensity and quality of the spatial mode of the state. This optimum depends entirely on the idiosyncrasies of the setup employed; there is no catch-all method for determining the best set of experimental parameters to use.

The remainder of the chapter describes the setup used, incorporating many of these considerations.

4.2 Source hardware

The source we use is type-II collinear parametric down-conversion (PDC) in potassium di-hydrogen phosphate (KH_2PO_4). The physics of the non-linear interaction underlying down-conversion is described in many texts, *e.g.* Boyd[107]. Furthermore, the background to the source we use is detailed extensively in the thesis by Peter Mosley[39]. Here we concentrate on the experimental implementation of the source. The setup for the source comprises three distinct stages: the laser system, second harmonic general and the down-conversion itself, as shown in figure 4.2. In this section we describe each stage in detail.

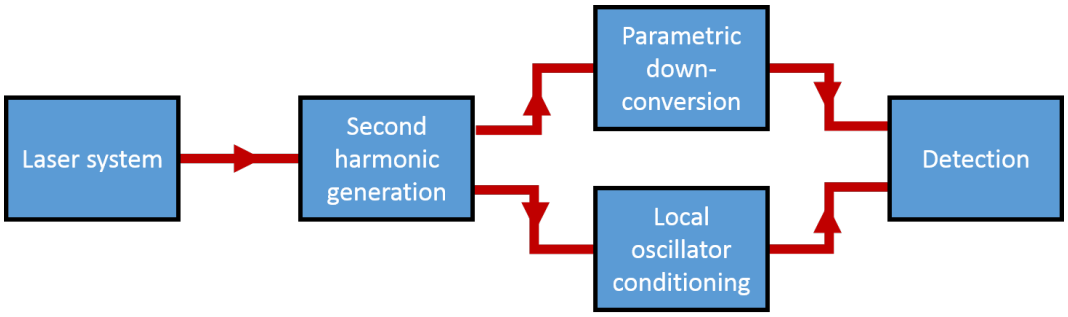


Figure 4.2: Schematic showing the major elements of all subsequent experiments. The laser system, second harmonic generation and down conversion are all described in this chapter. The local oscillator conditioning and detection setup depends on the particular experiment; these are discussed in the following chapters.

4.2.1 Laser system

The laser system with preparatory optics is shown in figure 4.3.

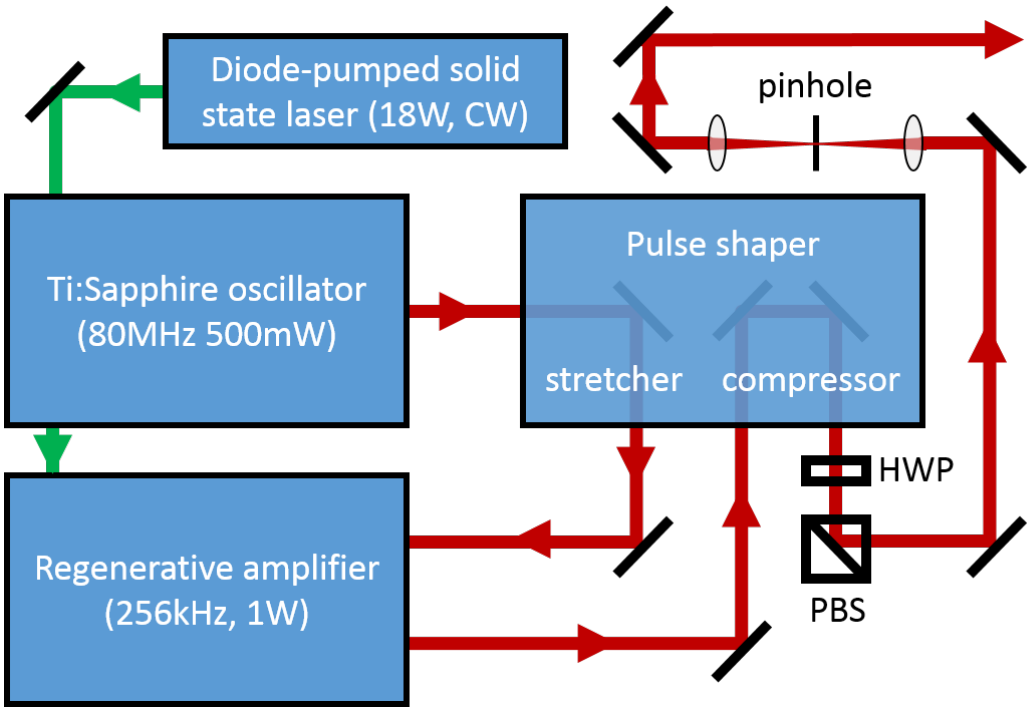


Figure 4.3: Laser system. A diode-pumped solid state laser (Coherent Verdi V18) pumps both a Ti:Sapph oscillator (Coherent Mira) and a regenerative amplifier (Coherent RegA). Prior to seeding the amplifier, the output of the oscillator is spectrally stretched. Similarly, pulses from the amplifier are recompressed before entering the experimental setup. A half waveplate (HWP) and polarising beam splitter (PBS) provided power control and polarisation filtering, and the pinhole is used for spatial-mode cleaning.

The laser system originates with a diode-pumped Titanium:Sapphire (Ti:Sapph) oscillator (Mira, Coherent Inc). The oscillator is mode-locked at 830 nm with $\gtrsim$ 30 nm bandwidth. This generates transform-limited 30 fs pulses at a repetition rate of 80 MHz. Run at an average power of 500-600 mW, each pulse delivers 7.5 nJ energy with 250 kW peak power. On its own, these pulse energies are insufficient to

generate the large squeezing parameters required.

The Ti:Sapph pulses are thus used to seed a regenerative amplifier (RegA, Coherent Inc). This is an additional Q-switched, cavity-dumped oscillator that amplifies the seed beam, at a cost of reduced repetition rate (and longer pulses). The result is 150 fs pulses at 830 nm at a repetition rate of 250 kHz. Run at an average power of 1 W, the energy in each pulse is thus 4 μJ (and peak powers of 26.7 MW), three orders of magnitude higher than the Ti:Sapph oscillator alone.

Prior to entering the amplifier, the Ti:Sapph pulses are temporally stretched by a pair of gratings. This reduces the peak intensity of pulses within the amplifier to avoid damaging it. However, the resulting pulses are too long for our experiments. Therefore, they are re-compressed by the same pair of gratings prior to the main experimental setup. This coherent pulse amplification process allows us to generate short pulses with very high peak power.

On leaving the compressor, a waveplate/polarising beam splitter combination is used both to define the polarisation and set the required power. A 75 μm pinhole at the centre of a 2:1 telescope, with fused silica lenses of $f = 200$ mm and $f = 100$ mm is used for spatial-mode cleaning prior to entering the setup. We end up with a collimated beam of $\sim$2 mm diameter, delivering $\lesssim$ 80 mW average power to the setup.

4.2.2 Second harmonic generation

Our source is based on an "up-down" frequency conversion scheme, meaning we start with the pump at the wavelength of the down-converted photons, 830 nm, up-convert to 415 nm using second harmonic generation (SHG), before down-converting to a two-mode squeezed state at the wavelength of the original beam (830 nm). The benefits of this approach are explored in more detail in the detection section.

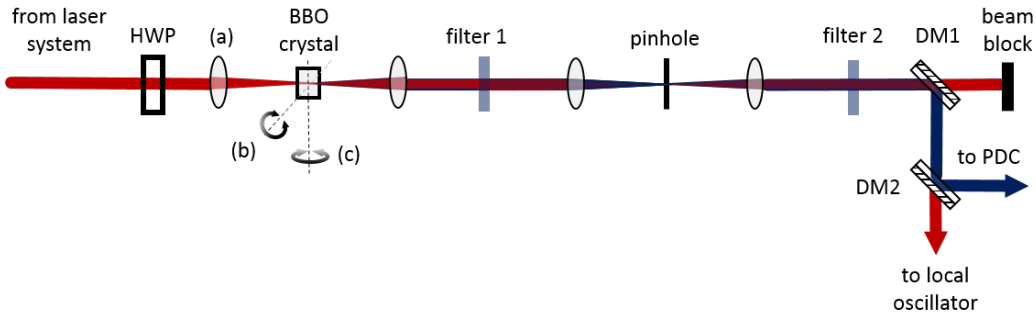


Figure 4.4: Setup for second harmonic generation (SHG). The pump beam is incident on a 0.8 mm BBO crystal (Foctek) cut to phase-match second harmonic generation from 830 nm to 415 nm. This is optimised by adjusting (a) the focussing lens $f = 125$ mm, (b) the tip angle of the crystal and to a lesser extent (c) the tilt of the crystal. The collimation lens after the crystal has a focal length $f = 150$ mm. A 50 μm pinhole in a 1:1 telescope with lenses with $f = 100$ mm provided spatial cleaning of the second harmonic beam, a positive side-effect of which is additional filtering of the pump. Filters 1 and 2 are 2 mm Schott BG40 & BG39 bandpass filters respectively. Two dichroic mirrors (DM), highly transmissive for 830 nm and highly reflective at 415 nm, provide further filtering of the residual SHG pump. The output of one of these mirrors is used as the local oscillator beam for subsequent weak-field homodyne detection (see sec 5.3).

This is shown in figure 4.4, our SHG crystal of choice is barium borate (BBO) of length 0.7 mm. Ideally, SHG is a parametric process which does not deliver energy to the crystal. However, the crystal is not perfectly transparent and residual absorption can heat the crystal locally, potentially introducing thermal lensing effects

or inducing damage. We minimise any absorption that does occur by using a short crystal. Additionally, running the source at 250 kHz means our average power is lower (80 mW as opposed to $\sim$ 500 mW used in typical experiments at 80 MHz), therefore no additional active cooling or dithering of the BBO was required.

The conversion efficiency from the fundamental (830 nm) to the second harmonic (415 nm) is optimised by tuning the polarisation, crystal angle, focussing and spectral compression. We achieved typical conversion efficiencies of 25% (we expect $\sim$ 20 mW at the second harmonic (at 415 nm) from 80 mW of the fundamental (original 830 nm)).

High pump power considerations

Since we are operating at such high peak intensities, a number of alterations were required from the original setup designed by Mosley [39]. One difference is the use of a looser focus into the BBO for second harmonic; we use an $f = 150$ mm lens as opposed to $f = 50$ mm.

Despite this, the spatial mode of the resulting blue beam was still corrupted, possibly due to self-focussing or other higher-order non-linear effects in the crystal when pumped with such high peak power. This result was one of many showing that the spatial-mode structure of both the pump and the down-conversion plays an important role in the quality and brightness of states generated in this way. Many problems encountered in this work arose from low efficiencies caused by poor spatial characteristics; more work is needed to engineer the spatial characteristics

of down-conversion sources to overcome these issues more elegantly, particularly in the high-squeezing regime.

To clean up the spatial mode of the SHG, we used a rather inefficient "brute-force" approach using a 50 μm pinhole. Throughput was typically 50%, which necessitated increasing the power of the SHG pump to compensate this loss. However, the spatial mode was far closer to a Gaussian beam and the count rates when using the pinhole were around twice that when using an unfiltered blue pump at fixed average blue power. This had the further advantage of additional filtering of the residual pump.

Following the SHG and spatial cleaning, the beam was recollimated once more using an $f = 125$ mm lens and passed through an iris to filter out higher-order Airy fringes. Excess light at the fundamental frequency was further filtered by dichroic mirrors and bandpass filters, as shown in figure 4.4. The result is a 5 mW second harmonic beam (415 nm), suitable for pumping a down-conversion crystal.[1].

4.2.3 Parametric down-conversion

The down-conversion itself was carried out in a 10 mm potassium di-hydrogen phosphate (KDP) crystal, cut for type-II collinear phase-matching following Mosley [39]. Type-II parametric down-conversion corresponds to the case where the daughter modes have orthogonal polarisations, one mode of which shares the polarisation of the pump. The setup of the source is shown in figure 4.5. This setup was sufficient

[1] This power was split equally between two down-conversion crystals, in preparation for a multi-source distillation experiment. Ultimately, the second crystal was not required and plays no further part in this thesis.

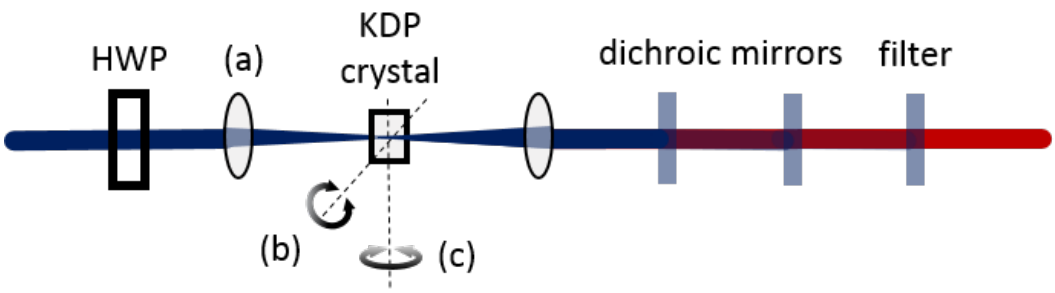


Figure 4.5: Setup for type-II collinear PDC. The pump beam at 415 nm is incident on a 10 mm KDP crystal (Foctek) cut to phase-match type-II collinear PDC, with the HWP set appropriately. As with SHG in figure 4.4, down-conversion is optimised by adjusting (a) the focussing lens $f = 250$ mm, (b) the tip angle of the crystal and (c) the tilt of the crystal. The collimation lens after the crystal has a focal length $f = 150$ mm. The residual pump is filtered by two long-pass dichroic mirrors followed by 2 mm-thick antireflection (AR) coated RG665 filters.

to carry out our high-squeezing experiments; no additional alterations to the original setup[39] were required.

4.3 Source alignment

This section outlines the alignment procedure used to find coincidence counts between signal and idler modes of the parametric down-conversion source described above.

4.3.1 Initial bright beam alignment

In the following we describe the general alignment procedure for the subsequent experiments. Note that we refer to the fundamental frequency as the "red" beam and the second harmonic as "blue."

1. Ensure RegA is working properly and delivering consistent power (> 1 W prior

to compressor) to setup.

2. Maximise power through the pinhole, and reduce power to 80 mW prior to the SHG setup.

3. Ensure that the waveplate is set correctly for SHG, and optimise blue as per above instructions (section 4.2.2). At 80 mW pump power, expect ∼20 mW second-harmonic.

4. Replace BG39 & BG40 filters with red filter (RG665) to allow red through to the KDP setup. The dichroic mirrors should allow ∼20-30 μW when measured just prior to the KDP, but the pinhole after the SHG crystal will need to be adjusted to allow transmission of the residual red pump.

5. Prior to the PDC crystal, put the red through a pair of irises, the larger separation the better (at least 1 m); we used a removable pick-off on a translation stage to achieve a long alignment distance. Single-mode fibre cannot be used legitimately since this procedure will be used later to determine the blue mode (and no fibre remains single mode at both 415 nm and 830 nm).

6. Having gone through the KDP, couple the bright red to the single-mode fibres that will lead to the detectors. If correctly collimated, ∼60% coupling efficiency should be achievable. Waveplates will need to be set to direct the red beam to the different single-mode fibre coupling stages (Elliot scientific) (see figure 4.6).

This procedure aligns the detection system to a close approximation to the single-photon-level modes from down-conversion. The general setup for counting photons

is shown in figure 4.6.

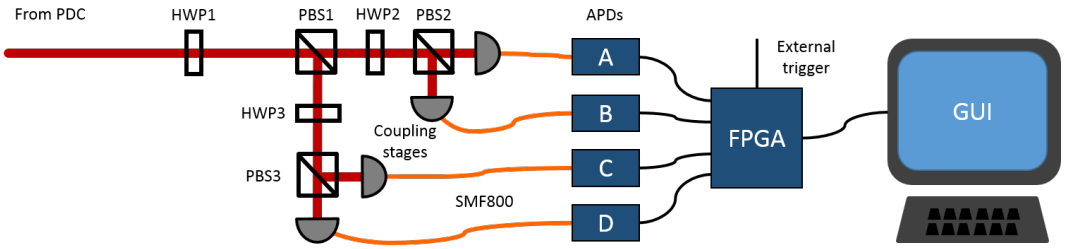


Figure 4.6: Detector setup for alignment. The PDC source emits photons into two orthogonal polarisation modes. HWP1 is set such that these modes are split at PBS1. Depending on the experiment, the further HWP PBS combinations direct the resulting modes via the coupling stages and single mode fibre (SMF800) to four APDs. These are read by a field programmable gate array (FPGA), which allows counting single clicks from each APD and coincidences between any combination thereof. The FPGA is externally triggered at the repetition rate of the laser system by the laser itself using a fast photodiode. This data is displayed in a graphical user interface (GUI) in Matlab.

4.3.2 Blue alignment

Having aligned the red beam as outlined above, the second harmonic (blue) should be aligned in order to pump the down-conversion. This is achieved as follows:

1. Replace the blue filter after the BBO and realign the mode-cleaning pinhole. About 50% of the blue input beam should be transmitted.

2. Ensure the spatial mode is circular and use an iris to block higher-order Airy fringes around the central mode.

3. Re-collimate the blue and use steering mirrors to place it back on the pair of irises before the KDP.

4. Ensure the KDP angles are set correctly by inspecting the back-reflected blue

beam. Roughly speaking, it should overlap the incoming beam as far as possible. If the photon-counting detection system is in place, switched on, and with the correct coincidence timing, photons should be seen.

5. Check that any counts seen are indeed down-conversion by rotating HWP1 (as shown in figure 4.5) to tune away from the correct setting for phase-matching. If the counts disappear then reappear, it is likely to be down-conversion.

6. Due to the relatively low repetition rate of the RegA, the initial counts may be only around 100 counts per second (cps). However, patient alignment of the coupling stages and beam-walking should yield around 6-8 kcps single-photon clicks (singles), under the conditions described above.

4.3.3 Coincidences

Once counts are seen from each down-converted mode, it is important to ensure they are coincident, *i.e.* that the correct modes from the down-converter are being measured. This is done by aligning the couplers to optimise the coincident rate, *i.e.* the ratio of coincidence counts to singles. This should be optimised towards 20%; though 10-15% is typical. Note that aligning to coincidences may not correspond precisely to the highest singles counts.

Heralding efficiency

The heralding efficiency η_H is a practical figure of merit for the source. It is given by

$$\eta_H = \sqrt{\frac{C^2}{S_1 S_2}} \,, \tag{4.1}$$

where C is the coincidence count rate and S_1, S_2 are the singles count rates on each mode, respectively. For our source, typical coincidence rates of 900 cps given 6 kcps singles on each detector correspond to a heralding efficiency η_H of 15%; at best, we achieved 20% although singles rates were then lower. By contrast, the heralding efficiency achieved by Mosley was 26%[39]. We attribute this discrepancy to a poor spatial mode profile when pumped with such high peak powers, similar to the spatial distortion in SHG. Unlike with SHG, we cannot filter the spatial mode of the down-conversion without losing count rates. This effect causes poor coupling into single-mode fibre, limiting our heralding efficiency.

Squeezing parameter

The heralding efficiency can also be used to put a lower bound on the efficiency of the detection systems[108]. To first order, this can then be used to put an upper bound on the rate of photon pairs emitted by the source (by neglecting higher-order terms). Taking the values used above, if we assume 6 kcps is 15% of the rate of photon pairs emitted by the source, then the source could emit up to 40 kps, corresponding to an emission probability of 16% and a squeezing parameter $\lambda = 0.4$. However, it is important to stress that this is a very coarse estimate, the primary assumption

being that the squeezing emits only into two modes. Multimode effects could cause this value to be artificially high; a more thorough analysis considers the higher-order mode structure when pumped at high powers. Such an analysis was carried out by Andrew Worsley, a former Masters student in our group[109,110].

4.3.4 Troubleshooting tips and tricks

There are myriad reasons why photons and or coincidences may not be seen in the first instance following realignment with bright beams. The first tip is to try and minimise the time between the alignment with the bright red beam and with the blue beam, and make sure all alignment is carried out only when correctly aligned through the pair of irises between SHG and PDC crystals.

KDP alignment

If the crystal angle is not optimised and no photons are seen, then adjust the angle to overlap the back-reflection with the incoming beam (ideally on the alignment irises). Once counts are seen, tune the crystal angle to maximise the coincidence rate.

Another tip is to use a well-calibrated narrow spectral filter (3-4 nm) in one of the modes. Optimising the KDP crystal angle at the correct wavelength ensures the correct phase-matching for PDC.

Fluorescence

It is common to see some counts caused by fluorescence in the KDP crystal. Check that any blue glow from the crystal is minimised. Any glow is likely to arise from a damaged spot of the crystal face. Translate the crystal until any glow is minimised (and the beam still passes through cleanly). A good approximation of the acceptable level of fluorescence is the counts that remain when HWP1 is turned to frustrate down-conversion. These should be less than 5% of the counts when the wave plate is optimised for down-conversion.

Detection electronics

One way of reducing noise counts is to direct the entry of the coupling stages away from the laser into the setup. Additional screens can be used at various points in the setup to avoid scatter into the coupling stages or detectors themselves. The low count rate means that coupling to noise sources is a definite possibility.

When looking for coincidences, ensure all of the time delays and coincidence windows used in the detection electronics are set correctly. Comparing the raw APD counts to counts coincident with the timing trigger pulse should give an indication of whether the coincidence window is optimised. Typically, the raw counts were about 1500 cps more than the windowed counts, which is consistent with the specified dark-count rates for these detectors (see appendix E).

Mismatched counts

It is fairly common to have one mode out of the down-converter well aligned but not the other, with correspondingly low coincidence counts. One trick is to swap the modes on the output of the down-converter to check collinearity. This is achieved by rotating HWP2 in figure 4.5 such that the down-conversion modes are directed to different coupling stages at the polarising beam splitter. Slight differences in alignment mean the source will never appear perfectly collinear, but it is often a good starting point.

A further strategy if one mode is well aligned is to overlap a bright ancillary beam. This beam can then be used to align the other mode by enforcing collinearity. Additionally, back-propagation of a bright beam from the detector fibres can be overlapped with the forward-propagating pump beam.

Chapter 5

Measuring local quantum states

In this chapter we discuss measurement and detection in a quantum optical setting. We show how different aspects of quantum measurement theory lend themselves to the design of different detectors. We describe weak-field homodyne detection and show two novel uses for such detectors in conditional state preparation and non-classical state characterisation.

5.1 Measurement

Measurement in quantum mechanics plays a significant role. It connects the underlying quantum phenomena with a classical signal observed by the experimentalist. Deducing non-classical phenomena from this signal is an intricate process and is in itself an active area of research, *e.g.* by developing a quantum-mechanical picture of the detection process[49,111]. In this section, we develop a model of measurement, and in the following section apply this model to different detectors.

5.1.1 Projective measurement

Classically, many measurements on a single system can be made, and future results are independent of prior outcomes. Quantum mechanically, measurement typically destroys any superposition (or"collapses the wavefunction" [112]) that may be present in a state, meaning future results are identical to the first. This is projective measurement: the act of measuring projects the state onto one of its eigenstates. In an optical setting, multiple measurements on a particular state are all but impossible. One typically measures the presence or absence of photons in a mode; once the photonic energy in that mode has been transferred into a measurement signal, the photons no longer exist. Therefore, in quantum optics, projective measurements on single-mode states can only be performed once.

If the state is entangled, that is, if it exists delocalised across more than one mode, then projective measurement takes on a more powerful role. For photon-number correlated states, of which the TMSS in Eq. 2.33 is an example, measuring a given photon number in one mode projects the other mode into exhibiting the same photon number. Comparing the measurement outcomes across each mode of a number-correlated state, therefore gives rise to the non-local correlations characteristic of entanglement.

Projective measurement plays an active role in many quantum protocols. Section 5.5 details how this technique can produce effective non-linearities for state engineering.

Mathematically, measurement is described by an operator $\hat{M}_m$, which returns

the eigenvalue (outcome) m when acting on a state $|\psi\rangle$. The probability P_m of obtaining the outcome m is $P_m = \langle\psi|\hat{M}_m^\dagger \hat{M}_m|\psi\rangle$. The set of operators $\left\{\hat{M}_m\right\}$ satisfies $\sum_m \hat{M}_m^\dagger \hat{M}_m = \mathbb{I}$, where $\mathbb{I}$ is the identity operator on the state space.

An Hermitian measurement operator $\hat{M}$ may be decomposed into the sum of *projective measurement operators* $\hat{P}_m$, *i.e.*

$$\hat{M} = \sum_m m\hat{P}_m \ , \tag{5.1}$$

weighted by the measurement outcomes m, which are the eigenvalues of $\hat{P}_m$. These projection operators $\hat{P}_m$ are necessarily Hermitian, satisfy $\hat{P}_m^\dagger \hat{P}_m = \hat{P}_m^2 = \hat{P}_m$, and are orthogonal, such that $\hat{P}_m \hat{P}_{m\prime} = \delta_{m,m\prime}\hat{P}_m$. However, this is not the most general class of measurement operators.

5.1.2 Positive operator valued measures

A more general approach to measurement in quantum mechanics is to treat the detector as a quantum object and look at its responses to different input states. The possible responses of a detector to a single input state is defined by its positive operator-valued measure (POVM). A POVM is a set of elements $\{\Pi_m\}$ which describe the outcome of measurements $M_m^\dagger M_m = \Pi_m$, whereby, in general, the outcomes are not orthogonal and $\Pi_m \Pi_{m'} \neq \delta_{mm\prime}\Pi_m$. Indeed, equality is achieved if and only if the POVM elements Π_m are projectors.

By construction, POVMs are positive $\Pi_m \geq 0$ and form a complete set $\sum_m \Pi_m = \mathbb{I}$, which requires $\sum_m M_m^\dagger M_m = \mathbb{I}$. The probability of a particular outcome p_m is

quantified in Born's rule[113,114]:

$$p_m = \mathrm{Tr}[\rho \Pi_m] \ , \tag{5.2}$$

where ρ is the state upon which the measurement is made.

The strength of this approach is exemplified in the Wigner picture. An analogy can be drawn between pure states $|\psi\rangle$ measured by projectors P_m, and density operators ρ measured by POVMs Π_m. Just as the Wigner function graphically represents ρ, so the POVM elements can be graphically represented in the same space, that is, in phase space (see section 2.2.2). Indeed, the probability identified in equation 5.2 is equivalent to the overlap of the Wigner function of the state ρ with that of the POVM Π_m:

$$p_m = \mathrm{Tr}[\rho \Pi_m] = \int \mathrm{d}X \int \mathrm{d}P \ W_\rho (X, P) \, W_m (X, P) \ , \tag{5.3}$$

where the Wigner functions of the respective elements are defined in equation 2.23 (and the density operator ρ is replaced by Π_m when calculating $W_m (X, P)$). Using this picture we relate measurement outcomes to quadrature values.

5.2 Detection

We distinguish detection from measurement as the physical device or process that extracts information from the state under investigation. In a quantum optical setting, detectors convert an electromagnetic intensity from an optical mode into an

electrical signal (typically current). Further information about the state can be extracted by specifying the particular mode(s) incident on the detector. We will not go into detail of the device physics involved in the energy conversion process, we will instead consider qualitatively the response of a number of relevant detectors.

5.2.1 On-off detectors

On-off detectors detect the presence or absence of photons: ideally, they "click" when at least one photon is incident and do not click when vacuum is incident. It is straightforward to write the ideal POVMs for these detectors:

$$\Pi_{\text{“no-click”}} = |0\rangle\langle 0| \ , \ \Pi_{\text{“click”}} = \mathbb{I} - |0\rangle\langle 0| \ . \tag{5.4}$$

Examples of on-off detectors include avalanche photodiodes (APDs), where the click is caused by a photoelectron-triggered avalanche in a reverse-biased PN diode, or a superconducting nanowire single-photon detector (SNSPD), whereby at least one photon incident on a superconducting nanowire causes a localised hotspot creating a macroscopic change in resistance. The work presented throughout this thesis used Perkin-Elmer APDs, the relevant parameters of which are a quantum efficiency of $\sim$50% and a dead time of $\sim 35\,\text{ns}$. For more details see appendix E.

5.2.2 Photon-number resolving detectors

Photon-number resolving detectors (PNRDs) provide more information about a quantum state due to their higher resolution (more POVM elements). For ideal

PNRDs, the response of the detector is a monotonic function of the number of input photons, such that the POVMs are simply number projectors:

$$\Pi_n = |n\rangle\langle n| \ . \tag{5.5}$$

An example of a PNRD of this kind is a transition edge sensor (TES) [68], based on the response of a superconductor held at the transition temperature to an incident photon packet. Note that this differs from the SNSPDs, which respond identically to one or many photons incident on their active area.

In fact, the TES detector boasts not only number resolution but also exceptional efficiency. Unfortunately, the hardware requirements are demanding (namely mK cryogenic systems), though such detectors are becoming more widespread [11,115].

(Time-)multiplexed detectors

An alternative is to exploit photon-number resolution from arrays of on-off detectors. Photon-number resolution can be achieved by splitting an input mode into a number of output modes, each of which are incident on an on-off detector such as an APD. These modes can be spatial or temporal; we use a combination of both as developed by Achilles *et al.* [116] and shown in figure 5.1

Such multiplexed detectors are characterised by the number of bins N into which an incident beam is divided, which results in a set of click statistics $\{c_i\}$. With increasing numbers of bins, the number of clicks c_i closely resembles the incident number of photons n [117]. However, in the regime of limited resources, combinatorics

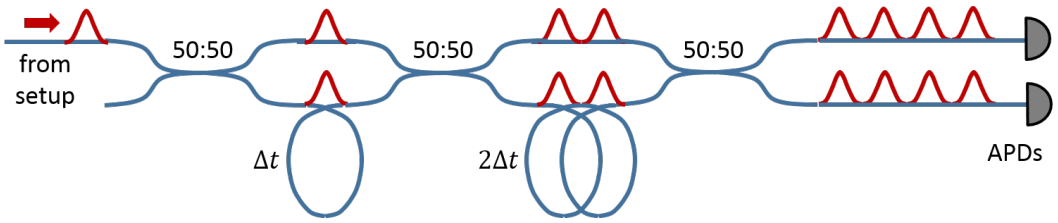


Figure 5.1: Setup for a time-multiplexed detector (TMD). The incident pulse is fibre-coupled to a 50:50 fibre beam splitter. One arm travels directly to the next fibre beam splitter, while the other undergoes a fibre delay of $\Delta t = 50\,\text{ns}$. This process is repeated, with the second fibre delay twice as long the first, *i.e.* $2\Delta t = 100\,\text{ns}$. Each output is incident on an APD, yielding four temporal modes each, allowing number resolution up to eight photons.

dictate how n photons are divided among N bins.

When writing the POVM of such detectors, one needs to take into account both the convolution $\mathbf{C}$ and loss $\mathbf{L}(\eta)$ within the multiplexing geometry. The convolution matrix describes how n input photons are mapped to c_i clicks in the detector, given the multiplexing architecture. Following Coldentstrodt-Ronge *et al.*[118], we can write the POVM elements as

$$\Pi_n = \sum_{c=0}^{n_0} \mathbf{C} \cdot \mathbf{L}(\eta) \, |c\rangle\langle c| \, , \tag{5.6}$$

where c is the number of clicks arising from n input photons incident on N bins, such that $n_0 = \min(n, N)$. Extracting the exact form of $\mathbf{C}$ and $\mathbf{L}(\eta)$ is detailed in Coldentstrodt-Ronge *et al.*[118]. Additionally, Worsley *et al.*[110] demonstrated how the efficiency parameter η could be measured when the detectors are coupled to a two-mode number-correlated photon source.

5.2.3 Quadrature detection

Quadrature detection in terms of POVMs is rather complicated. Since there exists in principle an infinite number of continuous phases from which to define the POVM element for quadrature detection, the set of POVMs is therefore also infinite. Determining the detector response of a continuous detector is a fledgling area of research [119].

The requirements of a measurement system for detecting optical quadrature variables arise from their definition. Quadrature operators are characterised by an amplitude at a given phase, therefore the POVMs of a suitable measurement device should recover this information from an input mode.

Homodyne detection

One detection scheme that extracts quadratures is optical homodyne detection [120]. A bright local oscillator (LO) interferes with a weak signal state, both outputs of which are incident on standard PIN photodiodes, as shown in figure 5.2. The photocurrent resulting from one photodiode is subtracted from the other. In this way correlated classical noise is extinguished such that only uncorrelated quantum noise remains. If the signal state is in the vacuum state, the resulting noise signature comprises the fluctuations inherent in the quantum vacuum.

Homodyne detection can be regarded as optical amplification: the LO amplifies the noise of the signal with which it interferes. Different input states have different noise signatures when measured in this way, and information at the single-photon

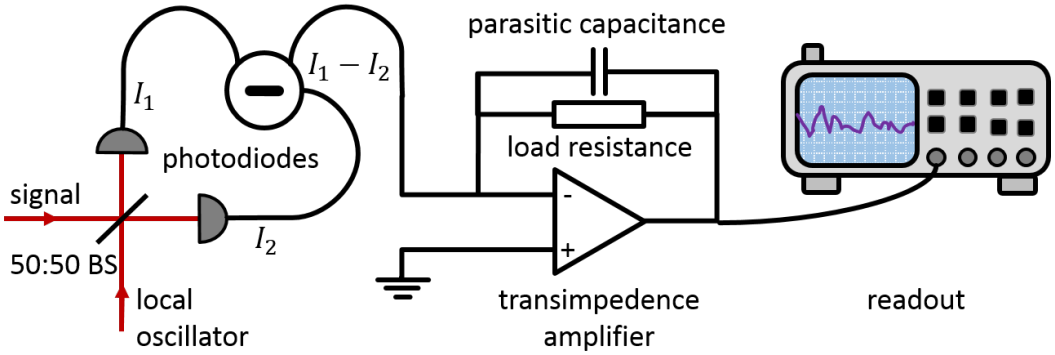


Figure 5.2: Optical and electronic setup for homodyne detection. The signal interferes with a strong local oscillator at a beam splitter (BS). The resulting modes are sent to two standard PIN photodiodes. Their photoncurrent is subtracted and then amplified in a transimpedence configuration to generate a photovoltage, which can be measured on some readout device, *e.g.* an oscilloscope. Any parasitic capacitance limits the temporal response of the detector.

level can be efficiently extracted without requiring detectors sensitive to single photons. Furthermore, by varying the phase of the bright LO, the noise structure of the marginal distribution of different quadratures can be found. From the marginals, the Wigner function can be reconstructed using *quantum state tomography* [46,121].

One of the major advantages of homodyne detection is its intrinsic mode selectivity. The mode of interest of the signal is defined completely by the local oscillator; all other photons are not detected. By contrast, the response of on-off detectors, whether in standard or multiplexed architecture, is inherently multimode. To isolate a particular mode, substantial filtering is required, which typically causes additional loss in the mode of interest.

Practical limits on homodyne detection

Practical considerations dictate how homodyne detection is best used. While the physics of quantum noise amplification is contained entirely within the optical setup, the extraction of this information is determined by the device physics of the photodiodes and photocurrent subtraction electronics.

Central to homodyne detection is that the optical noise remains larger than any electronic noise in the detector. Since technical noise typically increases with bandwidth, the operating speed of homodyne detection is therefore determined by the noise response at high frequencies. A major challenge in the pulsed optical regime—typically operating at 80 MHz (which is the repetition rate for most commercial modelocked oscillators)—is to build detectors that offer both a fast response and low noise. Recent results along these lines have proved very promising indeed [99,122–124].

5.3 Weak-field homodyne detection

Standard homodyne detection implements a quadrature projection in phase space. This projection is a Gaussian operation, and as such, it cannot be used as an active element in a distillation scheme. Furthermore, this type of measurement yields no information about the coefficients of the photon-number components (Fock layers). To bridge the gap between the discrete and continuous regimes, an alternative to standard homodyne detection has been developed [125].

An alternative to using a strong local oscillator as a phase reference is to use a weak local oscillator of similar intensity to the signal, and to measure the resulting

interference pattern directly. This process is conceptually different from strong-field homodyne detection described above, although the outcome—amplitude measurements made with respect to a phase reference—yields similar information.

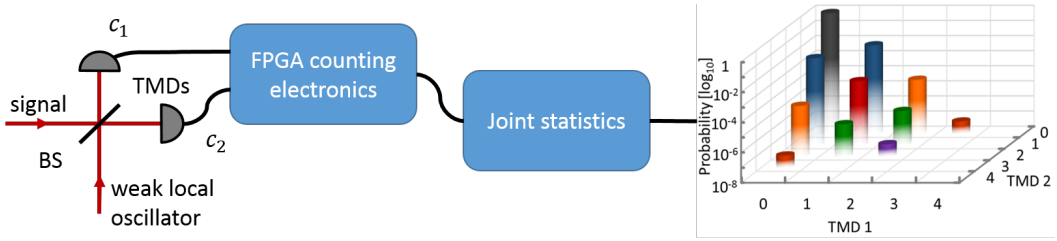


Figure 5.3: Optical and electronic setup for weak-field homodyne detection. The signal interferes with a local oscillator of similar intensity at a beam splitter. The resulting modes are sent to two TMDs, shown in figure 5.1. The counts c_1, c_2 are processed by a field programmable gate array (FPGA), from which a joint statistics matrix can be extracted.

The optical set up for a weak-field homodyne detector is shown in figure 5.3. A signal state of mean photon number $\bar{n}$ interferes with a coherent state of similar mean photon number $|\alpha|^2 \sim \bar{n}$, and the resultant modes are detected on time-multiplexed detectors[116], as described in the previous section.

5.3.1 Joint statistics

The result of a weak-field homodyne measurement is a pair of numbers of clicks c_1, c_2 from each TMD. Binning the results of repeated measurements (at a fixed phase setting) results in an $N \times N$ "joint statistics" matrix. After normalising this data to the number of measurements m taken, the elements $p_{i,j}$ of the joint statistics matrix represent the joint probability of obtaining i clicks in one output port and j clicks in the other output port. It is from these statistics that information about

the state is extracted.

5.3.2 Practical weak-field homodyne detection

While weak-field homodyne detection combines many of the advantages of both number projection and phase resolution, it also retains some of the disadvantages of both schemes. Strong-field homodyne detection probes an extremely well defined mode, whereas weak-field homodyne does not; all photons incident on the detector are measured, not only those that interfere with the weak-field local oscillator. Photons that don't interfere appear as noise in the joint statistics. It is therefore imperative to isolate a particular mode as well as possible. This means carefully matching the temporal, spectral, spatial and polarisation properties of the weak local oscillator and the signal modes.

Mode overlap

Spectral overlap is ensured with narrowband interference filters: 3 nm on the signal and 8 nm on the idler. The bandwidth of the local oscillator is typically 30 nm, but the effect of the loss caused by the filter is easily mitigated by increasing the power. Spatial overlap is determined by coupling both modes into single-mode fibre (SMF800), and the polarisation of each is set by wave plate and beam splitter combinations. Temporal mode-matching in the pulsed regime is found by setting the arrival time of each mode on the interference beam splitter; the bandwidth of the temporal mode is set in the spectral domain.

The total overlap of the two modes is most easily observed through Hong-Ou-Mandel-type interference[105]. To that end, we interfere a weak coherent state of intensity $|\alpha|^2$ with a heralded single photon. The ideal interference visibility of this scheme is given by[36]

$$V = \frac{|\alpha|^2}{2} \frac{e^{-|\alpha|^2/2}}{1 - e^{-|\alpha|^2/2}} \ . \tag{5.7}$$

This visibility is scaled by the mode overlap $\mathcal{O}_M$ to yield the measured visibility $V_{\text{meas.}}$; the mode overlap is thus extracted by

$$\mathcal{O}_M = \frac{V_{\text{meas.}}}{V} \ . \tag{5.8}$$

In aligning much of the experimental work that follows, dips were frequently measured to ensure the temporal overlap. The setup for this alignment experiment is shown in figure 5.4. We seek three-fold coincidences as a function of temporal delay between the heralded photon and the coherent state. An example is shown in figure 5.5. With a coherent state intensity of ~ 0.1 photons, this dip corresponds to a lower bound on the mode overlap of 60%.

A significant consideration when using heralded single-photon sources is correctly defining the signal and idler modes emerging from the down-conversion crystal. This means the down-conversion source should emit into as close to a two-mode state as possible—any multimode behaviour degrades the heralding process. Engineering the correct modal structure of heralded single photons in our source in the weakly-pumped regime is described in detail in the thesis by Mosley[39]. The behaviour of

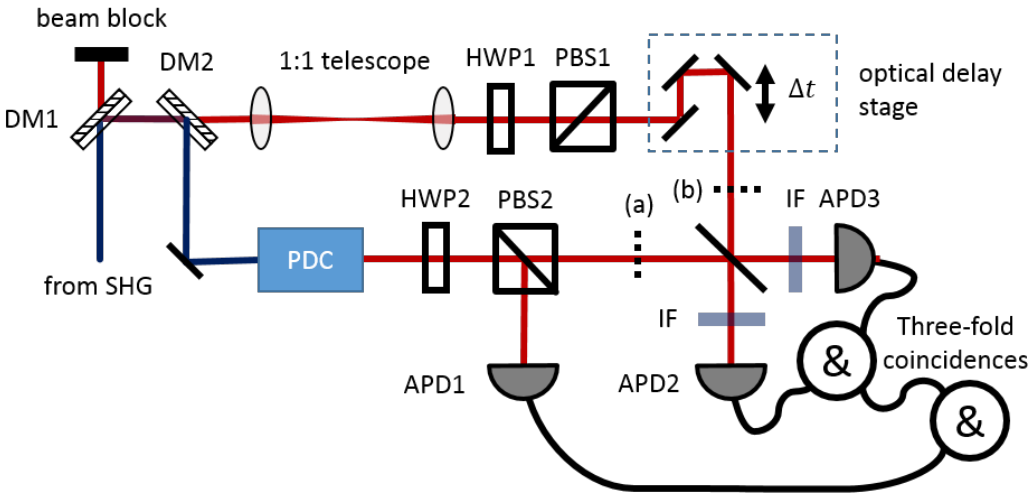


Figure 5.4: Setup to carry out a Hong-Ou-Mandel interference experiment between heralded down-conversion and a weak coherent state. The local oscillator mode is conditioned to overlap the down-conversion mode using a 1:1 telescope (comprising two $f = 100\,\text{mm}$ lenses separated by $2f$). The optical power of the coherent state is reduced to $\lesssim 1$ photon per pulse using a polarising power control comprising a half-wave plate (HWP1) and a polarising beam splitter (PBS1). Using a delay stage, the arrival time of the weak local oscillator is delayed with respect to the signal. PDC comprises the setup shown in figure 4.5. APD1 heralds the presence of down-conversion into the interference setup, whereby APDs 2 & 3 detect the resulting interference. A dip is seen as a function of delay in the three-fold coincidences, *i.e.* all three APDs fire simultaneously. The interference filters (IF) ensure that the LO and the signal are in the same spectral mode. When looking at the signal and heralding on the idler (the results of which are shown in figure 5.5), 3 nm filters were used.

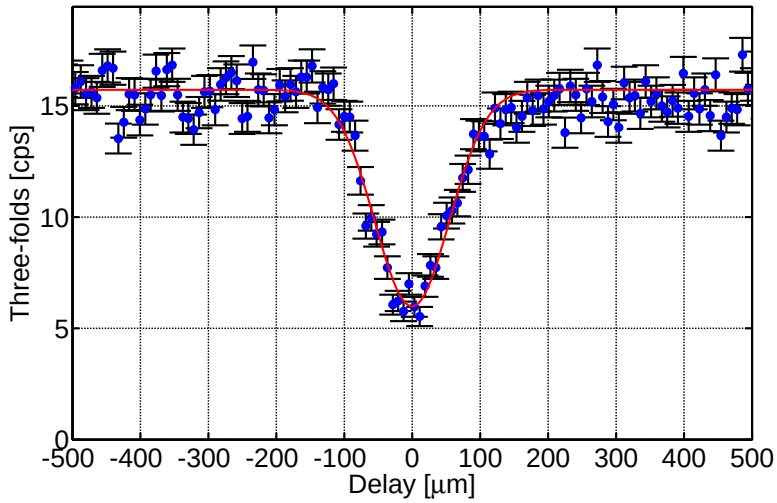


Figure 5.5: Hong-Ou-Mandel dip between heralded down-conversion and a weak coherent state. At maximum temporal overlap, the coincidence rate drops by 61%. The width of the dip is determined by the widths of the temporal modes of the LO and signal, which are themselves determined by a spectral filter. In this case we were looking at the narrower spectral mode emitted by our down converter, which we filtered down to 3 nm, corresponding to a full-width-half-maximum of 110 μm.

the source with higher pump power, as required for high squeezing, is described in chapter 4.

Sources of noise

The non-unit mode overlap can be attributed to a variety of noise sources. The most significant is background local-oscillator photons. These can be isolated by looking at the three-folds that occur when the heralded single photon is blocked (by placing a beam-block at position (a)) in figure 5.4. For the results shown in figure 5.3, this amounted to ~ 3 three-folds per second. This is an upper bound, based on our non-unit heralding efficiency; in the case of perfect heralding efficiency, these multiphoton events are accounted for in the visibility formula, Eq. 5.8.

A second source of noise is heralded two-photon events. Since we use an APD to detect at least one photon in the herald mode, there exists a small but finite probability of heralding two photons. This is isolated by blocking the local oscillator (placing a beam block at point (b) in figure 5.4) and counting three-folds, in the case above about 0.7 per second.

A further noise source is detector dark counts, that is, accidental three folds when no light is incident on the detectors. Though this is counted in each of the noise calibration procedures above, it is considered negligible. Raw detector dark counts are individually of the order of 1000 cps. Furthermore, the detectors are gated such that only clicks occurring in a 3 ns window around a trigger pulse are counted. The gated dark counts are no more than 100 cps. Given trigger pulses at 250 kHz,

this corresponds to a contribution of 1.6×10^{-5} cps. Further details on the counting hardware are give in appendix E.

5.4 Phase stability and control

A central feature of homodyne detection is its phase dependence; our weak-field homodyne detector should also extract any phase information. A translation stage allows coarse adjustment of the delay between the signal and the LO pulses. Additionally, fine delay, on the order of the wavelength, determines the relative phase between the modes. When taking measurements, we require not only phase stability, but stability at arbitrary phase settings.

5.4.1 Passive stability: scope of the problem

Before going on to discuss methods for active stabilisation, it is worth considering the level of stability that is required, and to what extent the interferometer is already passively stable. Regarding the stability required, a rough estimate of 5° was used. A more precise value depends on the noise analysis of the phase-dependent detection strategy discussed in section 6.4.

Measuring phase

The passive stability of the interferometer is calculated by extracting the phase from an interference pattern in the spectral domain. The setup to measure this interference pattern is shown in figure 5.6.

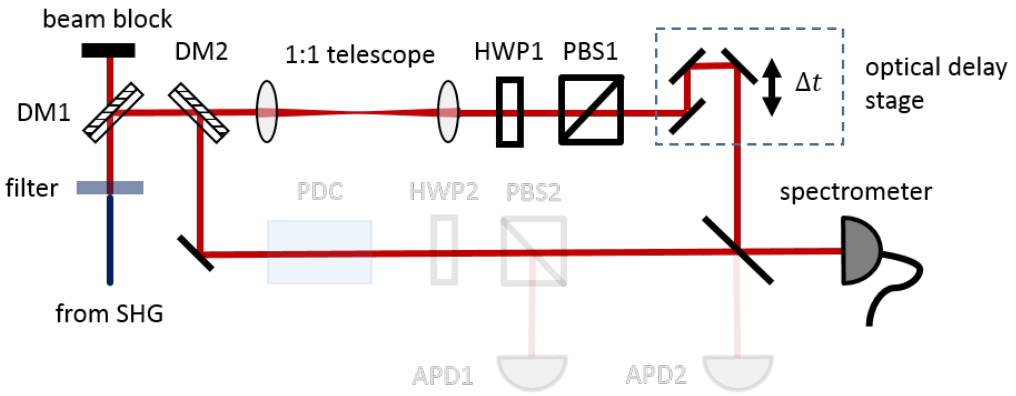
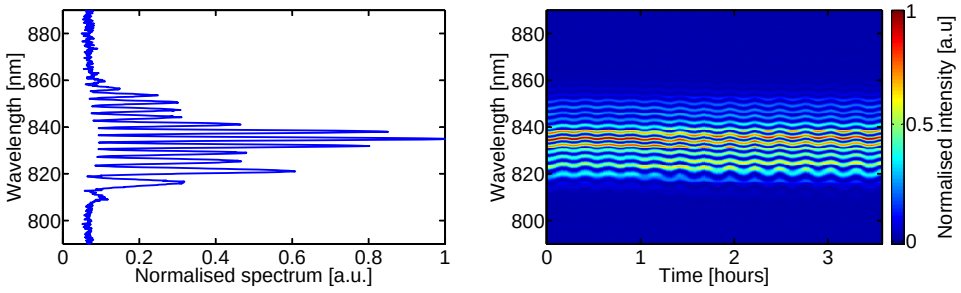


Figure 5.6: Setup required to measure phase from spectral interference fringes. The residual pump from the SHG is used to provide pulses of $\sim 20\,\text{nm}$ bandwidth. The half-wave plate and polarising beam splitter (HWP1, PBS1) are used to match the powers of the modes on the spectrometer (Ocean Optics). The semi-transparent optics are in place during this experiment but play no role within it.

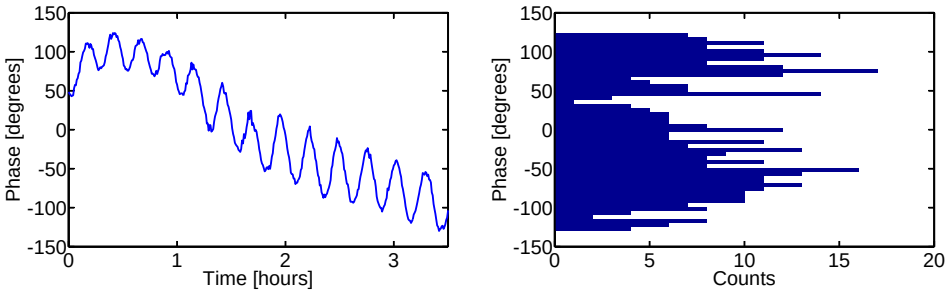
With the two pulses correctly mode-matched and with equal power incident on the spectrometer, interference fringes can be observed. Off-setting the temporal overlap slightly from zero delay shows a number of fringes, as shown in figure 5.7(a). Taking traces periodically allows the time-evolution of the fringe pattern to be seen. This is shown in figure 5.7(b). The phase instability of the interferometer causes the fringes to shift. We have a regular oscillation of around 90°, roughly four times per hour. This correlates precisely with the operating cycle of the laboratory air-conditioning system which is approximately 17 minutes.

The evolution of the phase itself can be extracted directly from the data shown in figure 5.7(b). By following one point on a fringe and knowing the fringe width, the phase is extracted and unwrapped using a MATLAB script. The results are shown in figure 5.8. They show that not only is there the 17-minute cycle to stabilise, but also a long-term drift. The short-term noise appears less critical on these timescales.



(a) Single interferogram (b) Time-aggregated interferograms

Figure 5.7: (a) The interference fringe pattern arising from the setup in figure 5.6. (b) Results of consecutive interference fringe patterns taken every 30 s for a total of 3.5 hours showing phase drift.



(a) Phase evolution (b) Phase histogram

Figure 5.8: (a) The phase as a function of time, as extracted from figure 5.7(b). (b) Resulting histogram of phases binned into 5° bins.

5.4.2 Active stabilisation

Each arm of the Mach-Zehnder interferometer is $\sim 2\,\mathrm{m}$ in length, because of the large number of optical components required for the experiments. The results above show that active stabilisation is required to keep any differences between each arm down to $\sim 10\,\mathrm{nm}$. Active stabilisation based on the quantum signal from a weak-field homodyne detector is all but impossible due to the low count rates and no direct phase signal (phase is inferred from the click statistics). Therefore a phase locking procedure with an ancillary beam was required. This ancillary beam must be well matched to the quantum modes in order to yield good stability in this regime. To that end we used a CW Helium-Neon (HeNe) laser (JDS Uniphase 1125P, 5 mW average power), since its wavelength (633 nm) was roughly halfway between the 415 nm SHG pump and 830 nm PDC and local oscillator. This allowed sufficient throughput in the setup given that the optical components were all optimised for one of these two wavelengths.

The problem now shifts to one of setting and stabilising an arbitrary phase of the ancillary beam, and verifying that the quantum beam in turn is suitably stable. Typically, one uses a Pound-Drever-Hall [126] technique to feed back on interference fringe intensity. In general, the error in a quantity to be stabilised depends on the derivative (with respect to this quantity) of the feedback signal. In our case, the error in the phase σ_ϕ is given by

$$\sigma_\phi \propto \left| \frac{\mathrm{d}}{\mathrm{d}\phi} I(\phi) \right| , \tag{5.9}$$

where $I(\phi) \propto \sin^2(\phi)$. Therefore,

$$\sigma_\phi \propto |\sin(2\phi)| \ . \tag{5.10}$$

It is clear that at phase values equal to integer multiples of $\pi/2$, the error is minimised while at odd-integer multiples of $\pi/4$, the error is maximised. In practise, this means it is relatively straightforward to lock to the rising and falling edge of interference fringes, but setting phases at fringe maxima or minima is impossible without large error. This makes active stabilisation at arbitrary phase rather challenging.

We used two techniques to achieve this. The first was developed by Jotzu [127], details of which are given in appendix F. Here, we concentrate on the scheme ultimately used for subsequent experiments.

5.4.3 Active stability and arbitrary phase setting

The method proposed by Jotzu *et al.* [128] uses two modes to achieve arbitrary phase stabilisation by offsetting the phase of one mode by $\pi/2$ in order to generate a low-error feedback signal at all phases. However, this mode-dependent phase shift is difficult to implement on an ancillary mode without affecting the quantum signal to be stabilised, rendering it unsuitable for our purpose.

The use of the ancillary mode offers a solution to this problem: it allows us to decouple the active stabilisation from the arbitrary phase setting of the quantum beam. This effectively removes the phase-dependent feedback of the quantum beam in Eq. (5.10). The ancillary beam is phase-locked using the standard Pound-Drever-

Hall algorithm [126], while phase setting is controlled by a Berry-phase [129,130] rotation setup.

Ancillary beam stabilisation

The phase in a Mach-Zehnder interferometer is altered by very small changes in path difference between each mode. These could arise due to random changes in refractive index, perhaps caused by air flow, or temperature-induced flexure in the optics. If the modes are collinear, then these changes affect each mode equally, and no path-length difference is observed.[1] Therefore, the active stabilisation need only control the spatially distinguishable sections of the Mach-Zehnder interferometer, *i.e.* between the second dichroic mirror (DM2) and the beam splitter in figure 5.6.

The setup for the ancillary beam is shown in figure 5.9. The ancillary HeNe laser is back-propagated to minimise the effect of stray ancilla photons entering the APDs. We use a feedback system based on locking the power into the photodiode by feeding back to a piezo-electrically actuated translation stage (Thorlabs NF5DP20/M). The piezo stage is controlled by an analogue PID controller (SRS SIM960). Note that this technique relies on the power stability of the HeNe beam; a more accurate system could involve splitting the power of the interference signal and using a ratiometric signal on which to feed back.

The response of the 830 nm light to stabilising the HeNe beam in this way is shown in figure 5.10. These results clearly show the success of this scheme: we are

[1] The intrinsic resistance to phase noise of co-propagating beams is widely exploited in real-world CV quantum communication tasks, all of which typically require a local oscillator for measurement. This is exemplified in free-space quantum cryptography [131].

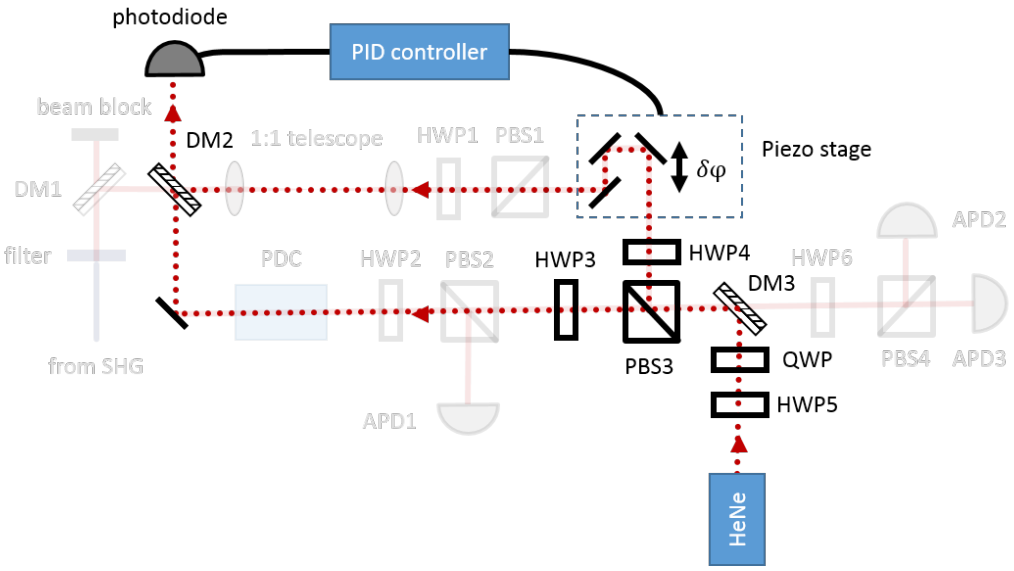
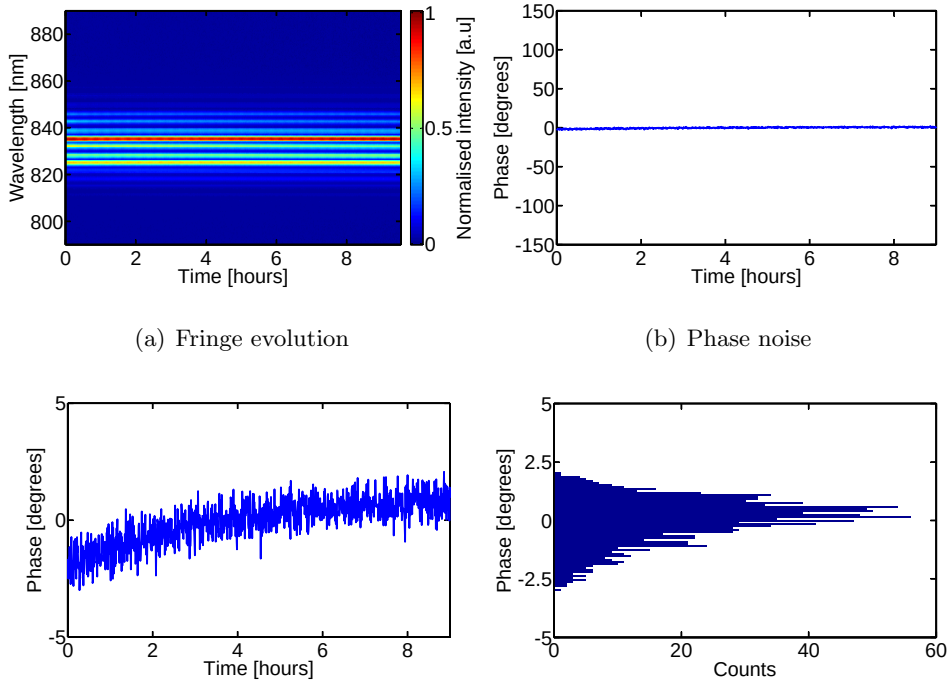


Figure 5.9: Setup for ancillary Helium-Neon (HeNe) laser used to stabilise the Mach-Zehnder interferometer. The HeNe beam is back-propagated through the setup, introduced using a dichroic mirror (DM3) downstream of the spatial recombination polarising beam splitter (PBS3). The half-wave plate HWP5 and quarter-wave plate (QWP) determine the polarisation state of the HeNe upon entering the interferometer. HWP5 is set such that the power from each arm is roughly equal on exiting the interferometer at the dichroic mirror (DM2) used to divide the SHG from the residual pump. The transition wavelength of this dichroic mirror is such that it acts as a beam splitter at 633 nm. HWP3 and HWP4 must be introduced to direct the beam to the correct outputs since the dichroic mirror is partially polarising at the HeNe wavelength.



(a) Fringe evolution

(b) Phase noise

(c) Phase evolution

(d) Phase noise

Figure 5.10: (a) Time-evolution of the fringe pattern of 830 nm interference when stabilised by an ancillary beam over nine hours. (b) Phase extracted from fringe pattern, plotted on the same scale as in figure 5.8(a). (c) As (b) with higher phase resolution. We attribute the very long-term drift to power fluctuations in the HeNe beam. (d) Histogram of phases into 0.1° bins. By construction, the mean is 0°; the standard deviation is 3.8°, well within the 5° specification.

able to fix the phase to less than 5° for at least nine hours.

Berry-phase rotator

The stabilisation system works well for locking the phase, but does not set it arbitrarily. For this, a new scheme is required to change the relative phases between each mode of the interferometer without affecting the ancillary beam. This is achieved by modifying the recombination beam splitter to include a Berry-phase[130] (see also Pancharatnam[129]) rotation setup, as shown in figure 5.11. In this way, the phase

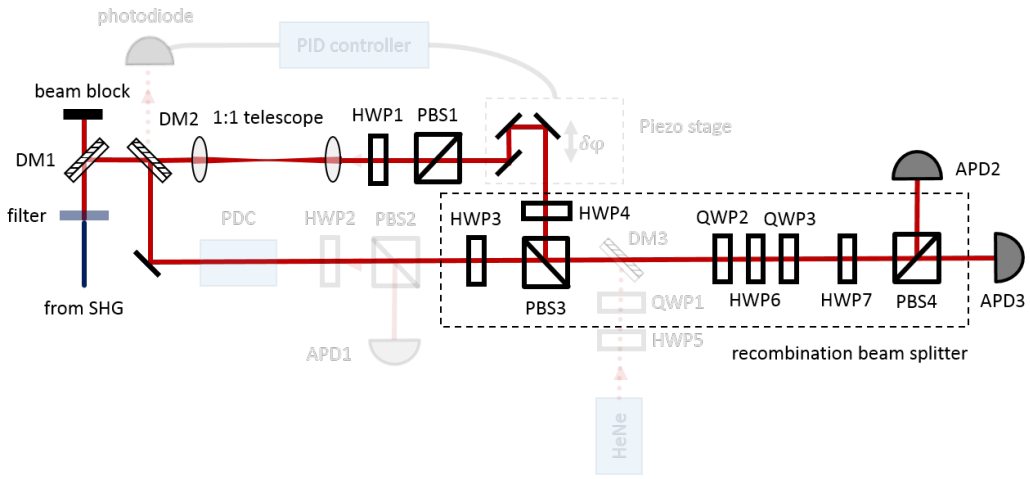


Figure 5.11: Mach-Zehnder interferometer formed by signal and LO beams incorporating Berry-phase control. The non-polarising beam splitter of figure 5.7(a) is replaced by the optics shown in the dashed box. The beams from each mode of the interferometer, which we assumed to be linearly polarised in the rectilinear $\{H, V\}$ basis, are spatially overlapped at PBS3 and directed to the correct output by HWP3 and HWP4. At this point, the beams are in orthogonal, linear polarisation modes. QWP2 and QWP3 are set to introduce a $\pm\pi/4$ phase shift, respectively. In this way, rotating HWP6 through an angle $\theta°$ introduces a 4θ phase shift between the modes. These modes are then interfered on PBS4, whereby HWP7 determines the relative power from each mode to a given output port. This setup implements a full variable beam splitter with both phase and amplitude control of the two modes.

stability provided by the HeNe is completely decoupled from the ability to set an ar-

bitrary phase between the modes. This can be readily exploited across two (collinear) interferometers to interrogate both modes arising from the down-conversion, which is the subject of experiments in the following chapter. In the single-mode case, this variable beam splitter arrangement allows a number of experiments to be performed, two of which we describe in the remainder of this chapter.

5.5 Conditional state preparation with weak-field homodyne detection

The optical setup required for weak-field homodyne lends itself very well to conditional state preparation. The scheme is based on measurement-induced non-linearity following interference between a single photon and a coherent state. We will show how this leads to some interesting quantum features, such as quadrature squeezing, super- and anti-bunched photon statistics and the generation of exotic optical states. Successive iterations of this protocol can lead to direct control over the weights of higher-order probability amplitudes in the Fock basis, paving the way towards conditional preparation of "designer" multiphoton states for applications in quantum computation, communication and metrology.

5.5.1 Non-Gaussian state generation

In section 2.4.1, we discussed the necessity of a non-Gaussian element in an entanglement distillation protocol [64]. In fact, this non-Gaussian requirement is more general. For any protocol to provide quantum advantages not attainable classically,

it is crucial that the quantum states involved are non-Gaussian[55,132,133]. For two-mode states, we showed in chapter 3 how such states can be generated through probabilistic non-Gaussian operations. These ideas can be readily applied to single-mode states. One can manipulate the quantum state by means of linear optical elements[134,135], which generate an effective non-linearity by accepting only particular outcomes of measurements on ancillary modes. Such schemes have allowed the production of superpositions of coherent states[136,137], and manipulation at the single-photon level[77,138–141].

5.5.2 Photon-catalysed optical coherent (PCOC) states

Based on measurement-induced non-linearity, we investigate the possibilities offered to multiphoton quantum state engineering by a particular interferometric scheme called quantum catalysis[134], which uses a Fock state to modulate the probability amplitudes of a coherent state. A coherent state is interfered with a k-photon Fock state at a beam splitter of variable transmissivity T, as shown in figure 5.12. Measuring k photons at one output mode projects the other output mode into a "photon-catalysed optical coherent state" $|\psi_{\mathrm{PCOC}}\rangle$. The analogy to catalysis is motivated by the conditioning measurement, which is successful only when measuring the same number of photons as initially interfered with the coherent state. We generalise the result from Lvovsky and Mlynek[134] (in which $k = 1$, $\alpha \ll 1$ and beam splitter transmissivity $T \ll 1$) across a wide range of parameters and to higher-order in the photon number distribution, introducing a broad family of multiphoton

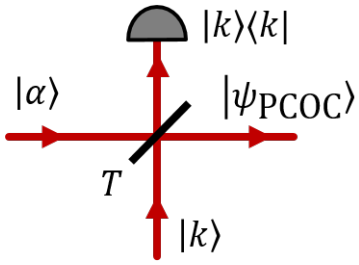


Figure 5.12: A photon catalysed optical coherent (PCOC) state $|\mathrm{PCOC}\rangle$ is produced following the interference between a coherent state $|\alpha\rangle$ and a k-photon Fock state $|k\rangle$ (at a beam splitter of reflectivity $T^2 = 1 - R^2$), conditional on measuring k photons at one output port.

quantum states.

Despite injecting and extracting the same number of photons, the photon-number distribution of the final quantum state is radically modified due to quantum interference. This arises because each Fock basis state contributing to the coherent input state interferes with the catalysing k photons, undergoing a generalised Hong-Ou-Mandel type interference[138]. Then the outcomes of these individual interferences then add coherently due to the inherent phase reference in a coherent state. This combination results in a novel class of multiphoton quantum states with a wide range of non-classical properties.

The schematic for the generation of a photon-catalysed optical coherent (PCOC) state is shown in figure 5.12. The conditioned state at the output is given by

$$|\psi_{\mathrm{PCOC}}\rangle = \mathcal{N}_{\alpha,T} \sum_{n=0}^{\infty} \frac{\alpha^n}{\sqrt{n!}} c_n\left(T, R, k\right) |n\rangle \ , \tag{5.11}$$

where

$$c_n\left(T,R,k\right)=\sum_{j=0}^{\min(n,k)}\left(\begin{array}{c} n \\ n-j \end{array}\right)\left(\begin{array}{c} k \\ j \end{array}\right)(-1)^j\,T^{n+k-2j}R^{2j}\ , \tag{5.12}$$

T, R are the transmissivity and reflectivity of the beam splitter, respectively (satisfying $T^2+R^2=1$) and $\mathcal{N}_{\alpha,T}$ is the normalisation constant. The states cover a range going from a coherent state ($T=1$) to a k-photon Fock state ($T=0$).

Single-photon PCOC state

Taking $k=1$, in Eq.(5.11) yields the state

$$\left|\psi_{\mathrm{PCOC}}\left(1\right)\right\rangle=\mathcal{N}_{\alpha,T}\sum_{n=0}^{\infty}\frac{e^{-|\alpha|^2/2}T^{n-1}\left(T^2-nR^2\right)\alpha^n}{\sqrt{n!}}\ . \tag{5.13}$$

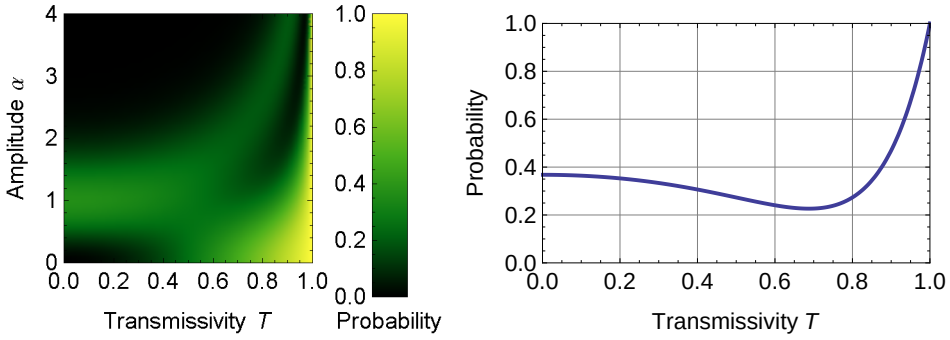
Further properties may be calculated based on these coefficients, as per appendix B. Just as in section 3.1.1, the normalisation factor $\mathcal{N}_{\alpha,T}$ is related to the probability of success, given by

$$P_1=\mathcal{N}_{\alpha,T}^{-2}=e^{-R^2|\alpha|^2}\left[R^4\alpha^2+T^2\left(R^2\alpha^2-1\right)^2\right]\ . \tag{5.14}$$

The probability of catalysis, as a function of the interaction parameters T and α, is shown in figure 5.13.

5.5.3 Non-classical features of PCOC states

By tuning the parameters of the interaction, namely the beam splitter transmissivity T, coherent state amplitude α and the number of catalyst photons k, the coefficients



(a) (b) $\alpha = 1$

Figure 5.13: (a) Probability of single-photon catalysis as a function of interaction parameters T and α. (b) Probability as a function of beam splitter transmissivity when $\alpha = 1$.

of the photon-number terms (Fock layers) may be modulated, generating a wide range of non-classical phenomena.

Squeezing

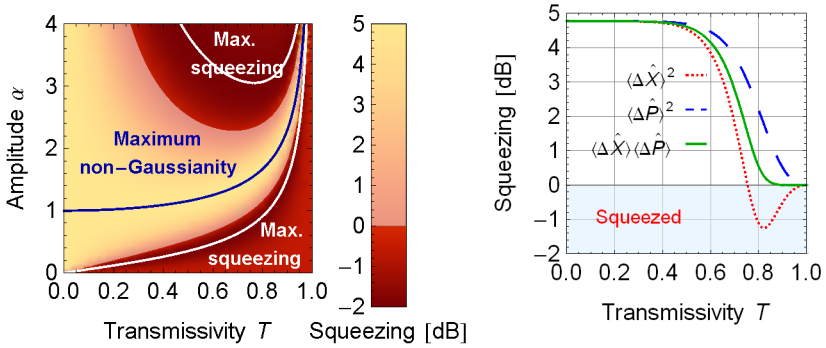
Single-mode squeezed states form an essential part of the quantum toolbox, and PCOC states can, for a range of parameters, yield an $\hat{X}$ quadrature variance $\Delta^2\hat{X}$ below the standard limit. As calculated in appendix D.1, analytical expressions for the variance of the quadratures are given by

$$\Delta^2\hat{X} = \frac{3R^8\alpha^4 + T^4\left(1 - R^2\alpha^2\right)^4}{4\left[R^4\alpha^2 + T^2\left(1 - R^2\alpha^2\right)^2\right]^2}\,, \tag{5.15}$$

and

$$\Delta^2\hat{P} = \frac{1}{4} + \frac{R^4\alpha^2}{2\left[R^4\alpha^2 + T^2\left(1 - R^2\alpha^2\right)^2\right]}\,. \tag{5.16}$$

These quadrature variances, relative to their vacuum values of 1/4, are plotted on a logarithmic scale (units of dB) in figures 5.14(a) and 5.14(b) (for $\alpha = 1$) showing the range of squeezing for α and T.



(a) Quadrature variance (b)

Figure 5.14: Squeezing behaviour as a function of interaction parameters T and α. (a) The range of parameter space that generates squeezing. The white lines show the parameters which generate the maximum squeezing of 1.25 dB below the shot-noise limit and the blue lines show the maximum non-Gaussianity, corresponding to a deviation from a minimum uncertainty state of 4.77 dB. The darker region corresponds to the parameter space for which squeezing occurs. (b) shows the quadrature variances, relative to the vacuum (unsqueezed) state in units of dB, at a coherent state amplitude of $\alpha = 1$. Red dotted line, blue dashed line: $\hat{X}$ and $\hat{P}$ quadrature variance, respectively. Green solid line: joint variance.

By minimizing the expressions above for $\Delta^2\hat{X}$, the largest attainable squeezing is 3/16, below the vacuum noise level of 1/4 by 1.25 dB. The maximum variance of 3/4 corresponds to 4.77 dB anti-squeezing (quadrature variance in excess of the vacuum level). The parameters that yield these values are found by solving $\Delta^2\hat{X}$=3/16 under the constraints $0 \leq T \leq 1, |\alpha| < 0$. The solutions to this equation are not uniquely valued: they form two continuous lines in (T, α) parameter space, as shown

in Fig. 2(a). The equations corresponding to the loci of minima are

$$\alpha_{\min} = \sqrt{\frac{3 - T^2}{2T^2R^2} \pm \frac{1}{2}\sqrt{\frac{9 + 3T^2}{T^4 - T^6}}} \ . \tag{5.17}$$

Similarly the locus of maximum non-Gaussianity is described by

$$\alpha_{\max} = \frac{1}{R} \ . \tag{5.18}$$

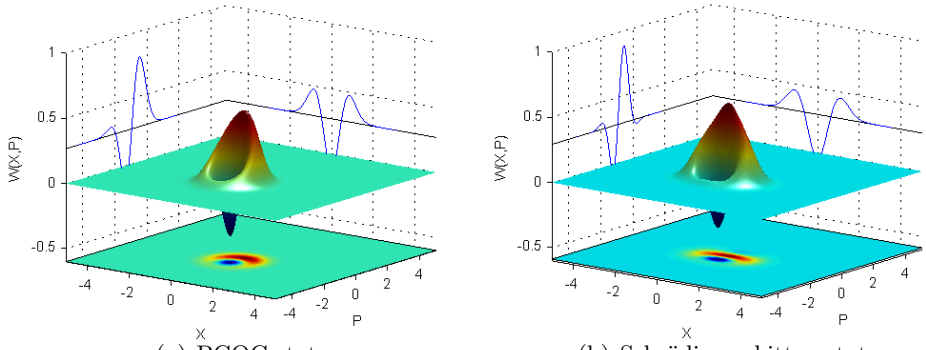
Reaching the maximum squeezing and non-Gaussianity by this scheme is therefore independent of the initial coherent state amplitude α.

However, the amount of squeezing obtainable, particularly at high α, is offset by the probability of successful catalysis: if the coherent state is large, the probability of detecting one photon is small. The probability of successful catalysis is shown in figure 5.13. For low α, catalysis is fairly likely. Indeed, at $\alpha = 1$ and $T = 0.82$, which generates maximum squeezing, the probability of successful catalysis is about 47%.

The behaviour of both quadrature variances at $\alpha = 1$ is shown in figure 5.14(b). The $\hat{P}$ quadrature is never squeezed, and the combined variances show that the state clearly satisfies the minimum variance condition. For $T \gtrsim 0.85$, the state asymptotically approaches a minimum uncertainty state, whereas this is lost for $T \lesssim 0.15$. Since the state is pure, this means states in this region are non-Gaussian, implying negativity in their Wigner distributions [50].

Non-Gaussian states

Non-Gaussian multiphoton states have been shown to be useful for computation [133,142] and communication [64]. One class of non-Gaussian states of particular interest are coherent state superposition (CSS) states. As a superposition of coherent state amplitudes separated in phase space, they are the optical analog of the Schrödinger cat "dead" and "alive" state [143]. When the separation between the amplitudes is small, the states are termed Schrödinger kitten states [101], and it has been shown that combining small CSS states can yield much larger CSS states necessary for universal quantum computation [144].



(a) PCOC state (b) Schrödinger kitten state

Figure 5.15: Wigner functions of (a) the photon catalysed state and (b) a displaced coherent state superposition (CSS) of amplitude $\alpha = 0.9$, displaced by $\beta = 0.8$, from Eq. (5.19). Their Wigner functions are similar, indeed the photon-catalysed state exhibits a fidelity of 0.9 with respect to the displaced coherent state superposition. This result shows that CSS states can be generated without squeezing using the catalysis scheme. Note that the lines on each axis are lineouts from the plots at the minimum of the Wigner function (*i.e.* they are not the marginal distributions).

A CSS state of amplitude α, displaced in phase space by $\hat{D}(\beta)$, is given by

$$|\psi_{\mathrm{CSS}}\rangle = \mathcal{N}\sum_{n=0}^{\infty}\frac{(\beta+\alpha)^n+(\beta-\alpha)^n}{\sqrt{n!}}\,|n\rangle. \tag{5.19}$$

An example of a weak CSS state ($\alpha = 0.9$), displaced in phase space ($\beta = 0.8$), is shown in 5.15(b). With a particular choice of interaction parameters ($T = 0.47,\ \alpha = 1.35$), the PCOC state approximates a displaced weak coherent superposition state, with $> 90\%$ fidelity, with a Wigner function as shown in figure 5.15(a), which is clearly non-Gaussian. Previous schemes have typically required some initial squeezing [101,145–148]; our results indicate a route to these states without such requirements.

5.5.4 Higher-order catalysis

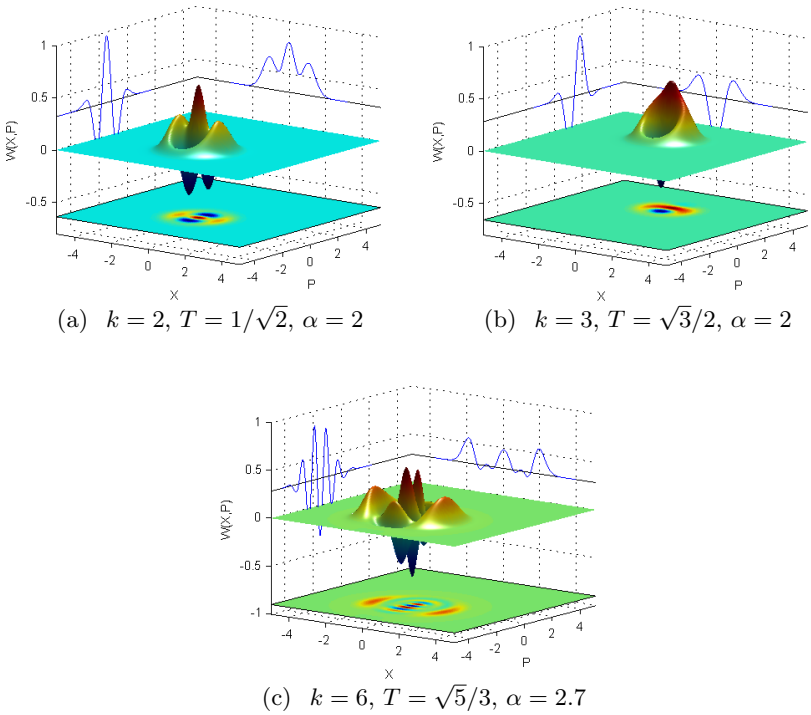
Simple extensions of the catalysis scheme allow for the preparation of more sophisticated quantum states. A catalyst of $k \geq 2$ photons in Eq. (5.11) leads to more elaborate Wigner functions as shown in figure 5.16. A further extension is to concatenate iterations of catalysis. Each iteration i introduces an additional transmissivity T_i, such that the total transmissivity is $\mathbf{T} = (T_1, \ldots, T_l)$. The state following l iterations may be written

$$|\psi_{\mathrm{PCOC}}\rangle_l = \mathcal{N}_{\alpha,\mathbf{T}}\sum_{n=0}^{\infty}\frac{\alpha^n}{\sqrt{n!}}\prod_{i=0}^{l}c_{n,i}|n\rangle\ , \tag{5.20}$$

where

$$c_{n,i} = \sum_{j=0}^{\min(n,k_i)}\binom{n}{n-j}\binom{k_i}{j}(-1)^j\,T_i^{n+k_i-2j}R_i^{2j}\ , \tag{5.21}$$

and $\mathcal{N}_{\alpha,\mathbf{T}}$ is the normalisation constant. Such an iterative scheme forms the basis of a number of conditional approaches towards quantum computation [135]. The coefficients of the Fock layers can be directly controlled by the reflectivities at each iteration. As such, arbitrary quantum states can be generated by heralding the successful catalysis interaction on a single mode, without requiring entanglement [149].



(a) $k = 2$, $T = 1/\sqrt{2}$, $\alpha = 2$ (b) $k = 3$, $T = \sqrt{3}/2$, $\alpha = 2$

(c) $k = 6$, $T = \sqrt{5}/3$, $\alpha = 2.7$

Figure 5.16: Wigner functions of higher-order catalysed states showing the rich structure that can be achieved.

5.5.5 Experimental generation of PCOC states

To demonstrate the practical efficacy of our proposal, we experimentally generate PCOC states catalysed by one photon. Using the setup shown in figure (5.17), we

measure the photon number distribution of the PCOC state at a range of beam splitter reflectivities. The variable beam splitter comprises a PBS (PBS3—to spatially overlap the coherent state and Fock states), a half-wave plate (HWP3) and interference beam splitter (PBS4). The beam splitter reflectivity and half-wave plate angle in the variable beam splitter are related by $T = 1 + \cos(2\theta)$.

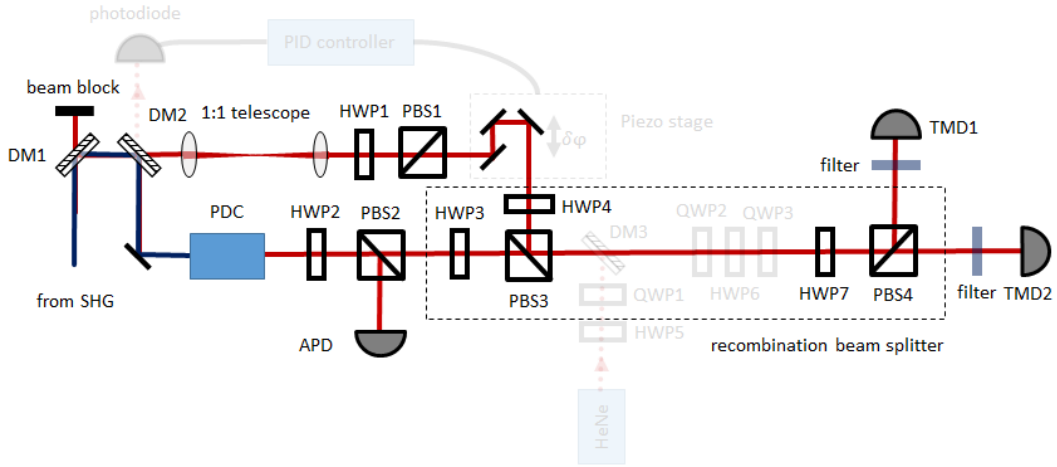
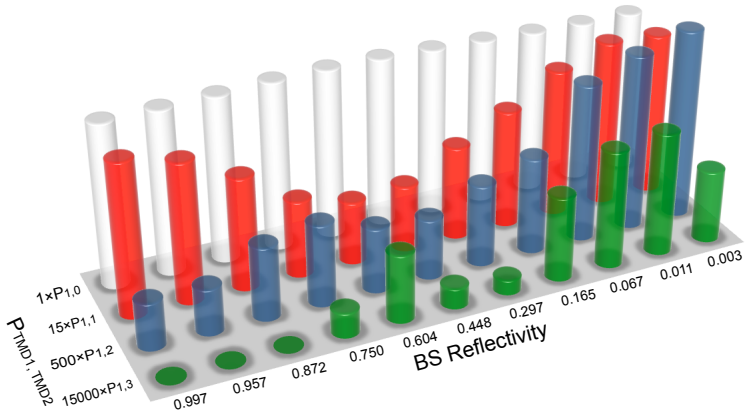


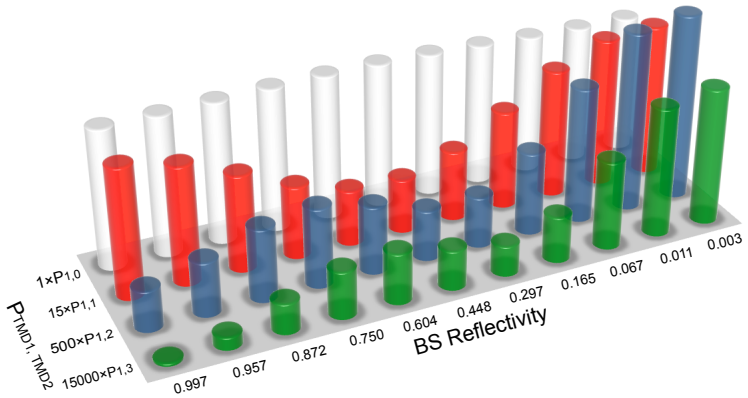
Figure 5.17: Experimental setup for probing single-photon catalysis. The second harmonic beam arrives from the setup shown in figure 4.4. The residual fundamental, which is used as the coherent state, is transmitted by the dichroic mirror DM2. This beam is then attenuated by a half-wave plate HWP1 and polarizing beam splitter PBS1 to single-photon level intensity. The second harmonic beam undergoes type II collinear parametric down-conversion (PDC), producing pairs of orthogonally polarized photons in pure spectral-temporal states, as shown in figure 4.5. HWP2 ensures that the H-polarized photon is detected by an avalanche photodiode (APD), which heralds the presence of a photon in the V polarization mode. The two beams are spatially recombined on PBS3, and their arrival times are synchronised by adjusting the position of a delay stage (as discussed in section 5.3.2). This operation is followed by interference on the variable beam splitter constituted by HWP7 and PBS4. The two polarization modes are then filtered by 3 nm interference filters, coupled to single-mode fibres and sent to photon-number-resolving TMDs for photon counting, as described in section 5.2.2.

Typical results from number-resolved counting are shown in figure (5.18), taking into account the binning of our detector. The action of catalysis as a Fock state

filter appears in the modulation of the higher-order photon terms as the reflectivity is tuned[138]. The single photon component is suppressed with respect to what one would expect in a coherent state. A similar effect is also present in the two- and three-photon components, albeit with a lower contrast.



(a) Experimental data



(b) Theoretical reconstruction

Figure 5.18: Measured (a) and theoretical (b) photon number distributions as a function of beam splitter reflectivity R for a coherent state mean photon number of $|\alpha|^2 = 1.11$. White shows the vacuum component, while red, blue and green represent the one-, two- and three-photon terms, respectively. Note that the higher-order terms have been scaled for clarity; the labels $y \times P_{i,j}$ corresponds to a scaling factor y multiplied by the probability P of a click corresponding to i photons detected in TMD1 and j photons detected in TMD2.

Tuning second order coherence

We also measured the second-order autocorrelation function [40] $g^{(2)}(0)$ and show its variation with the square of the beam splitter reflectivity R^2. Note that we use R^2 as it is a straightforward experimental quantity to measure; we thereby neglect any phase dependence. The $g^{(2)}(0)$ function is defined

$$g^{(2)}(0) = \frac{\langle \hat{n}^2 \rangle - \langle \hat{n} \rangle}{\langle \hat{n} \rangle^2} \ . \tag{5.22}$$

Different states have different $g^{(2)}(0)$ values depending on their photon-number distribution. States for which $g^{(2)}(0) < 1$ cannot be described using a classical distribution of the photon numbers.

Figure (5.19) shows that the $g^{(2)}(0)$ values which lie below the classical bound ($g^{(2)}(0) = 1$) are observed for PCOC states generated when the interfering beam splitter has high reflectivity $R^2 > 0.9$. In this region, our experiment realises a displacement of a single photon, as first observed by Lvovsky and Mlynek [134]. This signature of non-classicality disappears rather quickly as R^2 decreases below 0.9. At the other end where $R^2 \sim 0$, we clearly find coherence properties close to a coherent input state $|\alpha\rangle$. A significant feature in the curve is the presence of a peak centred around $R^2 = 0.6$, which attains a measured value of $g^{(2)}(0) = 2.5 \pm 0.23$, above the limit of thermal states, which has been termed "super-bunching" [150]. While this is not a signature of non-classicality *per se* (in principle any value can be achieved by a mixture of coherent states), we can still make inferences of non-classical features by

observing the corresponding statistics measured in figure 5.18(a). In the ideal case, the Fock state filter[138] should significantly suppress the single photon component for a reflectivity $R^2 = T^2 = 1/2$, by Hong-Ou-Mandel interference[105]. Its action on a coherent state should then bring it closer to a weakly squeezed state – which only contains contributions from even photon numbers, and can reach $g^{(2)}(0)$>3. While our detection scheme is not able to show squeezing explicitly, these photon counting measurements show evidence of non-classical statistics.

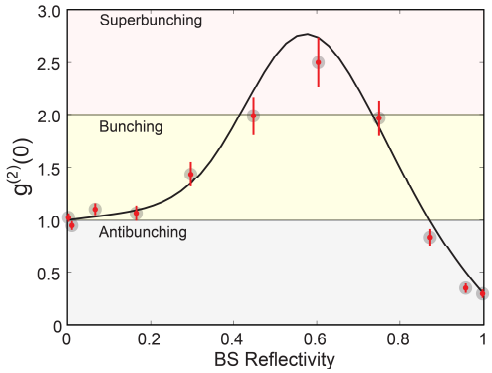


Figure 5.19: Second order autocorrelation function $g^{(2)}(0)$ as a function of beam splitter reflectivity, for a coherent state mean photon number of $|\alpha|^2 = 1.11$. The points are measured values based on the photon statistics in figure 5.18(a), while the line is the expected value, incorporating inefficiency in our detection system. For $R^2 = 0, 1$, $g^{(2)}(0)$ approaches the values for a coherent state and single photon, respectively. The regions showing anti-bunching $g^{(2)}(0) < 1$ (strictly non-classical), bunching $1 \leq g^{(2)}(0) \leq 2$ and super-bunching $g^{(2)}(0) > 2$ are indicated by different colours. Our experimental results lie in all regions.

5.5.6 Concluding remarks

We have introduced a general scheme for producing a broad class of useful multiphoton states without strong optical non-linearities, whose generation is feasible with current technology. We have exhibited how a broad range of sophisticated quan-

tum states can be designed starting from just single photons, coherent states, beam splitters and photon counters. In conjunction with quantum memories that can drastically increase multiphoton rates, and also act as tunable beam splitters[151], photon catalysis can be used as a building block in the construction of non-Gaussian states in quantum networks[67].

5.6 Sub-binomial light

A key capability in quantum optics is the ability to determine non-classical phenomena directly from experimental data. Previously, we calculated the second-order coherence function from the photon distribution. This required extracting the effect of our multiplexed detector from the click statistics we measured, as described by Coldenstrodt-Ronge *et al.*[118]. As detectors become increasingly complex, this process becomes increasingly challenging. A more elegant solution, proposed by Sperling, Vogel and Agarwal[152], characterises the classicality of the state directly from the click statistics. In this scheme one only needs to know the number of bins of a multiplexed detector onto which the photons are incident.

In the first experimental demonstration of this approach, we used the PCOC states described above to demonstrate that non-clasicality of multiphoton states can indeed be deduced directly from detector outcomes.

5.6.1 Characterising optical states

Determining what constitutes a non-classical state is not trivial; many criteria to establish where the quantum-classical boundary lies have been proposed. Typically, one considers pathological behaviours of distributions in phase space; one might seek negative values of the Wigner function [43,153] or values more singular than a delta function of the Glauber-Sudarshan P distribution in the phase-amplitude space [154–156]. Indeed, this definition covers a larger class of states than the negativity of the Wigner function. Experimentally, these criteria have been widely adopted, and inferred either by state tomography [75,76,101,136,157], or by direct measurement [153,158].

Mandel Q-parameter

A different approach consists of examining the photon-number distribution in a photon counting experiment [159–165]. When detecting photons directly, the Mandel parameter,

$$Q_M = \frac{\Delta^2 n}{\bar{n}} - 1 \ , \tag{5.23}$$

is often used [159]. This measure arises directly from the first and second moments of the photon number distribution, namely the mean $\bar{n}$ and variance $\Delta^2 n$. For a state exhibiting Poissonian statistics, $\bar{n} = \Delta^2 n$ such that $Q_M = 0$. For sub-Poissonian states, $Q_M < 0$ is therefore a witness of non-classicality.

A difficulty with this scheme arises when considering how the number statistics are measured. While actual PNRDs [68,166] are becoming more frequently utilised [148,167–169],

simpler solutions are still appealing since the hardware demands on such detectors limit their feasibility. Multiplexed detectors, such as those described in section 5.2.2, are a common choice for accessing higher order photon numbers, though these detectors do not output the photon number distribution directly. It is recognised that the Mandel parameter applied to the resulting click distribution would give false indications of non-classicality even for a large number of detection bins [117]. A linear inversion technique is therefore required [37,110,118,153,165] in order to obtain the actual number distribution from the distribution of the clicks. However, this becomes more sensitive to noise and less tractable with increasing system size.

5.6.2 The SVA parameter

The question arises whether there exists a way of observing non-classicality directly in the measured quantities $\{c_i\}$. A solution can be found by inspecting the Mandel parameter, Eq. 5.23. The negativity of this parameter establishes a sufficient criterion for non-classicality: this implies that the mean $\bar{n}=\sum_{n=0}^{\infty} np_n$ is larger than the variance $\Delta^2 n=\sum_{n=0}^{\infty}(n-\bar{n})^2 p_n$, *i.e.* if the statistics are sub-Poissonian. Coherent states, which benchmark classical light, display Poissonian number statistics. By contrast, Fock states display sub-Poissonian statistics, hence the corresponding Mandel parameter takes negative values. When using TMDs, a Poissonian distribution of the photons $\{p_n\}$ results in a binomial distribution of the counts $\{c_i\}$ [117]. Based on this, Sperling, Vogel and Agarwal (SVA) have developed a different non-

classicality criterion applying to the measured click statistics[152]:

$$Q_B = \frac{\Delta^2 c}{\bar{c}(1-\frac{\bar{c}}{N})} - 1, \tag{5.24}$$

where $\bar{c} = \sum_{i=0}^{N} i\, c_i$, and $\Delta^2 c = \sum_{i=0}^{N} (i-\bar{c})^2 c_i$. This extends Mandel's formula (5.23) to the case of a binomial distribution. Consequently, non-classicality can be directly inferred from the sub-binomial behaviour of the observed statistics, *i.e.* $Q_B < 0$.

5.6.3 Demonstrating sub-binomial light

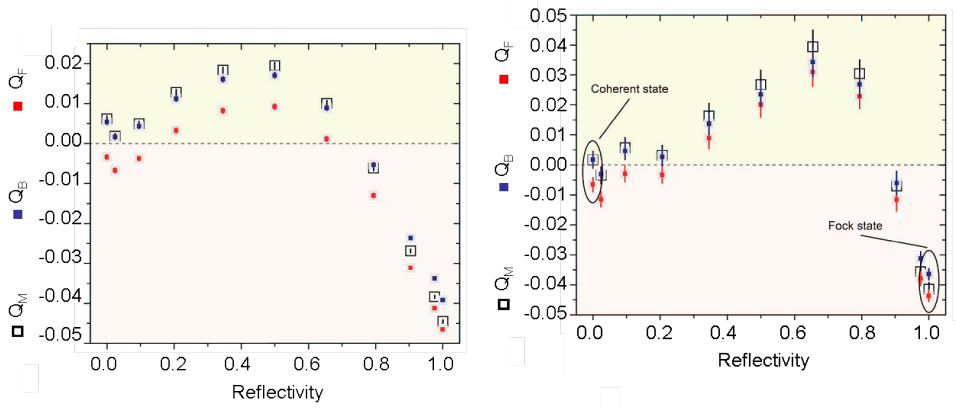
We experimentally measure both Q_B and Q_M for families of quantum states that may be tuned continually between the classical and non-classical regimes. To obtain such states, we use a variation of the setup described in section 5.5.5. For $k = 1$, we produce non-Gaussian states by performing photon catalysis[37,134]. These allow us to investigate the behaviour of Q_B in the experiment, as we tune the state from a single photon ($R = 1$) to a coherent state ($R = 0$). Furthermore, we condition on $k = 0$, which are photon-added states, for further demonstration.

We perform three different statistical analyses on the data, the results of which are shown in figure 5.20(a) for $k = 0$, and in figure 5.20(b) for k=1. Firstly, we directly assess the sub-Poissonian character of the raw click statistics using a Mandel-like parameter defined as:

$$Q_F = \frac{\Delta^2 c}{\bar{c}} - 1. \tag{5.25}$$

We then calculate the experimental result for the genuine Mandel parameter Q_M

from Eq. (5.23), after the photon distribution has been obtained by inversion [110]. Finally, we calculate the experimental values for the binomial parameter Q_B from Eq. (5.24) directly from the click statistics as described above.



(a) $k = 0$ (b) $k = 1$

Figure 5.20: Test of non-classicality for (a) a single-mode photon added coherent state heralded by k=0 and (b) single-mode PCOC states heralded by k=1. In both figures, the black boxes show the Mandel parameter Q_M and the blue points show the SVA parameter Q_B. The values of the Mandel-like parameter calculated from the clicks Q_F are shown as red points. The limit $R \sim 0$ correspond to coherent states for which one expects no non-classicality, while around reflectivity $R \sim 1$, the states approximate displaced single-photons [37]. All experimental points are obtained by 600 seconds of data collection. Errors are evaluated by a Monte Carlo technique assuming Poissonian noise.

In general, the Mandel-like parameter Q_F cannot be used to detect non-classicality, as it can take negative values even for the coherent states obtained when $R{\sim}0$ [117], as shown in figure 5.20(b). Further, its behaviour depends on the particular class of states under investigation. For the case in figure 5.20(a) the discrepancy between Q_F and the Mandel parameter Q_M is significant, while they are closer in figure 5.20(b). In both cases, a systematic failure of Q_F can be seen at low reflectivities. This issue is resolved by employing the binomial parameter Q_B, which performs as well as Q_M

for our eight-bin detector, and with similar uncertainties. However, to calculate Q_M, detailed knowledge of the detector response was required to perform an inversion from click statistics to photon number statistics. This might not be feasible in the general case, particularly as the number of bins increases. Furthermore, uncertainties in the small click probabilities associated with high-order bins can cause large errors following the inversion. Thus the direct approach of Q_B is useful in avoiding this source of error, as well as instabilities arising from noise.

Sub-binomial light from PDC

We also use the SVA parameter to characterise the output from the parametric down-converter in the strongly-pumped regime. This generates higher-order photon terms in the two polarisation modes. Using a PNRD, the observation of n photons on the H mode implies the presence of n photons, hence a sub-Poissonian state, on the V mode[170,171]. We observe similar behaviour in terms of sub-binomial light: a click from a TMD projects the other mode on to a sub-binomial state. The joint statistics from two TMDs, each measuring a different polarisation mode is shown in figure 5.21.

From this data, we perform the SVA test on the states obtained by conditioning on a given number of clicks from one TMD or the other. When all the events of TMD_2 are considered regardless of the measurement result at TMD_1, or *vice versa*, we observe classical behaviour, as expected for a thermal state (figure 5.22(a)): we obtain the values $Q_B = (9.3 \pm 0.6) \times 10^{-3}$ for the state on mode 1, and $Q_B =$

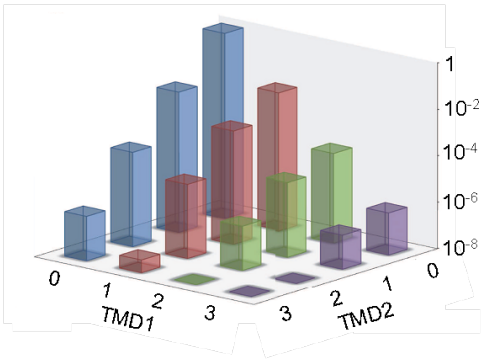


Figure 5.21: Joint click statistics from TMDs on each mode of a two-mode squeezed state. Due to limited efficiency ($\sim 7\%$), the most frequent event is when no clicks are registered at either side. All the events in coincidence with a trigger signal from the main laser are included.

$(10.9 \pm 0.6) \times 10^{-3}$ for the state on mode 2. Discrepancies between the expected symmetry can be attributed to the different detection efficiencies which have been measured. When only the events causing no clicks on TMD_1 are registered, we still observe a similar behaviour: the reduced efficiency of our detector, in fact, makes this event similar to tracing out the other mode. The measured values are $Q_B = (10.2 \pm 0.6) \times 10^{-3}$ (mode 1) and $Q_B = (8.5 \pm 0.6) \times 10^{-3}$ (mode 2). When single clicks are considered as heralds, the state becomes sub-binomial, and so it happens independently of the mode we use as the trigger: $Q_B = (-3.84 \pm 0.33) \times 10^{-2}$ (mode 1), and $Q_B = (-4.49 \pm 0.30) \times 10^{-2}$ (mode 2). Finally, when triggering on two clicks, the state does present some evidence for non-classicality. In this case, $Q_B = (-3.3 \pm 3.9) \times 10^{-2}$ for mode 1 and $Q_B = (-8.3 \pm 3.5) \times 10^{-2}$ for mode 2. A statistical analysis conducted by simulating experiments using a Monte Carlo technique is shown in figures 5.22(b) and (c): while the most likely values for both modes do lie well below zero, the tails of the distribution make the value of Q_B for

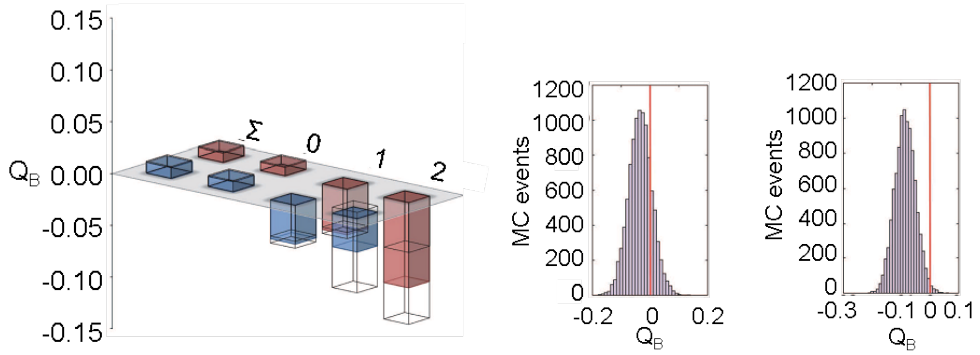


Figure 5.22: Sub-binomial light from parametric down-conversion. (a) Red: measured Q_B parameter for the state detected by TMD_2 conditioned on different click events on TMD_1; and blue: measured Q_B parameter for the state detected by TMD_1 conditioned on different click events on TMD_2. Statistical analysis of the Q_B parameter when conditioning on two clicks from (b) TMD_2 , and (c) TMD_1. The histograms are obtained based on 10^4 Monte Carlo simulations assuming Poissonian noise in the click statistics.

mode 1 (figure 5.22(b)) still compatible with positive values.

Assessing the detector

These experimental results, in the light of the retrodictive approach by Amri, Laurat and Fabre[172], also provides preliminary evidence for a test of non-classicality of the TMDs themselves. In the retrodictive framework, the non-classicality of a detector D can be ascertained by observing the non-classicality of one mode of $|\psi\rangle$ when the other mode is projected by the action of D in the limit of high squeezing $\lambda \to 1$. Although we are far from this regime, the observed negativity of Q_B resulting from conditioning one of the arms on a TMD points towards the non-classicality of the device.

Chapter 6

Measuring non-local quantum states

The previous chapter considered detection of single-mode states with a weak-field homodyne setup. In this chapter we extend our discussion to cover the joint detection of two-mode states, which provides access to entanglement and non-local behaviour of quantum states.

We demonstrate how weak-field homodyne can be extended to cover two modes of an entangled state. The phase reference provided by the local oscillators generate phase-dependent photon counting measurements, which can be used to demonstrate a range of interesting phenomena. We show phase coherence in joint measurements on the modes, which is characteristic of entanglement (but is not sufficient to prove it). Furthermore, the phase-dependent POVMs of the two-mode weak-field homodyne detector can be used to construct an "entanglement witness," since different

phases correspond to different bases in which to measure correlations in photon number. In contrast to complete quantum state tomography, a smaller set of POVMs can be used to detect ("witness") the presence of entanglement. We detail our experimental progress towards implementing this theoretical result, and highlight some of the difficulties associated with it.

6.1 Local and non-local phase dependence

Coherent superpositions are characterised by a fixed phase relationship between basis states. For example, the phase θ in the state

$$|\psi\rangle = \frac{1}{\sqrt{2}}\left(|0\rangle + e^{\mathrm{i}\theta}|1\rangle\right) \tag{6.1}$$

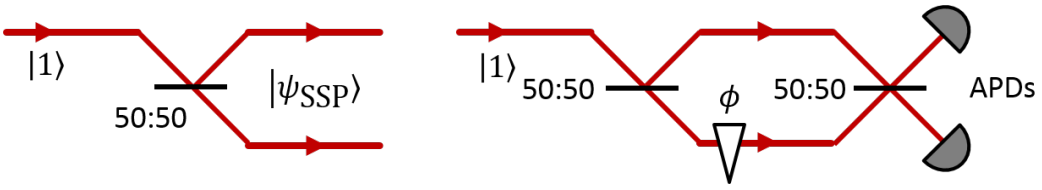
is local to the mode defined by the basis states $|0\rangle$ and $|1\rangle$. As the basis states reside in a single spatial mode, the phase is local, defined entirely by that mode.

For two-mode states, the situation is more complicated. Consider the split single photon (SSP) state

$$|\psi_{\mathrm{SSP}}\rangle = \frac{1}{\sqrt{2}}\left(|0,1\rangle + e^{i\theta}|1,0\rangle\right) \ , \tag{6.2}$$

which corresponds to a coherent superposition of one photon in two modes. In this case the phase is defined by the two-mode basis states $|0,1\rangle = |0\rangle_A|1\rangle_B$ and $|1,0\rangle = |1\rangle_A|0\rangle_B$, where A and B are the mode labels written explicitly. If these modes are, say, orthogonal polarisation modes of a single spatial mode, the phase is local. However, if the mode labels A and B denote different spatial modes, the

state is non-local, with a phase θ,. This non-local, two-mode state is generated by splitting a single photon at a beam splitter, as shown in figure 6.1(a).



(a) (b)

Figure 6.1: (a) Schematic for generating a split single-photon state $|\psi_{\mathrm{SSP}}\rangle$. This state is a non-local superposition of the photon in each output of the beam splitter. (b) Recombining the two entangled modes allows the phase of the state to be extracted.

Verifying that the phase θ exists exposes the coherence between basis states of a non-local superposition state. This phase characterises the relationship between basis states in a spatially-separated superposition, *i.e.* an entangled state; if we see no evidence of this phase, there is no evidence for entanglement. However, while demonstrating dependence on θ is a necessary condition for entanglement, it is not sufficient; we cannot use this as an entanglement witness *per se*[1].

6.1.1 Demonstrating phase coherence

In order to show coherence, one typically seeks fringes in an interference experiment. For a single mode state, one typically varies the phase between the state and a coherent reference, such that fringes can be seen in an intensity measurement.

For two-mode states, coherence between the modes is typically shown by recombining and interfering them. Returning to our example state in Eq. (6.2), the two-

[1]This is trivial, since the same arguments hold for classical light in a interferometer. In this case, a demonstration of non-classicality is required, for instance showing a non-classical $g^{(2)}(0) < 1$.

mode state generated when the split single photon is recombined (see figure 6.1(b)) is

$$|\psi_{\text{Recomb.}}\rangle = \frac{1}{2}\left[\left(1+e^{i(\theta+\phi)}\right)|0,1\rangle + \left(1-e^{i(\theta+\phi)}\right)|1,0\rangle\right] \ , \tag{6.3}$$

where ϕ is an additional phase accumulated between each mode. The probability of a click in one of the detectors $P(0,1)$ is thus

$$P(0,1) = \langle 0,1|\psi_{\text{Recomb.}}\rangle\langle\psi_{\text{Recomb.}}|0,1\rangle = \frac{1}{4}\left|1+e^{\mathrm{i}(\theta+\phi)}\right|^2 = \frac{1}{2}\left(1+\cos\left(\theta+\phi\right)\right) \ . \tag{6.4}$$

If θ is fixed, then varying ϕ will show the sinusoidal dependence of $P(0,1)$. Without loss of generality, we can fix θ to an arbitrary value. For the remainder of the calculations which follow, we set $\theta = 0$; the important point is that θ is defined, *i.e.* that the superposition is coherent. However, if θ is noisy or undefined, then no dependence on ϕ can be observed. Note that an undefined θ means the state is *incoherent*, *i.e.* a classical mixture of basis states with no fixed phase relationship between them, given by

$$\rho = \frac{1}{2}|0,1\rangle\langle 0,1| + \frac{1}{2}|1,0\rangle\langle 1,0| \ . \tag{6.5}$$

6.1.2 Single-mode measurement of a two-mode state

We now ask the question whether there is a way to show that θ is fixed without recombining the modes. If the two modes of the non-local state are sent to two parties, Alice and Bob, can Alice and Bob make measurements to determine that

the mode they receive is one mode of a two-mode state?

In general, without comparing their results, they cannot. To demonstrate, we begin with the density matrix representation of the split single photon state,

$$\begin{aligned}\hat{\rho}_{\mathrm{SSP}} &= |\psi_{\mathrm{SSP}}\rangle\langle\psi_{\mathrm{SSP}}| \\ &= \frac{1}{2}\left(|0,1\rangle\langle 0,1| + e^{-\mathrm{i}\theta}|0,1\rangle\langle 1,0| + e^{i\theta}|1,0\rangle\langle 0,1| + |1,0\rangle\langle 1,0|\right) \end{aligned} \tag{6.6}$$

where the two-mode basis states $|X,Y\rangle\langle X',Y'|$ may be written in terms of the modes $|X\rangle\langle X'|_A \otimes |Y\rangle\langle Y'|_B$. If Alice considers her state alone, she must trace out Bob's modes, leaving

$$\hat{\rho}_{\mathrm{SSP}}^{(\mathrm{Alice})} = \mathrm{Tr}[\hat{\rho}_{\mathrm{SSP}}]_B = \frac{1}{2}\left(|0\rangle\langle 0| + |1\rangle\langle 1|\right) \ . \tag{6.7}$$

All dependence on θ is lost, therefore Alice cannot (in isolation) deduce that $\hat{\rho}_{\mathrm{SSP}}^{(\mathrm{Alice})}$ is one part of a coherent superposition. This is characteristic of all non-local states—single-party measurements cannot deduce non-locality.

6.1.3 Joint measurements

Evidence for entanglement of a state requires measurements on both modes, and it is correlations between the outcomes of those measurements that highlights properties of an underlying entangled state. When counting photons in both modes of the split single photon state, it is straightforward to show that, in the ideal case, measurements are completely (anti-)correlated. The probabilities of coincident measurement events are zero, *i.e.* $P(0,0) = P(1,1) = 0$, while the cross terms

are $P(0,1) = P(1,0) = 1/2$. That is to say, when Alice measures a photon, Bob definitely measures no photon, and vice versa.

However, simply measuring photons says nothing about the non-locality of the state. Indeed, this particular correlation between measurement results is easily generated by purely classical means—simply choosing whether to send a photon to Alice or Bob (but not both or neither). What is required is some verification of a *non-local* quantity in the state, *e.g.* the phase θ. It is clear that projective measurements of photon number on the state in Eq. (6.6) cannot extract any phase information. However, introducing a shared common phase reference with projective photon number measurement does indeed provide means to show that θ is well-defined for two-mode non-local states. This is achieved using two-mode weak-field homodyne detection.

6.1.4 Two-mode weak-field homodyne detection

Two-mode weak-field homodyne detection consists of applying the weak-field homodyne detector described in the previous chapter to each of the two modes. Each mode of a two-mode state is interfered with its own local oscillator, following which TMDs then count photons resulting from the interference pattern, as shown in figure 6.2. In this regime, each weak-field homodyne detection is a local operation; the joint statistics are generated from the TMDs acting on different modes. Coincidence statistics arising from different combinations of TMD clicks are generated by combining the counting statistics from each detector.

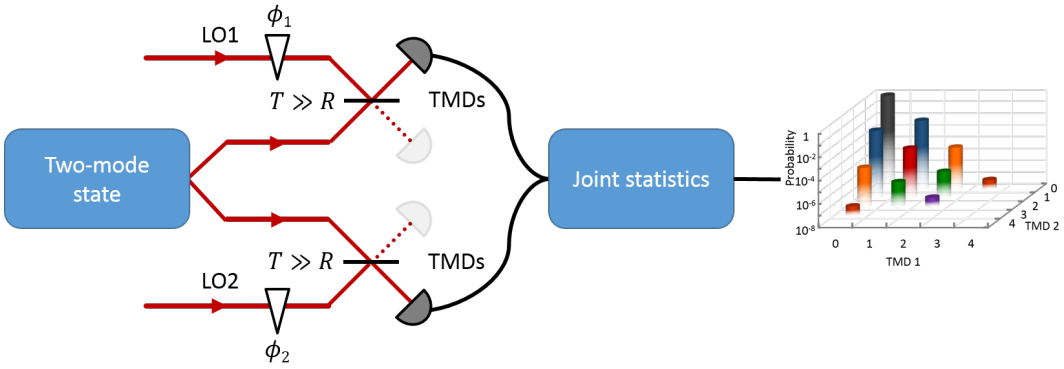


Figure 6.2: Schematic of two-mode weak-field homodyne detection. Each mode of the two-mode state is interfered with independent local oscillators. The use of an imbalanced beam splitter allows much more of the signal state into one TMD, while the power in the local oscillator is increased to compensate. The resulting click statistics from each TMD are combined in a joint statistics matrix, a graphical example of which is shown on the right.

This type of measurement highlights any phase-dependent correlations in the joint photon-number basis. To demonstrate this feature, we apply two-mode weak-field homodyne detection to two non-local states, the split single photon state discussed in the example above, and the two-mode squeezed state emitted from our down-conversion source.

6.2 Non-local phase dependence of a split single photon (SSP)

We begin our analysis of two-mode weak-field homodyne detection of a split single photon state by considering the state evolution as it interferes with the two independent local oscillators. The full calculation is detailed in appendix G. We consider the probabilities $P_{i,j}(\phi_-)$ of measuring combinations of photon numbers i, j on each

mode following the interference, where $\phi_- = \phi_A - \phi_B$ is the *joint phase difference* of the two local oscillators. Note that the joint phase difference ϕ_- is in some sense a non-local quantity, as it can only be defined as a combination of Alice's and Bob's local oscillator settings. If the phase of either (or indeed each) local oscillator is undefined, then so is ϕ_-. Analytical expressions for $P_{i,j}(\phi_-)$ are given in Eq. (G.16), for all combinations of $\{i, j\} = \{0, 1, 2\}$.

In figure 6.3, the probabilities of the various combinations of click events can be seen as a function of the joint phase difference ϕ_-. Clear phase dependence can be seen, highlighting the coherence arising from a non-local phase across the modes.

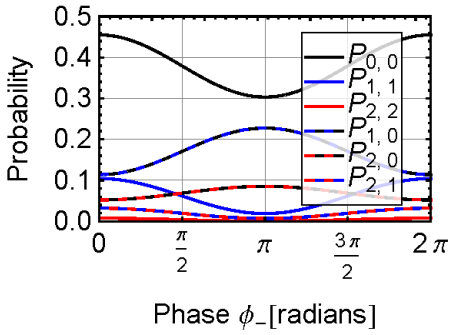


Figure 6.3: Theoretical probabilities of photon number combinations in each mode as a function of the joint phase difference ϕ_-, given interference between a split single photon state and two independent coherent states. There is clear dependence on ϕ_- for all combinations of probabilities, indicating the presence of a non-local phase between each mode of the two-mode state. The coherent state intensities are both set to the mean photon number of the split single photon (0.5), and we consider 50:50 beam splitters, such that the parameters are $\alpha = \beta = 1/\sqrt{2}$ and $T = R = 1/\sqrt{2}$.

Visibility

The fringe patterns shown in figure 6.3 do not all have equal visibilities. Indeed, if we define the visibility of the $P_{i,j}$ photon number combination as

$$V_{i,j} = \frac{P_{i,j}(0) - P_{i,j}(\pi)}{P_{i,j}(0) + P_{i,j}(\pi)} , \tag{6.8}$$

then for $P_{1,0}$ and $P_{2,0}$, the visibility is negative, *i.e.* a fringe pattern which is π radians out of phase with the other terms.

The visibility as a function of coherent state mean photon number is shown in figure 6.4, whereby we have fixed the beam splitter reflectivity $R = 1/\sqrt{2}$. This plot

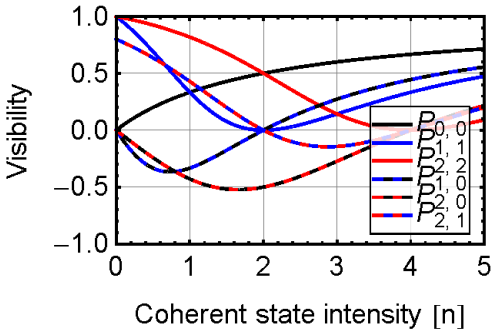


Figure 6.4: Two-mode interference visibility as a function of coherent state mean photon number $|\alpha|^2$ (in units of photons) of the interference visibility in the probability of photon number combination basis. We take the beam splitter reflectivity $R = T = 1/\sqrt{2}$. Note that visibilities at $\alpha = 0$ are undefined.

shows many interesting features. The asymmetric visibilities corresponding to the cases $P_{i,j\neq i}$ can have negative visibilities for a particular $|\alpha|^2$, though at $|\alpha|^2 > 4$, all visibilities shown are positive. Note also that all curves can have zero visibility at some $|\alpha|^2$; all curves representing at least one mode measuring exactly one photon

achieve this at $|\alpha|^2 = 2$.

6.2.1 Experimental two-mode weak-field homodyne detection

Using the two-mode weak-field homodyne scheme outlined in the previous section, non-local phase coherence can be demonstrated experimentally. The setup used to achieve this is shown in figure 6.5. This allows full and independent tuning not only

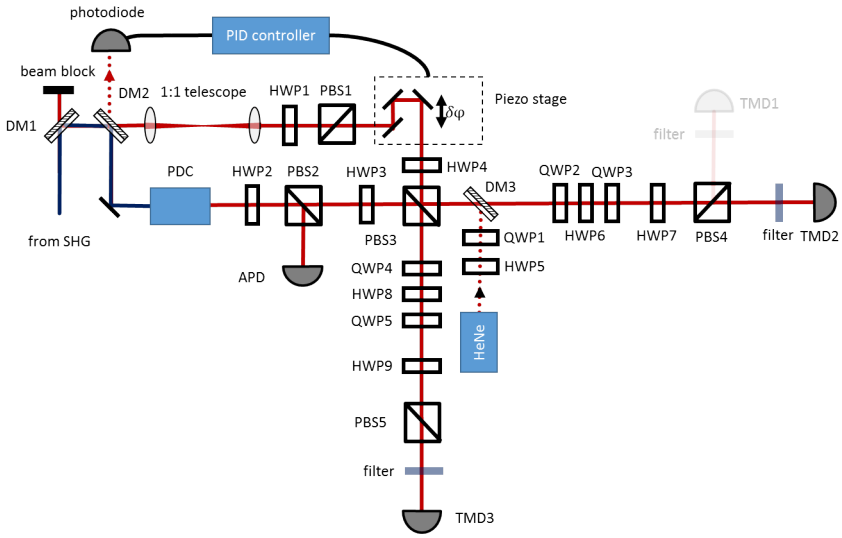


Figure 6.5: Setup used to probe each mode of a heralded single-photon split at a beam splitter. Various half-wave plates (HWP) are used to generate the desired state and measurements. HWP3 splits the heralded photon into a superposition of H and V polarisation states. This is translated into a spatial superposition (an entangled state) across the output modes of PBS3. Similarly, HWP4 is set such that the local oscillator contains both H and V polarisation components when it is incident on PBS3. The two Berry-phase rotators (see section 5.4.3) adjust the relative phase between each entangled mode and their respective local oscillator. HWP7(9) allow tuning of the relative intensities of the local oscillator (see figure 5.17) and signal into the interference beam splitters PBS4(5), the outputs of which are measured using TMD2(3), respectively.

of the phase of the local oscillator with respect to each mode of the entangled state,

but also the ratio of the interference beam splitter.

The half-wave plates that control the phase, HWP6,8 in figure 6.5, were placed in motorised rotation mounts. Random phase settings in the range 0 to 2π were picked for each mode independently by a Labview program. At each combination of phases, the data acquisition system collected photon number statistics from each of the TMDs over a period of 1 minute, before a new set of phases were used and the data collection process repeated. This turned any long-term drift over the duration of the experiment ($\sim$1 hour) into randomised noise in the counts. Note also that the data that follows are raw counting statistics from the TMD; no inversion accounting for loss or based on characterisation of the detector was required. Furthermore, note that ϕ_- is degenerate in ϕ_A and ϕ_B, *i.e.* that many different combinations of ϕ_A and ϕ_B can contribute to the same ϕ_-. In the results that follow, we explicitly include all *combinations* of the different phases, rather than averaging over all combinations for each ϕ_-.

Local phase independence

A central feature of multimode coherent superposition states is that coherence cannot be seen in isolated measurements on one mode. Therefore, for spatially multimode states, no phase dependence should be seen when considering just local measurements. These data are shown in figure 6.6. The results show a slight phase dependence, particularly in the singles counts. We attribute this to small imperfections in the Berry phase rotator used to set the phase (see figure 5.11). If the

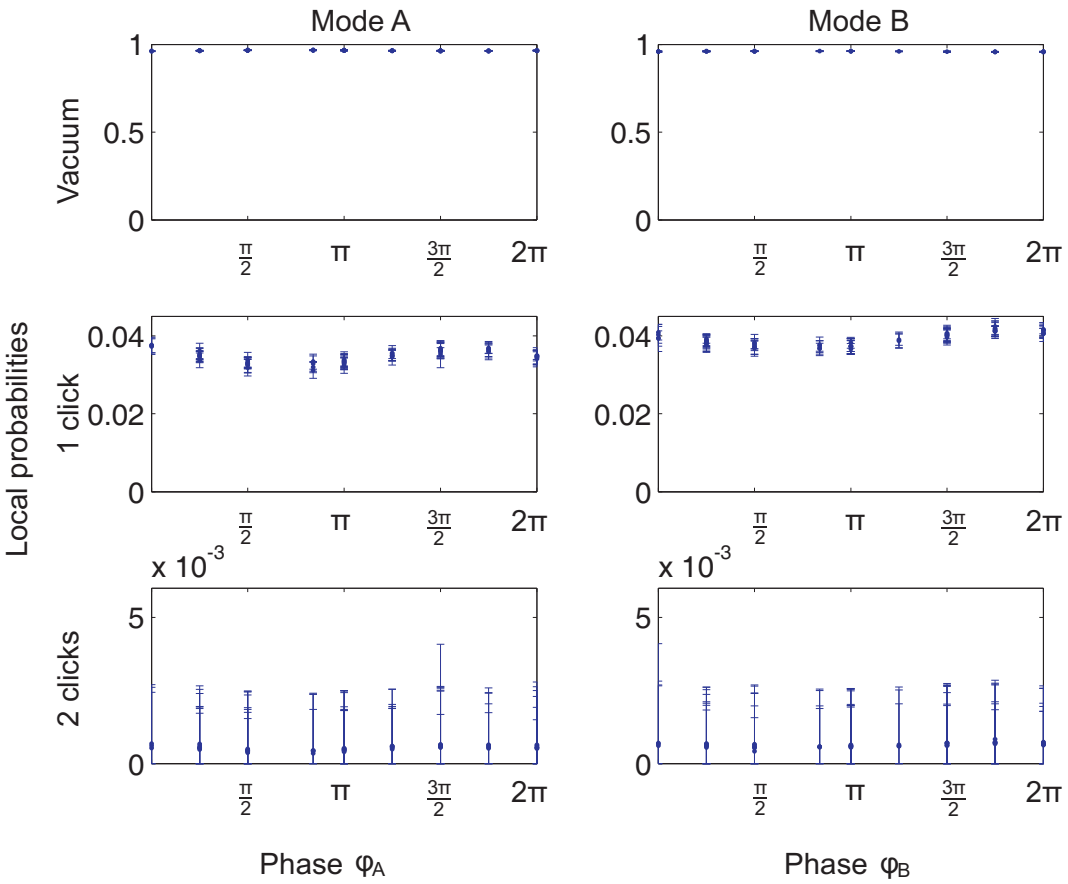


Figure 6.6: Probability of different photon number outcomes following local weak-field homodyne measurements on each mode of a split single photon. The top row is the vacuum, the second row for the singles counts and the third row corresponds to two counts in the TMD. Error bars arise from assuming Poissonian statistics.

polarisation of the incoming state is not precisely linear (in either the H or V basis), and/or if there is any error in the setting of the quarter-wave plates, then the half-wave plate used to change the phase will also introduce some polarisation change in the beam. Rotating this wave-plate will thus introduce an unwanted linear component of polarisation, which is directed to the wrong port at the final PBS. This manifests itself as fringes in probabilities of measurement outcomes.

The extent of this effect when considering non-local interference is discussed in detail when considering two-mode weak-field homodyne detection on a two-mode squeezed state in section 6.3, where this effect is clearer. Here, the effect is small enough to be neglected; we cannot attribute the visibilities of the interference patterns in the results that follow solely to extraneous polarisation effects.

Non-local phase dependence

By plotting the joint statistics as a function of the phase difference between each local oscillator, clear phase dependence can be seen, as shown in figure 6.7. This phase dependence is most clearly seen in the $(1,1)$ case. Similarly, in the $(2,1)$ and $(1,2)$ cases, phase dependence is also apparent, though due to the limited number of measurements taken, the errors are rather large. This low data rate is further evident from the lack of counts in the $(2,2)$ case. Notwithstanding the small data set, as a proof-of-principle experiment, this is sufficient to show coherence dependent on a non-local phase.

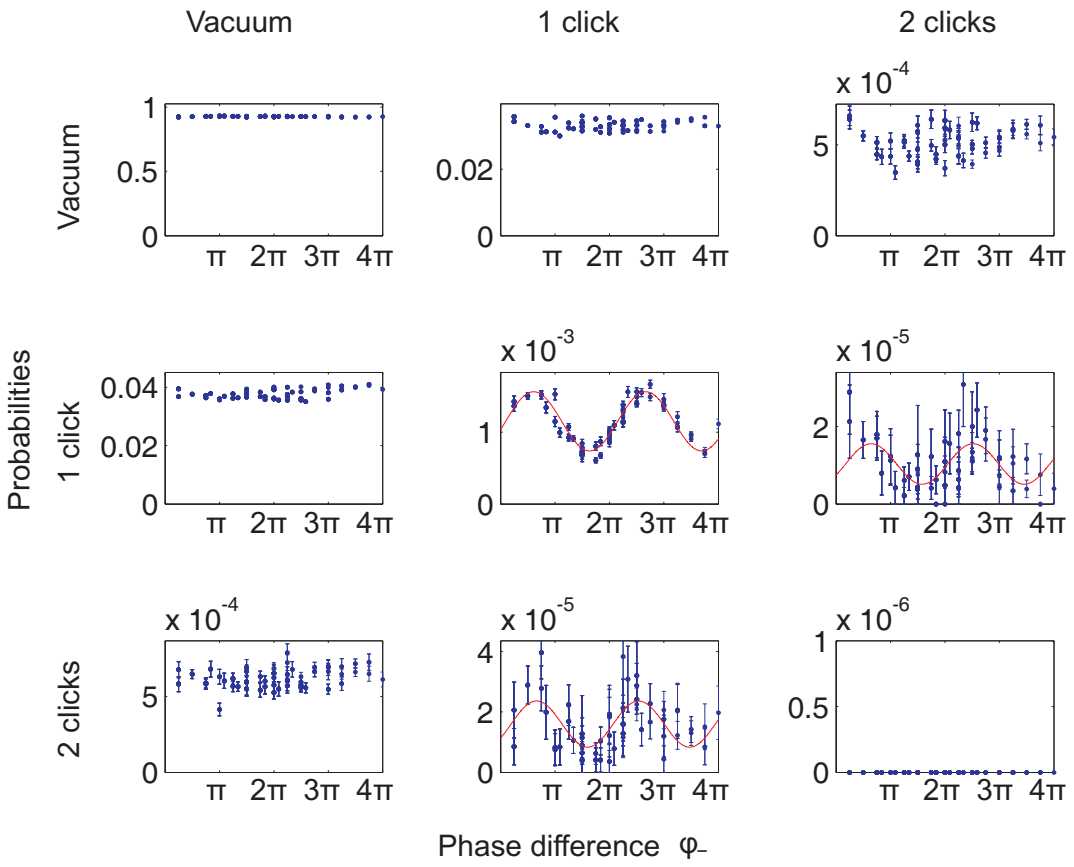


Figure 6.7: Probability of different terms in the joint statistics of two-mode weak-field homodyne detection on a split single photon as a function of phase difference. The $i+1, j+1^{\text{th}}$ plot corresponds to the probability $P_{i,j}(\phi_-)$ of measuring i, j photons. Error bars arise from assuming Poissonian photon statistics. The red lines in the (1,1), (2,1) and (1,2) click plots are sinusoidal fits to the data using the "fourier1" library in MATLAB's curve fitting toolbox. No starting parameters were required. The RMS errors in the fits are 1.0×10^{-4}, 6.2×10^{-6} and 7.1×10^{-6} for (1,1), (1,2) and (2,1) respectively. Using the mean of the distributions, the relative error in the fits are 0.088, 0.60 and 0.44, respectively. A more thorough analysis of these errors could use χ^2 test.

Marginal distributions

Further figures of merit that can be extracted from this data set are the marginal distributions for each mode. These distributions are found by tracing out one mode and looking at results from the other mode. This has the effect of averaging out any local phase dependence of the mode that is traced out, which would reveal any local phase dependence in the untraced mode. As expected for one mode of a non-local state, as in the local measurement case, no phase dependence should be seen. This is indeed the case, as shown in figure 6.8. This result shows that the phase dependence

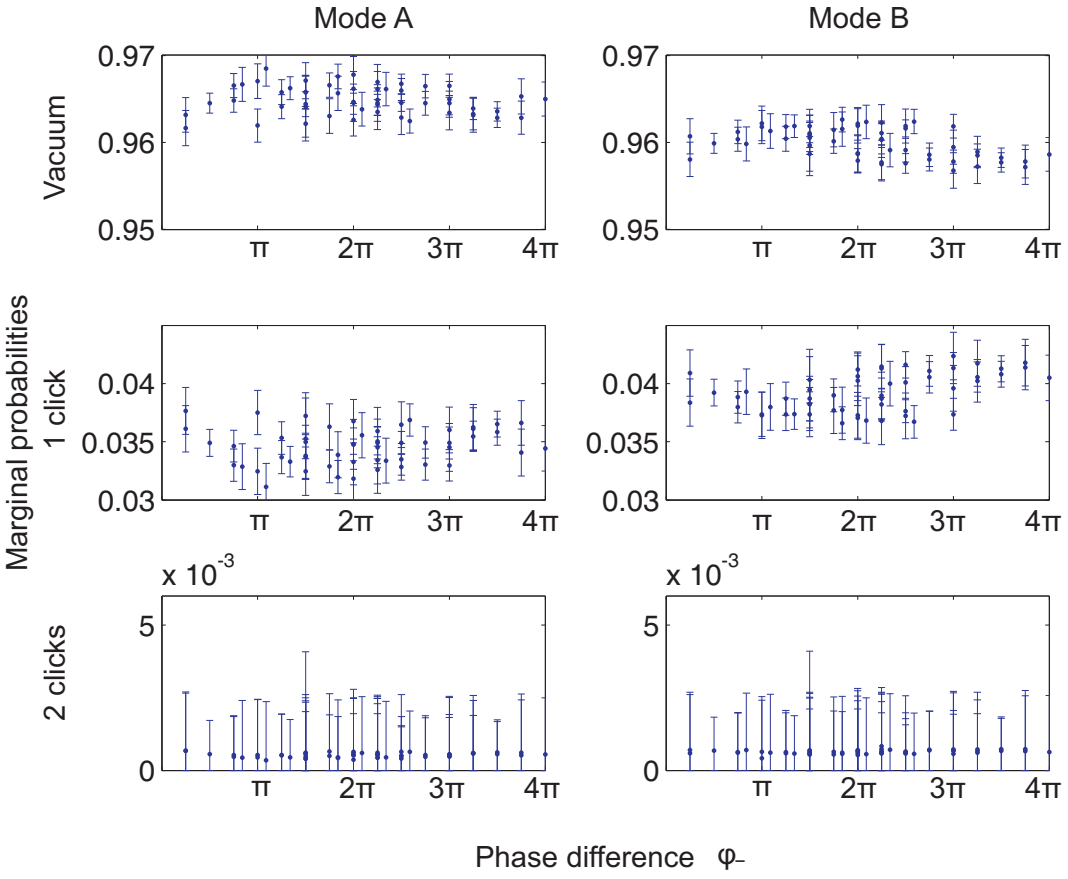


Figure 6.8: Marginal probability distributions of measuring vacuum, one and two photons. The lack of phase dependence, in comparison with the phase dependence of the joint probability distributions, shows that the state is non-local.

seen in figure 6.7 cannot be explained by local coherence—our conclusion is that the interference effect is non-local.

6.3 Non-local coherence of a two-mode squeezed state

Just as in the case for split single photon, we can look at the coherence of the down-converted two-mode squeezed state $|\psi_{\mathrm{TMSS}}\rangle$. By interfering each mode with a local oscillator and counting photons as before, interference fringes in these counts will be seen as a function of the phases of each local oscillator. Again, the state evolution of this case is calculated in appendix G, section G.2, where we consider an approximation of the two mode squeezed state, namely $|\psi_{\mathrm{TMSS}}\rangle \approx (|0,0\rangle + \lambda|1,1\rangle)/\sqrt{1+\lambda^2}$.

6.3.1 Phase dependence

By contrast to the split single photon state, the joint probabilities depend on the sum of the two local oscillator phases, *i.e.* $\phi_+ = \phi_A + \phi_B$. The phase dependence of the probabilities $\{P_{i,j}(\phi_+)\}$ of detecting i, j photons at a joint phase ϕ_+ following interference is shown in figure 6.9. The reason for the change in phase dependence is as follows. In down-conversion, both modes assume the phase of the pump, therefore fringes are seen as a function of the sum of the phases of the two local oscillators. In the split single photon case, the phase is defined upon splitting at a beam splitter, therefore it is the phase difference between the split modes that determines the fringe pattern. These dependencies arise from the derivations of the expressions for probabilities detailed in appendix G.

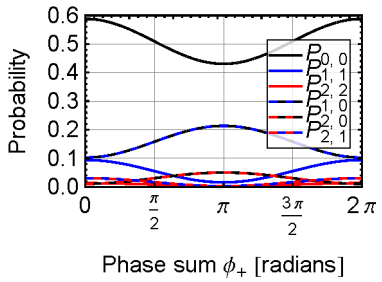
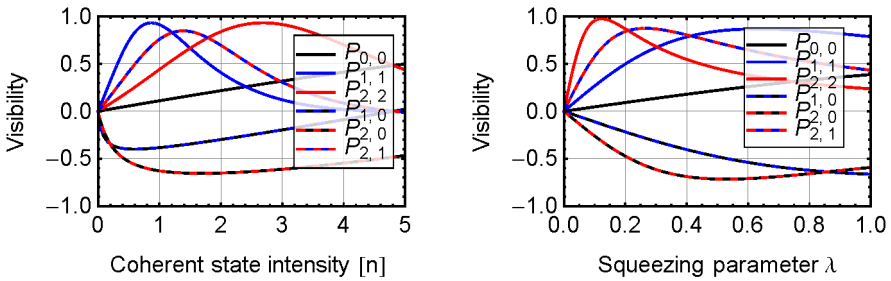


Figure 6.9: Theoretical probabilities of photon number combinations in each mode as a function of phase sum $\phi_+ = \phi_1 + \phi_2$ (in contrast to the phase difference ϕ_- in the split single photon case), given interference between a two-mode squeezed state and two independent coherent states. As with the split single photon state, the dependence on a non-local phase is evident. In anticipation of the experimental results, the coherent state intensities are both set to $|\alpha|^2 = |\beta|^2 = 1.4$ and the initial squeezing $\lambda = 0.34$, and we consider beam splitters of transmissivity $T = 0.89$.

Visibilities

As before, we can show how the visibilities of the interference pattern change as a function of different parameters. Two examples are shown in figure 6.10. By



(a) Varying local oscillator amplitude $|\alpha|^2 = |\beta|^2$

(b) Varying initial squeezing parameter λ

Figure 6.10: Interference visibilities for different photon-number combinations as a function of (a) coherent state amplitudes $|\alpha|^2 = |\beta|^2$ at $\lambda = 0.34$ and (b) squeezing parameter λ at $|\alpha|^2 = |\beta|^2 = 1.4$. The transmissivities of the beam splitters remain $T = 0.89$.

contrast to figure 6.4, the $P_{0,0}$ term shows very low visibilities across a wide range of parameters.

6.3.2 Experimental demonstration

In order to show this coherence experimentally we adapt the experimental setup from the split single photon case. This setup is shown in figure 6.11. An additional

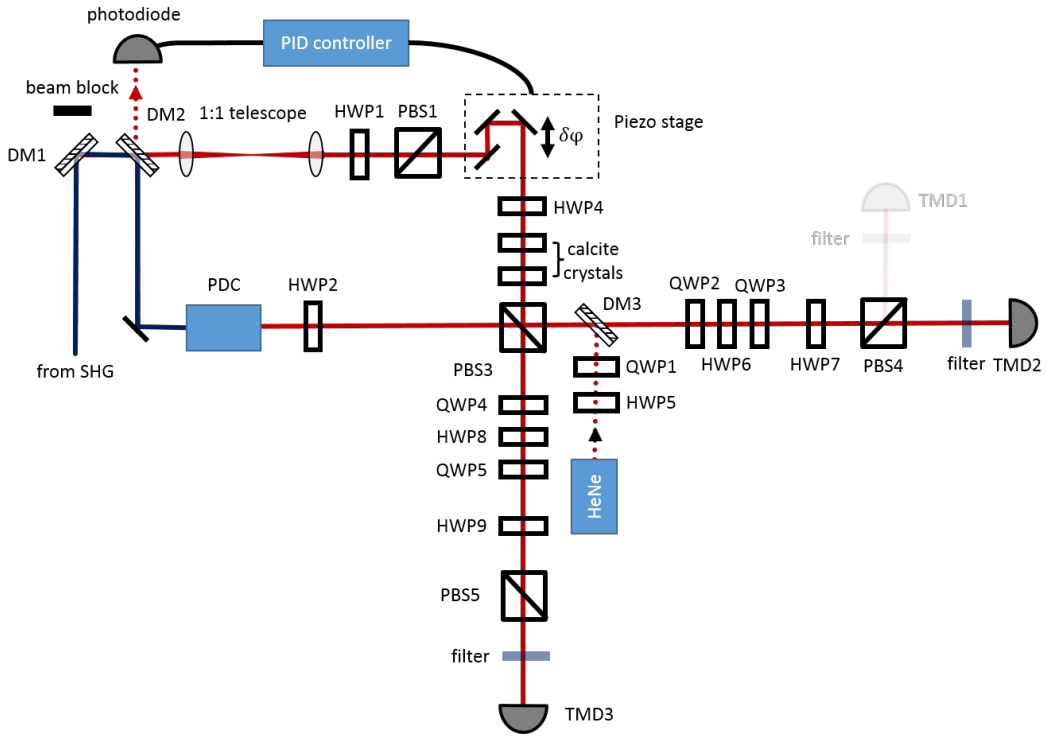


Figure 6.11: Setup used to probe each mode of a two-mode squeezed state. This setup is equivalent to that shown in figure 6.5, with some important adjustments for the two-mode squeezed state case. PBS2 is removed to allow both down-converted modes into each Berry-phase measurement setup. The addition of two calcite crystals, one of length 10 mm and the other of length 8 mm, ensure that each polarisation mode of the local oscillator is temporally well overlapped with each mode from the down-converter.

constraint in this configuration is the temporal overlap of the local oscillator with each mode of the down-converter. Due to birefringence in the KDP crystal, the vertically polarised mode (V-mode) is delayed by an amount proportional to the length of the crystal. This must be compensated for in the local oscillator. This

is achieved with two calcite crystals of combined length 18 mm placed in the local oscillator arm. Placing them in the local oscillator (and not in the mode containing the PDC crystal) maintains the temporal delay between the down-converted pulses, preventing any possible crosstalk or parasitic interference effects.

Results

In contrast to the split single photon experiment, the relevant phase (in this case the sum of the phases of the two local oscillators) was varied between 0 and 4π on just one mode (mode 2). In this case, the marginal distribution is equivalent to the local distribution, since one of the phases was constant. This marginal distribution is shown in figure 6.12. The probabilities of measuring different photon numbers in mode 1 remains independent of changing the phase in mode 2. Mode 2, however, does see changes. In the absence of other measurements or assumptions about the state, it is impossible to conclude whether or not this apparent phase dependence is due to genuine local coherence or the polarisation steering experimental imperfection as described above in section 6.2.1.

However, by looking at the joint photon statistics as before, further insight can be gained. Figure 6.13 shows the raw data for joint measurements on a TMSS. Each of the fringe patterns are fitted to a sinusoidal function using the "fourier1" library in MATLAB's curve fitting toolbox. Note that the phase of the fringe patterns relative to one another do not correspond to those predicted by the theory. Not only is there a phase offset between each curve, we expect the fringes in the $(i,0),(0,j)\,;\ i,j>0$

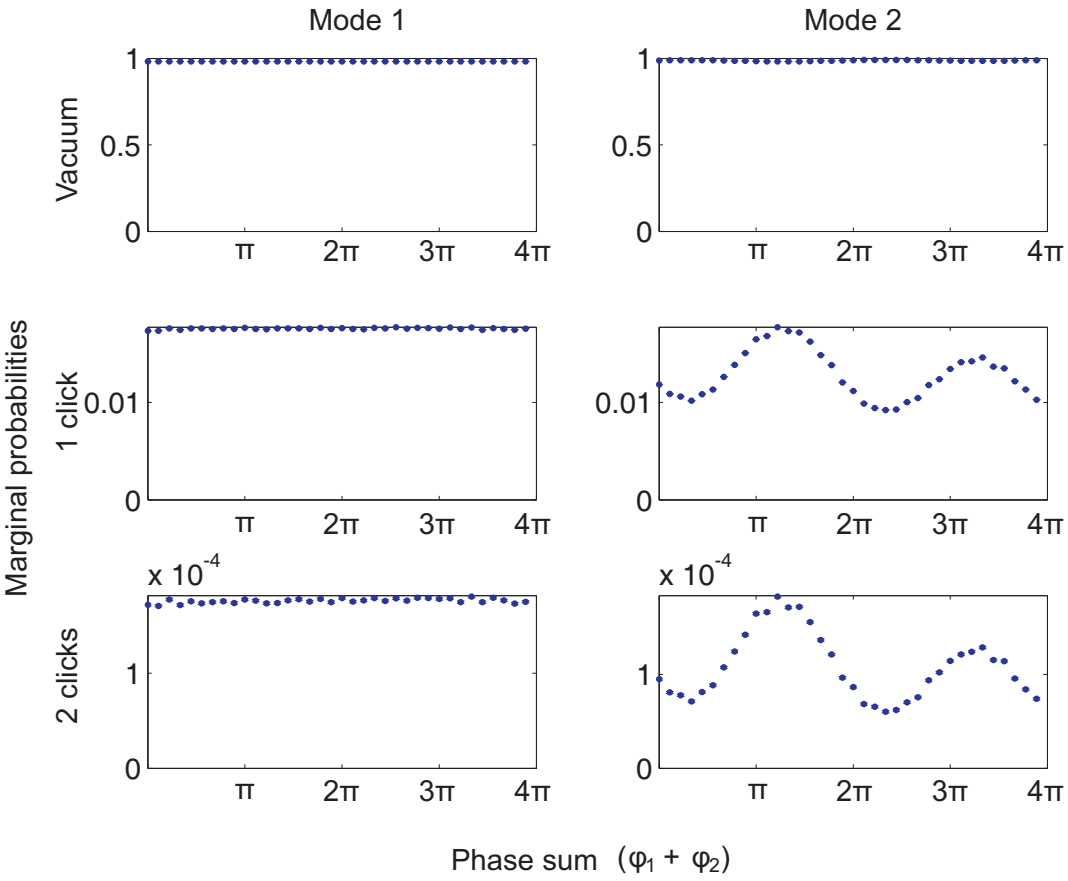


Figure 6.12: Marginal probability distributions of measuring vacuum, one and two photons. Error bars arise from assuming Poissonian statistics, so that the error bars are of similar size to the symbols indicating the mean values. In contrast to the split single photon case, the marginal distribution shows some dependence on the setting of the waveplate.

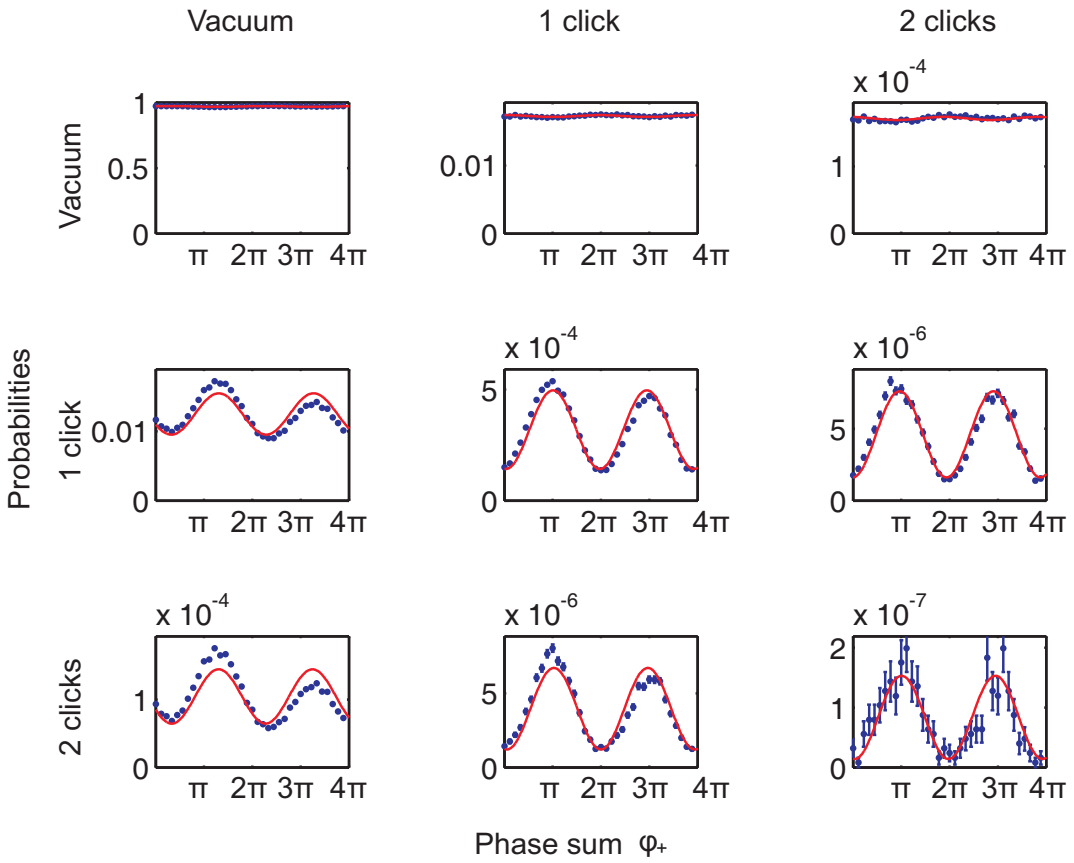


Figure 6.13: Raw joint statistics of weak-field homodyne detection on a two-mode squeezed state. Error bars arise from assuming Poissonian photon statistics, and are too small to see in some plots. The red lines are sinusoidal fits to the data using the "fourier1" library in MATLAB's curve fitting toolbox. No starting parameters were required.

terms to be π out of phase with all the other terms (see figure 6.9)To remedy the situation, we need to account for the polarisation effect caused by the wave-plate used to change the phase. By normalising the joint statistics to the marginal distribution above[2], this effect is removed; any fringes that remain must be caused by non-local phase dependence. These results are shown in figure 6.14. Now all non-local effects

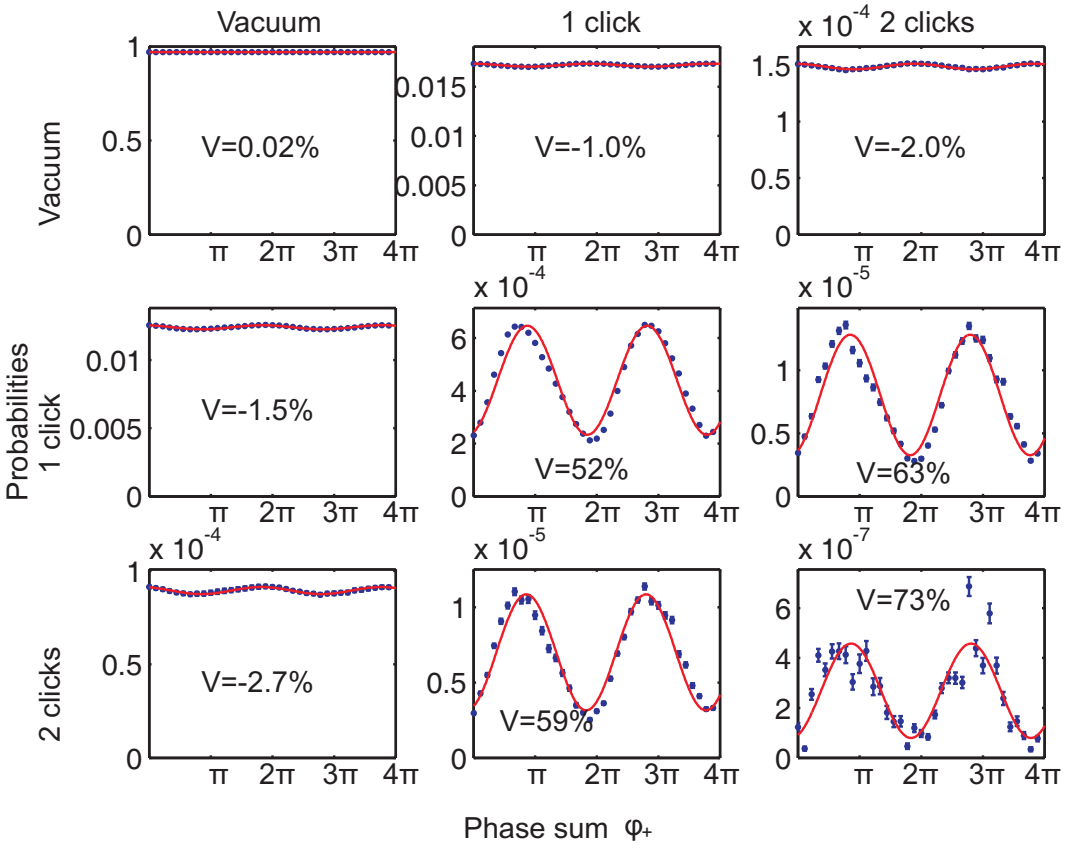


Figure 6.14: Joint statistics of weak-field homodyne detection on a two-mode squeezed state corrected for polarisation steering. The error bars arise from assuming Poissonian number statistics, and the red lines are numerical fits to the data.

are clearly seen and the expected sign of the visibilities are correct. Indeed, the

[2]By normalising we mean dividing the value of each data point by the value of each marginal distribution at that point.

visibilities of the terms that do not contain vacuum contributions are remarkably close to those calculated in the ideal case, shown in figure 6.10. We attribute the discrepancy to the role of loss in generating more clicks in the lower bins.

Loss

This analysis does not include any compensation for loss. However, despite our detectors' relatively low efficiency of $\sim 10\%$, the effects are still clear. One reason is that loss in this system manifests itself as photon count cascading down towards the vacuum. This causes artificially high numbers of counts at low photon numbers. Different losses on each mode also account for the asymmetry about the leading diagonal in figure 6.14. However, much can still be learnt from this analysis. In terms containing vacuum, the relative magnitudes of the visibilities are consistent with the theory above, *i.e.* that the ratio $V_{2,0}/V_{1,0} \sim V_{0,2}/V_{0,1} \sim 2$.

The qualitative effect we show—phase-dependent joint photon number statistics–is remarkably robust to losses and detector inefficiency. However, further work may well incorporate these effects to provide a more precise analysis, both to gain closer agreement with the theory and perhaps yield more information about the nature of the non-local state used to generate the effect. Indeed, using this scheme not just to characterise the non-locality of such a state, but also to bound any entanglement present, remains an open question.

6.3.3 Concluding remarks

We have shown quite clearly how two-mode weak-field homodyne detection can be used to show the effect of a phase between two modes of a non-local state. This represents a novel way of probing entangled states in quantum optics. Up to now, entangled states in the discrete variable (DV) regime are typically probed in two ways: either locally through the violation of a Bell inequality based on correlations of dichotomic measurement outcomes, or non-locally by interfering the entangled modes and violating the concurrence criterion [173].

In the continuous variable (CV) regime, entanglement between modes is typically witnessed by identifying squeezing in non-local quadratures by an inseparability criterion [174]. While meeting this criterion is a necessary and sufficient condition for a Gaussian state to be entangled, it is only sufficient for non-Gaussian states. That is, some non-Gaussian states do not violate this condition. Furthermore, measuring quadrature variances alone completely neglects the rich, phase-dependent structure that exists in the photon-number basis. This information is recovered by full state reconstruction, albeit at a cost of the considerable time required to obtain a tomographically complete set of measurements. In cases where taking large amounts of data may be unfeasible (since the probability of generating exotic states typically decreases with the complexity of the state), a more efficient approach may be beneficial.

This measurement scheme paves the way for a hybrid approach that combines few-photon states and several modes to dramatically increase the dimensionality of

quantum protocols. By utilising the CV ensemble approach to quantum optics and applying photon counting with phase referencing, this richness is still evident even in the presence of the high losses of our detectors. Schemes that exploit this hybrid approach of many photons across many modes are yet to be developed, but this tool shows great potential in terms of feasibility.

6.4 Witnessing entanglement

In the preceding sections, we have been careful to stress that non-local coherence is a non-classical phenomenon consistent with entanglement, but not by itself sufficient to establish its presence. In order to be entangled, one must show the inseparability of the state. This can be achieved in two ways: either by fully reconstructing the state or by using some specific measurement strategy that returns a binary answer as to whether the state is entangled (but typically no other information). The former requires many measurements and may be impractical in some cases. The latter is known as an *entanglement witness* and typically takes the form of violating some bound based on correlations between measurements, of which the set of Bell tests is perhaps the most famous example[2,3,175]. Indeed, the Bell tests are even more stringent than just witnessing entanglement; when violated, they rule out *local hidden variables* (LHV) as a cause for the correlations.

6.4.1 A CV entanglement witness

Bell measurements are ideally suited to the finite dimensional regime since they are based around dichotomic measurements, *i.e.* photons being either horizontally or vertically polarised. In the CV domain, such statements cannot be straightforwardly formulated. In fact, it is impossible to violate a Bell inequality using Gaussian states (two-mode squeezed states) and Gaussian measurements (homodyne detection). However, if one uses non-Gaussian measurement, one can circumvent this limitation, suggested by Grangier *et al.*[176] and shown by Kuzmich, Walmsley and Mandel[177]. In their work, weak-field homodyne detection—a non-Gaussian detection strategy—was performed with single-photon detectors which did not resolve photon number.

The use of number-resolved weak-field homodyne increases the dimensionality of the systems to be probed. While this does not necessarily lend itself directly to the violation of a Bell inequality, Puentes *et al.*[69] showed how an entanglement witness can be constructed from the POVMs describing our detector. Indeed, this proposal goes a step further than a conventional witness: not only does it ascertain the presence of entanglement, it also places a lower bound on the amount of entanglement present. This process answers the question "what is the entanglement content of the least entangled state consistent with the available measurement data?"

A little intuitive insight into this process can be gained from looking at the data on non-local coherence above, particularly figure 6.13. The visibilities of these fringes place bounds on the coherence present in the state. To demonstrate clearly

the coherence between modes, we chose many phase settings in order to highlight the phase dependence. However, to calculate the visibility of these fringes, just three well-chosen data points are required. Similarly, the dependence on amplitude can be determined by varying the strength of the local oscillators, *i.e.* sampling from the visibility distribution shown in figure 6.10(a).

Using carefully-chosen measurement settings, the witness gathers data on the non-local phase dependence at different local oscillator strengths. Heuristically, one can imagine searching through all states consistent with this data, given the known phases and LO strengths, and calculating the entanglement in each state. In fact, the exact form of the state is not required; instead, the POVMs themselves are sufficient to calculate entanglement [69].

The precise mathematical formulation of the construction of the witness from the POVMs of our detector is detailed extensively in the work by Puentes *et al.* [69]. Much of the theoretical support, including numerical data analysis codes, were provided by our collaborators at the Freie Universität Berlin, namely Earl T. Campbell and Jens Eisert. Here, we instead describe how the entanglement witness manifests itself experimentally.

6.4.2 Witnessing entanglement experimentally

In practical terms, the entanglement witness comprises processing measurements arising from a set of POVMs $\left\{\Pi^A, \Pi^B\right\}$ implemented on each mode A, B. We denote the set of elements of the POVMs $\left\{\Pi^A_{\mu,i}\right\}$, $\left\{\Pi^B_{\nu,j}\right\}$, which describe the

measurement outcome μ given a measurement setting i, and similarly for mode B for outcomes ν given settings j. For our weak-field homodyne detector, the physical implementation of these settings simply consists of phases and amplitudes of the local oscillator for each mode, and the outcomes are the click statistics from the TMDs.

The motivation to use an entanglement witness over full state tomography is that far fewer measurement settings are required to calculate a lower bound on entanglement. The tightness of the bound increases with the number of measurement settings. However, not all settings generate equal information; the aim is to choose a small number of settings that yield a useful bound on the entanglement of the state.

A graphical representation of this process is illustrated in figure 6.15. If one considers the convex state space containing all states, then the set of separable states is enclosed within that set. Each witness measurement $\hat{W}_i$ traces a tangent to that set, and yields a binary answer as to whether the state is separable or not. More formally, if $\mathrm{Tr}[\hat{\rho}\hat{W}_i] < 0$, then the state is not separable.

By collecting the outcomes of several different witness measurements, the distance from the set of separable states can be bounded. This distance is directly related to the minimum entanglement present in the state.

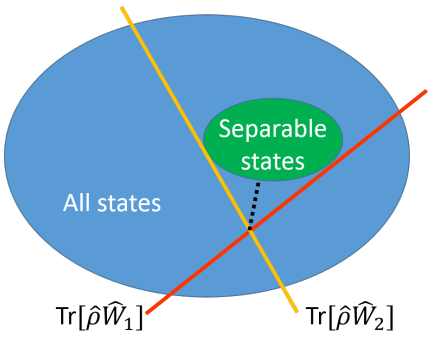


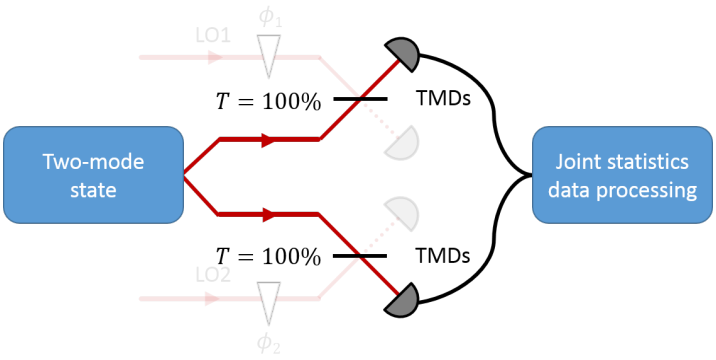
Figure 6.15: Graphical representation of the entanglement witness operation. The convex set of all states (blue) contains the set of separable states (green). Bounding the region in state space with witness measurements $\hat{W}_1$ (red) and $\hat{W}_2$ (orange) allows one to find the minimum distance from separable states (black dotted line), which is proportional to the amount of entanglement in the state.

Building the witness

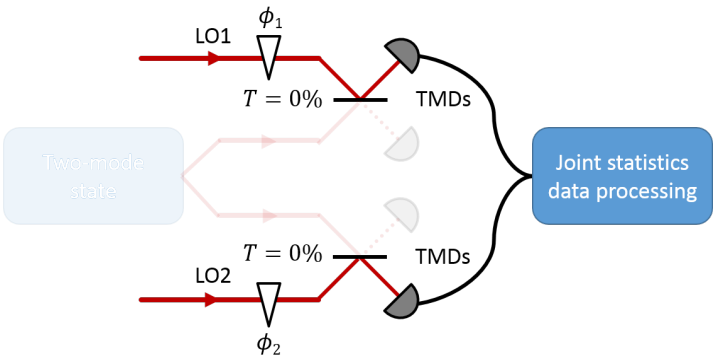
Each witness measurement $\hat{W}_i$ is constructed from weighted sum of the POVMs arising from different measurements of the state [69]. To build our witness, nine measurement settings were required. These nine settings comprise two local oscillator amplitudes ($|\alpha|^2 \sim 1$ and $|\alpha|^2 = 0$) and two phase settings ($\phi_{A,B} \in \{\pi/2, 3\pi/2\}$) on each mode. Note that the phase settings are only defined for non-zero LO amplitudes.

The POVM elements of the detector are determined by four parameters: the detector efficiency, beam splitter reflectivity, LO amplitude and LO phase. The setup for determining each parameter is shown in figure 6.16.

One can calculate the different parameters by measuring different states in the TMDs. This is achieved by tuning the beam splitters in figure 6.16. With the beam splitters specified for 100% transmission, as shown in figure 6.16(a), no LO is present



(a)

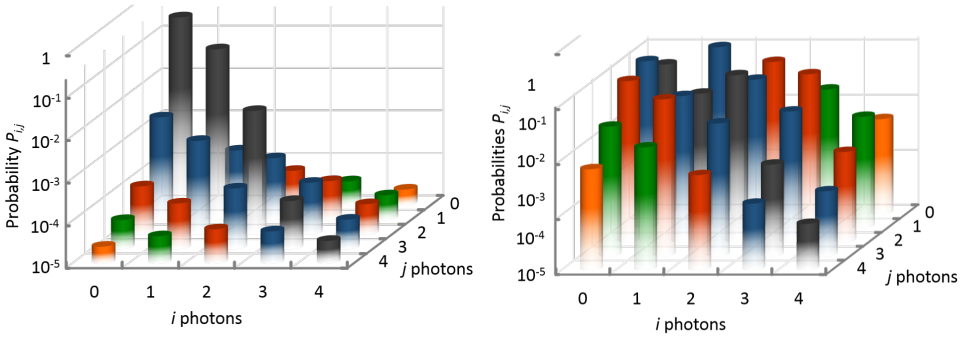


(b)

Figure 6.16: Setups used to characterise the joint statistics for (a) the TMSS and (b) the local oscillators. This is achieved by using the tunable beam splitter setup shown in figure 5.11.

and the complete two-mode state is detected by TMDs on each mode. From these data we can extract the mean photon number of the TMSS, as well as calculate the efficiency of each TMD [110]. Similarly, tuning the beam splitters to 0% transmission (100% reflection), as in figure 6.16(b) allows the mean photon number of the LO to be calculated. Tuning the beam splitter to some intermediate transmissivity allows interference between the LO and the state; typical reflectivities were of the order 20-40%. These are precisely calculated as the fraction of LO detected at the reflectivities required for interference compared with the total LO detected at 100% reflectivity.

Applying the TMD inversion algorithm developed by Coldenstrodt-Ronge *et al.* [36,118] to the resulting joint statistics generates photon number information from raw detector clicks. Examples of these are shown in figures 6.17(a) and 6.17(b) for a TMSS and two independent local oscillators (coherent states), respectively. Processing the data in this way allows further figures of merit to be calculated di-



(a) (b)

Figure 6.17: Joint photon number distributions for (a) the TMSS and (b) the local oscillators. Note that both are plotted on log scales. The TMSS is largely populated along the diagonals while the LO has the expected distribution of the logarithm of a Poissonian distribution).

rectly from the number distribution. From the marginal distributions of the data in figure 6.17, one can readily calculate the mean photon number $\bar{n}$ and second order correlation function $g^{(2)}(0)$ for each mode A, B. For the results shown in figure 6.17, these are as follows:

	$TMSS$	LO
$\bar{n}_A$	0.1329	1.4702
$\bar{n}_B$	0.1287	1.3385
$g^{(2)}(0)_A$	2.3014	1.0674
$g^{(2)}(0)_B$	2.1685	1.0579

(6.9)

Note that we expect the $g^{(2)}(0)$ values to be around 2 for the TMSS (since one mode of a TMSS is a thermal state) and 1 for the LO (since they are coherent states).

The relevant phase setting of each LO is measured from some arbitrary phase offset; in the Berry-phase rotation system we employ, the relative angle of the phase rotation half-wave plate (HWP6 in figure 5.11) corresponds to a quarter of the phase imparted onto the LO (*i.e.* moving the wave plate 45° corresponds to a phase shift of π radians).

All parameters are thus determined prior to processing the witness data[3]. We assume that the efficiencies and reflectivities remain fixed throughout the experiment and are independent of LO amplitude and phase, where the latter two parameters determine the settings of the POVM elements as described above. We assume also that the LO amplitudes remain fixed (*i.e.* that the power is constant), and we place bounds on the phase noise based on the results shown in section 5.4.

[3]That is to say, no postselection is required.

Results

Joint statistics corresponding to the set of measurement outcomes were collected at each of the nine measurement settings. The witness program then calculates the entanglement present in the range of states consistent with the measurement outcomes, and returns the lowest entanglement of the state in this range. Note that the possible states are never explicitly used during the calculation; lower bounds on the entanglement are extracted directly from the measurement outcomes during the convex optimisation process based on a semidefinite program (SDP) [69]. We applied a witness to both a TMSS and a split single photon state. Unfortunately, despite several data runs on each set, no entanglement was witnessed.

6.4.3 Comparison with simulation

The failure of the analysis program to detect entanglement is disappointing but not entirely without value; it allows further insight into the structure of the two-mode state. Included within the analysis program is a routine to simulate data based on the expected experimental conditions. Given reasonable experimental parameters, the simulated data invariably showed some non-zero entanglement, even in the presence of noise. Therefore, comparing experimental with simulated data should shed some light on the discrepancy between the two data sets.

Quantifying the discrepancy

The form of the data sets, whether measured or simulated, are matrices corresponding to the measurement outcomes given the measurement settings. The elementwise-difference between these matrices quantify the discrepancy between each of the elements. Further, taking the Frobenius norm [4] of this matrix returns a single number that quantifies the difference from simulation. By varying some parameters, one can attempt to isolate why the simulation fails to describe our data. Note that *absolute* value of the Frobenius norm does not yield much information, rather we are interested in *relative* changes of this quantity as we vary the parameters.

Determining the input state

The simulation takes the same POVMs as the measured data and applies them to some input state $\hat{\rho}$. The POVMs are experimentally determined independently of the witness and are common to both the simulated and measured data, therefore any discrepancy must arise in the input state for each case. In the absence of state tomography, we cannot know the exact form of $\hat{\rho}$ so, for the simulations, we model $\hat{\rho}$ on a TMSS parameterised by λ, given in Eq. (2.34). We can estimate λ in two ways, both of which are independent of the witness experiment. Based on calculating the mean photon number in each mode of the TMSS, we can calculate λ by inverting Eq. (2.25) to yield

$$\lambda = \sqrt{\frac{\bar{n}}{1+\bar{n}}} \, . \tag{6.10}$$

[4] The Frobenius norm of a matrix A is $||A||_F = \sum_{i,j} |A_{i,j}|^2$.

Furthermore, by looking at the joint photon-number statistics matrix following the inversion (an example of which is shown in figure 6.17(a)), λ can be directly extracted from the ratio of the diagonal terms, *i.e.*

$$\lambda = \sqrt{\frac{P_{i+1,i+1}}{P_{i,i}}} \,, \tag{6.11}$$

where $P_{i,i}$ is the probability of i photons coincident in both modes. The results of Eqs. (6.10) and (6.11) should agree, notwithstanding large errors in Eq. (6.11) at $i \gtrsim 2$. Note that for an ideal TMSS, $P_{i,j} = \delta_{i,j}$, that is, only coincident terms should be present. This is evident from figure 6.17(a), where the black bars denote the diagonal elements; while there exists non-zero off-diagonal terms (plotted on a log scale for clarity) they are nonetheless small.

Modelling the squeezing parameter λ

To test the simulation, we vary some parameters and see how the difference to measured data changes: the smaller the difference, the closer the simulation is to our experimental data. Our first test is to vary the squeezing parameter and see if the simulation closely matches our data for the λ we expect following the calculations above. This is shown for three experimental runs at different values of λ in figure 6.18. As can be seen, the difference between simulated and experimental data is minimised at values of λ extracted from the measurement data. In other words, "the best values of λ to simulate our data are the same, within error, as the values measured independently. We conclude from this that the discrepancy between

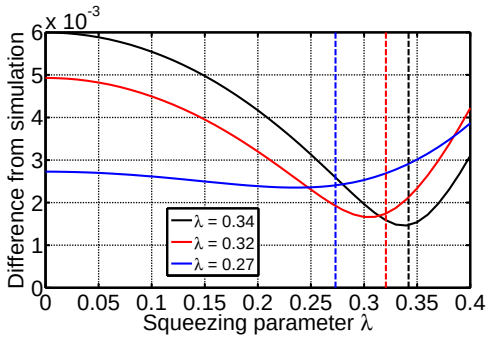


Figure 6.18: Difference between simulated and measured data as a function of squeezing parameter λ, for three different runs of the experiment. The dotted lines correspond to the value of λ extracted from the measured data. For each case, these match reasonably well with the value of λ in the simulated data that most closely approximate the experimental data.

simulated and measured data cannot be accounted for by an incorrect value of λ.

Modelling mixture

Our next test is to change the model of the state. Our assumption above is that the input state corresponds exactly to the TMSS described in Eq. (2.34), parameterised solely by λ. One naïve correction to this assumption is to introduce some fraction ϵ of vacuum into the state, such that it may be written

$$\rho = \epsilon|0\rangle\langle 0| + (1-\epsilon)\,\hat{\rho}_{\mathrm{TMSS}}\ . \tag{6.12}$$

This model accounts for mixing in the state that is not accounted for in the efficiencies of the detector, which are built into the POVM elements. By varying the fraction ϵ, we can again see which ϵ most closely resembles our experimental data. Note that in this case we fix λ to the experimentally extracted values. This is shown

in figure 6.19. The level of extra vacuum in the state, particularly for the experimen-

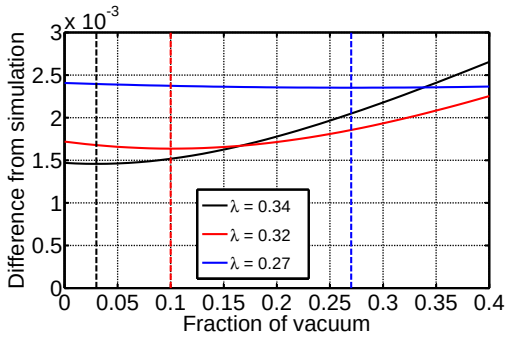


Figure 6.19: Difference between simulated and measured data as a function of the fraction of vacuum ϵ, for three different runs of the experiment. The dotted lines correspond to the value of ϵ that minimise the difference from simulation.

tal run at $\lambda = 0.34$, is low; most of the loss is already accounted for in the POVMs. Moreover, the dependence on the ϵ is smaller than λ in figure 6.18, indicating it is not a crucial parameter to be optimised in the simulation. However, the simulated data still generates a non-zero entanglement witness at these values.

6.4.4 Concluding remarks

To account fully for the disparity between measured and simulated data is a complex and involved task. Our initial attempts to shed some light on the problem, while inconclusive in themselves, indicate a route for further study. Figures of merit other than the Frobenius norm may be more insightful, particularly in absolute terms, but this method seemed to suggest that the simulations were accurate with respect to the two parameters we tried. Clearly, further models of states would need to be investigated to try and build a more accurate simulation. Indeed, to build the best input state for the simulation is to reconstruct precisely the experimental state

itself, which amounts to full state tomography.

However, trying to modify the simulation to match the data is not the aim of this experiment; the fact remains that a reliable entanglement witness using weak-field homodyne detection is yet to be demonstrated. By following the witness described by Puentes *et al.*[69], we have taken a "bottom-up" approach to an entanglement witness. That is to say, given the possible measurement settings of weak-field homodyne detectors, can a witness be constructed? The answer, theoretically and backed up by simulation appears to be an emphatic "yes." Unfortunately, this was not corroborated by the data.

At this point, one can only speculate as to why the experimental data did not confirm the simulations undertaken using the theoretical mode. Previous experimental results indicated that the setup generated states that were sufficient to carry out such an experiment. The non-local coherence results demonstrate quite clearly that any phase noise does not wash out the coherence between modes. Furthermore, these results show that photon counting errors in the state are largely Poissonian—there is no long-term additional technical effects such as drifting laser power that would otherwise cause additional noise in the joint statistics. If the problem arises from the reconstruction of the POVMs, then the simulated data should not witness entanglement using those same POVMs. And as discussed, the parameters used in those simulations are backed up by independent measurements.

Central to the approach taken by Puentes *et al.*[69] is its generality. However, this generality is a double-edged sword. By searching over all possible states that could

generate the data, it takes just a single state with no entanglement to cause the witness to return zero. Indeed, this may well be its downfall. The simulation considers the *same state* to generate data, and noise is added to the POVMs. However, the state used in the experiment will inevitably change subtly shot-to-shot. The average of the state may well be consistent with the simulation, but the way a noise in the state (rather than POVMs) propagates through the witness program may well allow a state with zero entanglement to be found and therefore no entanglement to be witnessed.

Despite the failure of the witness program, the results of using two-mode weak-field homodyne detection to show coherence are encouraging. Placing bounds on the visibilities of the two-mode coherence, given the marginal statistics, may be an alternative route to witnessing entanglement, although it may be more difficult to quantify. Further work taking this "top-down," empirical approach is ongoing.

Chapter 7

Conclusions and outlook

We conclude this thesis by summarising the results obtained in each chapter. We place them in the wider context of the entanglement distillation protocol and, more generally, a hybrid approach to continuous/discrete-variable quantum optics. We conclude with an outlook of the prospects for the protocol specifically, and the hybrid approach in general.

The overarching aim of this thesis was to investigate the experimental feasibility of the entanglement distillation protocol proposed by Browne *et al.*[25]. The problem of efficiently distributing entanglement across a wide area is predominantly technological. However, new physics arises from exploiting quantum mechanics to develop operations that perform useful tasks efficiently (with respect to time and energy). As quantum engineers, we imposed a number of practical specifications on our approach to distillation. Central to our strategy was using a pulsed source of entanglement. Knowing precisely when a probabilistic event has succeeded, and (perhaps more im-

portantly) when it hasn't, is crucial in both practical and theoretical terms. Not only is a pulsed source essential if many probabilistic events need to be synchronised in a larger scheme, but also the definition of a trial is fundamental to many tests of quantum mechanics[178]. While theoretically attractive, using ultrashort pulses, particularly in the high-power regime, poses some significant practical challenges. In addition, demonstrating an efficient entanglement measurement strategy—a CV entanglement witness—proved equally difficult. It appears that attempting to show an untested entanglement distillation protocol using an untested measurement strategy was highly ambitious and extremely challenging.

However, as we will summarise below, the results that did arise from this strategy were highly interesting in their own right, demonstrating physics with relevance far beyond the scope of entanglement distillation alone.

7.1 Summary of results

The work in this thesis can be summarised as an experimental and theoretical analysis of some of the major components of a continuous-variable entanglement distillation experiment in the pulsed regime. To that end, the broad approach taken in this work was to analyse continuous-variable quantum optics operations in a discrete-variable basis. Experiments with these operations have shown their applicability far beyond the remit of entanglement distillation.

In this section we will summarise the results and place them in the context of both entanglement distillation and their wider significance.

7.1.1 A practical analysis of probabilistic non-Gaussian operations

We began our investigation into experimental entanglement distillation by considering some of the practical limitations imposed on a probabilistic entanglement-enhancement operation. In chapter 3, we developed general figures of merit to account for the trade-off between success probability and increase in entanglement. We highlighted three single-photon-level non-Gaussian operations—photon subtraction, photon addition and photon replacement—and analysed each with respect to the figures of merit. As the most experimentally feasible approach, a more in-depth analysis of photon subtraction accounting for loss was carried out. We derived the optimal set of experimental parameters to show the largest increase in entanglement most often. Through this analysis, it was shown that the optimal parameters were well within the range of experimental feasibility.

While these results were highly relevant to our particular experiment, the approach taken and the figures of merit developed were very general, and could be readily applied to many probabilistic non-Gaussian operations.

7.1.2 Developing a pulsed source of two-mode squeezed states

In chapter 4 we detailed the experimental construction of our source of two-mode squeezed states (TMSS). This was the workhorse upon which the subsequent experiments were based. The source generated TMSSs with an estimated squeezing parameter $\lambda \lesssim 0.35$.

7.1.3 Single-mode measurement with weak-field homodyne detection

Having detailed the source of states we were able to produce, we then described the weak-field homodyne detector we used to measure them. This scheme combines photon number resolving detectors (through time-multiplexing) with phase referencing to provide both phase and amplitude information about quantum states.

Active phase stabilisation

Since this scheme requires phase stability, we detailed our active phase stabilisation scheme based on a Pound-Drever-Hall feedback loop. This reduced our phase noise to $\lesssim 5^\circ$ over many hours. In combination with a Berry-phase rotator setup, this level of stability at arbitrary phase was readily achieved.

This scheme is readily applied across many different experiments requiring phase stability. We have demonstrated in particular that, with a suitable ancillary beam wavelength and carefully-chosen optics, the method can be applied to interferometers containing wavelength-conversion elements and thus two colours. This is extremely useful in phase locking experiments containing many sources of pulsed quantum light based on frequency conversion.

Conditional state preparation with weak-field homodyne detection

In a demonstration of the versatility of weak-field homodyne detection, we showed how the setup could be used for probabilistic, heralded state generation. We de-

veloped a broad class of states—photon-catalysed optical coherent (PCOC) states, which, dependent on their interaction parameters, boast a range of non-classical properties. We showed theoretically how up to 2dB of squeezing could be generated based on measurement-induced non-linearity, as well as states approximating Schrödinger kitten states (coherent state superpositions).

The range of phenomena that can be produced with these states hint at their utility. Furthermore, the scheme can be readily extended in an iterative manner to produce even more exotic states. Finally, although not demonstrated experimentally, the phase-dependent projective measurement offered by the weak-field homodyne detector in this configuration suggests further investigation into non-Gaussian states using this scheme could well be fruitful.

Demonstration of sub-binomial light

The states generated above were extremely useful in demonstrating a novel feature of quantum light if it is measured by a multiplexed detector, namely sub-binomial light. The range of tunability offered by the PCOC states allows the response of a multiplexed detector—in our case a TMD—to be carefully analysed. We were able to demonstrate conclusively the proposal by Sperling, Vogel and Agarwal [152] that states exhibiting sub-Poissonian statistics in their photon-number distribution will show sub-binomial statistics in the click distribution when measured with a multiplexed detector. We were able to show this for a range of states, as well as showing inconsistencies when using the click-statistics directly to evaluate the

Mandel Q-parameter[159].

The direct experimental observation of the non-classicality of light fields is an important aspect of foundational studies and technological applications of quantum mechanics. Our technique provides a very compact and general method to classify multiphoton states with multiplexed detectors. This represents an unambiguous procedure for confirming "quantumness" than their indirect verification by deconvolving the action of a detector.

7.1.4 Two-mode weak-field homodyne detection

The final chapter dealt with applying weak-field homodyne detection across two modes of an entangled state. Using this scheme, we were able to show correlations in photon counts dependent on the joint phase of independent local oscillators. In general this phase dependence is a necessary feature of entanglement, although we do not derive conditions to show that demonstrating it is sufficient to witness an entangled state.

Instead, we attempted to show entanglement by using the witness developed by Puentes *et al.*[69]. However, despite encouraging results from the simulations, we did not witness any entanglement. We briefly analysed a number of possible improvements to our model, however there remained a discrepancy between simulated and measured data which allowed entanglement to be witnessed in the former but not the latter. The precise reason for this is still not certain, although we anticipate some problems arising from a noise source for which the simulations do not account.

While the particular witness we tried did not work, we remain confident that this two-mode weak-field detection strategy can be used to witness entanglement. The oscillations based on joint measurements shown in chapter 6 are characteristic of an entangled state; building a witness based on bounding the visibility of these fringes remains ongoing work.

Even if a witness cannot be found, the detector remains a highly interesting tool in quantum optics. It allows us to probe both wave- and particle-like behaviour of an entangled state simultaneously, combining two of the most counter-intuitive features of quantum mechanics. In terms of measurement, it is tomographically complete, allowing full state tomography to be carried out. Furthermore, as a phase-resolving non-Gaussian detector, it will allow a wide variety of non-Gaussian states to be synthesised by phase-dependent measurement-induced non-linearity.

7.2 Outlook

Distributing entanglement efficiently across long distances remains a major challenge in practical quantum communication. As a tool to mitigate losses in any realistic scheme, entanglement distillation will continue to play a role. However, the requirements of such schemes remain demanding[179]. The need for non-Gaussian states, which, in the absence of third-order non-linearities at the single-photon level, are impractical to generate deterministically. Maximising the associated probabilities and reducing how they scale in an iterative protocol are necessary next-steps to ensure the feasibility of entanglement distillation.

In general, our hybrid approach to quantum optics is fertile territory, bringing a phase dimension into the discrete variable picture, and embracing the wealth of exotic non-Gaussian states in the continuous-variable domain. Such states are not readily available in the laboratory, but they are necessary in a variety of complex quantum information protocols.

Looking at continuous-variables in the discrete but infinite photon-number basis strikes at the heart of wave-particle duality. Couple that with entanglement and one has a powerful set of tools and techniques to probe two of the most fundamental and counter-intuitive aspects of quantum theory. Future work in this direction is likely to prove extremely fruitful.

7.2.1 Integration on-chip

Current trends in optical implementations of quantum-enhanced protocols involve integrating quantum optical technology onto waveguide chips. This technology addresses many of the issues raised in CV quantum optics including losses, noise, phase stability and component density. Adapting a hybrid approach to quantum optics on-chip would enable a gamut of previously unfeasible CV experiments to become a reality. Many of these experiments require technology demonstrated in this thesis, including pulsed sources of squeezed states, measurement-induced non-linearity and single-photon-level phase-referenced photon counting.

Integrating these technologies on chip is very challenging, primarily due to a lack of suitable integrated sources and detectors in this regime. Recently, significant

progress has been made in both integrated CV sources[180] and detectors[181]. It is my firm belief that the future of CV quantum enhanced technology lies in integration and that it will be this approach that will enable the benefits of CV quantum optics to be exploited.

Appendix A

Position, momentum and ladder operators

In this appendix we relate the quantum harmonic oscillator model, in terms of position and momentum operators, to operators governing the raising and lowering of the energy of the oscillator.

A.1 Ladder operators

As stated in Chapter 2, the energy contained within a harmonic oscillator is found by solving the time-independent Schrödinger equation

$$\hat{H}|\psi_n\rangle = E_n|\psi_n\rangle \ , \tag{A.1}$$

where E_n are the quantised eigenenergies.

It is useful to define an annihilation operator $\hat{a}$ which reduces the energy by one quantum, such that

$$\hat{H}\hat{a}|\psi_n\rangle = E_{n-1}\hat{a}|\psi_n\rangle \ . \tag{A.2}$$

Furthermore, it is customary to choose eigenstates $|\psi_n\rangle = |n\rangle$, $n \in \mathbb{N}$ such that we may write

$$\hat{a}|n\rangle = c_n|n-1\rangle \ , \tag{A.3}$$

with c_n to be determined. We define $c_1 = 1$ and $c_0 = 0$ such that annihilating the first excited state $|1\rangle$ generates the ground state, i.e. $\hat{a}|1\rangle = |0\rangle$.

The Hermitian conjugate of the annihilation operator defines the creation operator $\hat{a}^\dagger$, with the corresponding equation

$$\begin{aligned} \langle n|\hat{a}^\dagger &= \langle n-1|c_n^* \ , \\ \Rightarrow \hat{a}^\dagger|n\rangle &= c_{n+1}^*|n+1\rangle \ . \end{aligned} \tag{A.4}$$

Combining these definitions yields

$$\langle n|\hat{a}^\dagger\hat{a}|n\rangle = |c_n^*|^2\langle n-1|n-1\rangle = |c_n^*| \ , \tag{A.5a}$$
$$\langle n|\hat{a}^\dagger\hat{a}|n\rangle = c_n\langle n|\hat{a}^\dagger|n-1\rangle = |c_n|^2\langle n|n\rangle = |c_n|^2 \ , \tag{A.5b}$$
$$\langle n|\hat{a}\hat{a}^\dagger|n\rangle = c_{n+1}^*\langle n|\hat{a}|n+1\rangle = |c_{n+1}|^2\langle n|n\rangle = |c_{n+1}|^2 \ , \tag{A.5c}$$

from which the commutator is calculated

$$\langle n|[\hat{a}, \hat{a}^\dagger]|n\rangle = \langle n|\hat{a}\hat{a}^\dagger|n\rangle - \langle n|\hat{a}^\dagger\hat{a}|n\rangle = |c_{n+1}|^2 - |c_n|^2 = k \ , \tag{A.6}$$

where k is a constant. In fact, because we are modelling a harmonic oscillator, we know that the energy between levels is independent of the level number, *i.e.* that k is independent of n. Therefore, $k = 1$ since $c_0 = 0$ and $c_1 = 1$ by definition. From the recurrence relation

$$|c_{n+1}|^2 = |c_n|^2 + 1 \ , \tag{A.7}$$

it is clear that $c_n = \sqrt{n}$ and therefore $c_{n+1} = \sqrt{n+1}$; substituting these into Eqs. (A.3) and (A.4) yield their standard definitions

$$\hat{a}|n\rangle = \sqrt{n}|n-1\rangle \tag{A.8a}$$
$$\hat{a}^\dagger|n\rangle = \sqrt{n+1}|n+1\rangle \ . \tag{A.8b}$$

From Eq. (A.5a), we can define the number operator $\hat{n} = \hat{a}^\dagger\hat{a}$ which satisfies the eigenvalue equation

$$\hat{n}|n\rangle = n|n\rangle \ . \tag{A.9}$$

The number operator $\hat{n}$ extracts the energy level of the oscillator, equivalent to the number of energy quanta it contains. This provides the link between the creation and annihilation operators and the Hamiltonian of the harmonic oscillator. It allows the Hamiltonian to be written

$$\hat{H} = \hbar\omega\left(\hat{n} + \frac{1}{2}\right) = \hbar\omega\left(\hat{a}^\dagger\hat{a} + \frac{1}{2}\right) \ , \tag{A.10}$$

such that

$$\hat{a}^\dagger\hat{a} = \frac{\hat{p}^2}{2m\hbar\omega} + \frac{m\omega\hat{x}^2}{2\hbar} + \frac{1}{2} \ . \tag{A.11}$$

A.2 Relating $\hat{a}, \hat{a}^\dagger$ with $\hat{x}, \hat{p}$

The ladder operators $\hat{a}$, $\hat{a}^\dagger$ are related to the position and momentum operators thus,

$$\hat{x} = \sqrt{\frac{\hbar}{2m\omega}}\left(\hat{a}^\dagger + \hat{a}\right) \ , \tag{A.12a}$$

$$\hat{p} = \mathrm{i}\sqrt{\frac{m\hbar\omega}{2}}\left(\hat{a}^\dagger - \hat{a}\right) \ , \tag{A.12b}$$

with commutator $[\hat{x}, \hat{p}] = \mathrm{i}\hbar$. This is consistent with the standard canonical operator definitions $\hat{x}$, $\hat{p} = -\mathrm{i}\hbar\frac{\partial}{\partial\hat{x}}$. Thus, from quantised, discrete eigenenergies n we have derived the continuous variables x and p. To write $\hat{a}$, $\hat{a}^\dagger$ in terms of $\hat{x}$, $\hat{p}$, we postulate the linear combination

$$\hat{a} = \alpha\hat{x} + \beta\hat{p} \ , \tag{A.13a}$$

$$\hat{a}^\dagger = \alpha^*\hat{x} + \beta^*\hat{p} \ , \tag{A.13b}$$

where α, β are to be determined and we use the fact that $\hat{x}$, $\hat{p}$ are Hermitian operators (satisfying $\hat{O}^\dagger = \hat{O}$) that represent observables. Using Eqs. (A.13) and (A.11), by equating coefficients we find

$$|\alpha|^2 = \frac{m\omega}{2\hbar} \ , \tag{A.14a}$$

$$|\beta|^2 = \frac{1}{2m\hbar\omega} \ , \tag{A.14b}$$

$$\alpha\beta^* = -\alpha^*\beta \ . \tag{A.14c}$$

Additionally, from the commutator $\left[\hat{a}, \hat{a}^\dagger\right] = 1$ it is readily shown that the commutator

$$[\hat{x}, \hat{p}] = \frac{1}{(\alpha\beta^* - \alpha^*\beta)} = \frac{1}{2\alpha\beta^*} \ , \tag{A.15}$$

Further manipulation yields the relation

$$\frac{|\alpha|^2}{|\beta|^2} = -\frac{\alpha^2}{\beta^2} \tag{A.16}$$

which, by direct substitution from Eqs. (A.14), determines that $\alpha = -im\omega\beta$. This result, combined with rearranging Eqs. (A.13), leads to the standard operator definitions and commutator

$$\hat{x} = \sqrt{\frac{\hbar}{2m\omega}}\left(\hat{a}^\dagger + \hat{a}\right) \ , \tag{A.17a}$$

$$\hat{p} = \mathrm{i}\sqrt{\frac{m\hbar\omega}{2}}\left(\hat{a}^\dagger - \hat{a}\right) \ , \tag{A.17b}$$

$$[\hat{x}, \hat{p}] = i\hbar \ , \tag{A.17c}$$

which is commensurate with the standard definitions $\hat{x}$, $\hat{p} = -\mathrm{i}\hbar\frac{\mathrm{d}}{\mathrm{d}\hat{x}}$. Thus, from quantised, discrete eigenenergies n we have derived the continuous variables x and p.

A.3 Relating position and momentum to quadrature operators

The quadrature operators $\hat{X}$ and $\hat{P}$ are the dimensionless equivalent of position and momentum $\hat{x}$ and $\hat{p}$. We therefore define

$$\hat{X} = \frac{\hat{x}}{\sqrt{\frac{\hbar}{m\omega}}} = \frac{1}{2}\left(\hat{a}^\dagger + \hat{a}\right) \ , \tag{A.18a}$$

$$\hat{P} = \frac{\hat{p}}{\sqrt{m\hbar\omega}} = \frac{\mathrm{i}}{2}\left(\hat{a}^\dagger - \hat{a}\right) \ , \tag{A.18b}$$

with commutator

$$\left[\hat{X}, \hat{P}\right] = \frac{\mathrm{i}}{2} \ . \tag{A.19}$$

Appendix B

Calculating quadrature expectation values and variances

The expectation value of an operator $\hat{O}$ acting on a general state $\hat{\rho}$ is

$$\langle \hat{O} \rangle = \mathrm{Tr}[\hat{O}\hat{\rho}] \ . \tag{B.1}$$

For pure states, this simplifies to $\langle \hat{O} \rangle = \langle \psi | \hat{O} | \psi \rangle$.

B.1 Single-mode quadratures

As a relevant example, we calculate $\langle \hat{X} \rangle$ and $\langle \hat{X}^2 \rangle$. Quadrature expectation values are readily calculated from the expectation values of the ladder operators:

$$\langle \hat{X} \rangle = \frac{1}{2} \left(\langle \hat{a}^\dagger \rangle + \langle \hat{a} \rangle \right) \ , \tag{B.2a}$$

$$\langle \hat{X^2} \rangle = \frac{1}{4} \left(\langle \hat{a}^{\dagger 2} \rangle + \langle \hat{a}^2 \rangle + 2\langle \hat{n} \rangle + 1 \right) \ , \tag{B.2b}$$

where in the expression for $\langle \hat{X} \rangle$ we have uses the commutator of $\hat{a}, \hat{a}^\dagger$ and the definition of the number operator $\hat{n}$.

For a state written in the form

$$|\psi\rangle = \sum_{n=0}^{\infty} c_n |n\rangle \ , \tag{B.3}$$

where c_n are the normalised coefficients, the expectation values of the ladder operators are calculated by

$$\langle \psi | \hat{a} | \psi \rangle = \sum_{n=0}^{\infty} c_n^* c_{n+1} \sqrt{n+1} \tag{B.4a}$$

$$\langle\psi|\hat{a}^\dagger|\psi\rangle = \sum_{n=0}^{\infty} c_{n+1}^* c_n \sqrt{n+1} \tag{B.4b}$$

$$\langle\psi|\hat{a}^2|\psi\rangle = \sum_{n=0}^{\infty} c_{n+2}^* c_n \sqrt{(n+2)(n+1)} \tag{B.4c}$$

$$\langle\psi|\hat{a}^{\dagger 2}|\psi\rangle = \sum_{n=0}^{\infty} c_n^* c_{n+2} \sqrt{(n+2)(n+1)} \tag{B.4d}$$

$$\langle\psi|\hat{n}|\psi\rangle = \langle\psi|\hat{a}^\dagger\hat{a}|\psi\rangle = \langle\psi|\hat{a}\hat{a}^\dagger|\psi\rangle - 1 = \sum_{n}^{\infty} n|c_n|^2. \tag{B.4e}$$

Thus $\langle\hat{X}\rangle$, $\langle\hat{X}^2\rangle$ are given by

$$\langle\hat{X}\rangle = \frac{1}{2}\sum_{n=0}^{\infty}\sqrt{n+1}\left(c_{n+1}^* c_n + c_n^* c_{n+1}\right), \tag{B.5a}$$

$$\langle\hat{X}^2\rangle = \frac{1}{4} + \frac{1}{4}\sum_{n=0}^{\infty}\left(2n|c_n|^2 + \sqrt{(n+2)(n+1)}\left(c_n^* c_{n+2} + c_{n+2}^* c_n\right)\right), \tag{B.5b}$$

and the equivalent expressions for $\langle\hat{P}\rangle$, $\langle\hat{P}^2\rangle$ are

$$\langle\hat{P}\rangle = \frac{1}{2}\sum_{n=0}^{\infty}\sqrt{n+1}\left(c_{n+1}^* c_n - c_n^* c_{n+1}\right), \tag{B.6a}$$

$$\langle\hat{P}^2\rangle = \frac{1}{4} + \frac{1}{4}\sum_{n=0}^{\infty}\left(2n|c_n|^2 - \sqrt{(n+2)(n+1)}\left(c_n^* c_{n+2} + c_{n+2}^* c_n\right)\right). \tag{B.6b}$$

From these definitions, one can calculate the quadrature variances

$$\langle(\Delta\hat{X})^2\rangle = \langle\hat{X}^2\rangle - \langle\hat{X}\rangle^2 \tag{B.7a}$$

$$= \frac{1}{4}\big(2\langle\hat{a}^\dagger\hat{a}\rangle + \langle\hat{a}^{\dagger 2}\rangle + \langle\hat{a}^2\rangle + 1 - \langle\hat{a}^\dagger\rangle^2 - \langle\hat{a}\rangle^2 - 2\langle\hat{a}\rangle\langle\hat{a^\dagger}\rangle\big)$$

$$= \frac{1}{4}\left(1 + 2\left(\langle\hat{a}^\dagger\hat{a}\rangle - \langle\hat{a}^\dagger\rangle\langle\hat{a}\rangle\right) + \langle(\Delta\hat{a}^\dagger)^2\rangle + \langle(\Delta\hat{a})^2\rangle\right) \tag{B.7b}$$

and

$$\langle(\Delta\hat{P})^2\rangle = \langle\hat{P}^2\rangle - \langle\hat{P}\rangle^2 \tag{B.8a}$$

$$= \frac{1}{4}\left(2\langle\hat{a}^\dagger\hat{a}\rangle - \langle\hat{a}^{\dagger 2}\rangle - \langle\hat{a}^2\rangle + 1 + \langle\hat{a}^\dagger\rangle^2 + \langle\hat{a}\rangle^2 - 2\langle\hat{a}^\dagger\rangle\langle\hat{a}\rangle\right)$$

$$= \frac{1}{4}\left(1 + 2\left(\langle\hat{a}^\dagger\hat{a}\rangle - \langle\hat{a}^\dagger\rangle\langle\hat{a}\rangle\right) - \langle(\Delta\hat{a}^\dagger)^2\rangle - \langle(\Delta\hat{a})^2\rangle\right), \tag{B.8b}$$

where $\langle(\Delta\hat{a}^\dagger)^2\rangle$, $\langle(\Delta\hat{a})^2\rangle$ are the variances of the ladder operators, although they have no physical underpinning (since $\hat{a}^\dagger$, $\hat{a}$ do not represent observables).

B.2 Two-mode quadratures

The two-mode superposition quadratures, Eq. (2.39a), are

$$\hat{\mathcal{X}} = \frac{1}{2^{\frac{3}{2}}}\left(\hat{a}_1^\dagger + \hat{a}_1 + \hat{a}_2^\dagger + \hat{a}_2\right) \tag{B.9a}$$

$$\hat{\mathcal{P}} = \frac{i}{2^{\frac{3}{2}}}\left(\hat{a}_1^\dagger - \hat{a}_1 + \hat{a}_2^\dagger - \hat{a}_2\right) \ . \tag{B.9b}$$

The variance in the two-mode $\hat{\mathcal{X}}$ quadrature is

$$\langle(\Delta\hat{\mathcal{X}})^2\rangle = \langle\hat{\mathcal{X}}^2\rangle \ , \tag{B.10}$$

since $\langle\psi|\hat{a}|\psi\rangle = \langle\psi|\hat{a}^\dagger|\psi\rangle = 0$. The expansion of $\langle\hat{\mathcal{X}}^2\rangle$ contains 16 terms. For a number correlated state of the form

$$|\psi\rangle = \sum_{n=0}^{\infty} c_n|n,n\rangle \ , \tag{B.11}$$

the non-zero terms in this expansion are of the form $\langle\hat{a}^\dagger a_i\hat{a}_j\rangle_{i\neq j}$, $\langle\hat{a}^\dagger a_i\hat{a}_i\rangle\delta_{ij}$, $i,j \in 1,2$, and their complex conjugates. This yields eight terms:

$$\langle\hat{\mathcal{X}}^2\rangle = \frac{1}{8}\big(\langle\hat{a}_1^\dagger\hat{a}_1\rangle + \langle\hat{a}_1^\dagger\hat{a}_2^\dagger\rangle + \langle\hat{a}_1\hat{a}_1^\dagger\rangle + \langle\hat{a}_1\hat{a}_2\rangle \tag{B.12a}$$

$$+ \langle\hat{a}_2^\dagger\hat{a}_1^\dagger\rangle + \langle\hat{a}_2^\dagger a_2\rangle + \langle\hat{a}_2\hat{a}_1\rangle + a_2\hat{a}_2^\dagger\big) \tag{B.12b}$$

$$= \frac{1}{8}\left(4\langle\hat{n}\rangle + 2\left(\langle\hat{a}_1^\dagger\hat{a}_2^\dagger\rangle + \langle\hat{a}_1\hat{a}_2\rangle\right) + 2\right) \tag{B.12c}$$

where we have used $\langle\hat{a}_1^\dagger\hat{a}_1\rangle = \langle\hat{a}_2^\dagger\hat{a}_2\rangle = \langle\hat{n}\rangle$ and the commutator $[\hat{a}_i,\hat{a}_j^\dagger] = \delta_{ij}$. These quantities are straightforward to calculate:

$$\langle n\rangle = \sum_{n=0}^{\infty}|c_n|^2 n \tag{B.13a}$$

$$\langle\hat{a}_1^\dagger\hat{a}_2^\dagger\rangle = \sum_{n=0}^{\infty} c_{n+1}^* c_n\,(n+1) \tag{B.13b}$$

$$\langle\hat{a}_1\hat{a}_2\rangle = \sum_{n=0}^{\infty} c_n^* c_{n+1}\,(n+1) \ . \tag{B.13c}$$

If the coefficients c_n are real, then $\langle\hat{a}_1^\dagger\hat{a}_2^\dagger\rangle = \langle\hat{a}_1\hat{a}_2\rangle$, such that

$$\langle\hat{\mathcal{X}}^2\rangle = \frac{1}{4}\left(2\left(\langle\hat{n}\rangle + \langle\hat{a}_1\hat{a}_2\rangle\right) + 1\right) \tag{B.14a}$$

$$= \frac{1}{4}\left(2\left(\sum_{n=0}^{\infty} n c_n^2 + \sum_{n=0}^{\infty} c_{n+1}c_n\,(n+1)\right)+1\right)\ . \tag{B.14b}$$

Similarly for $\langle(\Delta\hat{\mathcal{P}})^2\rangle = \langle\hat{\mathcal{P}}^2\rangle$:

$$\langle\hat{\mathcal{P}}^2\rangle = \frac{1}{4}\left(2\left(\langle\hat{n}\rangle - \langle\hat{a}_1\hat{a}_2\rangle\right)+1\right) \tag{B.15a}$$

$$= \frac{1}{4}\left(2\left(\sum_{n=0}^{\infty} n c_n^2 - \sum_{n=0}^{\infty} c_{n+1}c_n\,(n+1)\right)+1\right)\ . \tag{B.15b}$$

B.2.1 Excess variance

We define the excess variance $\Delta\text{Var} = \sqrt{\langle(\Delta\hat{\mathcal{X}})^2\rangle\langle(\Delta\hat{\mathcal{P}})^2\rangle - 16}$. This gives an indication of the Gaussian nature of pure states. The smaller the ΔVar, the closer the state is to being Gaussian.

B.2.2 Properties of common states

Using the relations above, we calculate the mean photon number $\bar{n} = \langle\hat{n}\rangle$, two-mode ladder operator expectations values $\langle\hat{a}_1^\dagger\hat{a}_2^\dagger\rangle = \langle\hat{a}_1\hat{a}_2\rangle$, and two-mode quadrature variances $\langle\Delta\hat{\mathcal{X}}\rangle$, $\langle\Delta\hat{\mathcal{P}}\rangle$.

Two-mode squeezed states $|\psi_{\mathbf{TMSS}}\rangle$

$$\langle n\rangle = \frac{\lambda^2}{1-\lambda^2} \tag{B.16a}$$

$$\langle\hat{a}_1^\dagger\hat{a}_2^\dagger\rangle = \langle\hat{a}_1\hat{a}_2\rangle = \frac{\lambda}{1-\lambda^2} \tag{B.16b}$$

$$\langle(\Delta\hat{\mathcal{X}})^2\rangle = \frac{1}{4}\left(\frac{1+\lambda}{1-\lambda}\right) \tag{B.16c}$$

$$\langle(\Delta\hat{\mathcal{P}})^2\rangle = \frac{1}{4}\left(\frac{1-\lambda}{1+\lambda}\right) \tag{B.16d}$$

The TMSS is clearly a minimum uncertainty state since $\sqrt{\langle\hat{\mathcal{X}}^2\rangle\langle\hat{\mathcal{P}}^2\rangle} = 1/4$.

Photon subtracted state $|\psi_{\mathbf{sub}}\rangle$

$$\langle\hat{n}\rangle = \frac{2T^4\lambda^2\left(2+T^4\lambda^2\right)}{1-T^8\lambda^4} \tag{B.17a}$$

$$\langle\hat{a}_1^\dagger\hat{a}_2^\dagger\rangle = \langle\hat{a}_1\hat{a}_2\rangle = \frac{2\lambda\left(T^2+2T^6\lambda^2\right)}{1-T^8\lambda^4} \tag{B.17b}$$

$$\langle(\Delta\hat{\mathcal{X}})^2\rangle = \frac{1}{4}\left(\frac{1+3T^2\lambda+5T^4\lambda^2+3T^6\lambda^3}{4-T^2\lambda+T^4\lambda^2-T^6\lambda^3}\right) \tag{B.17c}$$

$$\langle(\Delta\hat{\mathcal{P}})^2\rangle = \frac{1}{4}\left(\frac{1-3T^2\lambda+5T^4\lambda^2-3T^6\lambda^3}{1+T^2\lambda+T^4\lambda^2+T^6\lambda^3}\right) \tag{B.17d}$$

$$\Delta\mathrm{Var} = \frac{T^4\lambda^2}{\sqrt{2}\,(1+T^4\lambda^2)} \tag{B.17e}$$

Photon added state $|\psi_{\mathbf{add}}\rangle$

$$\langle\hat{n}\rangle = \frac{1+4T^4\lambda^2+T^8\lambda^4}{1-T^8\lambda^4} \tag{B.18a}$$

$$\langle\hat{a}_1^\dagger\hat{a}_2^\dagger\rangle = \langle\hat{a}_1\hat{a}_2\rangle = \frac{2T^2\lambda\left(2+T^4\lambda^2\right)}{1-T^8\lambda^4} \tag{B.18b}$$

$$\langle(\Delta\hat{\mathcal{X}})^2\rangle = \frac{1}{4}\left(\frac{3+5T^2\lambda+3T^4\lambda^2+T^6\lambda^3}{1-T^2\lambda+T^4\lambda^2-T^6\lambda^3}\right) \tag{B.18c}$$

$$\langle(\Delta\hat{\mathcal{P}})^2\rangle = \frac{1}{4}\left(\frac{3-5T^2\lambda+3T^4\lambda^2-T^6\lambda^3}{1+T^2\lambda+T^4\lambda^2+T^6\lambda^3}\right) \tag{B.18d}$$

$$\Delta\mathrm{Var} = \frac{1}{\sqrt{2}\,(1+T^4\lambda^2)^2} \tag{B.18e}$$

Single-mode photon replaced state $|\psi_{\mathbf{rep(1)}}\rangle$

$$\langle\hat{n}\rangle = \frac{\lambda^2\left(1+T^2\left\{\lambda^4-4\left[1-\lambda^2\right]+T^2\left[4+2\left(-4+T^2\right)\lambda^2\right]\right\}\right)}{(1-T^2\lambda^2)\left\{\lambda^2+T^2\left[1-\left(4-T^2\right)\lambda^2+\lambda^4\right]\right\}} \tag{B.19a}$$

$$\langle\hat{a}_1^\dagger\hat{a}_2^\dagger\rangle = \langle\hat{a}_1\hat{a}_2\rangle = \frac{T\lambda\left[4\lambda^2+T^4\lambda^2\left(4-\lambda^2\right)+2T^2\left(1-5\lambda^2+\lambda^4\right)-1\right]}{(1-T^2\lambda^2)\left\{\lambda^2+T^2\left[1+\left(T^2-4\right)\lambda^2+\lambda^4\right]\right\}} \tag{B.19b}$$

$$\langle(\Delta\hat{\mathcal{X}})^2\rangle = \frac{1}{4}\left(\frac{(1+T\lambda)\left[T^2-2T\left(1-T^2\right)\lambda+\left(3-8T^2+3T^4\right)\lambda^2+2T\left(1-T^2\right)\lambda^3+T^2\lambda^4\right]}{(1-T\lambda)\left\{\lambda^2+T^2\left[1-\left(4-T^2\right)\lambda^2+\lambda^4\right]\right\}}\right) \tag{B.19c}$$

$$\langle(\Delta\hat{\mathcal{P}})^2\rangle = \frac{1}{4}\left(\frac{(1+T\lambda)\left[T^2+2T\left(1-T^2\right)\lambda+\left(3-8T^2+3T^4\right)\lambda^2-2T\left(1-T^2\right)\lambda^3+T^2\lambda^4\right]}{(1-T\lambda)\left\{\lambda^2+T^2\left[1-\left(4-T^2\right)\lambda^2+\lambda^4\right]\right\}}\right) \tag{B.19d}$$

$$\Delta\mathrm{Var} = \frac{\left(1-T^2\right)^2\lambda^2}{\sqrt{2}\left\{\lambda^2+T^2\left[1+\left(T^2-4\right)\lambda^2+\lambda^4\right]\right\}} \tag{B.19e}$$

Double-mode photon replaced state $|\psi_{\mathbf{rep(2)}}\rangle$

Although analytically tractable, the expressions are too lengthy to reproduce here.

Appendix C

Calculating the log-negativity of a pure two mode squeezed state

The density matrix for a TMSS, with squeezing parameter λ (which we take to be real and positive), is

$$\hat{\rho} = \left(1 - |\lambda|^2\right) \sum_{n=0}^{\infty} \sum_{m=0}^{\infty} \lambda^n \lambda^m \left|n\right\rangle_s \left\langle m\right| \otimes \left|n\right\rangle_i \left\langle m\right| \ . \tag{C.1}$$

This has log-negativity, defined in Eq. (2.43),

$$E_N\left(\hat{\rho}\right) = \log_2 \left|\left|\hat{\rho}^{\Gamma}\right|\right|_1 \ , \tag{C.2}$$

found by taking the partial transpose (in this case with respect to mode i)

$$\hat{\rho}^{\Gamma} = \left(1 - |\lambda|^2\right) \sum_{n=0}^{\infty} \sum_{m=0}^{\infty} \lambda^n \lambda^m \left|n\right\rangle_s \left\langle m\right| \otimes \left|m\right\rangle_i \left\langle n\right| \ , \tag{C.3}$$

with the trace norm of this state, defined in section 2.3.4 as $||\hat{\rho}||_1 = \mathrm{Tr}[\sqrt{\hat{\rho}^{\dagger}\hat{\rho}}]$, given by

$$\begin{aligned}
\left|\left|\hat{\rho}^{\Gamma}\right|\right|_1 &= \mathrm{Tr}[\left(1 - |\lambda|^2\right) \sum_{n=0}^{\infty} \sum_{m=0}^{\infty} |\lambda|^n |\lambda|^m \left(\left|m\right\rangle_s \left\langle n\right| \otimes \left|n\right\rangle_i \left\langle m\right|\right) \left(\left|n\right\rangle_s \left\langle m\right| \otimes \left|m\right\rangle_i \left\langle n\right|\right)] \\
&= \mathrm{Tr}[\left(1 - \lambda^2\right) \sum_{n=0}^{\infty} \sum_{m=0}^{\infty} \lambda^n \lambda^m \left|m\right\rangle_s \left\langle m\right| \otimes \left|n\right\rangle_i \left\langle n\right|] \\
&= \left(1 - \lambda^2\right) \mathrm{Tr}[\sum_{m=0}^{\infty} \lambda^m \left|m\right\rangle_s \left\langle m\right| \otimes \sum_{n=0}^{\infty} \lambda^n \left|n\right\rangle_i \left\langle n\right|] \\
&= \left(1 - \lambda^2\right) \mathrm{Tr}[\sum_{m=0}^{\infty} \lambda^m \left|m\right\rangle_s \left\langle m\right|] \mathrm{Tr}[\sum_{n=0}^{\infty} \lambda^n \left|n\right\rangle_i \left\langle n\right|]
\end{aligned}$$

$$
\begin{aligned}
&= \left(1-\lambda^2\right)\sum_{m=0}^{\infty}\lambda^m\sum_{n=0}^{\infty}\lambda^n \\
&= \frac{\left(1-\lambda^2\right)}{\left(1-\lambda\right)^2} = \frac{1+\lambda}{1-\lambda}\,. \qquad \text{(C.4)}
\end{aligned}
$$

Taking the logarithm of this yields the log-negativity

$$E_N\left(\hat{\rho}\right) = \log_2\left(\frac{1+\lambda}{1-\lambda}\right)\,. \qquad \text{(C.5)}$$

Appendix D

Properties and calculations of photon-replaced states

In this appendix we present some of the calculations involved when dealing with photon-replaced states. For the replacement operation applied to a coherent state, we call these states photon-catalysed optical coherent (PCOC) states.

D.1 Single-mode states

The general expression for a k-photon PCOC state is

$$|\psi_{\mathrm{PCOC}}(k)\rangle = \mathcal{N}_{\alpha,T} \sum_{n=0}^{\infty} \frac{\alpha^n}{\sqrt{n!}} c_n(T,R,k)\,|n\rangle \ , \tag{D.1}$$

where the normalisation constant $\mathcal{N}_{\alpha,T}$ depends on the coherent state amplitude α and beam splitter transmissivity $T = \sqrt{1-R^2}$. The coefficients $c_n(T,R,k)$ are given by

$$c_n(T,R,k) = \sum_{j=0}^{\min(n,k)} \binom{n}{n-j} \binom{k}{j} (-1)^j\, T^{n+k-2j} R^{2j} \ , \tag{D.2}$$

such that the $k=1$ case reduces to

$$|\psi_{\mathrm{PCOC}}(1)\rangle = \mathcal{N}_{\alpha,T} \sum_{n=0}^{\infty} \frac{e^{-\alpha^2/2} T^{n-1} \left(T^2 - nR^2\right) \alpha^n}{\sqrt{n!}} \ , \tag{D.3}$$

which happens with probability

$$P_1 = \mathcal{N}_{\alpha,T}^{-2} = e^{R^2\alpha^2} \left[R^4\alpha^2 + T^2\left(R^2\alpha^2 - 1\right)^2\right] \ . \tag{D.4}$$

From the results in appendix B, the variances are given by

$$\Delta^2\hat{X} = \frac{3R^8\alpha^4 + T^4\left(1-R^2\alpha^2\right)^4}{4\left[R^4\alpha^2 + T^2\left(1-R^2\alpha^2\right)^2\right]^2} , \tag{D.5}$$

and

$$\Delta^2\hat{P} = \frac{1}{4} + \frac{R^4\alpha^2}{2\left[R^4\alpha^2 + T^2\left(1-R^2\alpha^2\right)^2\right]} . \tag{D.6}$$

D.2 Two-mode states

We consider the two-mode photon-replaced states

$$|\psi_{\text{rep}(1)}\rangle = \mathcal{N}_{\text{rep}(1)} \sum_{n=0}^{\infty} \sqrt{1-\lambda^2}\lambda^n T^{n-1}\left[T^2 - n\left(1-T^2\right)\right]|n,n\rangle , \tag{D.7a}$$

$$|\psi_{\text{rep}(2)}\rangle = \mathcal{N}_{\text{rep}(2)} \sum_{n-0}^{\infty} \sqrt{1-\lambda^2}\lambda^n T^{2(n-1)}\left[T^2 - n\left(1-T^2\right)\right]^2|n,n\rangle , \tag{D.7b}$$

where $|\psi_{\text{rep}(1)}\rangle$, $|\psi_{\text{rep}(2)}\rangle$ correspond to the states where a single photon is replaced in one or both modes of a two-mode squeezed state, respectively, and $\mathcal{N}_{\text{rep}(1)}$, $\mathcal{N}_{\text{rep}(2)}$ are the normalisation constants in each case.

D.2.1 Probability of photon-replacement

The success probabilities $P_{\text{rep}(j)} = \mathcal{N}^{-2}_{\text{rep}(j)}$ are given by

$$P_{\text{rep}(1)} = \frac{\left(1-\lambda^2\right)\left\{\lambda^2 + T^2\left[1 + \left(T^2-4\right)\lambda^2 + \lambda^4\right]\right\}}{\left(1-T^2\lambda^2\right)^3} , \tag{D.8a}$$

$$\begin{aligned} P_{\text{rep}(2)} = &\frac{(1-\lambda)(1+\lambda)}{\left(1-T^4\lambda^2\right)^5}\left[T^4 + \left(1 - 8T^2 + 24T^4 - 32T^6 + 11T^8\right)\lambda^2\right. \\ &+ T^4\left(11 - 56T^2 + 96T^4 - 56T^6 + 11T^8\right)\lambda^4 \\ &\left.+ T^8\left(11 - 32T^2 + 24T^4 - 8T^6 + T^8\right)\lambda^6 + T^{12}\lambda\right]^8 . \end{aligned} \tag{D.8b}$$

D.2.2 Entanglement of photon replacement

The log-negativity is calculated by $E_N(\hat{\rho}) = \log_2\left[\left(\sum_{n=0}^{\infty}|C_n|\right)^2\right]$. In the single-mode replaced state $|\psi_{\text{rep}(1)}\rangle$, for $0 \leq T \leq 1$, the only positive C_n is C_0. All $C_{n>0}$ are negative for the range $0 \leq T\sqrt{n/n+1}$, therefore the entanglement in this case

is

$$E_N\left(\hat{\rho}_{\mathrm{rep}(1)}\right) = \log_2\left[\left(C_0 - \sum_{n=1}^{\infty} C_n\right)^2\right]$$
$$= \frac{(1+T\lambda)^3\left\{\lambda + T\left[1+2T\lambda\left(T\lambda-2\right)\right]\right\}^2}{(1-T\lambda)\left\{\lambda^2 + T^2\left[1+\left(T^2-4\right)\lambda^2+\lambda^4\right]\right\}} \,. \tag{D.9a}$$

Calculating the entanglement in the case where photons are replaced in both modes $|\psi_{\mathrm{rep}(2)}\rangle$ requires no such tricks. In this case it is

$$E_N\left(\hat{\rho}_{\mathrm{rep}(2)}\right) = \log_2\left[\left(\sum_{n=0}^{\infty} C_n\right)^2\right]$$
$$= \left[\left(1+T^2\lambda\right)^5\left\{\lambda + T^2\left[1+\lambda\left(-4+T^2+\lambda\right)\right]\right\}^2\right]$$
$$\times\left\{\left[1-T^2\lambda\right]\left[T^4 + (1-8T^2+24T^4-32T^6+11T^8)\lambda^2\right.\right.$$
$$+ T^4\left(11-56T^2+96T^4-56T^6+11T^8\right)\lambda^4$$
$$\left.\left.+ T^8\left(11-32T^2+24T^4-8T^6+T^8\right)\lambda^6 + T^{12}\lambda^8\right]\right\}^{-1} \tag{D.10a}$$

D.2.3 Quadrature variance

The quadrature variance calculations can be found in section B.2.2, alongside the photon-subtracted and photon-added state calculations.

Appendix E

Hardware specifications

We used a variety of optical detector configurations, discussed in greater detail in chapters 5 and 6. All experiments culminated in photons coupled into single-mode fibre (SMF800), incident on avalanche photodiodes (APDs). Here, we concentrate on the hardware employed once the optical signal has been converted to an electrical one.

E.1 Avalanche photodiodes

The single-photon detectors used for all experiments present in this thesis used Perkin-Elmer AQRH avalanche photodiodes. These exhibit typical efficiencies of $\sim 50\%$ at the relevant wavelength of 830 nm, and dead times of 35 ns. They convert an optical signal to a 15 ns, 2.5 V TTL pulse, ready for the coincidence electronics. Dark counts in our system were typically $\sim$1000 cps (counts per second).

E.2 Coincidence counting electronics

For all experiments, measurements comprised many combinations of coincidence counts from APDs looking at different optical modes. These signals were processed in two ways: initially with NIM electronics and subsequently with a purpose-built FPGA (field-programmable gate array) board.

Both sets of counting apparatus were triggered using a clock pulse from a fast photodiode that used a pick-off mode from the pump laser. This provided a 250 kHz reference against which coincidence events could be correctly binned.

E.2.1 NIM

The NIM electronics comprised signal conditioning (TTL to NIM converters) time delays and coincidence board. We used typical coincidence windows of 3 ns. This cut out some of the uncorrelated dark counts from the APD, and any long-lived fluorescence arising in the optical setup. The desired coincidences between APDs were

then sent to a fast counter (National Instruments) and displayed using a Labview programme.

E.2.2 FPGA

The FPGA served the same purpose as the NIM logic, but in a much more streamlined manner. Coincidences and timing were all computer-controlled through a MATLAB programme, which also displayed and saved data.

Appendix F

Active phase stabilisation based on two modes

This appendix is a copy of the phase stabilisation paper by Jotzu *et al.*[128].

Abstract

We present a computer-based active interferometer stabilisation method that can be set to an arbitrary phase difference and does not rely on modulation of the interfering beams. The scheme utilises two orthogonal modes propagating through the interferometer with a constant phase difference between them to extract a common relative phase and generate a linear feedback signal. Switching times of 50 ms over a range of 0 to 6π radians at 632.8 nm are experimentally demonstrated. The relative interferometer phase can be stabilised up to several days to within $\pm 3°$.

F.1 Introduction

The ability to continuously adjust and stabilise the optical phase difference between two arms of an interferometer is of great importance to a wide range of applications including homodyne detection for quantum state tomography[46], phase-shift keying in optical telecommunications[182], phase-shifting interferometry[183], ultrafast pump-probe spectroscopy[184–186], interference-based optical lattices[187] and near-field scanning microscopy[188]. Previous approaches have typically relied on fringe-lock methods, in which a useful error signal can only be produced near integer multiples of $\pi/2$. These methods are prone to fringe skipping, where noise causes the phase lock circuit to hop to a neighboring interference fringe, a half wavelength away. In many applications the ability to continuously adjust the phase difference to an arbitrary value is required, and cannot be achieved with fringe-lock methods. Continuous relative phase locking has been previously accomplished in two ways. The first approach used frequency modulation of one of the interfering beams and detection at the fundamental and second harmonic frequencies[189]. This method, which

produces a sinusoidal error signal, is still susceptible to fringe skipping. Furthermore, the phase modulation requires specialised signal analysis and is undesirable when signal acquisition rates faster than the modulation frequency are necessary. More recently, a technique that utilises tilting of the beam in one arm of the interferometer and spatially resolved measurements at the output to create a linear error signal was introduced[190]. However, this scheme requires precise alignment and stabilisation of photodetector positioning, and suffers from chromatic aberrations of the glass wedge used for the tilt.

In this Letter, we present a general approach to phase control capable of stabilisation to an arbitrary phase setting by producing a linear error signal in the relative phase. The basic principle lies in utilizing two distinct optical modes passing through the interferometer with non-identical optical path length differences resulting in two phase offsets. The modes could consist of different transverse-spatial, temporal, frequency or polarisation modes depending upon the nature of the experiment and noise involved. Indeed, this mode multiplexing approach can be seen as the key physical principle behind previous schemes to continuous phase stabilisation, which utilised frequency[189], and spatial modes[190]. Both modes experience a common phase shift ϕ, and one mode undergoes an additional, but constant phase offset δ. Monitoring both modes at the output of the interferometer, with knowledge of the offset phase difference δ, enables an accurate linear estimation of the phase common to both, and thus stable feedback control over a continuous range of ϕ.

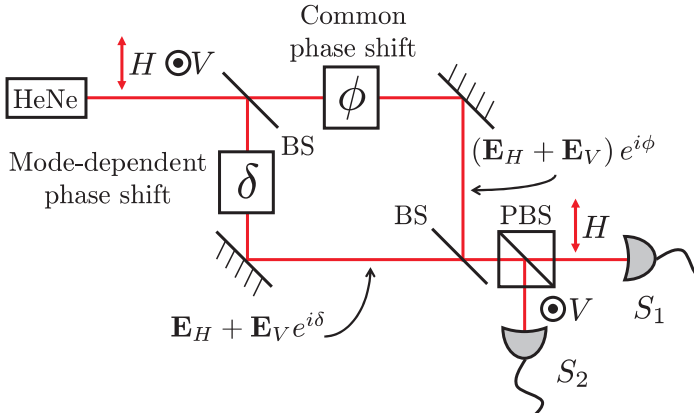


Figure F.1: Setup of our Mach-Zehnder interferometer (MZI) with two polarization modes. Both horizontal (H) and vertical (V) modes are subject to a controllable common phase ϕ, while one mode, V, picks up an additional phase δ in the lower branch of the MZI. The interference signals S_1 and S_2 of each mode are measured independently, from which the phase ϕ is calculated by software.

F.2 Continuous phase measurement using two modes

As a concrete example, consider two polarisation modes as depicted in Fig. F.1, similar to Refs.[191,192]. A reference laser in an equal superposition of horizontal and vertical polarisation is launched into a balanced Mach-Zehnder interferometer (MZI), constructed with non-polarising 50:50 beam splitters (BS). Both horizontal and vertical polarisations traverse the upper path containing a controllable phase ϕ. A wave plate in the lower path of the MZI produces a constant relative phase shift δ between the horizontal and vertical polarisation modes. The polarisation modes from one output port of the MZI are split by a polarising beam splitter (PBS), and directed to photodiode detectors. This scheme need not rely on polarisation and can be easily generalized to other modes, e.g. two transversely displaced co-propagating laser beams.

The output currents from the photodiodes are converted into voltages across resistors and monitored by a computer using a fast analog-to-digital converter (ADC). The signal voltages have the form

$$S_1 = A_1 \cos(\phi) + B_1, \quad S_2 = A_2 \cos(\phi + \delta) + B_2. \tag{F.1}$$

Here $A_{1(2)}$ and $B_{1(2)}$, which depend on the input intensity, interference visibility, detector gain, background light and electronic noise levels, are calibrated prior to stabilisation. These equations can be combined to estimate the common phase value

$$\phi = U\left\{\tan^{-1}\left[\frac{\cos(\delta)}{\sin(\delta)} - \frac{A_1(S_2 - B_2)}{A_2(S_1 - B_1)\sin(\delta)}\right]\right\}, \tag{F.2}$$

where the U is the phase unwrapping function. This estimate works accurately as long as the phase does not change by more than π, corresponding to a half wavelength path difference, within a sampling period. If ϕ_0 is the desired phase setting at which the interferometer is to be locked, the estimated phase in Eq. (F.2) can be used to implement a linear error signal to drive the feedback control of ϕ

$$err = -f(\phi - \phi_0), \tag{F.3}$$

where f is a constant feedback gain parameter.

F.3 Experimental setup

To experimentally test this phase stabilisation technique we used a Helium-Neon (HeNe) reference laser (JDS Uniphase 1125P, 5 mW average power) polarised at 45° with respect to the horizontal, as shown in Fig. F.1. The phase ϕ in the upper arm of the MZI is set by a computer controlled piezo-electric translation (PZT) stage (Thorlabs NF5DP20/M) delay line. A quarter wave plate (QWP) with vertically aligned slow axis sets the constant relative phase $\delta \approx 90°$ in the lower MZI arm. Note that a wide range of δ can be tolerated, so that a multi-order wave plate or

arbitrary birefringent medium could potentially be used. A PBS at one output of the MZI splits the horizontal and vertical polarisation modes, which are subsequently focused onto fast photodiodes (Thorlabs DET10A/M). The voltages produced by the photodiodes are monitored using a fast 16-bit analog-to-digital / digital-to-analog converter (AD/DAC) (National Instruments USB-6221 BNC) connected to a personal computer (PC) at a rate of 10 kHz. A software program calculates the error signal in Eq. (F.3), which is sent to the PZT stage using the AD/DAC.

F.3.1 Calibration

To implement the stabilization scheme the parameters $A_{1(2)}$, $B_{1(2)}$ and δ must first be calibrated. This is done by scanning the phase ϕ, and collecting the detector voltages. A parametric plot of $(S_1(\phi), S_2(\phi))$ as the phase ϕ is scanned sweeps out a rotated and displaced ellipse, as shown in Fig. F.2 (a). Fitting this ellipse to Eq. (F.1) directly yields the calibration parameters to be used in the phase stabilisation protocol. To obtain more accurate values of the feedback parameters, we repeated this process multiple times. As long as δ differs sufficiently from 0 and π, i.e. the ellipse does not become a line, successful stabilisation can be accomplished. Roughly speaking, the phase ϕ can be stabilized to within

$$\Delta\phi \geq \frac{\Delta P}{\bar{P}} \frac{1+\sqrt{2}}{2V|\sin(\delta/2)|}, \tag{F.4}$$

where $\bar{P}$ and ΔP are the average and standard deviation in the reference laser power, V is the fringe visibility for the two modes (assumed equal), and δ is the phase offset between the two modes. This can be derived from assuming the signal voltages are given by $S_1 = gP(1+V\cos(\phi))/2$ and $S_2 = gP(1+V\cos(\phi+\delta))/2$, where g is the detector gain, assumed to be equal for both detectors. This result puts quantitative bounds on the intensity fluctuation, fringe visibility, and offset phase that can be tolerated to yield phase stability within $\Delta\phi$.

F.3.2 Feedback

Once calibrated, the interferometer can be stabilised at a desired setting ϕ_0, by continuous monitoring of the phase ϕ and feedback to the control PZT stage on a ms timescale. The feedback voltage applied to the PZT, derived from Eq. (F.3), was $V_f = -f\langle\phi-\phi_0\rangle$, where the average was taken over previous measurements. The best stability was achieved with a feedback gain of $f = 3.65\,\mathrm{mV/degree}$. The optimal feedback function, that is, the relationship between error signal and the feedback control voltage, will generally depend on the details of the experiment [193].

The performance of our active feedback stabilisation scheme was limited primarily by power fluctuations of the reference laser and the feedback response time (i.e. the time delay between estimating the phase and the implementation of the feedback signal voltage). Power fluctuations can be eliminated by monitoring the input laser power and normalising the output data, or use of a more stable laser system.

The time lag was mainly due to the PC processing time and PZT response time, which varied between 4 ms and 7 ms. This implies high-frequency noise could not be compensated. This issue could be improved using faster AD/DAC electronics and lower-level programming to implement the phase estimation and feedback.

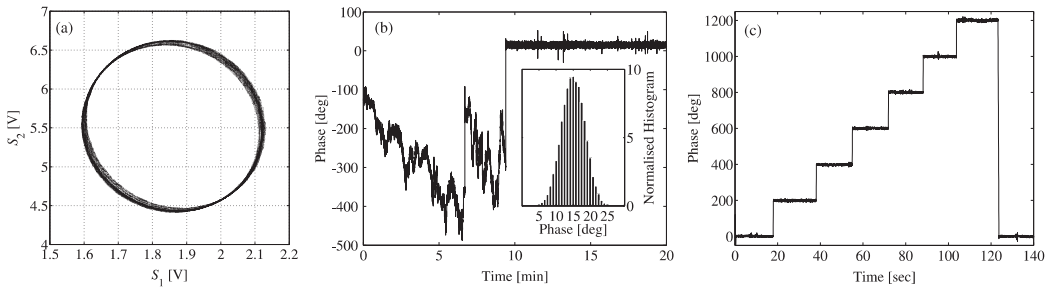


Figure F.2: (a) Parametric plot of $(S_1(\phi), S_2(\phi))$ when scanning the phase ϕ yields the calibration ellipse. By fitting the data, the values of the constants in Eq. (F.2) are determined. (b) After allowing the phase to fluctuate naturally for 10 minutes, the stabilizer is switched on to lock the phase at 15°. The root-mean-squared error in the locked phase is 3°, which can be maintained for over 24 hours. (c) The phase of the stabilizer can be arbitrarily set to any value within the range of the computer controlled delay stage. Here, we show phase locking to various phases from 0 to 6π radians.

F.4 Results

The results shown in Fig. F.2 (b) and (c) were achieved with calibration parameters $A_1 = 0.260$, $A_2 = 1.083$, $B_1 = 1.859$, $B_2 = 5.511$, and $\delta = 93.5°$. At what would be an unstable phase setting for fringe lock methods, $\phi_0 = 15°$, we are able to stabilise to within a standard deviation of $\Delta\phi \approx 3°$. This corresponds to length variations of approximately 5 nm between the two 3.5 m long arms of the interferometer. Given we have power fluctuations $\Delta P/\bar{P}$ of 0.6%, Eq. (F.4) yields phase fluctuations of 2.9°, which is in good agreement. This stability can be maintained for over 24 hours. Furthermore, the desired phase setting ϕ_0 can be changed in real time as shown in Fig. F.2 (c). Changing the phase setting ϕ_0 by more than 6π could be achieved with switching time near 50 ms, which is primarily limited by the feedback response time. The current scheme thus allows one to set and stabilise an interferometer to any optical path length difference with a precision of a few nanometers and a range limited only by the movement of the PZT stage (about 35 μm), and ultimately the coherence length of the reference laser.

F.5 Conclusion

In conclusion, we have shown a general approach to interferometric phase control capable of locking to any chosen phase value. Key elements in this scheme are precise measurement of an arbitrary relative phase and fast closed loop feedback. We use two orthogonal modes with known, fixed phase offset to obtain a precise estimate of the interferometer phase for arbitrary path length difference and implement high-speed analogue-to-digital, digital-to-analogue (AD-DAC) conversion for measurement and control. This enables highly accurate and long-term interferometer phase stability.

Depending upon the nature of the interferometer to be stabilised, in particular, considering the main sources of phase noise, choice of what degree of freedom to utilise can be made to optimise the stabilisation scheme. This general approach to phase stabilisation allows control under diverse noise conditions. Polarisation modes are extremely useful when there is little change in birefringence between the two interferometer arms as demonstrated here. Frequency modes could be used in optical fibre based interferometers where the dispersion is known. Improvements to the feedback electronics will likely lead to faster switching times and increased stability against higher-frequency noise. To increase the precision of this scheme requires improved stability or continuous monitoring of the reference laser, as eluded to in Eq. (F.4). Furthermore, implementing a more sophisticated feedback signal, e.g. using a proportional-integral-derivative (PID) control algorithm [193], should lead to improved performance. The techniques developed here should be of use for a wide range of applications due to the applicability of the stabilisation scheme to all optical degrees of freedom.

Appendix G

Weak-field homodyne state evolution

G.1 Split single photon

The initial state is given by

$$|\psi_{\text{in}}\rangle = |\psi_{\text{SSP}}\rangle \otimes |\alpha\rangle \otimes |\beta\rangle \ , \tag{G.1}$$

which describes a split single-photon state

$$|\psi_{\text{SSP}}\rangle = \frac{1}{\sqrt{2}}\left(|0,1\rangle + |1,0\rangle\right) = \frac{1}{\sqrt{2}}\left(\hat{b}^\dagger|0,0\rangle + \hat{a}^\dagger|0,0\rangle\right) \tag{G.2}$$

and two coherent states

$$|\alpha\rangle = e^{-|\alpha|^2/2}\sum_{n=0}^{\infty}\frac{|\alpha|^n e^{in\phi_1}}{\sqrt{n!}}|n\rangle = e^{-|\alpha|^2/2}\sum_{n=0}^{\infty}\frac{|\alpha|^n e^{in\phi_1}\hat{c}^{\dagger n}}{n!}|0\rangle \ , \tag{G.3a}$$

$$|\beta\rangle = e^{-|\beta|^2/2}\sum_{n=0}^{\infty}\frac{|\beta|^n e^{in\phi_2}}{\sqrt{n!}}|n\rangle = e^{-|\beta|^2/2}\sum_{n=0}^{\infty}\frac{|\beta|^n e^{in\phi_2}\hat{d}^{\dagger n}}{n!}|0\rangle \ . \tag{G.3b}$$

This state in Eq. (G.1) undergoes pair-wise interference at two beam splitters, such that the creation operators of each mode evolve according to

$$\hat{a}^\dagger \to T_A\hat{e}^\dagger - R_A\hat{f}^\dagger \tag{G.4a}$$

$$\hat{b}^\dagger \to T_B\hat{g}^\dagger - R_B\hat{h}^\dagger \tag{G.4b}$$

$$\hat{c}^\dagger \to T_A\hat{f}^\dagger + R_A\hat{e}^\dagger \tag{G.4c}$$

$$\hat{d}^\dagger \to T_B\hat{h}^\dagger + R_B\hat{g}^\dagger \tag{G.4d}$$

where the reflectivity and transmissivity of the beam splitter $A\,(B)$ are real and related by $R^2_{A(B)} + T^2_{A(B)} = 1$. We now consider the symmetric beam splitters such

that $T_A = T_B = T$ and therefore $R_A = R_B = R$. The state evolves according to the above transformations such that we can write in the number basis as follows:

$$|\psi_{\text{out}}\rangle = \sum_{n,n'=0}^{\infty} c\,(n, n\prime, T, R, \phi_1, \phi_2)\,(|A_{nn'kk'}\rangle + |B_{nn'kk'}\rangle + |C_{nn'kk'}\rangle + |D_{nn'kk'}\rangle)\ , \tag{G.5}$$

where the coefficients $c\,(n, n', T, R, \phi_1, \phi_2)$ are given by

$$c\left(n, n', T, R, \phi_1, \phi_2\right) = \frac{e^{-\frac{|\alpha|^2+|\beta|^2}{2}}}{\sqrt{2}} e^{\mathrm{i}(n\phi_1 + n'\phi_2)} \sum_{k,k'=0}^{n,n'} \frac{\alpha^n \beta^{n'} T^{k+k'} R^{n+n'-k-k'}}{\sqrt{(n-k)!k!\,(n'-k')!k'!}}\ . \tag{G.6}$$

and we have simplified the basis states by making the transformation

$$|A_{nn'kk'}\rangle = T\sqrt{n'-k'+1}|n-k\rangle_E \otimes |k\rangle_F \otimes |n'-k'+1\rangle_G \otimes |k'\rangle_H \tag{G.7}$$

$$|B_{nn'kk'}\rangle = T\sqrt{n-k+1}|n-k+1\rangle_E \otimes |k\rangle_F \otimes |n'-k'\rangle_G \otimes |k'\rangle_H \tag{G.8}$$

$$|C_{nn'kk'}\rangle = -R\sqrt{k'+1}|n-k\rangle_E \otimes |k\rangle_F \otimes |n'-k'\rangle_G \otimes |k'+1\rangle_H \tag{G.9}$$

$$|D_{nn'kk'}\rangle = -R\sqrt{k+1}|n-k\rangle_E \otimes |k+1\rangle_F \otimes |n'-k'\rangle_G \otimes |k'\rangle_H\ , \tag{G.10}$$

such that the density matrix $\hat{\rho}$ can be written

$$\begin{aligned}\hat{\rho}_{\text{out}} = \sum_{n,n',\tilde{n},\tilde{n}'=0}^{\infty} & c\left(n, n', T, R, \phi_1, \phi_2\right) c^*\left(n^*, n'^*, T, R, \phi_1, \phi_2\right) \\ & \big(|A_{nn'kk'}\rangle\langle A_{\tilde{n}\tilde{n}'\tilde{k}\tilde{k}'}| + |A_{nn'kk'}\rangle\langle B_{\tilde{n}\tilde{n}'\tilde{k}\tilde{k}'}| + |A_{nn'kk'}\rangle\langle C_{\tilde{n}\tilde{n}'\tilde{k}\tilde{k}'}| + |A_{nn'kk'}\rangle\langle D_{\tilde{n}\tilde{n}'\tilde{k}\tilde{k}'}| \\ & + |B_{nn'kk'}\rangle\langle A_{\tilde{n}\tilde{n}'\tilde{k}\tilde{k}'}| + |B_{nn'kk'}\rangle\langle B_{\tilde{n}\tilde{n}'\tilde{k}\tilde{k}'}| + |B_{nn'kk'}\rangle\langle C_{\tilde{n}\tilde{n}'\tilde{k}\tilde{k}'}| + |B_{nn'kk'}\rangle\langle D_{\tilde{n}\tilde{n}'\tilde{k}\tilde{k}'}| \\ & + |C_{nn'kk'}\rangle\langle A_{\tilde{n}\tilde{n}'\tilde{k}\tilde{k}'}| + |C_{nn'kk'}\rangle\langle B_{\tilde{n}\tilde{n}'\tilde{k}\tilde{k}'}| + |C_{nn'kk'}\rangle\langle C_{\tilde{n}\tilde{n}'\tilde{k}\tilde{k}'}| + |C_{nn'kk'}\rangle\langle D_{\tilde{n}\tilde{n}'\tilde{k}\tilde{k}'}| \\ & + |D_{nn'kk'}\rangle\langle A_{\tilde{n}\tilde{n}'\tilde{k}\tilde{k}'}| + |D_{nn'kk'}\rangle\langle B_{\tilde{n}\tilde{n}'\tilde{k}\tilde{k}'}| + |D_{nn'kk'}\rangle\langle C_{\tilde{n}\tilde{n}'\tilde{k}\tilde{k}'}| + |D_{nn'kk'}\rangle\langle D_{\tilde{n}\tilde{n}'\tilde{k}\tilde{k}'}|\big)\ ,\end{aligned} \tag{G.11}$$

whereby c^* is the complex conjugate of c, indicating that the indices n, n', k, k' become $\tilde{n}, \tilde{n}', \tilde{k}, \tilde{k}'$.

In our detector, we probe only modes E and G, therefore we must trace out modes F, H. This results in delta functions in the expression of the reduced density matrix $\hat{\rho}_{E,G} = \mathrm{Tr}[\hat{\rho}_{\text{out}}]_{F,H}$, given by

$$\hat{\rho}_{\text{out}} = \sum_{n,n',\tilde{n},\tilde{n}'=0}^{\infty} c\left(n, n', T, R, \phi_1, \phi_2\right) c^*\left(\tilde{n}, \tilde{n}', T, R, \phi_1, \phi_2\right) \sum_{i,j} |\psi_{inn'kk'}\rangle\langle\psi_{j\tilde{n}\tilde{n}'\tilde{k}\tilde{k}'}| \tag{G.12}$$

where $|\psi_{inn'kk'}\rangle$ are the basis states $\{|A\rangle \ldots |D\rangle\}$. Their contributions to the density

matrix is explicitly given by

$$\begin{aligned}\sum_{i,j}|\psi_i\rangle\langle\psi_j| =&|A_{nn'kk'}\rangle\langle A_{\tilde{n}\tilde{n}'\tilde{k}\tilde{k}'}|\delta_{k,\tilde{k}}\delta_{k,\tilde{k}'}+|A_{nn'kk'}\rangle\langle B_{\tilde{n}\tilde{n}'\tilde{k}\tilde{k}'}|\delta_{k,\tilde{k}}\delta_{k',\tilde{k}'}\\&+|A_{nn'kk'}\rangle\langle C_{\tilde{n}\tilde{n}'\tilde{k}\tilde{k}'}|\delta_{k,\tilde{k}}\delta_{k',\tilde{k}'+1}+|A_{nn'kk'}\rangle\langle D_{\tilde{n}\tilde{n}'\tilde{k}\tilde{k}'}|\delta_{k,\tilde{k}+1}\delta_{k',\tilde{k}'}\\&+|B_{nn'kk'}\rangle\langle A_{\tilde{n}\tilde{n}'\tilde{k}\tilde{k}'}|\delta_{k,\tilde{k}}\delta_{k',\tilde{k}'}+|B_{nn'kk'}\rangle\langle B_{\tilde{n}\tilde{n}'\tilde{k}\tilde{k}'}|\delta_{k,\tilde{k}}\delta_{k',\tilde{k}'}\\&+|B_{nn'kk'}\rangle\langle C_{\tilde{n}\tilde{n}'\tilde{k}\tilde{k}'}|\delta_{k,\tilde{k}}\delta_{k',\tilde{k}'+1}+|B_{nn'kk'}\rangle\langle D_{\tilde{n}\tilde{n}'\tilde{k}\tilde{k}'}|\delta_{k,\tilde{k}+1}\delta_{k',\tilde{k}'}\\&+|C_{nn'kk'}\rangle\langle A_{\tilde{n}\tilde{n}'\tilde{k}\tilde{k}'}|\delta_{k,\tilde{k}}\delta_{k'+1,\tilde{k}'}+|C_{nn'kk'}\rangle\langle B_{\tilde{n}\tilde{n}'\tilde{k}\tilde{k}'}|\delta_{k,\tilde{k}}\delta_{k'+1,\tilde{k}'}\\&+|C_{nn'kk'}\rangle\langle C_{\tilde{n}\tilde{n}'\tilde{k}\tilde{k}'}|\delta_{k,\tilde{k}}\delta_{k',\tilde{k}'}+|C_{nn'kk'}\rangle\langle D_{\tilde{n}\tilde{n}'\tilde{k}\tilde{k}'}|\delta_{k,\tilde{k}+1}\delta_{k'+1,\tilde{k}'}\\&+|D_{nn'kk'}\rangle\langle A_{\tilde{n}\tilde{n}'\tilde{k}\tilde{k}'}|\delta_{k+1,\tilde{k}}\delta_{k',\tilde{k}'}+|D_{nn'kk'}\rangle\langle B_{\tilde{n}\tilde{n}'\tilde{k}\tilde{k}'}|\delta_{k+1,\tilde{k}}\delta_{k',\tilde{k}'}\\&+|D_{nn'kk'}\rangle\langle C_{\tilde{n}\tilde{n}'\tilde{k}\tilde{k}'}|\delta_{k+1,\tilde{k}}\delta_{k',\tilde{k}'+1}+|D_{nn'kk'}\rangle\langle D_{\tilde{n}\tilde{n}'\tilde{k}\tilde{k}'}|\delta_{k,\tilde{k}}\delta_{k',\tilde{k}'}\ ,\end{aligned}\tag{G.13}$$

where $|X_{nn'kk'}\rangle\langle Y_{\tilde{n}\tilde{n}'\tilde{k}\tilde{k}'}|$ is the reduced state vector corresponding to modes E, G (whereby X, Y are all 16 combinations of A, B, C, D). From this expression, the probability of any combination of photon numbers in each mode may be calculated.

G.1.1 Probabilities

We will calculate the probabilities $P_{i,j}$ of photon number combinations up to $i = 0, 1, 2; j = 0, 1, 2$. Projecting onto specific photon numbers in each mode has the effect of putting more delta functions on the terms above. The resulting set of constraints on $\tilde{n}, \tilde{n}', k, k'$ can be grouped in similar terms, namely

$$\{|A\rangle\langle A|, |A\rangle\langle C|\} \propto |n-k\rangle\langle\tilde{n}-k| \otimes |n'+k'+1\rangle\langle\tilde{n}'+k'+1| \Rightarrow ① \tag{G.14a}$$
$$\{|A\rangle\langle B|, |A\rangle\langle D|\} \propto |n-k\rangle\langle\tilde{n}-k+1| \otimes |n'+k'+1\rangle\langle\tilde{n}'+k'| \Rightarrow ② \tag{G.14b}$$
$$\{|B\rangle\langle A|, |B\rangle\langle C|\} \propto |n-k+1\rangle\langle\tilde{n}-k| \otimes |n'+k'\rangle\langle\tilde{n}'+k'+1| \Rightarrow ③ \tag{G.14c}$$
$$\{|B\rangle\langle B|, |B\rangle\langle D|\} \propto |n-k+1\rangle\langle\tilde{n}-k+1| \otimes |n'+k'\rangle\langle\tilde{n}'+k'| \Rightarrow ④ \tag{G.14d}$$
$$\{|C\rangle\langle A|, |C\rangle\langle C|, |D\rangle\langle B|, |D\rangle\langle D|\} \propto |n-k\rangle\langle\tilde{n}-k| \otimes |n'+k'\rangle\langle\tilde{n}'+k'| \Rightarrow ⑤ \tag{G.14e}$$
$$\{|C\rangle\langle B|, |C\rangle\langle D|\} \propto |n-k\rangle\langle\tilde{n}-k+1| \otimes |n'+k'\rangle\langle\tilde{n}'+k'-1| \Rightarrow ⑥ \tag{G.14f}$$
$$\{|D\rangle\langle A|, |D\rangle\langle C|\} \propto |n-k\rangle\langle\tilde{n}-k-1| \otimes |n'+k'\rangle\langle\tilde{n}'+k'+1| \Rightarrow ⑦ \tag{G.14g}$$

where we have dropped the indices $|X_{nn'kk'}\rangle\langle Y_{\tilde{n}\tilde{n}'\tilde{k}\tilde{k}'}| = |X\rangle\langle Y|$ for brevity.

Projection onto specific photon numbers mean only specific terms of the expansion are kept, as the enforced by the delta functions. This sets specific values for $\tilde{n},\ \tilde{n}',\ k,\ k'$ in Eq. (G.12). For each of the 7 cases in Eq. (G.14), and for measuring

i photons in one mode and j in the other, we show a table of the specific values:

	$\tilde{n}$	$\tilde{n}'$	k	k'
①	n	n'	$n-i$	$n'+1-j$
②	$n-1$	$n'+1$	$n-i$	$n'+1-j$
③	$n+1$	$n'-1$	$n+1-i$	$n'-j$
④	n	n'	$n+1-i$	$n'-j$
⑤	n	n'	$n-i$	$n'-j$
⑥	$n-1$	$n'+1$	$n-i$	$n'-j$
⑦	$n+1$	$n'-1$	$n-i$	$n'-j$

(G.15)

For example, the values of $|C\rangle\langle D|_{EG}$ when projecting onto $(i,j)=(2,1)$ are: $\tilde{n}\to n-1$, $\tilde{n}'\to n'+1$, $k\to n-2$ and $k'\to n'-1$, since $|C\rangle\langle D|_{EG}$ belongs to case ⑥.

The resulting summations over n, n' are (perhaps surprisingly) analytically tractable, meaning all probabilities can be expressed in analytic form as follows:

$$P_{0,0}=\frac{e^{-R^2\left(|\alpha|^2+|\beta|^2\right)}}{2}R^2\left[2+T^2\left(|\alpha|^2+|\beta|^2\right)+2T^2|\alpha||\beta|\cos\left(\phi_2-\phi_1\right)\right] \tag{G.16a}$$

$$\begin{aligned}P_{1,1}=&\frac{e^{-R^2\left(|\alpha|^2+|\beta|^2\right)}}{2}R^2\Big[T^2\left(|\beta|^2+\alpha^2\left\{1-R^2|\beta|^2\left[4-R^2\left(|\alpha|^2+|\beta|^2\right)\right]\right\}\right)\\&+2R^4|\alpha|^2|\beta|^2+2T^2|\alpha||\beta|\left(1-R^2|\alpha|^2\right)\left(1-R^2|\beta|^2\right)\cos\left(\phi_2-\phi_1\right)\Big]\end{aligned} \tag{G.16b}$$

$$\begin{aligned}P_{2,2}=&\frac{e^{-R^2\left(|\alpha|^2+|\beta|^2\right)}}{8}R^6|\alpha|^2|\beta|^2\big[2R^4|\alpha|^2|\beta|^2\\&+T^2\left(4|\beta|^2+|\alpha|^2\left\{4-R^2|\beta|^2\left[8-R^2\left(|\alpha|^2+|\beta|^2\right)\right]\right\}\right)\\&+2T^2|\alpha||\beta|\left(2-R^2|\alpha|^2\right)\left(2-R^2|\beta|^2\right)\cos\left(\phi_2-\phi_1\right)\big]\end{aligned} \tag{G.16c}$$

$$P_{1,0}=P_{0,1}\left(\alpha\leftrightarrows\beta\right)=\frac{e^{-R^2\left(|\alpha|^2+|\beta|^2\right)}}{2}\Big\{2R^4|\alpha|^2+T^2\left[\left(1-R^2|\alpha|^2\right)^2+R^4|\alpha|^2|\beta|^2\right] \tag{G.16d}$$

$$-2R^2T^2|\alpha||\beta|\left(1-R^2|\alpha|^2\right)\cos\left(\phi_2-\phi_1\right)\Big\} \tag{G.16e}$$

$$P\left(2,0\right)=P_{0,2}\left(\alpha\leftrightarrows\beta\right)=\frac{e^{-R^2\left(|\alpha|^2+|\beta|^2\right)}}{4}R^2|\alpha|^2\Big\{2R^4|\alpha|^2+T^2\left[\left(2-R^2|\alpha|^2\right)^2+R^4|\alpha|^2|\beta|^2\right] \tag{G.16f}$$

$$-2R^2T^2|\alpha||\beta|\left(2-R^2|\alpha|^2\right)\cos\left(\phi_2-\phi_1\right)\Big\}$$

$$P\left(2,1\right)=P_{1,2}\left(\alpha\leftrightarrows\beta\right)=\frac{e^{-R^2\left(|\alpha|^2+|\beta|^2\right)}}{4}R^4|\alpha|^2\Big[2R^4|\alpha|^2|\beta|^2$$

$$+ T^2\left(4|\beta|^2 + |\alpha|^2\left\{1 - R^2|\beta|^2\left[6 - R^2\left(|\alpha|^2 + |\beta|^2\right)\right]\right\}\right)$$
$$+ 2T^2|\alpha||\beta|\left(2 - R^2|\alpha|^2\right)\left(1 - R^2|\beta|^2\right)\cos\left(\phi_2 - \phi_1\right)\Bigg] \tag{G.16g}$$

where $\alpha \leftrightarrows \beta$ denotes that α is replaced by β, and vice versa, in the expression.

G.2 Parametric down-conversion

We now carry out the same calculation for the state following parametric down-conversion. The initial state is

$$|\psi_{\text{in}}\rangle = |\psi_{\text{PDC}}\rangle \otimes |\alpha\rangle \otimes |\beta\rangle \ , \tag{G.17}$$

where the $|\alpha\rangle$, $|\beta\rangle$ are the same coherent states as above, and we approximate $|\psi_{\text{PDC}}\rangle \approx \left(|0,0\rangle + \lambda|1,1\rangle\right)/\sqrt{1+\lambda^2}$. Making this approximation allows us to take the same approach as above, and arrive at analytical forms for the photon number probabilities. The state is evolved using the same beam splitter unitaries as above, such that the final state becomes

$$|\psi_{\text{out}}\rangle = \sum_{n,n'=0}^{\infty} c\left(n,n',T,R,\phi_1,\phi_2,\lambda\right)\left(|A_{nn'kk'}\rangle + |B_{nn'kk'}\rangle + |C_{nn'kk'}\rangle + |D_{nn'kk'}\rangle + |E_{nn'kk'}\rangle\right) \ , \tag{G.18}$$

where the coefficients $c\left(n,n',T,R,\phi_1,\phi_2,\lambda\right)$, now depending on an additional parameter λ, are given by

$$c\left(n,n',T,R,\phi_1,\phi_2,\lambda\right) = \frac{e^{-\frac{|\alpha|^2+|\beta|^2}{2}}}{\sqrt{1+\lambda^2}} e^{i(n\phi_1 + n'\phi_2)} \sum_{k,k'=0}^{n,n'} \frac{\alpha^n \beta^{n'} T^{k+k'} R^{n+n'-k-k'} \left(-1\right)^{n+n'-k-k'} \lambda}{\sqrt{(n-k)!k!\left(n'-k'\right)!k'!}} \ . \tag{G.19}$$

and the basis states are as follows:

$$|A_{nn'kk'}\rangle = \lambda^{-1}|n-k, k-n'-k', k'\rangle \tag{G.20a}$$
$$|B_{nn'kk'}\rangle = T^2\sqrt{(n-k+1)\left(n'-k'+1\right)}|n-k+1, k, n'-k'+1, k'\rangle \tag{G.20b}$$
$$|C_{nn'kk'}\rangle = RT\sqrt{(k+1)\left(n'-k'+1\right)}|n-k, k+1, n'-k'+1, k'\rangle \tag{G.20c}$$
$$|D_{nn'kk'}\rangle = RT\sqrt{(n-k+1)\left(k'+1\right)}|n-k+1, k, n'-k', k'+1\rangle \tag{G.20d}$$
$$|E_{nn'kk'}\rangle = R^2\sqrt{(k+1)\left(k'+1\right)}|n-k, k+1, n'-k', k'+1\rangle \ . \tag{G.20e}$$

Thus, when calculating the density matrix $\hat{\rho} = |\psi_{\text{out}}\rangle\langle\psi_{\text{out}}|$, there are 25 terms. When tracing out the two undetected modes, each of these terms picks up a pair of delta functions, imposing constraints on values of $\tilde{k}$ and $\tilde{k}'$, as in the split single-

photon case. These delta functions are summarised in the table below:

	$\langle A_{\tilde{n}\tilde{n}'\tilde{k}\tilde{k}'}\|$	$\langle B_{\tilde{n}\tilde{n}'\tilde{k}\tilde{k}'}\|$	$\langle C_{\tilde{n}\tilde{n}'\tilde{k}\tilde{k}'}\|$	$\langle D_{\tilde{n}\tilde{n}'\tilde{k}\tilde{k}'}\|$	$\langle E_{\tilde{n}\tilde{n}'\tilde{k}\tilde{k}'}\|$
$\|A_{nn'kk'}\rangle$	$\delta_{k,\tilde{k}}\delta_{k',\tilde{k}'}$	$\delta_{k,\tilde{k}}\delta_{k',\tilde{k}'}$	$\delta_{k,\tilde{k}+1}\delta_{k',\tilde{k}'}$	$\delta_{k,\tilde{k}}\delta_{k',\tilde{k}'+1}$	$\delta_{k,\tilde{k}+1}\delta_{k',\tilde{k}'+1}$
$\|B_{nn'kk'}\rangle$	$\delta_{k,\tilde{k}}\delta_{k',\tilde{k}'}$	$\delta_{k,\tilde{k}}\delta_{k',\tilde{k}'}$	$\delta_{k,\tilde{k}+1}\delta_{k',\tilde{k}'}$	$\delta_{k,\tilde{k}}\delta_{k',\tilde{k}'+1}$	$\delta_{k,\tilde{k}+1}\delta_{k',\tilde{k}'+1}$
$\|C_{nn'kk'}\rangle$	$\delta_{k,\tilde{k}-1}\delta_{k',\tilde{k}'}$	$\delta_{k,\tilde{k}-1}\delta_{k',\tilde{k}'}$	$\delta_{k,\tilde{k}}\delta_{k',\tilde{k}'}$	$\delta_{k,\tilde{k}-1}\delta_{k',\tilde{k}'+1}$	$\delta_{k,\tilde{k}}\delta_{k',\tilde{k}'+1}$
$\|D_{nn'kk'}\rangle$	$\delta_{k,\tilde{k}}\delta_{k',\tilde{k}'-1}$	$\delta_{k,\tilde{k}}\delta_{k',\tilde{k}'-1}$	$\delta_{k,\tilde{k}+1}\delta_{k',\tilde{k}'-1}$	$\delta_{k,\tilde{k}}\delta_{k',\tilde{k}'}$	$\delta_{k,\tilde{k}+1}\delta_{k',\tilde{k}'}$
$\|E_{nn'kk'}\rangle$	$\delta_{k,\tilde{k}-1}\delta_{k',\tilde{k}'-1}$	$\delta_{k,\tilde{k}-1}\delta_{k',\tilde{k}'-1}$	$\delta_{k,\tilde{k}}\delta_{k',\tilde{k}'-1}$	$\delta_{k,\tilde{k}-1}\delta_{k',\tilde{k}'}$	$\delta_{k,\tilde{k}}\delta_{k',\tilde{k}'}$

(G.21)

Applying these delta functions to the number terms in the basis states leads to nine different basis states of the reduced density matrix, given by

$$\left\{ \begin{array}{l} |A\rangle\langle A|, |E\rangle\langle B|, \\ |E\rangle\langle C|, |E\rangle\langle D|, |E\rangle\langle E| \end{array} \right\} \propto |n-k\rangle\langle\tilde{n}-k| \otimes |n'-k'\rangle\langle\tilde{n}'-k'| \text{ ①} \tag{G.22a}$$

$$\left\{ \begin{array}{l} |A\rangle\langle B|, |A\rangle\langle C|, \\ |A\rangle\langle D|, |A\rangle\langle E| \end{array} \right\} \propto |n-k\rangle\langle\tilde{n}-k+1| \otimes |n'-k'\rangle\langle\tilde{n}'-l'+1| \text{ ②} \tag{G.22b}$$

$$|B\rangle\langle A| \propto |n-k+1\rangle\langle\tilde{n}-k| \otimes |n'-k'+1\rangle\langle\tilde{n}'-k'| \text{ ③} \tag{G.22c}$$

$$\left\{ \begin{array}{l} |B\rangle\langle B|, |B\rangle\langle C|, \\ |B\rangle\langle D|, |B\rangle\langle E| \end{array} \right\} \propto |n-k+1\rangle\langle\tilde{n}-k+1| \otimes |n'-k'+1\rangle\langle\tilde{n}'-k'+1| \text{ ④} \tag{G.22d}$$

$$|C\rangle\langle A| \propto |n-k\rangle\langle\tilde{n}-k-1| \otimes |n'-k'+1\rangle\langle\tilde{n}'-k'| \text{ ⑤} \tag{G.22e}$$

$$\left\{ \begin{array}{l} |C\rangle\langle B|, |C\rangle\langle C|, \\ |C\rangle\langle D|, |C\rangle\langle E| \end{array} \right\} \propto |n-k\rangle\langle\tilde{n}-k| \otimes |n'-k'+1\rangle\langle\tilde{n}'-k'+1| \text{ ⑥} \tag{G.22f}$$

$$|C\rangle\langle A| \propto |n-k\rangle\langle\tilde{n}-k-1| \otimes |n'-k'+1\rangle\langle\tilde{n}'-k'| \text{ ⑦} \tag{G.22g}$$

$$\left\{ \begin{array}{l} |D\rangle\langle B|, |D\rangle\langle C|, \\ |D\rangle\langle D|, |D\rangle\langle E| \end{array} \right\} \propto |n-k+1\rangle\langle\tilde{n}-k+1| \otimes |n'-k'\rangle\langle\tilde{n}'-k'| \text{ ⑧} \tag{G.22h}$$

$$|E\rangle\langle A| \propto |n-k\rangle\langle\tilde{n}-k-1| \otimes |n'-k'-1\rangle\langle\tilde{n}'-k'| \text{ ⑨} \tag{G.22i}$$

where again we have omitted the indices for brevity. From these expressions, we can build a table of the values of the indices $\tilde{n},\ \tilde{n}',\ k,\ k'$ given particular photon numbers $i,\ j$ in each mode.

	$\tilde{n}$	$\tilde{n}'$	k	k'
①	n	n'	$n-i$	$n'-j$
②	$n-1$	$n'-1$	$n-i$	$n'-j$
③	$n+1$	$n'+1$	$n+1-i$	$n'+1-j$
④	n	n'	$n+1-i$	$n'+1-j$
⑤	$n+1$	$n'+1$	$n-i$	$n'+1-j$
⑥	n	n'	$n-i$	$n'+1-j$
⑦	$n+1$	$n'+1$	$n+1-i$	$n'-j$
⑧	n	n'	$n+1-i$	$n'-j$
⑨	$n+1$	$n'+1$	$n-i$	$n'-j$

(G.23)

G.2.1 Probabilities

Using the results above, we can write the probability $P_{i,j}$ of finding $i,\ j$ photons in each mode. For simplicity we take $\beta = \alpha$.

$$P_{0,0} = \frac{e^{-2R|\alpha|^2}}{1+\lambda^2}\left[1 + R^4\left(1+T^2|\alpha|^2\right)^2\lambda^2 + 2R^2T^2|\alpha|^2\lambda\cos\left(\phi_1+\phi_2\right)\right] \tag{G.24a}$$

$$\begin{aligned} P_{1,1} =& \frac{e^{-2R|\alpha|^2}}{1+\lambda^2}\{R^4|\alpha|^4 + \left[R^4|\alpha|^2 + T^2\left(1-R^2|\alpha|^2\right)^2\right]^2\lambda^2 \\ &+ 2R^2T^2|\alpha|^2\left(1-R^2|\alpha|^2\right)^2\lambda\cos\left(\phi_1+\phi_2\right)\} \end{aligned} \tag{G.24b}$$

$$\begin{aligned} P_{2,2} =& \frac{e^{-2R|\alpha|^2}}{4\left(1+\lambda^2\right)}R^4|\alpha|^4\Big\{R^4|\alpha|^4 + \left[R^4|\alpha|^2 + T^2\left(2-R^2|\alpha|^2\right)^2\right]^2\lambda^2 \\ &+ 2R^2T^2|\alpha|^2\left(2-R^2|\alpha|^2\right)^2\lambda\cos\left(\phi_1+\phi_2\right)\Big\} \end{aligned} \tag{G.24c}$$

$$P_{1,0} = P_{0,1} = \frac{e^{-2R|\alpha|^2}}{1+\lambda^2}R^2\Big(T^2\lambda^2 + |\alpha|^2\left\{1 + \left[T^2 - R^2\left(1+T^2|\alpha|^2\right)\right]^2\lambda^2\right\} \tag{G.24d}$$

$$- 2T^2|\alpha|^2\left(1-R^2|\alpha|^2\right)\lambda\cos\left(\phi_1+\phi_2\right)\Big) \tag{G.24e}$$

$$\begin{aligned} P_{2,0} = P_{0,2} =& \frac{e^{-2R|\alpha|^2}}{2\left(1+\lambda^2\right)}R^4|\alpha|^2\Big\{|\alpha|^2 + \left(1+T^2|\alpha|^2\right)\left[R^4|\alpha|^2 + T^2\left(2-R^2|\alpha|^2\right)^2\right]\lambda^2 \\ &- 2T^2|\alpha|^2\left(2-R^2|\alpha|^2\right)\lambda\cos\left(\phi_1+\phi_2\right)\Big\} \end{aligned} \tag{G.24f}$$

$$\begin{aligned} P_{2,1} = P_{1,2} =& \frac{e^{-2R|\alpha|^2}}{2\left(1+\lambda^2\right)}R^2|\alpha|^2\Big\{R^4|\alpha|^4 + \big[R^8|\alpha|^4 + 2R^4T^6|\alpha|^6 + T^4\left(2-3R^2|\alpha|^2+R^4|\alpha|^4\right)^2 \\ &+ R^4T^2|\alpha|^2\left(5-6R^2|\alpha|^2+2R^4|\alpha|^4\right)\big]\lambda^2 \\ &+ 2R^2T^2|\alpha|^2\left(2-3R^2|\alpha|^2+R^4|\alpha|^4\right)\lambda\cos\left(\phi_1+\phi_2\right)\Big\} \end{aligned} \tag{G.24g}$$

Bibliography

[1] A. Einstein, M. Born, and H. Born, *The Born-Einstein letters: correspondence between Albert Einstein and Max and Hedwig Born from 1916 to 1955*, Walker (1971). 1

[2] A. Aspect, P. Grangier, and G. Roger, *Experimental Tests of Realistic Local Theories via Bell's Theorem*, Physical Review Letters, **47**, pp. 460–463 (1981). 3, 182

[3] A. Aspect, P. Grangier, and G. Roger, *Experimental Realization of Einstein-Podolsky-Rosen-Bohm Gedankenexperiment: A New Violation of Bell's Inequalities*, Physical Review Letters, **49**, pp. 91–94 (1982). 182

[4] Z. Y. Ou and L. Mandel, *Violation of Bell's Inequality and Classical Probability in a Two-Photon Correlation Experiment*, Physical Review Letters, **61**, pp. 50–53 (1988).

[5] P. G. Kwiat, K. Mattle, H. Weinfurter, A. Zeilinger, A. V. Sergienko, and Y. Shih, *New High-Intensity Source of Polarization-Entangled Photon Pairs*, Physical Review Letters, **75**, pp. 4337–4341 (1995).

[6] G. Weihs, T. Jennewein, C. Simon, H. Weinfurter, and A. Zeilinger, *Violation of Bell's Inequality under Strict Einstein Locality Conditions*, Physical Review Letters, **81**, pp. 5039–5043 (1998).

[7] M. A. Rowe, D. Kielpinski, V. Meyer, C. A. Sackett, W. M. Itano, C. Monroe, and D. J. Wineland, *Experimental violation of a Bell's inequality with efficient detection*, Nature, **409**, pp. 791–794 (2001).

[8] M. Ansmann, H. Wang, R. C. Bialczak, M. Hofheinz, E. Lucero, M. Neeley, A. D. O'Connell, D. Sank, M. Weides, J. Wenner, A. N. Cleland, and J. M. Martinis, *Violation of Bell's inequality in Josephson phase qubits*, Nature, **461**, pp. 504–506 (2009).

[9] K. C. Lee, M. R. Sprague, B. J. Sussman, J. Nunn, N. K. Langford, X.-M. Jin, T. Champion, P. Michelberger, K. F. Reim, D. England, D. Jaksch, and I. A. Walmsley, *Entangling Macroscopic Diamonds at Room Temperature*, Science, **334**, pp. 1253–1256 (2011).

[10] J. Hofmann, M. Krug, N. Ortegel, L. Gérard, M. Weber, W. Rosenfeld, and H. Weinfurter, *Heralded Entanglement Between Widely Separated Atoms*, Science, **337**, pp. 72–75 (2012).

[11] M. Giustina, A. Mech, S. Ramelow, B. Wittmann, J. Kofler, J. Beyer, A. Lita, B. Calkins, T. Gerrits, S. W. Nam, R. Ursin, and A. Zeilinger, *Bell violation using entangled photons without the fair-sampling assumption*, Nature, **497**, p. 227230 (2013). 3, 45, 116

[12] A. Einstein, B. Podolsky, and N. Rosen, *Can Quantum-Mechanical Description of Physical Reality Be Considered Complete?*, Physical Review, **47**, p. 777 (1935). 4, 36

[13] W. Heisenberg, *Über den anschaulichen Inhalt der quantentheoretischen Kinematik und Mechanik*, Zeitschrift für Physik, **43**, pp. 172–198 (1927). 4

[14] A. Peres and D. R. Terno, *Quantum information and relativity theory*, Reviews of Modern Physics, **76**, pp. 93–123 (2004). 5

[15] C. H. Bennett and G. Brassard, *Quantum Cryptography: Public key distribution and coin tossing*, Proceedings of the IEEE International Conference on Computers, Systems, and Signal Processing, Bangalore, p. 175 (1984). 6

[16] A. K. Ekert, *Quantum cryptography based on Bells theorem*, Physical Review Letters, **67**, pp. 661–663 (1991). 6

[17] M. A. Nielsen and I. L. Chuang, *Quantum computation and quantum information*, Cambridge University Press (2000). 6, 25, 36

[18] P. Shor, *Algorithms for quantum computation: discrete logarithms and factoring*, in *Foundations of Computer Science, Annual IEEE Symposium on*, pp. 124–134, IEEE Computer Society, Los Alamitos, CA, USA (1994). 6

[19] L. K. Grover, *A fast quantum mechanical algorithm for database search*, in *Proceedings of the twenty-eighth annual ACM symposium on Theory of computing*, STOC '96, p. 212219, ACM, New York, NY, USA (1996). 6

[20] C. H. Bennett, *Quantum cryptography using any two nonorthogonal states*, Physical Review Letters, **68**, pp. 3121–3124 (1992). 6

[21] C. M. Caves, *Quantum-mechanical noise in an interferometer*, Physical Review D, **23**, pp. 1693–1708 (1981). 6

[22] M. J. Holland and K. Burnett, *Interferometric detection of optical phase shifts at the Heisenberg limit*, Physical Review Letters, **71**, pp. 1355–1358 (1993). 6

[23] C. H. Bennett, G. Brassard, and S. Popescu, *Purification of noisy entanglement and faithful teleportation via noisy channels*, Physical Review Letters, **76**, pp. 722–725 (1996). 7, 36

[24] P. G. Kwiat, S. Barraza-Lopez, A. Stefanov, and N. Gisin, *Experimental entanglement distillation and 'hidden' non-locality*, Nature, **409**, pp. 1014–1017 (2001). 7, 37

[25] D. E. Browne, J. Eisert, S. Scheel, and M. B. Plenio, *Driving non-Gaussian to Gaussian states with linear optics*, Physical Review A, **67**, p. 062320 (2003). 7, 9, 38, 91, 197

[26] J. Eisert, D. Browne, S. Scheel, and M. B. Plenio, *Distillation of continuous-variable entanglement with optical means*, Annals of Physics, **311**, pp. 431–458 (2004). 38

[27] J. Eisert, M. Plenio, D. Browne, S. Scheel, and A. Feito, *On the experimental feasibility of continuous-variable optical entanglement distillation*, Optics and Spectroscopy, **103**, pp. 173–177 (2007). 7

[28] R. Dong, M. Lassen, and J. Heersink, *Experimental entanglement distillation of mesoscopic quantum states*, Nature Physics, **4**, pp. 919–923 (2008). 7, 37, 38, 93

[29] B. Hage, A. Samblowski, J. DiGuglielmo, J. Fiurášek, and R. Schnabel, *Iterative Entanglement Distillation: Approaching full Elimination of Decoherence*, Physical Review Letters, **105**, p. 230502 (2010). 93

[30] R. Dong, M. Lassen, J. Heersink, C. Marquardt, R. Filip, G. Leuchs, and U. L. Andersen, *Continuous-variable entanglement distillation of non-Gaussian mixed states*, Phys. Rev. A, **82**, p. 012312 (2010).

[31] H. Takahashi, J. S. Neergaard-Nielsen, M. Takeuchi, M. Takeoka, K. Hayasaka, A. Furusawa, and M. Sasaki, *Entanglement distillation from Gaussian input states*, Nature Photonics, **4**, pp. 178–181 (2010). 38, 43, 93

[32] Y. Kurochkin, A. S. Prasad, and A. I. Lvovsky, *Distillation of the two-mode squeezed state*, arXiv e-print 1307.3397 (2013). 7, 37, 43, 93, 94

[33] S. L. Braunstein and P. van Loock, *Quantum information with continuous variables*, Reviews of Modern Physics, **77**, pp. 513–577 (2005). 8, 36

[34] C. Silberhorn, T. C. Ralph, N. Lütkenhaus, and G. Leuchs, *Continuous Variable Quantum Cryptography: Beating the 3 dB Loss Limit*, Phys. Rev. Lett., **89**, p. 167901 (2002). 9

[35] P. J. Mosley, J. S. Lundeen, B. J. Smith, P. Wasylczyk, A. B. U'Ren, C. Silberhorn, and I. A. Walmsley, *Heralded Generation of Ultrafast Single Photons in Pure Quantum States*, Physical Review Letters, **100**, pp. 133601–4 (2008). 9, 10, 39, 91, 95

[36] H. B. Coldenstrodt-Ronge, *Experimental techniques for continuous variable photonic quantum information*, DPhil Thesis, Oxford University (2011). 9, 12, 123, 188

[37] T. J. Bartley, G. Donati, J. B. Spring, X.-M. Jin, M. Barbieri, A. Datta, B. J. Smith, and I. A. Walmsley, *Multiphoton state engineering by heralded interference between single photons and coherent states*, Physical Review A, **86**, p. 043820 (2012). 9, 152, 153, 154

[38] T. J. Bartley, G. Donati, X.-M. Jin, A. Datta, M. Barbieri, and I. A. Walmsley, *Direct Observation of Sub-Binomial Light*, Physical Review Letters, **110**, p. 173602 (2013). 9

[39] P. J. Mosley, *Generation of Heralded Single Photons in Pure Quantum States*, DPhil Thesis, University of Oxford (2007). 12, 95, 97, 101, 102, 103, 107, 123

[40] R. Loudon, *The quantum theory of light*, Oxford University Press (2000). 14, 148

[41] B. H. Bransden and C. C. J. Joachain, *Introduction to Quantum Mechanics*, Prentice Hall PTR (2000). 21

[42] C. C. Gerry and P. L. Knight, *Introductory quantum optics*, Cambridge University Press (2005). 23, 24

[43] E. Wigner, *On the Quantum Correction For Thermodynamic Equilibrium*, Physical Review, **40**, p. 749 (1932). 23, 151

[44] U. Leonhardt, *Measuring the Quantum State of Light*, Cambridge University Press (1997). 24, 26

[45] K. Vogel and H. Risken, *Determination of quasiprobability distributions in terms of probability distributions for the rotated quadrature phase*, Physical Review A, **40**, pp. 2847–2849 (1989). 26

[46] D. T. Smithey, M. Beck, M. G. Raymer, and A. Faridani, *Measurement of the Wigner distribution and the density matrix of a light mode using optical homodyne tomography: Application to squeezed states and the vacuum*, Physical Review Letters, **70**, pp. 1244–1247 (1993). 26, 119, 222

[47] I. L. Chuang and M. A. Nielsen, *Prescription for experimental determination of the dynamics of a quantum black box*, Journal of Modern Optics, **44**, pp. 2455–2467 (1997). 26

[48] J. F. Poyatos, J. I. Cirac, and P. Zoller, *Complete Characterization of a Quantum Process: The Two-Bit Quantum Gate*, Physical Review Letters, **78**, pp. 390–393 (1997). 26

[49] J. S. Lundeen, A. Feito, H. Coldenstrodt-Ronge, K. L. Pregnell, C. Silberhorn, T. C. Ralph, J. Eisert, M. B. Plenio, and I. A. Walmsley, *Tomography of quantum detectors*, Nature Physics, **5**, pp. 27–30 (2009). 26, 111

[50] R. Hudson, *When is the wigner quasi-probability density non-negative?*, Reports on Mathematical Physics, **6**, pp. 249–252 (1974). 27, 55, 142

[51] M. B. Plenio and S. Virmani, *An introduction to entanglement measures*, Quantum Information and Computation, **7**, p. 001 (2006). 27, 34

[52] G. Giedke and J. I. Cirac, *Characterization of Gaussian operations and distillation of Gaussian states*, Physical Review A, **66**, p. 032316 (2002). 37

[53] S. Olivares, *Quantum optics in the phase space*, The European Physical Journal Special Topics, **203**, pp. 3–24 (2012). 27

[54] C. Weedbrook, S. Pirandola, R. García-Patrón, N. J. Cerf, T. C. Ralph, J. H. Shapiro, and S. Lloyd, *Gaussian quantum information*, Reviews of Modern Physics, **84**, pp. 621–669 (2012). 28

[55] S. D. Bartlett, B. C. Sanders, S. L. Braunstein, and K. Nemoto, *Efficient Classical Simulation of Continuous Variable Quantum Information Processes*, Physical Review Letters, **88**, p. 097904 (2002). 28, 137

[56] A. Peres, *Separability Criterion for Density Matrices*, Physical Review Letters, **77**, p. 1413 (1996). 29, 35

[57] R. Horodecki, P. Horodecki, M. Horodecki, and K. Horodecki, *Quantum entanglement*, Reviews of Modern Physics, **81**, p. 865 (2009). 29

[58] S. M. Barnett and P. M. Radmore, *Methods in theoretical quantum optics*, Oxford University Press (2003). 30

[59] M. B. Plenio, *Logarithmic Negativity: A Full Entanglement Monotone That is not Convex*, Physical Review Letters, **95**, p. 090503 (2005). 34, 35

[60] M. Horodecki, P. Horodecki, and R. Horodecki, *Separability of mixed states: necessary and sufficient conditions*, Physics Letters A, **223**, pp. 1–8 (1996). 35

[61] K. Audenaert, M. B. Plenio, and J. Eisert, *Entanglement Cost under Positive-Partial-Transpose-Preserving Operations*, Physical Review Letters, **90**, p. 027901 (2003). 35

[62] J. Eisert and M. B. Plenio, *Introduction to the basics of entanglement theory in continuous-variable systems*, International Journal of Quantum Information, **1**, pp. 479–506 (2003). 36

[63] C. H. Bennett, H. J. Bernstein, S. Popescu, and B. Schumacher, *Concentrating partial entanglement by local operations*, Physical Review A, **53**, p. 2046 (1996). 36

[64] J. Eisert, S. Scheel, and M. B. Plenio, *Distilling Gaussian States with Gaussian Operations is Impossible*, Physical Review Letters, **89**, p. 137903 (2002). 37, 136, 143

[65] J. Fiurášek, *Gaussian transformations and distillation of entangled Gaussian states*, Physical Review Letters, **89**, p. 137904 (2002). 37

[66] B. Hage, A. Samblowski, and J. DiGuglielmo, *Preparation of distilled and purified continuous-variable entangled states*, Nature Physics, **4**, pp. 915–918 (2008). 38, 93

[67] A. Datta, L. Zhang, J. Nunn, N. K. Langford, A. Feito, M. B. Plenio, and I. A. Walmsley, *Compact Continuous-Variable Entanglement Distillation*, Physical Review Letters, **108**, p. 060502 (2012). 39, 150

[68] A. E. Lita, A. J. Miller, and S. W. Nam, *Counting near-infrared single-photons with 95% efficiency*, Optics Express, **16**, pp. 3032–3040 (2008). 39, 45, 116, 151

[69] G. Puentes, A. Datta, A. Feito, J. Eisert, M. B. Plenio, and I. A. Walmsley, *Entanglement quantification from incomplete measurements: applications using photon-number-resolving weak homodyne detectors*, New Journal of Physics, **12**, p. 033042 (2010). 39, 81, 183, 184, 186, 190, 195, 202

[70] T. Opatrný, G. Kurizki, and D.-G. Welsch, *Improvement on teleportation of continuous variables by photon subtraction via conditional measurement*, Physical Review A, **61**, p. 032302 (2000). 42, 58

[71] P. T. Cochrane, T. C. Ralph, and G. J. Milburn, *Teleportation improvement by conditional measurements on the two-mode squeezed vacuum*, Physical Review A, **65**, p. 062306 (2002). 42, 58, 59

[72] J. Wenger, R. Tualle-Brouri, and P. Grangier, *Non-Gaussian Statistics from Individual Pulses of Squeezed Light*, Physical Review Letters, **92**, p. 153601 (2004). 42

[73] N. Namekata, Y. Takahashi, G. Fujii, D. Fukuda, S. Kurimura, and S. Inoue, *Non-Gaussian operation based on photon subtraction using a photon-number-resolving detector at a telecommunications wavelength*, Nature Photonics, **4**, pp. 655–660 (2010). 42, 94

[74] B. G. Christensen, K. T. McCusker, J. B. Altepeter, B. Calkins, T. Gerrits, A. E. Lita, A. Miller, L. K. Shalm, Y. Zhang, S. W. Nam, N. Brunner, C. C. W. Lim, N. Gisin, and P. G. Kwiat, *Detection-Loophole-Free Test of Quantum Nonlocality, and Applications*, Physical Review Letters, **111**, p. 130406 (2013). 45

[75] A. Zavatta, S. Viciani, and M. Bellini, *Quantum-to-Classical Transition with Single-Photon-Added Coherent States of Light*, Science, **306**, pp. 660–662 (2004). 45, 151

[76] A. Zavatta, V. Parigi, and M. Bellini, *Experimental nonclassicality of single-photon-added thermal light states*, Physical Review A, **75**, p. 052106 (2007). 151

[77] V. Parigi, A. Zavatta, M. Kim, and M. Bellini, *Probing Quantum Commutation Rules by Addition and Subtraction of Single Photons to/from a Light Field*, Science, **317**, pp. 1890–1893 (2007). 137

[78] M. S. Kim, H. Jeong, A. Zavatta, V. Parigi, and M. Bellini, *Scheme for Proving the Bosonic Commutation Relation Using Single-Photon Interference*, Physical Review Letters, **101**, p. 260401 (2008). 45

[79] D. E. Browne, *Generation and Manipulation of Entanglement in Quantum Optical Systems*, PhD Thesis, Imperial College, London (2004). 45

[80] S.-Y. Lee, S.-W. Ji, H.-J. Kim, and H. Nha, *Enhancing quantum entanglement for continuous variables by a coherent superposition of photon subtraction and addition*, Physical Review A, **84**, p. 012302 (2011). 45, 58

[81] S. L. Braunstein and H. J. Kimble, *Teleportation of Continuous Quantum Variables*, Physical Review Letters, **80**, pp. 869–872 (1998). 48, 58

[82] C. Navarrete-Benlloch, R. García-Patrón, J. H. Shapiro, and N. J. Cerf, *Enhancing quantum entanglement by photon addition and subtraction*, Physical Review A, **86**, p. 012328 (2012). 55

[83] C. H. Bennett, G. Brassard, C. Crépeau, R. Jozsa, A. Peres, and W. K. Wootters, *Teleporting an unknown quantum state via dual classical and Einstein-Podolsky-Rosen channels*, Physical Review Letters, **70**, pp. 1895–1899 (1993). 58

[84] L. Vaidman, *Teleportation of quantum states*, Physical Review A, **49**, pp. 1473–1476 (1994).

[85] T. C. Ralph and P. K. Lam, *Teleportation with Bright Squeezed Light*, Physical Review Letters, **81**, pp. 5668–5671 (1998). 61

[86] A. Furusawa, J. L. Sørensen, S. L. Braunstein, C. A. Fuchs, H. J. Kimble, and E. S. Polzik, *Unconditional Quantum Teleportation*, Science, **282**, pp. 706–709 (1998). 61

[87] D. Bouwmeester, J.-W. Pan, K. Mattle, M. Eibl, H. Weinfurter, and A. Zeilinger, *Experimental quantum teleportation*, Nature, **390**, pp. 575–579 (1997). 58

[88] S. Olivares, M. G. A. Paris, and R. Bonifacio, *Teleportation improvement by inconclusive photon subtraction*, Physical Review A, **67**, p. 032314 (2003). 58

[89] H. F. Hofmann, T. Ide, T. Kobayashi, and A. Furusawa, *Fidelity and information in the quantum teleportation of continuous variables*, Physical Review A, **62**, p. 062304 (2000). 59

[90] F. Grosshans and P. Grangier, *Quantum cloning and teleportation criteria for continuous quantum variables*, Physical Review A, **64**, p. 010301 (2001). 61

[91] T. J. Bartley, P. J. D. Crowley, A. Datta, J. Nunn, L. Zhang, and I. Walmsley, *Strategies for enhancing quantum entanglement by local photon subtraction*, Physical Review A, **87**, p. 022313 (2013). 63

[92] M. A. Nielsen, *Conditions for a Class of Entanglement Transformations*, Physical Review Letters, **83**, pp. 436–439 (1999). 65

[93] *DLMF: 26.4 Lattice Paths: Multinomial Coefficients and Set Partitions*. 69

[94] A. Kitagawa, M. Takeoka, M. Sasaki, and A. Chefles, *Entanglement evaluation of non-Gaussian states generated by photon subtraction from squeezed states*, Physical Review A, **73**, p. 042310 (2006). 70, 74

[95] S. L. Zhang and P. van Loock, *Distillation of mixed-state continuous-variable entanglement by photon subtraction*, Physical Review A, **82**, p. 062316 (2010). 70, 71, 73, 74, 75, 82, 87

[96] A. Cantoni and P. Butler, *Eigenvalues and eigenvectors of symmetric centrosymmetric matrices*, Linear Algebra and its Applications, **13**, pp. 275–288 (1976). 73

[97] J. Eisert, F. G. S. L. Brandão, and K. M. R. Audenaert, *Quantitative entanglement witnesses*, New Journal of Physics, **9**, p. 46 (2007). 81

[98] A. Ourjoumtsev, A. Dantan, R. Tualle-Brouri, and P. Grangier, *Increasing entanglement between Gaussian states by coherent photon subtraction*, Physical Review Letters, **98**, p. 030502 (2007). 93

[99] H. Hansen, T. Aichele, C. Hettich, P. Lodahl, A. I. Lvovsky, J. Mlynek, and S. Schiller, *Ultrasensitive pulsed, balanced homodyne detector: application to time-domain quantum measurements*, Optics Letters, **26**, pp. 1714–1716 (2001). 94, 120

[100] A. Zavatta, S. Viciani, and M. Bellini, *Tomographic reconstruction of the single-photon Fock state by high-frequency homodyne detection*, Physical Review A, **70**, p. 053821 (2004). 94

[101] A. Ourjoumtsev, R. Tualle-Brouri, J. Laurat, and P. Grangier, *Generating optical Schrodinger kittens for quantum information processing*, Science, **312**, pp. 83–86 (2006). 143, 144, 151

[102] Y. Eto, T. Tajima, Y. Zhang, and T. Hirano, *Observation of squeezed light at 1.535 μm using a pulsed homodyne detector*, Optics Letters, **32**, pp. 1698–1700 (2007).

[103] A. Ourjoumtsev, F. Ferreyrol, R. Tualle-Brouri, and P. Grangier, *Preparation of non-local superpositions of quasi-classical light states*, Nature Physics, **5**, pp. 189–192 (2009). 94

[104] M. D. Eisaman, J. Fan, A. Migdall, and S. V. Polyakov, *Invited Review Article: Single-photon sources and detectors*, Review of Scientific Instruments, **82**, p. 071101 (2011). 94

[105] C. K. Hong, Z. Y. Ou, and L. Mandel, *Measurement of subpicosecond time intervals between two photons by interference*, Physical Review Letters, **59**, pp. 2044–2046 (1987). 95, 123, 149

[106] F. Marsili, V. B. Verma, J. A. Stern, S. Harrington, A. E. Lita, T. Gerrits, I. Vayshenker, B. Baek, M. D. Shaw, R. P. Mirin, and S. W. Nam, *Detecting single infrared photons with 93% system efficiency*, Nature Photonics, **7**, pp. 210–214 (2013). 96

[107] R. W. Boyd, *Nonlinear optics*, Academic Press (2008). 97

[108] D. N. Klyshko, *Use of two-photon light for absolute calibration of photoelectric detectors*, Soviet Journal of Quantum Electronics, **10**, pp. 1112–1117 (1980). 107

[109] A. Worsley, *Measurement of the joint statistics of a single photon source generating pure quantum states*, MPhys thesis, University of Oxford, Oxford (2008). 108

[110] A. P. Worsley, H. B. Coldenstrodt-Ronge, J. S. Lundeen, P. J. Mosley, B. J. Smith, G. Puentes, N. Thomas-Peter, and I. A. Walmsley, *Absolute efficiency estimation of photon-number-resolving detectors using twin beams*, Optics Express, **17**, p. 4397 (2009). 108, 117, 152, 154, 188

[111] L. Zhang, H. B. Coldenstrodt-Ronge, A. Datta, G. Puentes, J. S. Lundeen, X.-M. Jin, B. J. Smith, M. B. Plenio, and I. A. Walmsley, *Mapping coherence in measurement via full quantum tomography of a hybrid optical detector*, Nature Photonics, **6**, pp. 364–368 (2012). 111

[112] N. Bohr, *The Quantum Postulate and the Recent Development of Atomic Theory*, Nature, **121**, pp. 580–590 (1928). 112

[113] M. Born, *Quantenmechanik der Stoßvorgänge*, Zeitschrift für Physik, **38**, pp. 803–827 (1926). 114

[114] J. A. Wheeler and W. H. Zurek, *Quantum Theory and Measurement*, Princeton University Press (1984). 114

[115] D. H. Smith, G. Gillett, M. P. de Almeida, C. Branciard, A. Fedrizzi, T. J. Weinhold, A. Lita, B. Calkins, T. Gerrits, H. M. Wiseman, S. W. Nam, and A. G. White, *Conclusive quantum steering with superconducting transition-edge sensors*, Nature Communications, **3**, p. 625 (2012). 116

[116] D. Achilles, C. Silberhorn, C. Sliwa, K. Banaszek, I. A. Walmsley, M. J. Fitch, B. C. Jacobs, T. B. Pittman, and J. D. Franson, *Photon-number-resolving detection using time-multiplexing*, Journal of Modern Optics, **51**, p. 1499 (2004). 116, 121

[117] J. Sperling, W. Vogel, and G. S. Agarwal, *True photocounting statistics of multiple on-off detectors*, Physical Review A, **85**, p. 023820 (2012). 116, 152, 154

[118] H. B. Coldenstrodt-Ronge, J. S. Lundeen, K. L. Pregnell, A. Feito, B. J. Smith, W. Mauerer, C. Silberhorn, J. Eisert, M. B. Plenio, and I. A. Walmsley, *A proposed testbed for detector tomography*, Journal of Modern Optics, **56**, pp. 432–441 (2009). 117, 150, 152, 188

[119] M. Cooper, M. Karpinski, and B. J. Smith, *Quantum state estimation with unknown measurements*, arXiv e-print 1306.6431 (2013). 118

[120] H. P. Yuen and V. W. S. Chan, *Noise in homodyne and heterodyne detection*, Optics Letters, **8**, pp. 177–179 (1983). 118

[121] A. I. Lvovsky and M. G. Raymer, *Continuous-variable optical quantum-state tomography*, Reviews of Modern Physics, **81**, pp. 299–332 (2009). 119

[122] O. Haderka, V. Michálek, V. Urbášek, and M. Ježek, *Fast time-domain balanced homodyne detection of light*, Applied Optics, **48**, pp. 2884–2889 (2009). 120

[123] R. Kumar, E. Barrios, A. MacRae, E. Cairns, E. Huntington, and A. Lvovsky, *Versatile wideband balanced detector for quantum optical homodyne tomography*, Optics Communications, **285**, pp. 5259–5267 (2012).

[124] M. F. Cooper, C. Söller, and B. J. Smith, *High-stability time-domain balanced homodyne detector for ultrafast optical pulse applications*, Journal of Modern Optics, **60**, pp. 611–616 (2013). 120

[125] G. Puentes, J. S. Lundeen, M. P. A. Branderhorst, H. B. Coldenstrodt-Ronge, B. J. Smith, and I. A. Walmsley, *Bridging Particle and Wave Sensitivity in a*

Configurable Detector of Positive Operator-Valued Measures, Physical Review Letters, **102**, p. 080404 (2009). 120

[126] R. W. P. Drever, J. L. Hall, F. V. Kowalski, J. Hough, G. M. Ford, A. J. Munley, and H. Ward, *Laser phase and frequency stabilization using an optical resonator*, Applied Physics B, **31**, pp. 97–105 (1983). 130, 132

[127] G. Jotzu, *Methods for Measuring and Manipulating Quantum States of Light*, MPhil Project, Oxford (2009). 131

[128] G. Jotzu, T. J. Bartley, H. B. Coldenstrodt-Ronge, B. J. Smith, and I. A. Walmsley, *Continuous phase stabilization and active interferometer control using two modes*, Journal of Modern Optics, **59**, pp. 42–45 (2012). 131, 222

[129] S. Pancharatnam, *Generalized theory of interference, and its applications*, Proceedings of the Indian Academy of Sciences - Section A, **44**, pp. 247–262 (1956). 132, 135

[130] M. Berry, *The Geometric Phase*, Scientific American; (USA), **259:6** (1988). 132, 135

[131] D. Elser, T. Bartley, B. Heim, C. Wittmann, D. Sych, and G. Leuchs, *Feasibility of free space quantum key distribution with coherent polarization states*, New Journal of Physics, **11**, p. 045014 (2009). 132

[132] S. Lloyd and S. L. Braunstein, *Quantum Computation over Continuous Variables*, Physical Review Letters, **82**, pp. 1784–1787 (1999). 137

[133] J. Niset, J. Fiurášek, and N. J. Cerf, *No-Go Theorem for Gaussian Quantum Error Correction*, Physical Review Letters, **102**, p. 120501 (2009). 137, 143

[134] A. I. Lvovsky and J. Mlynek, *Quantum-Optical Catalysis: Generating Nonclassical States of Light by Means of Linear Optics*, Physical Review Letters, **88**, p. 250401 (2002). 137, 148, 153

[135] S. Scheel, K. Nemoto, W. J. Munro, and P. L. Knight, *Measurement-induced nonlinearity in linear optics*, Physical Review A, **68**, p. 032310 (2003). 137, 145

[136] A. Ourjoumtsev, H. Jeong, R. Tualle-Brouri, and P. Grangier, *Generation of optical "Schrödinger cats" from photon number states*, Nature, **448**, pp. 784–786 (2007). 137, 151

[137] R. Blandino, F. Ferreyrol, M. Barbieri, P. Grangier, and R. Tualle-Brouri, *Characterization of a π-phase shift quantum gate for coherent-state qubits*, New Journal of Physics, **14**, p. 013017 (2012). 137

[138] K. Sanaka, K. J. Resch, and A. Zeilinger, *Filtering Out Photonic Fock States*, Physical Review Letters, **96**, p. 083601 (2006). 137, 138, 147, 149

[139] K. J. Resch, J. L. O'Brien, T. J. Weinhold, K. Sanaka, B. P. Lanyon, N. K. Langford, and A. G. White, *Entanglement Generation by Fock-State Filtration*, Physical Review Letters, **98**, p. 203602 (2007).

[140] F. Ferreyrol, M. Barbieri, R. Blandino, S. Fossier, R. Tualle-Brouri, and P. Grangier, *Implementation of a Nondeterministic Optical Noiseless Amplifier*, Physical Review Letters, **104**, p. 123603 (2010).

[141] G. Y. Xiang, T. C. Ralph, A. P. Lund, N. Walk, and G. J. Pryde, *Heralded noiseless linear amplification and distillation of entanglement*, Nature Photonics, **4**, pp. 316–319 (2010). 137

[142] H. Jeong and T. Ralph, *Schrodinger cat states for quantum information processing*, in N. J. Cerf, G. Leuchs, and E. S. Polzik (editors), *Quantum information with continuous variables of atoms and light*, Imperial College Press, London (2007). 143

[143] E. Schrödinger, *Die gegenwärtige Situation in der Quantenmechanik*, Die Naturwissenschaften, **23**, pp. 807–812 (1935). 143

[144] A. P. Lund, H. Jeong, T. C. Ralph, and M. S. Kim, *Conditional production of superpositions of coherent states with inefficient photon detection*, Physical Review A, **70**, p. 020101 (2004). 143

[145] M. Dakna, T. Anhut, T. Opatrný, L. Knöll, and D.-G. Welsch, *Generating Schrödinger-cat-like states by means of conditional measurements on a beam splitter*, Physical Review A, **55**, pp. 3184–3194 (1997). 144

[146] J. S. Neergaard-Nielsen, B. Melholt Nielsen, C. Hettich, K. Mølmer, and E. S. Polzik, *Generation of a superposition of odd photon number states for quantum information networks*, Physical Review Letters, **97**, p. 083604 (2006).

[147] H. Takahashi, K. Wakui, and S. Suzuki, *Generation of large-amplitude coherent-state superposition via ancilla-assisted photon subtraction*, Physical Review Letters, **101**, p. 233605 (2008).

[148] T. Gerrits, S. Glancy, T. S. Clement, B. Calkins, A. E. Lita, A. J. Miller, A. L. Migdall, S. W. Nam, R. P. Mirin, and E. Knill, *Generation of optical coherent-state superpositions by number-resolved photon subtraction from the squeezed vacuum*, Physical Review A, **82**, p. 031802 (2010). 144, 151

[149] E. Bimbard, N. Jain, A. MacRae, and A. I. Lvovsky, *Quantum-optical state engineering up to the two-photon level*, Nature Photonics, **4**, pp. 243–247 (2010). 145

[150] T. S. Iskhakov, A. M. Pérez, K. Y. Spasibko, M. V. Chekhova, and G. Leuchs, *Superbunched bright squeezed vacuum state*, Optics Letters, **37**, pp. 1919–1921 (2012). 148

[151] K. F. Reim, J. Nunn, X.-M. Jin, P. S. Michelberger, T. F. M. Champion, D. G. England, K. C. Lee, W. S. Kolthammer, N. K. Langford, and I. A. Walmsley, *Multipulse Addressing of a Raman Quantum Memory: Configurable Beam Splitting and Efficient Readout*, Physical Review Letters, **108**, p. 263602 (2012). 150

[152] J. Sperling, W. Vogel, and G. S. Agarwal, *Sub-Binomial Light*, Physical Review Letters, **109**, p. 093601 (2012). 150, 153, 201

[153] K. Laiho, K. N. Cassemiro, D. Gross, and C. Silberhorn, *Probing the Negative Wigner Function of a Pulsed Single Photon Point by Point*, Physical Review Letters, **105**, p. 253603 (2010). 151, 152

[154] R. J. Glauber, *Photon Correlations*, Physical Review Letters, **10**, pp. 84–86 (1963). 151

[155] E. C. G. Sudarshan, *Equivalence of Semiclassical and Quantum Mechanical Descriptions of Statistical Light Beams*, Physical Review Letters, **10**, pp. 277–279 (1963).

[156] W. Vogel and D.-G. Welsch, *Quantum Optics: An Introduction*, Wiley (2006). 151

[157] A. I. Lvovsky, H. Hansen, T. Aichele, O. Benson, J. Mlynek, and S. Schiller, *Quantum State Reconstruction of the Single-Photon Fock State*, Physical Review Letters, **87**, p. 050402 (2001). 151

[158] A. Mari, K. Kieling, B. M. Nielsen, E. S. Polzik, and J. Eisert, *Directly Estimating Nonclassicality*, Physical Review Letters, **106**, p. 010403 (2011). 151

[159] L. Mandel, *Sub-Poissonian photon statistics in resonance fluorescence*, Optics Letters, **4**, pp. 205–207 (1979). 151, 202

[160] R. Short and L. Mandel, *Observation of Sub-Poissonian Photon Statistics*, Physical Review Letters, **51**, pp. 384–387 (1983).

[161] J. G. Rarity, K. D. Ridley, and P. R. Tapster, *Absolute measurement of detector quantum efficiency using parametric downconversion*, Applied Optics, **26**, pp. 4616–4619 (1987).

[162] G. Zambra, A. Andreoni, M. Bondani, M. Gramegna, M. Genovese, G. Brida, A. Rossi, and M. G. A. Paris, *Experimental Reconstruction of Photon Statistics without Photon Counting*, Physical Review Letters, **95**, p. 063602 (2005).

[163] A. B. U'Ren, C. Silberhorn, J. L. Ball, K. Banaszek, and I. A. Walmsley, *Characterization of the nonclassical nature of conditionally prepared single photons*, Physical Review A, **72**, p. 021802 (2005).

[164] F. Bussires, J. A. Slater, N. Godbout, and W. Tittel, *Fast and simple characterization of a photon pair source*, Optics Express, **16**, pp. 17060–17069 (2008).

[165] M. Avenhaus, K. Laiho, M. V. Chekhova, and C. Silberhorn, *Accessing Higher Order Correlations in Quantum Optical States by Time Multiplexing*, Physical Review Letters, **104**, p. 063602 (2010). 151, 152

[166] J. Kim, S. Takeuchi, Y. Yamamoto, and H. H. Hogue, *Multiphoton detection using visible light photon counter*, Applied Physics Letters, **74**, pp. 902–904 (1999). 151

[167] E. Waks, E. Diamanti, B. C. Sanders, S. D. Bartlett, and Y. Yamamoto, *Direct Observation of Nonclassical Photon Statistics in Parametric Down-Conversion*, Physical Review Letters, **92**, p. 113602 (2004). 151

[168] T. Gerrits, N. Thomas-Peter, J. C. Gates, A. E. Lita, B. J. Metcalf, B. Calkins, N. A. Tomlin, A. E. Fox, A. L. Linares, J. B. Spring, N. K. Langford, R. P. Mirin, P. G. R. Smith, I. A. Walmsley, and S. W. Nam, *On-chip, photon-number-resolving, telecommunication-band detectors for scalable photonic information processing*, Physical Review A, **84**, p. 060301 (2011).

[169] G. Brida, L. Ciavarella, I. P. Degiovanni, M. Genovese, L. Lolli, M. G. Mingolla, F. Piacentini, M. Rajteri, E. Taralli, and M. G. A. Paris, *Quantum characterization of superconducting photon counters*, New Journal of Physics, **14**, p. 085001 (2012). 151

[170] H. B. Coldenstrodt-Ronge, B. J. Smith, G. Puentes, J. S. Lundeen, A. Feito, A. Datta, P. J. Mosley, J. Eisert, M. Plenio, and I. A. Walmsley, *Joint Photon Statistics of Photon-Subtracted Squeezed Light*, in *Conference on Lasers and Electro-Optics/International Quantum Electronics Conference*, OSA Technical Digest (CD), Optical Society of America (2009). 155

[171] L. Dovrat, M. Bakstein, A. Shaham, E. Megidish, A. Halevy, L. Cohen, D. Istrati, and H. Eisenberg, *Direct Measurements of the Non-classicality Degree in Photon-number Correlations*, in *Research in Optical Sciences*, OSA Technical Digest, Optical Society of America (2012). 155

[172] T. Amri, J. Laurat, and C. Fabre, *Characterizing Quantum Properties of a Measurement Apparatus: Insights from the Retrodictive Approach*, Physical Review Letters, **106**, p. 020502 (2011). 157

[173] W. K. Wootters, *Entanglement of Formation of an Arbitrary State of Two Qubits*, Physical Review Letters, **80**, pp. 2245–2248 (1998). 181

[174] L.-M. Duan, G. Giedke, J. I. Cirac, and P. Zoller, *Inseparability Criterion for Continuous Variable Systems*, Physical Review Letters, **84**, pp. 2722–2725 (2000). 181

[175] J. S. Bell, *On the Einstein Podolsky Rosen Paradox*, Physics, **1**, pp. 195–200 (1964). 182

[176] P. Grangier, M. J. Potasek, and B. Yurke, *Probing the phase coherence of parametrically generated photon pairs: A new test of Bell's inequalities*, Physical Review A, **38**, pp. 3132–3135 (1988). 183

[177] A. Kuzmich, I. A. Walmsley, and L. Mandel, *Violation of Bell's Inequality by a Generalized Einstein-Podolsky-Rosen State Using Homodyne Detection*, Physical Review Letters, **85**, pp. 1349–1353 (2000). 183

[178] J.-Å. Larsson and R. D. Gill, *Bell's inequality and the coincidence-time loophole*, Europhysics Letters, **67**, pp. 707–713 (2004). 198

[179] M. Vidrighin, T. J. Bartley, G. Donati, X.-M. Jin, M. Barbieri, W. S. Kolthammer, A. Datta, and I. A. Walmsley, *Requirements for two-source entanglement concentration*, Quantum Measurements and Quantum Metrology, **1**, pp. 5–11 (2013). 203

[180] G. Harder, V. Ansari, B. Brecht, T. Dirmeier, C. Marquardt, and C. Silberhorn, *An optimized photon pair source for quantum circuits*, Optics Express, **21**, pp. 13975–13985 (2013). 205

[181] B. Calkins, P. L. Mennea, A. E. Lita, B. J. Metcalf, W. S. Kolthammer, A. L. Linares, J. B. Spring, P. C. Humphreys, R. P. Mirin, J. C. Gates, P. G. R. Smith, I. A. Walmsley, T. Gerrits, and S. W. Nam, *High quantum-efficiency photon-number-resolving detector for photonic on-chip information processing*, Optics Express, **21**, pp. 22657–22670 (2013). 205

[182] A. Gnauck and P. Winzer, *Optical phase-shift-keyed transmission*, Journal of Lightwave Technology, **23**, pp. 115–130 (2005). 222

[183] K. Creath, *V Phase-Measurement Interferometry Techniques*, in E. Wolf (editor), *Progress in Optics*, volume 26, pp. 349–393, Elsevier (1988). 222

[184] T. Zhang, C. Borca, X. Li, and S. Cundiff, *Optical two-dimensional Fourier transform spectroscopy with active interferometric stabilization*, Optics Express, **13**, pp. 7432–7441 (2005). 222

[185] M. P. A. Branderhorst, P. Londero, P. Wasylczyk, C. Brif, R. L. Kosut, H. Rabitz, and I. A. Walmsley, *Coherent Control of Decoherence*, Science, **320**, pp. 638–643 (2008).

[186] D. Brinks, F. D. Stefani, F. Kulzer, R. Hildner, T. H. Taminiau, Y. Avlasevich, K. Müllen, and N. F. van Hulst, *Visualizing and controlling vibrational wave packets of single molecules*, Nature, **465**, pp. 905–908 (2010). 222

[187] J. Sebby-Strabley, M. Anderlini, P. S. Jessen, and J. V. Porto, *Lattice of double wells for manipulating pairs of cold atoms*, Physical Review A, **73**, p. 033605 (2006). 222

[188] H. Gersen, T. J. Karle, R. J. P. Engelen, W. Bogaerts, J. P. Korterik, N. F. van Hulst, T. F. Krauss, and L. Kuipers, *Real-Space Observation of Ultraslow Light in Photonic Crystal Waveguides*, Physical Review Letters, **94**, p. 073903 (2005). 222

[189] A. A. Freschi and J. Frejlich, *Adjustable phase control in stabilized interferometry*, Optics Letters, **20**, pp. 635–637 (1995). 222, 223

[190] V. V. Krishnamachari, E. R. Andresen, S. R. Keiding, and E. O. Potma, *An active interferometer-stabilization scheme with linear phase control*, Optics Express, **14**, pp. 5210–5215 (2006). 223

[191] V. Greco, G. Molesini, and F. Quercioli, *Accurate polarization interferometer*, Review of Scientific Instruments, **66**, pp. 3729–3734 (1995). 224

[192] M. A. Zumberge, J. Berger, M. A. Dzieciuch, and R. L. Parker, *Resolving Quadrature Fringes in Real Time*, Applied Optics, **43**, pp. 771–775 (2004). 224

[193] J. Bechhoefer, *Feedback for physicists: A tutorial essay on control*, Reviews of Modern Physics, **77**, pp. 783–836 (2005). 225, 227